RICE UNIVERSITY

Quantum Simulation of the Hubbard Model: Higher Symmetry Fermions and New Architectures

By

Eduardo Ibarra Garcia Padilla

A THESIS SUBMITTED
IN PARTIAL FULFILLMENT OF THE
REQUIREMENTS FOR THE DEGREE

Doctor of Philosophy

APPROVED, THESIS COMMITTEE

Kaden Hazzard
Kaden Hazzard (Aug 20, 2022 13:49 CDT)

Kaden R.A. Hazzard
Professor of Physics and Astronomy

Thomas Killian

Thomas C. Killian
Dean of the Wiess School of Natural Sciences
Professor of Physics and Astronomy

Gustavo Scuseria
Gustavo Scuseria (Aug 19, 2022 18:37 CDT)

Gustavo E. Scuseria
Robert A. Welch Professor of Chemistry
Professor of Physics and Astronomy
Professor of Materials Science and NanoEngineering

HOUSTON, TEXAS

August 2022

RICE UNIVERSITY

Quantum Simulation of the Hubbard Model: Higher Symmetry Fermions and New Architectures

by

Eduardo Ibarra García Padilla

A Thesis Submitted
in Partial Fulfillment of the
Requirements for the degree

Doctor of Philosophy

Approved, Committee:

Kaden R. A. Hazzard, Chair
Professor of Physics and Astronomy

Thomas C. Killian
Dean of the Wiess School of Natural Sciences
Professor of Physics and Astronomy

Gustavo Scuseria
Robert A. Welch Professor of Chemistry
Professor of Physics and Astronomy
Professor of Materials Science and NanoEngineering

Houston, Texas

Aug, 2022

Si puedes mirar, ve. Si puedes ver, repara.

Ensayo sobre la ceguera. José Saramago

No lo van a impedir la golondrinas,
Ni ventanales rotos, ni lunas nuevas,
Ni todos los andamios, ni las hormigas,
Ni flores, ni herejías, ni colmeneras.

No lo van a impedir los corre mundos,
Ni los soldados, ni las primaveras,
Ni aun negándolo el viento de muro en muro,
Ni aun negándolo, al fin, donde se crea.

No lo van a impedir ni andén, ni esquina,
Ni el temor de la virgen si obscurece,
Ni el humo de las calles y llovizna,
Ni el canto del verano que anochece.

No lo van a impedir ni el falso amigo,
Ni el que alimenta el cepo y la tortura,
Ni el pequeño ladrón de mano fría,
Ni el terrible don Juan de cara dura.

No lo van a impedir ni moralistas,
Ni el indiscreto encanto del embrujo,
Ni ausentes millonarios, ni arribistas,
Ni aspirantes al hacha del verdugo.

No lo van a impedir las bandoleras,
Ni el letrado galán de poco vuelo,
Ni inquisidores, ni aguafiestas,
Ni eternos sembradores de veneno.

No lo van a impedir los enemigos,
Ni atentos intimistas alabados,
Ni burócratas tiernos, ni podridos,
Ni herederos, ni apóstoles errados.

No lo van a impedir del valle al cielo,
Ni reyes del honor, ni periodistas,
Ni antiguos comediantes, ni embusteros,
Ni estudiantes de leyes, ni alquimistas.

No lo van a impedir los generales,
Ni adorables doncellas pervertidas,
Ni apelables procesos judiciales,
Ni perros, ni cometas, ni suicidas.

No lo van a impedir ni prohibidos,
Ni novios convencidos, ni hechiceros,
No lo van a impedir las soledades
A pesar del otoño creceremos,
Creceremos.

No lo van a impedir, Amaury Pérez

Abstract

Quantum Simulation of the Hubbard Model:

Higher Symmetry Fermions and New Architectures

by

Eduardo Ibarra García Padilla

Over the past few decades, quantum simulation with ultracold atoms in optical lattices has proven to be a useful tool for understanding many-body Hamiltonians. One of its primary directions is the experimental study of the Fermi Hubbard Model (FHM), which aims to capture the fundamental properties of cuprate superconductors and has produced a wide range of intriguing phenomena, including the metal-to-Mott insulator transition, antiferromagnetism, strange metallicity, pseudogap physics, and is frequently used in the study of superconductivity. In recent years, new kinds of quantum simulators have emerged, and in particular we focus on two of them: 1) quantum simulators that study high symmetry fermions in optical lattices, and 2) optical tweezer arrays which provide a bottom-up approach to engineering the FHM.

The first class of emerging quantum simulators utilizes alkaline-earth-like atoms (AEA's) – which have large nuclear spin I (such as ^{173}Yb and ^{87}Sr) – to engineer the SU($N = 2I+1$) symmetric FHM, where $N = 2, \ldots, 10$. The second class corresponds to quantum simulators based on optical tweezer arrays which combine deterministic single tweezer ground state loading and tunneling coupled sites. Both classes of quantum simulators are interesting on their own. For example, the SU(N) FHM is generating a lot of interest due to its connections to multiorbital solid state systems and theoretical predictions of rich phase diagrams which exhibit exotic phases of matter, including unusual ones like spin liquids. On the other hand, optical tweezer arrays have gained a lot of attention since they can be used to study arbitrary geometries and access very low-entropy samples.

This thesis reports on the numerical study of both quantum simulation architec-

tures. Results of the SU(N) FHM at finite temperature, for different fillings and interaction strengths that span the non-interacting to the strongly interacting limit are obtained using Determinant Quantum Monte Carlo, Exact Diagonalization, and Numerical Linked Cluster Expansion. In particular, we focus on how thermodynamic and magnetic observables, such as the number of on-site pairs, energy, entropy, spin correlations, and structure factors depend on N, the interaction strength U/t, temperature T/t, and the anisotropy of tunneling rates. Our results demonstrate that in a homogeneous square lattice with one particle per site on average, thermodynamic observables as a function of temperature obey a universal scaling with N, and that short-range antiferromagnetic correlations are stronger for larger N and in lower dimensions. In addition, we present theory-experiment comparisons where possible, where we perform thermometry and provide a precise characterization of the equation of state of the SU(N) FHM. Our results emerge as a tool to perform thermometry in experiments from theory-experiment comparison and also provide guidance for future experiments with AEAs in optical lattices.

Additionally, we present calculations using numerically precise discrete variable representation methods for two-dimensional stroboscopic tweezer arrays and compare the outcomes with experimental data. We quantify the effects of stroboscopic potentials on Hubbard parameters like the interaction strength U and the tunneling t in optical tweezer arrays and illustrate how heating from the stroboscopic potential relies on strobe frequency. Our calculations enable evaluation and optimization of two-dimensional tweezer array experiments.

An important milestone of the results of this thesis corresponds to the record temperatures and entropies achieved with these quantum simulation architectures: 1) the coldest fermions ever created in nature in absolute temperature and in cold atoms, and 2) the lowest entropy per particle fermions ever created, albeit in a so-far small system.

Acknowledgements

La vida no es la que uno vivió, sino la que recuerda
y cómo la recuerda para contarla.

Vivir para contarla. Gabriel García Márquez

Writing the acknowledgment section has always been the best part of writing any type of document that marks the conclusion of an stage, and as so provides me with the opportunity to reflect not only on what I learnt in every aspect of my life, not limited to the academic environment, and also thank the people who have played an important role during that time.

I would like to start by thanking my parents, Claudia and Eduardo, this has been an journey where I know that although you didn't experiment in first person the hassles, frustrations and difficulties, you tried to understand and hear them. You have always been here to support me and I am more than grateful for the opportunity we have to see each other often or play board games over Steam. As a way of acknowledging this I wanted to start this thesis with the song of the last birthday present I received from you mom before I moved to Houston. A song, that I feel reflects strongly on how the journey of growing has been.

Of course, I want to thank my brother, Roy. The journey of doing a PhD together has been and interesting one. We have always been here to support each other and have fun going on bike rides, playing board games and embarking on our musical journey together. I love you.

Naturally, I'd like to thank my advisor Kaden Hazzard, who is a great mentor and a pleasure to work with. His profound knowledge of the physics (not only in the theory, but also the experiments) is amazing. Also, he has forced me to think cleverly about physics problems, developing intuition for what are good questions and how to address them. I am very grateful for his patience and guidance.

I want to also thank Richard Scalettar who has been my "second" advisor and an excellent professor to collaborate with. Everything I know from DQMC is thanks to him and I am very grateful for all the scientific input and coding hours we shared together.

Thanking more of the faculty, I want to thank Randy Hulet for believing in me and bringing me to Rice and the useful physics discussions we had. I want to thank Doug Natelson for all the time helping me and PAGSA implementing programs such as the PhD proposal writing seminar and professional development opportunities. I want to thank Mustafa Amin and Ming Yi for whom I had the honor to TA the tutorial sessions and are very involved in advocating for graduate students. I also want to thank Lam Yu who gave me the opportunity to lecture my first class ever.

I am grateful for my fellow graduate students in the group, in particular Hao-Tian Wei and Sohail Dasgupta with whom I had the opportunity to collaborate, discuss a lot of interesting physics and also hang out at Valhalla. It has been a pleasure sharing the third floor of Brockman with you.

This is a great opportunity to thank my friends in the Physics Department, in particular to PAGSA, with whom has been a privilege to advocate for graduate students and organize fun events. I am grateful for the long conversations with all of them.

I also want to thank to my extended physics family, in particular to Jackson Poveda, Victor Romero, and Rosario Paredes who have provided me the emotional and academic support that I needed when things were not very clear.

A big shoutout goes to friends with whom sharing joys and issues has been important in the past few years. I am grateful for having Emily Yedinak, Celine Fliedner, Shah Alam, Ana Newheart, Diego Fallas, Alana Semple, Charlotte Evans, Jake Fry, and Mariana de Botton in my life and to know I had people caring for me throught the whole process. Your presence has played a major role in keeping me sane and I

care for all of you.

I am also extremely grateful to the Biosciences Department, which I am not part of but they adopted me like one of them. They are all lovely people and I am very glad to have share this time with you. It's a long list, but y'all know who you are!

I would like to also thank the LAGSA family, who has always being very welcoming and throws the best parties on campus. Is a long list of people, but I want to explicitely thank Santiago Legaspi and Oihane Iglesias for always holding down the fort for the annual party we held at Valhalla. I want to thank the brazilian crew lead by Bárbara de Freitas Magalhães for teaching us all the choreographies.

I want to thank the music companions I had during the PhD, in particular Carlos Gallardo, Colby Beserra, Nathan Richardson, the Plan B crew with whom playing music on Fridays was one of the best activities, to my Batalá family, and to my Plug n' play friends.

I also want to thank everyone in the Grad STRIVE team, and to Curtis Henry from the Wellbeing Center. I appreciate the enthusiasm and the support.

I am grateful for the old friends and the new that throught the whole journey were always willing to grab coffee, chat over zoom, play board games, or just rant together. I appreciate y'all.

Without further remarks, I hope you enjoy this thesis and looking forward to celebrate with y'all soon.

Contents

List of Figures

Tables

Chapter 1

Quantum simulation
A route to study many-body physics

> Los científicos dicen que estamos hechos de átomos, pero a mí un parajito me dijo que estamos hechos de historias.
>
> Eduardo Galeano

In this chapter we present the many-body problem of strongly correlated matter and how quantum simulation with ultracold atoms presents a route to study it.

1.1 Strongly correlated materials

The field of condensed matter physics studies the physical properties of matter, i.e. the many-body problem of interacting electrons in a solid. One can think of a neutral solid as positively charge nuclei that form a periodic structure, known as lattice, and their corresponding negatively charged particles (electrons). The ions are heavy and mainly remain in their place, providing an electrostatic potential to the electrons. The electrons in turn have kinetic energy, which allows them to delocalize in the lattice and interact with the ions and with other electrons via the Coulomb potential.

Although some physical properties of matter can be explained by knowing a priori the microscopic laws that describe the ensemble of particles, there are other phenomena that arise from the organization of the many and cannot be predicted or anticipated from such a priori knowledge. In the words of Philip Anderson, the idea that *More is Different* [1]: "The behavior of large and complex aggregations of elementary particles, it turns out, is not to be understood in terms of a simple extrapolation of the properties of a few particles. Instead, at each level of complexity entirely

new properties appear, and the understanding of the new behaviors requires research which I think is as fundamental in its nature as any other".

In other words, it is the collective emergent phenomena of the ensemble of interacting particles that gives rise to the myriad of important, interesting, and puzzling problems that we observe. For example, the only similarity magnetism, superconductivity, insulation and strange metallicity have is that all of these fascinating properties arise from the behavior of electrons in a lattice.

1.1.1 The many-body problem of electrons in a lattice

The microscopic physics that governs condensed matter systems is contained in the many-body wavefunction that is a solution to the many-body Hamiltonian [2],

$$H = H_{\text{ions}} + H_{\text{electrons}} + H_{\text{ions-electrons}}, \tag{1.1}$$

where H_{ions} describes the subsystem of ions, $H_{\text{electrons}}$ the subsystem of electrons and $H_{\text{ions-electrons}}$ the electrons-ions interaction. These terms are given by,

$$H_{\text{ions}} = \sum_I \frac{\mathbf{P_I}^2}{2M_I} + \frac{1}{2}\sum_{I\neq J} \frac{Z_I Z_J e^2}{|\mathbf{R}_I - \mathbf{R}_J|} = K_{\text{ions}} + V_{\text{ions}} \tag{1.2}$$

$$H_{\text{electrons}} = \sum_i \frac{\mathbf{p_i}^2}{2m} + \frac{1}{2}\sum_{i\neq j} \frac{e^2}{|\mathbf{r}_i - \mathbf{r}_j|} = K_{\text{electrons}} + V_{\text{electrons}} \tag{1.3}$$

$$H_{\text{ions-electrons}} = -\sum_{i,I} \frac{Z_I e^2}{|\mathbf{r}_i - \mathbf{R}_I|} = V_{\text{ions-electrons}} \tag{1.4}$$

where electrons are denoted by lowercase subscripts, coordinates $\mathbf{r}_i$, charge e and mass m, while nuclei are denoted by uppercase subscripts, coordinates $\mathbf{R}_I$, charge $Z_I e$, and mass M_I.

In Eq. (1.1) only the the kinetic energy of the ions can be neglected K_{ions}, since it is proportional to $1/M_I$. For the most part we can neglect this term and focus on the eletronic problem with fixed nuclei, since we also know that the equilibrium positions

of the ions R_I define a crystal lattice [*]. Under these justified approximations, the interaction of nuclei with each other is a constant that can be added to the zero of energy. Thus, the essential Hamiltonian for describing interacting electrons in a lattice consists of the kinetic energy of the electrons, their interaction with the ions and the electron-electron interaction,

$$H = K_{\text{electrons}} + V_{\text{electrons}} + V_{\text{ions}-\text{electrons}}. \tag{1.5}$$

Although we are able to state such equation, solving it is not an easy task. This is because the problem does not allow for analytic solutions (except for certain specific cases, such as some one-dimensional problems) given the complicated terms in the Hamiltonian, and also because the Hilbert space grows exponentially fast rendering numerical simulations unable to deal with the exponentially large number of degrees of freedom.

1.1.2 The rich physics of strongly correlated matter

To first approximation, one can consider the non-interacting system, i.e. drop the $V_{\text{electrons}}$ and understand the band structure of the solid in question. Such a crude simplification is enough to understand the basic principles of metals, semiconductors and band insulators. As interactions are adiabatically introduced into the system, the principle of *adiabatic continuity* comes into play. This principle states that one can understand a complicated, interacting system by studying a simple non-interacting

[*]This is the adiabatic Oppenheimer approximation and it is valid as long as $m/M_I \ll 1$ and lattice vibrations relative to the equilibrium positions are small, i.e. $\Delta_R/a \ll 1$ (where a is the lattice spacing), which holds for temperatures much below the Debye temperature $T/\Theta_D \ll 1$. The essence of the Oppenheimer approximation lies in the large separation of scales of the velocities of the electrons v_F (Fermi velocity) and the ions (v_{ion}), $v_{\text{ion}} \sim (m/M_I)^{3/4} v_F$. When $m/M_I \ll 1$ the ions can be treated as essentially static relative to the electrons, which then allows us to solve for the electronic motion assuming fixed ion positions [3]. For light nuclei (such as hydrogen and helium), or at $T/\Theta_D \gtrsim 1$ ionic motion is substantial and cannot be neglected. The ions do exhibit oscillations around their equilibrium positions and the energy of these oscillations is quantized, i.e. phonons. One could then write the $V_{\text{ions}} = V^{(0)}_{\text{ions}} + V_{\text{phonon}}$, where the first term describes the bonding in the solid and the second one the lattice dynamics [4].

system that contains the essential nature of the original system. In other words, according to this principle, the low-energy excitations of an interacting system are weakly-interacting quasiparticles that are closely related to the constituent particles of the original system.

The most clear example of the principle of *adiabatic continuity* is Fermi's Liquid Theory (FLT) [5], where one starts from a non-interacting Fermi Gas and then adiabatically introduces interactions between particles. There is a one-to-one correspondence between the non-interacting system and the Fermi liquid, an even though many-body interactions exist among the constituent particles, by considering quasiparticles renormalized by the interactions, one can treat them as independent particles. In doing so, even strongly interacting Fermi systems are simplified and an understanding of the properties can be obtained by studying the properties of the emerging quasiparticles. Some important examples of where FLT has been successfully applied are liquid ^{3}He, electrons in metals at low temperatures, and in the core of neutron stars [6].

However, despite FLT being a powerful tool and is recognized for its accomplishments, it's also known for the phenomena if fails to explain, such as unconventional superconductivity that goes beyond the BCS framework, and topological semimetals induced by the Kondo interaction [7]. In these materials, known as strongly correlated matter, the physics of the interacting electrons does not have an effective description in terms of non-interacting quasiparticles, but instead of quasiparticles with different effective masses, weights and quantum numbers. Following the perturbative approach of adiabatically introducing interactions, if the system reaches a critical point and experiences a phase transition, the principle of *adiabatic continuity* no longer holds. Strongly correlated matter are clear examples of emergent phenomena where FLT fails and it is very challenging to establish a link between the microscopic degrees of freedom and the collective low-energy excitations. To make this statement more pre-

cise, conventional metals, semiconductors, band insulators, and semimetals of band theory are materials in which the $H_{\text{electrons}}$ in this sense can be considered weak. In these materials, their electronic states are mainly built of s and p electrons which are fairly delocalized, and their kinetic energy dominates over the electron-electron interaction. In contrast, materials such as transition metal oxides, heavy fermion materials and iron pnictide high temperature superconductors, the $H_{\text{electrons}}$ plays a central role in the determination of their physical properties. In these materials, the electronic states are primarily built from d and f orbitals, which are more localized, and it is the competition between kinetic and potential energies that gives rise to quantum magnetism and superconductivity [8].

The field of strongly correlated matter is fertile for discovery due to the complex interplay between the lattice structure, kinetic energy, the electron-electron interaction, and the spin and orbital degrees of freedom (see Fig. 1.1). For these reasons it has developed rapidly in the last few decades, with the synthesis of a large number of exciting materials exhibiting rich physics like topological properties, quantum critical points and exotic superconductivity [7, 9, 10].

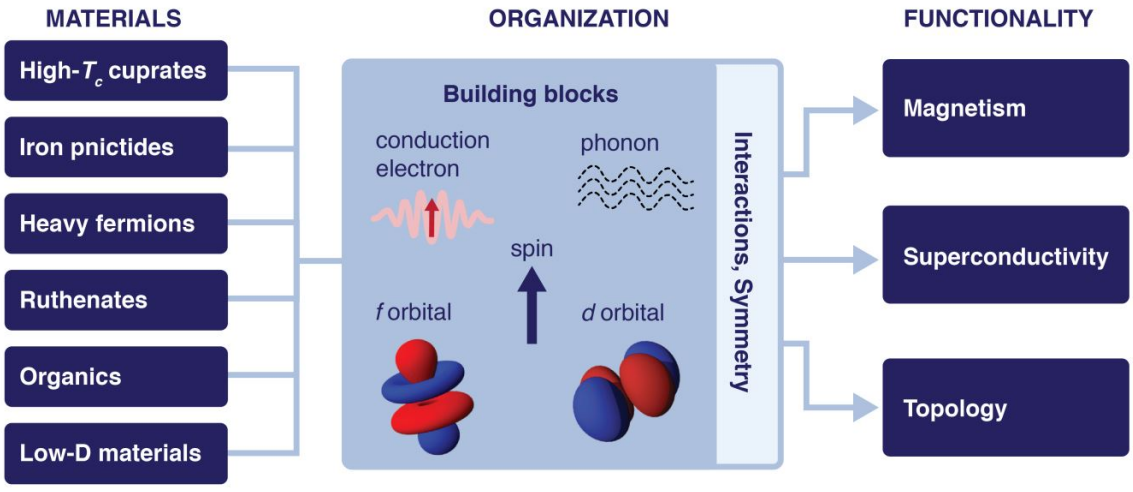

Figure 1.1 : **Strongly correlated materials**. Examples of strongly correlated materials and how interactions between their low-energy degrees of freedom and symmetry lead to different properties. Figure reprinted with copyright permission of Ref. [7].

1.2 Ultracold atoms

Historically, the field of Atomic, Molecular and Optical physics dealt only with atoms and or diatomic molecules (perhaps polyatomic if one was feeling very adventurous). However in the last decades, with the development of laser cooling techniques and the capabilities to engineer arbitrary optical potentials [11], the field of quantum simulation was was born [12]. Here one uses engineered quantum systems to realize many-body models (analogous to the ones used in Condensed Matter) that are extremely hard to solve due the Hilbert space explosion (exponential growth with system size) and the fact that interactions are not necessarily small and perturbative approaches fail [see eq. (1.1)].

A prototypical example of quantum simulation is using ultracold fermionic atoms in an optical lattice to realize the SU(2) symmetric Fermi-Hubbard model (FHM) [13–17], where atoms in two different hyperfine states emulate spin-1/2 particles. These experiments' high degree of control and tunability allows the quantum simulators to tune the lattice geometry, energy scales, and lattice fillings. This has recently led to observations of striking phenomena into this long-studied problem, such as the characterization of Mott Insulating phases [18, 19], the observation of antiferromagnetism [20, 21], the measurement of charge and spin transport properties [22, 23], and new insights like the structure of string correlations and the influence of holes on magnetic correlations [24].

1.2.1 The power of quantum simulation

In the past few decades the field of quantum simulation has seen a rapid growth of its technological capabilities. Of particular interest are the the development of quantum gas microscopes [16, 17] along with spin-dependent imaging techniques [25] which allow access to the microscopic states of the Hamiltonian. By having access to *snapshots* of the spin and density distributions, experiments have direct access

to correlation function that are not directly accessible in solid state systems [26, 27]. These *snapshots* provide spin-dependent single atom detection with near unity detection efficiency in optical lattices [25], which essentially provide a "photograph" of the microscopic arrangement of particles and holes in the system. Such images permit the direct calculation of correlation functions and structure factors, and can be fed into neural networks to extract transition temperatures and elucidate phases of matter which might not have simple order parameters or ordered phases [26, 28, 29]

In addition, as opposed to condensed matter systems, quantum simulators with ultracold atoms are extremely clean, i.e. there are no defects of imperfections (which on their own are very interesting), which allows for the study of effective models, such as the Fermi-Hubbard model, and aim to gain insight of strongly correlated matter. Furthermore, the high degree of control permits to explore the phase diagram and if desired introduce disorder or arbitrary potentials into the model, which have important implications on many-body localization [30].

For completeness is important to mention that quantum simulators are not restricted to the Fermi-Hubbard model. For example, quantum spin models can be studied in optical lattices with Rydberg interactions [31], or with trapped ion platforms [32]. Other architectures, such as Rydgberg atom arrays, have been used to study dimer models which exhibit interesting topological phases [33].

1.2.2 The challenges of quantum simulation

Despite the power and tunability of ultracold atom quantum simulators, it exhibits certain drawbacks and challenges. The most important ones related to cooling, equilibration, and methods to characterize their behavior.

At first glance it sounds counterintuitive that ultracold atoms have a cooling problem. The underlying issue is that although experiments on a daily basis create the coldest matter in the world ($\sim$ nK), these samples are still at temperatures above

the relevant energy scales where novel phases of matter appear. In the context of the system exhibiting quantum mechanical properties we present the degeneracy densities and temperatures for different systems in Table 1.1. In the case of electrons in a metal, the densities correspond to roughly Avogadro's number and it needs a quantum mechanical description at room temperatures ($\sim$ 300 K). On the other hand, ultracold atomic gases require temperatures below the μK to exhibit quantum mechanical behavior and reaching such low temperatures is vital for accessing the power quantum simulators offer.

System	Density	T_c [K]
H_2 gas	10^{19}	5×10^{-2}
^{4}He liquid	10^{22}	2.17
Electrons in a metal	10^{22}	10^4
Ultracold atomic gas	10^{14}	$< 10^{-5}$

Table 1.1 : Degeneracy temperatures of different physical systems [34, 35].

In the context of quantum simulation, where these cold atomic gases are loaded into optical lattices or tweezers to emulate many-body Hamiltonians, experiments are trying to push the temperatures below the bandwidth ($\sim$ nK) and below temperatures where superexchange, magnetism, and possible superfluidity becomes important ($\lesssim$ 100pK) [36]. There are intense efforts to develop and implement cooling protocols to reach lower temperatures [37, 38], as well as the creation of new quantum simulation architectures, such as optical tweezers [39, 40] which would allow for the exploration of systems at lower temperatures. Along these lines, the results of this thesis discuss our contributions to this question, where the quantum simulators explored represent 1) the coldest fermions ever created in nature in absolute temperature and in cold atoms ($k_BT/t \sim 0.1$) [41], and 2) the lowest entropy per particle fermions ever created, albeit in a so-far small system ($\sim 0.2k_B$) [40].

Since we are interested in understanding equilibrium properties of the quantum mechanical Hamiltonians (although there are exciting directions regarding driven and

out-of-equilibrium physics [42]), one issue that appears is the separation of timescales between the lifetime of experiments (a few seconds) and tunneling rates ($\sim$ 10's of ms). As temperatures are lowered, timescales of interest become longer as well, and reaching equilibrium is harder. The problem is particularly bad at low temperatures and near fillings where the systems are insulating, the transport is exponentially slow.

Finally, quantum simulation needs techniques to characterize the different phases of matter the engineered Hamiltonian might support. The development of experimental techniques to access correlation functions and response functions [†] is of paramount relevance to understand the the physics.

Here I would like to mention that these issues are not unique to experimental techniques, but also theoretical ones. As we will discuss later in the thesis, numerical techniques also have to overcome problems that hinder access to low-temperature physics and equilibration problems (like non-ergodicities). Finally, as theorists is our interest to understand which observables, order parameters, and correlation functions are of interest to characterize novel states and behaviors and provide guidance and comparison to experiments.

1.3 Thesis Outline

In this thesis we focus on two classes of emerging quantum simulators: those that use alkaline-earth-like atoms to engineer the SU(N) Fermi-Hubbbard model, and those using optical tweezer arrays. The thesis is organized as follows:

Chapter 2 introduces the FHM in its original SU(2) symmetric form and discusses under which approximations is valid. This is then followed by a presentation of some of its properties and a series of experimental and theoretical results.

Chapter 3 presents the generalization of the FHM to N components, with an

[†] In the case of one- and two-dimensional optical lattices quantum gas microscopes allow to access real-space correlations. However in higher dimensions, this is not possible and indirect techniques such as Bragg spectroscopy are required [20].

enhanced SU(N) symmetry. We present a discussion of its symmetries, important limits such as the non-interacting, the single-site, and the Heisenberg limit. This is then followed by a review of the relevant literature.

Chapter 4 gives an introduction to the physics of alkaline-earth-like atoms which are used to engineer the SU(N) FHM in optical lattices, since they present natural SU(N) symmetric interactions in their ground state.

Chapter 5 gives an overview of the numerical techniques we have used to answer questions about the thermodynamic and magnetic properties of the SU(N) FHM. This chapter covers high-temperature series expansions, exact diagonalization, numerical linked cluster expansion and determinant Quantum Monte Carlo.

Chapters 6-10 present the results of this work. We have presented a project per chapter, as follows.

Chapter 6 presents the results of studying an anisotropic FHM, which characterizes the thermodynamic and magnetic properties of the two-dimensional (2D) to three-dimensional (3D) crossover. This project demonstrates that at a fixed interaction strength U/t, the magnetic structure factor can be enhanced relative to both 2D and 3D results, but that such enhancement occurs at U/t below those for which the Néel temperature is largest. Furthermore, our results suggest a possible cooling protocol for atoms in optical lattices in which the dimensionality is adiabatically changed from 3D to 2D.

Chapter 7 presents the results of the SU(N) FHM in the two-dimensional square lattice, where we explore its thermodynamic properties as a function of N. An important finding of this project is the unexpected feature that thermodynamic observables as a function of temperature obey a universal scaling with N above the superexchange energy, which can be explained with a second order numerical linked order expansion.

Chapter 8 presents the results of studying the SU(N) FHM in optical lattices where we explore short-range antiferromagnetic correlations as a function of N and

dimensionality. This project shows that nearest-neighbor antiferromagnetic correlations are stronger for larger N and in lower dimensions. Moreover, theory-experiment comparison allows us to infer the temperature to be lowest achieved for a cold atom Fermi-Hubbard model.

Chapter 9 presents the results of studying Fermi gases in optical tweezer arrays where we focus on theoretically understanding heating effects induced by the experimental techniques. This project demonstrates the use of a strobing protocol to generate tunneled coupled two-dimensional lattices. An important conclusion of this work is the creation of the lowest entropy per particle fermions ever.

Chapter 10 presents the results of ongoing work, which have not been published yet, but that are under preparation. These include: the precise measurement and characterization of the equation of state of the SU(N) FHM, the study of magnetic correlations for SU(3) fermions in square lattices, and the study of Hubbard parameters in optical tweezers.

Chapter 11 provides a big picture summary of our work and gives and outlook of the future directions that will be explored.

Finally, the Appendices A- C present a series of useful information to people in the group regarding details of the Determinant Quantum Monte Carlo.

1.4 Publications arising from this work

1.4.1 Publications in chronological order

- *Thermodynamics and magnetism in the 2D-3D crossover of the Hubbard model*, **Eduardo Ibarra-García-Padilla**, Rick Mukherjee, Randall G. Hulet, Kaden R. A. Hazzard, Thereza Paiva, and Richard T. Scalettar, Phys. Rev. A **102**, 033340 (2020) [43].

- *Universal thermodynamics of an SU(N) Fermi-Hubbard Model*, **Eduardo Ibarra-García-Padilla**, Sohail Dasgupta, Hao-Tian Wei, Shintaro Taie, Yoshiro Takahashi, Richard T. Scalettar, and Kaden R. A. Hazzard, Phys. Rev. A **104**, 043316 (2021) [Editors' Suggestion] [44].

- *Observation of antiferromagnetic correlations in an ultracold SU(N) Hubbard model*, Shintaro Taie*, **Eduardo Ibarra-García-Padilla***, Naoki Nishizawa, Yosuke Takasu, Yoshihito Kuno, Hao-Tian Wei, Richard T. Scalettar, Kaden R. A. Hazzard, and Yoshiro Takahashi, arXiv:2010.07730 (accepted at Nat. Phys). *This authors contributed equally to this work [41].

- *A two-dimensional programmable tweezer array of fermions*, Zoe Z Yan, Benjamin M Spar, Max L Prichard, Sungjae Chi, Hao-Tian Wei, **Eduardo Ibarra-García-Padilla**, Kaden R. A. Hazzard, and Waseem S Bakr, arXiv:2203.15023 (accepted at Phys. Rev. Lett.) [40].

1.4.2 Manuscripts under preparation

- *Precise measurement and characterization of the equation of state of the SU(N) Fermi-Hubbard model.* In collaboration with Simon Folling's group at LMU, Germany.

- *Mott transition and magnetism of SU(3) fermions in a square lattice.*

- *The Quantum Critical point of the SU(3) Fermi-Hubbard Model.*

- *Hubbard parameters in optical tweezers.*

Chapter 2

The Fermi-Hubbard model

> Los poetas, como los ciegos, pueden ver en la oscuridad.
>
> Jorge Luis Borges

In this chapter we introduce the Fermi-Hubbard Model (FHM) in its original spin-1/2 SU(2) symmetric form, discuss some its properties, and present a review of its exploration with quantum simulators.

In the words of Assa Auerbach in his book *Interacting Electrons and Quantum Magnetism* [8]: "Many theorists have devoted a considerable part of their careers to the Hubbard model. Nevertheless, it remains a source of much fascination and bewilderment. Perhaps it is because the Hubbard model is the simplest many-particle model one can write down, which cannot be reduced to a single-particle theory".

The FHM is an effective model that plays a pivotal role in the understanding of strongly correlated fermionic many-body systems. This is partly because it contains the minimal ingredients that are necessary to describe the behavior of strongly interacting electrons in a periodic lattice, capturing the essential features of real materials; and also because it exhibits a variety of canonical correlated phases of matter. It is central to condensed matter physics, as it accounts for many phenomena observed in solid state systems, for example it exhibits a metal-to-insulator crossover (for which conventional band theory predicts a metallic state), long-range antiferromagnetic order and charge density waves. Moreover, in the two-dimensional square lattice it is extensively studied in the context of stripe ordering, pseudogap physics, strange metallicity, and d-wave superconductivity [45–50].

2.1 The Hamiltonian

The FHM is defined by the grand-canonical Hamiltonian,

$$H = -t \sum_{\langle i,j \rangle} \sum_{\sigma=\uparrow,\downarrow} \left(c^{\dagger}_{i\sigma} c_{j\sigma} + c^{\dagger}_{j\sigma} c_{i\sigma} \right) + U \sum_{i} n_{i\uparrow} n_{i\downarrow} - \mu \sum_{i} \sum_{\sigma=\uparrow,\downarrow} n_{i\sigma}, \tag{2.1}$$

where $c^{\dagger}_{i\sigma}(c_{i\sigma})$ is the creation (annihilation) operator for a fermion with spin σ on site $i = 1, 2, ..., N_s$, and $n_{i\sigma}$ is the number operator. t is the hopping amplitude between nearest-neighbor sites i and j, U is the interaction strength and μ is the chemical potential controlling the fermion density (see Fig. 2.1).

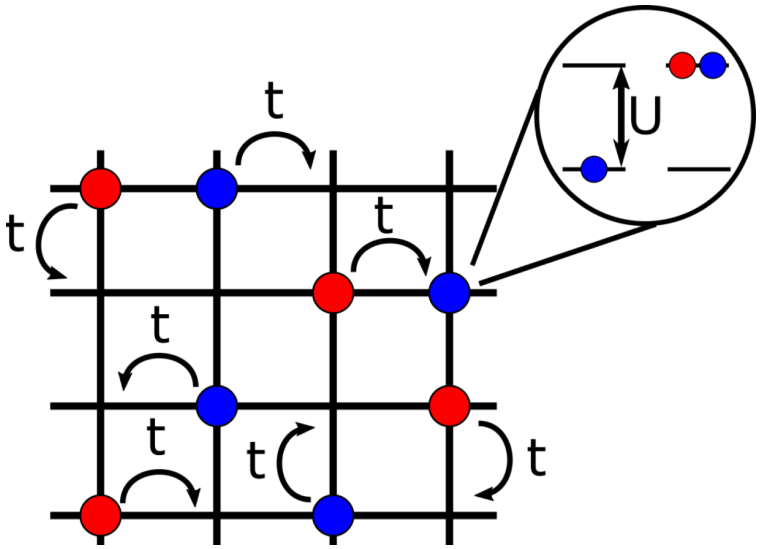

Figure 2.1 : **Fermi Hubbard Model**. In its SU(2) symmetric form the Fermi Hubbard Model consists of spin-1/2 particles living on a lattice (denoted by red and blue) that can tunneling to nearest neighboring sites with hopping amplitude t. When two atoms of different color occupy the same site, this raises the energy by U. The filling fraction is controlled by the chemical potential μ.

Despite is apparent simplicity, the FHM only allows for analytic solutions in special limits such as in one-dimension, where a series of techniques can be used [8]: Bethe Ansatz, bosonization, Luttinger liquid theory, and perturbative renormalization group, just to mention some. In higher dimensions, controlled approximation schemes and numerical techniques such as those discussed in Chapter 5 have been

used to gain insight about its physics.

2.1.1 How to get the FHM?

In Chapter 1 we introduced the many-body Hamiltonian for interacting electrons [eq. (1.1)]. We then discussed how we can focus only in the problem of interacting electrons by considering the ions fixed in place, arriving to eq. (1.5) that had three terms involved: The kinetic energy of the electrons, the interaction of the ions with the electrons, and the electron-electron interaction. The problem can be then written in the following form,

$$H = H_0 + H_{\text{int}}, \tag{2.2}$$

where H_0 is the single-particle Hamiltonian that consists of the electron's kinetic energy and the potential generated by the crystalline lattice. H_0 describes a single electron moving a periodic potential and is given by,

$$H_0 = \sum_{\sigma=\uparrow,\downarrow} \int d\mathbf{r} \psi_\sigma^\dagger(\mathbf{r}) \left[-\frac{\hbar^2}{2m}\nabla^2 + V_{\text{ion}}(\mathbf{r}) \right] \psi_\sigma(\mathbf{r}), \tag{2.3}$$

where $\psi_\sigma^\dagger(\mathbf{r})[\psi_\sigma(\mathbf{r})]$ is the field operator that creates [annihilates] an electron with spin σ at site $\mathbf{r}$. Now, the electron-electron interaction is the long-range Coulomb interaction $\propto e^2/r$. There is however a large collective screening of the core and valence electrons. Much of the screening effect is to renormalize the effective electron ion-potential V_{ion} [8]. Therefore the interactions are taken to be,

$$H_{\text{int}} = \frac{1}{2} \sum_{\sigma\neq\tau} \int \int d\mathbf{r} d\mathbf{r}' \psi_\sigma^\dagger(\mathbf{r}) \psi_\tau^\dagger(\mathbf{r}') V_{\text{electrons}}(\mathbf{r}-\mathbf{r}') \psi_\tau(\mathbf{r}') \psi_\sigma(\mathbf{r}). \tag{2.4}$$

In order to write this Hamiltonian in terms of the creation and annihilation operators $c_{i\sigma}^\dagger$ and $c_{i\sigma}$, we use the band structure energies $\epsilon_{\alpha,\mathbf{q}}$ and Bloch wave functions (which are solutions to the single particle Hamiltonian) to construct the maximally

localized Wannier states w_i^α, with lattice index i and band index α [*]. The Wannier states form a basis and allow us to write the field operators in the following form,

$$\psi_\sigma^\dagger(\mathbf{r}) = \sum_{i,\alpha} w_i^{\alpha *} c_{\alpha i\sigma}^\dagger. \tag{2.5}$$

With these expressions, the field operators in the Hamiltonian are replaced by Wannier operators and eq. (2.2) is now written as,

$$H = -\sum_\sigma \sum_{\alpha,\beta} \sum_{i,j} t_{ij}^{\alpha\beta} c_{\alpha i\sigma}^\dagger c_{\beta j\sigma} + \sum_{\sigma\neq\tau} \sum_{\alpha,\beta,\gamma,\eta} \sum_{i,j,k,l} U_{ijkl}^{\alpha\beta\gamma\eta} c_{\alpha i\sigma}^\dagger c_{\beta j\tau}^\dagger c_{\gamma k\tau} c_{\eta l\sigma}, \tag{2.6}$$

$$-t_{ij}^{\alpha\beta} = \int d\mathbf{r} w_i^{\alpha *} \left[-\frac{\hbar^2}{2m}\nabla^2 + V_{\text{ion}}(\mathbf{r}) \right] w_j^\beta = \frac{1}{V} \sum_{\mathbf{q}} e^{i\mathbf{q}\cdot(\mathbf{r}_i - \mathbf{r}_j)} \epsilon_{\alpha,\mathbf{q}} \delta_{\alpha,\beta} \tag{2.7}$$

$$U_{ijkl}^{\alpha\beta\gamma\eta} = \frac{1}{2} \int\int w_i^{\alpha *}(\mathbf{r}) w_j^{\beta *}(\mathbf{r}') V_{\text{electrons}}(\mathbf{r} - \mathbf{r}') w_k^\gamma(\mathbf{r}') w_l^\eta(\mathbf{r}). \tag{2.8}$$

So far it seems we have not simplified the problem but complicated it. However as we will discuss in the following paragraphs, these expressions will simplify.

2.1.1.1 Tunneling matrix elements

Let us start with eq. (2.7). The first thing to notice is that there is no matrix element to go between states in two different bands $\delta_{\alpha,\beta}$. This indicates that the first term in eq. (2.6) is now,

$$H_1 = -\sum_\sigma \sum_\alpha \sum_{i,j} t_{ij}^\alpha c_{\alpha i\sigma}^\dagger c_{\alpha j\sigma}. \tag{2.9}$$

Then we will focus only in a single band model, the lowest band α. In order to justify ignoring the matrix elements t_{ij}^α for higher bands, the following conditions must hold:

- The Fermi surface lies within a single conduction band.
- The temperature must be small compared to the energy gap between the bands.

[*] We leave the derivation of Bloch and Wannier states for Chapter 4 where we discuss the physics of alkaline-earth-like atoms in optical lattices.

- The interaction energy is also small compared to the energy gap between bands.

Under these approximations, the single band model is,

$$H_1 = -\sum_{\sigma}\sum_{i,j} t_{ij} c^{\dagger}_{i\sigma} c_{j\sigma}. \tag{2.10}$$

It is convenient to split this expression into $i = j$ and $i \neq j$,

$$H_1 = -\sum_{\sigma}\sum_{i\neq j} t_{ij} c^{\dagger}_{i\sigma} c_{j\sigma} - \sum_{\sigma,i} V_i n_{i\sigma}, \tag{2.11}$$

where we have defined the on-site potential $V_i = t_{ii}$. If one assumes translational invariance V_i is indepedent from i and V is therefore a constant that corresponds to the mean energy of the band that just offsets the chemical potential μ [†].

The final thing to notice is to take the tight-binding limit, where one retains a minimal set of short-range bonds t_{ij} on the lattice. This is justified since the hopping matrix elements depend on overlap integrals of the Wannier states, which are exponentially small. In the single band Hubbard model we only keep the nearest-neighbor terms $\langle i, j\rangle$ and neglect the others, [‡].

$$H_1 = -t\sum_{\sigma}\sum_{\langle i,j\rangle} c^{\dagger}_{i\sigma} c_{j\sigma} - \mu\sum_{\sigma,i} n_{i\sigma}. \tag{2.12}$$

2.1.1.2 The interaction term

Let us now focus on the interaction term eq. (2.8),

$$U^{\alpha\beta\gamma\eta}_{ijkl} = \frac{1}{2}\int\int w^{\alpha *}_i(\mathbf{r}) w^{\beta *}_j(\mathbf{r}') V_{\text{electrons}}(\mathbf{r}-\mathbf{r}') w^{\gamma}_k(\mathbf{r}') w^{\eta}_l(\mathbf{r}). \tag{2.13}$$

[†]As we will see in Chapter 9, for optical tweezer arrays, $V_i \neq V$ since translational invariance is not present.

[‡]This approximation is justified for optical lattices with lattice depths $\gtrsim 5E_R$ [51]. It is however important to mention that next-nearest neighbor tunneling amplitudes play an important role in the ground state properties of the FHM, where there is a competition between stripe order and superconductivity [52].

This expression seems very daunting at first, but owing to the small overlap of the Wannier states which are centered on different lattice positions, the matrix element $i = j = k = l$ predominates. In addition, in order to only consider a single band $\alpha = \beta = \gamma = \eta$ the on-site interaction $U = 2U_{iiii}$ must be small compared to the energy gap between bands [§]. In this case, the interaction term now reads as

$$H_2 = U \sum_i c^\dagger_{i\uparrow} c^\dagger_{i\downarrow} c_{j\downarrow} c_{j\uparrow} = U \sum_i n_{i\uparrow} n_{i\downarrow}. \tag{2.14}$$

Putting together eqs. (2.12) and (2.14), one obtains eq. (2.1), the Fermi-Hubbard Hamiltonian.

2.2 Symmetries of the Fermi Hubbard Model

The Fermi Hubbard Model exhibits a series of symmetries of interest. The first one is a global U(1) symmetry which reflects a global charge conservation, i.e. the total particle number $N_{\text{ptcl}} = \sum_{i,\sigma} n_{i\sigma}$ is conserved. The second one is a global SU(2) symmetry which corresponds to spin isotropy, and the generators of the group are the spin permutation operators [¶], which in the SU(2) case correspond to:

$$S^+ = \sum_i S^+_i = \sum_i c^\dagger_{i\uparrow} c_{i\downarrow} \tag{2.15}$$

$$S^- = \sum_i S^-_i = \sum_i c^\dagger_{i\downarrow} c_{i\uparrow} \tag{2.16}$$

$$S^z = \frac{1}{2} \sum_i \left(c^\dagger_{i\uparrow} c_{i\uparrow} - c^\dagger_{i\downarrow} c_{i\downarrow} \right) \tag{2.17}$$

[§] If this condition is not met, then the single band model no longer holds and corrections to the interaction energy term and the hopping terms need to be incorporated. See for example Ref. [53] for a discussion of the validity of the FHM with ultracold atoms in optical lattices.

[¶] Although the generators of the group are hermitian linear combinations of the spin permutation operators, it is customary in the literature to refer to the spin permutation operators as the generators.

All the generators of the algebra commute with the Hubbard Hamiltonian [eq. (2.1)], and therefore the system exhibits an SU(2) symmetry. Particularly, not only the total number of particles is conserved by the Hamiltonian, but the populations of each spin component. In other words, there are no spin-flip terms.

One other type of symmetry that is worth discussing is the Particle-Hole Symmetry (PHS) in a bipartite lattice. In a bipartite lattice the set of lattice sites can be divided into two sublattices A and B, such that sites in sublattice A only has neighbors that are members of B and viceversa (see Fig. 2.2).

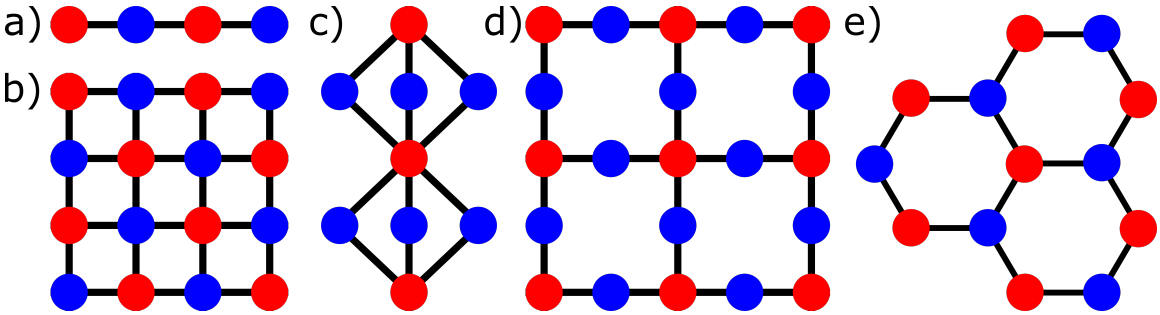

Figure 2.2 : **Bipartite lattices**. a) One-dimensional linear chain. b) Square lattice. c) One-dimensional Lieb lattice. d) Two-dimensional Lieb lattice. e) Honeycomb lattice. The solid lines denote tunneling amplitudes between lattice sites. In bipartite lattices members of the A sublattice (red) only have members of the B sublattice (blue).

In bipartite lattices one can perform the following transformation, named particle-hole transformation (PHT),

$$c_{j\sigma} \rightarrow \eta_j c^{\dagger}_{j\sigma}, \tag{2.18}$$

where $\eta = \pm$ on alternate sublattices. Under this transformation (which obeys the canonical fermionic anticommutation relationships),

$$n_{i\sigma} \rightarrow 1 - n_{i\sigma}, \tag{2.19}$$

$$c^{\dagger}_{i\sigma} c_{j\sigma} \rightarrow \eta_i \eta_j c_{j\sigma} c^{\dagger}_{i\sigma} = c^{\dagger}_{i\sigma} c_{j\sigma}. \tag{2.20}$$

From this expressions one infers that the kinetic energy part of the Hamiltonian is invariant under such transformation and is therefore convenient to rewrite the interaction term in a way which is PHS as well. This is done by considering the term

$$U\left(n_{i\uparrow}-\frac{1}{2}\right)\left(n_{i\downarrow}-\frac{1}{2}\right)=Un_{i\uparrow}n_{i\downarrow}-\frac{U}{2}\left(n_{i\uparrow}+n_{i\downarrow}\right)+\frac{U}{4}, \tag{2.21}$$

that is invariant under the PHT and only differs from the original interaction term by a trivial shift in the chemical potential and an overall additive constant to the energy. Thus, the PHS version of the Hubbard model is,

$$H=-t\sum_{\langle i,j\rangle,\sigma}\left(c^{\dagger}_{i\sigma}c_{j\sigma}+c^{\dagger}_{j\sigma}c_{i\sigma}\right)+U\sum_{i}\left(n_{i\uparrow}-\frac{1}{2}\right)\left(n_{i\downarrow}-\frac{1}{2}\right)-\mu\sum_{i,\sigma}n_{i\sigma}. \tag{2.22}$$

In this form one notices that in this form the only part of the Hamiltonian that is not invariant under a PHT is the one associated to the chemical potential, except $\mu = 0$ where the Hamiltonian is particle hole symmetric. This has profound and useful consequences for the computation of observables of interest. For example, the density $\rho = \langle n\rangle = \sum_{\sigma}\langle n_{\sigma}\rangle$ is given by

$$\rho(\mu)=2-\rho(-\mu), \tag{2.23}$$

which implies that half-filling, i.e. $\rho = 1$, occurs at $\mu = 0$ for all values of T/t and U/t. This has also important implications for computational methods such as Determinant Quantum Monte Carlo, where at half-filling is free of the *sign problem*, rendering low temperature calculations feasible [54, 55]. However, some of the most important questions regarding the FHM lie away from this point. As we will see in section 3.1, the SU(N) FHM can also be rewritten in PHS form in bipartite lattices and we will present observables of interest and their expressions after the PHT.

For further details on the FHM we refer to the reader to Refs [48, 49].

2.3 Quantum simulation of the Fermi Hubbard Model

The interest in the Fermi-Hubbard model arose from the desire to understand the physics of electrons in solids. Much of the appeal in the FHM stems from its relevance in connection the cuprate high-temperature superconductors. These high-T_c superconductors shared a layered structure which containts copper-oxygen planes [56]. Physicists have gain insight into the low energy physics of these planes studying the two-dimensional (2D) square lattice FHM. The phase diagram of the FHM mirrors many of the features observed in the $T-$doping plane [‖] cuprates phase diagram (see Fig. 2.3). Simulations of the FHM in the 2D square lattice have found regions of the phase diagram where antiferromagnetism, stripes, pseudogap, strange metallicity, Fermi liquid, and d-wave superconducting correlations are observed.

However, given the simplified nature of the FHM, we do not expect it will fully describe the cuprates. For example, the Hubbard model is a single orbital model, while copper-oxygen planes contain d and p orbitals, necessitating the consideration of at least three orbitals, as well as nonlocal hopping and interaction terms [49].

On the other hand, quantum simulators with ultracold atomic gases are well described by the FHM (as we will see in Chapter 4). In these systems, a series of experiments have been performed in one-dimensional chains [59–61], two-dimensional lattices [21, 62, 63], and three-dimensional cubic lattices [20]. Experiments have measured spin correlation functions [20, 21, 59], explored the pseudogap region for attractive interactions [64], studied how the presence of holes affects quantum magnetism [65, 66]. Furthermore, experiments are not limited only to static quantities, but also transport measurements of the spin and charge degrees of freedom have been performed probing the strange metallic region of FHM [22, 23]. Some of these results are illustrated in Fig. 2.4 where experiments in two-dimensional optical lattices with

[‖] In condensed matter, hole or electron doping occurs by chemical substitution. In this case, since different ions are introduced this not only increases/decreases the number of carriers in the material, but also might induce structural distortion [57]. In this thesis when we refer to doping this corresponds to hole-doping and we neglect any structural changes of the lattice.

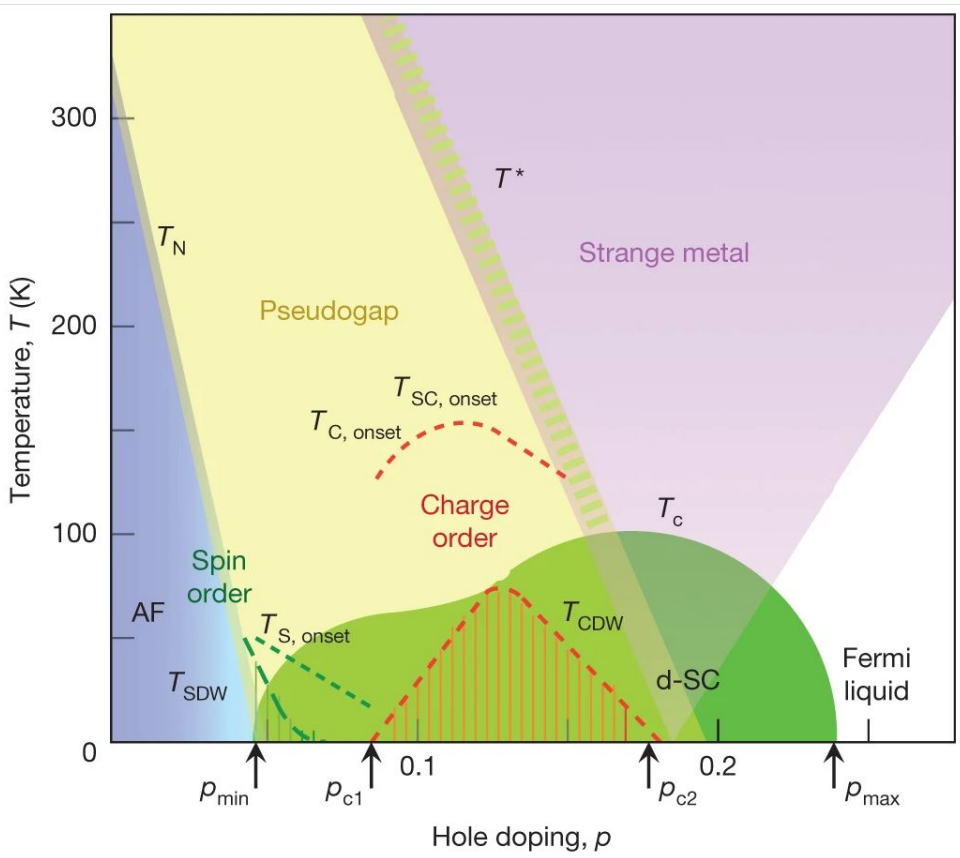

Figure 2.3 : **Phase diagram of the copper oxides**. Temperature vs hole doping phase diagram. It exhibits antiferromagnetism (AF), pseudogap, strange metal, charge density wave (CDW) and d-wave superconductivity (d-SC). Onset temperatures of spin, charge, and superconducting fluctations are denoted by $T_{S,\text{onset}}, T_{C,\text{onset}}, T_{SC,\text{onset}}$, respectively. T_N corresponds to the Néel transition temperature and T_c the superconducting transition temperature. T^* corresponds to the crossover temperature to the pseudogap. The red striped area indicates the presence of fully developed charge order. Arrows in the x-axis denote quantum critical points for superconductivity and charge order. Figure reprinted with copyright permission of Ref. [58].

quantum gas microscope capabilities have gained insight into the phase diagram by measurement of static and dynamic quantities [21–23, 27, 62, 63, 65–70]. The challenges to cool further down and access the temperature scales where charge desnsity waves and d-wave superconductivity still remains. Possible architectures to overcome the temperature scales are quantum simulators with higher symmetry fermions [**?**, 71] and optical tweezer arrays [39, 40] as we will discuss in Chapters 8 and 9.

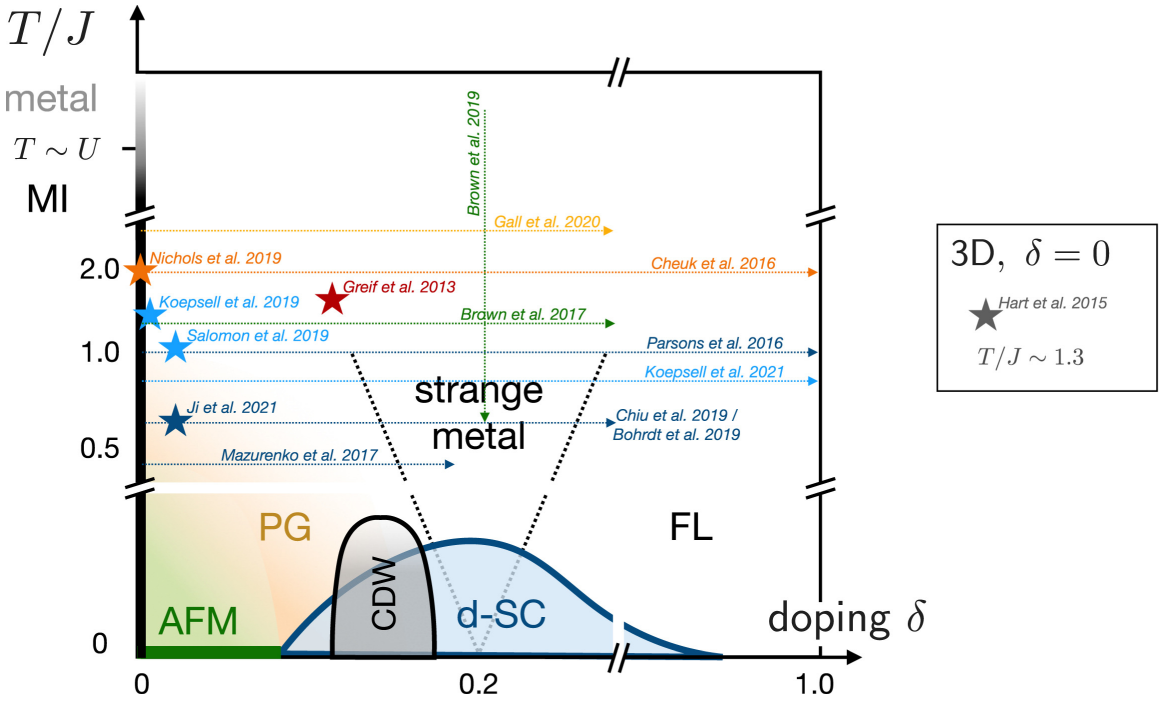

Figure 2.4 : **Exploration of the SU(2) FHM phase diagram with ultracold atoms**. Results from a series of experiments in the two-dimensional square lattice FHM model are depicted by stars and lines. These experiments span the proposed phase diagram of the FHM: Mott insulator (MI), antiferromagnet (AFM), pseudogap (PG), charge density wave (CDW), d-wave superconductor (d-SC), strange metal, and Fermi liquid (FL). Results in the three-dimensional cubic lattice from Randy Hulet's group at Rice (Ref. [20]) are also presented for completeness. Figure reprinted with copyright permission of Ref. [24].

2.4 Summary

In this chapter we introduced the Fermi Hubbard in its original spin-1/2 SU(2) symmetric form. We discussed how it is the simplest interacting model one can write for electrons in a solid. We discussed the conditions for which this single band model is valid, i.e. the on-site interaction U, temperature and energy must be smaller than the energy gap between the lowest and first excited band. We also discussed the symmetries of the FHM, including the U(1) global symmetry, the SU(2) spin symmetry, and the particle-hole symmetry. Finally we presented its connection to the cuprate superconductors and the achievements of quantum simulation in quantum gas microscopes.

Chapter 3

The SU(N) Fermi-Hubbard Model

> En esta tierra en donde puedo caminar
> Bajo la dirección que le ponga a mis pasos
> Siempre habrá tiempo para venirle a cantar
> Por ser lo más que sé ofrecer como regalo.
>
> *Hoy hace un buen día.* Fernando Delgadillo

In the previous chapter we introduced the Fermi-Hubbard Model (FHM) in its original SU(2) symmetry form and discussed some its properties and expected phase diagram. In this chapter we follow a similar approach and introduce the SU(N) FHM and its properties, in particular the SU(N) symmetry and the particle hole symmetry. Finally we present a literature review of a series of theoretical predictions and experimental results of the SU(N) FHM.

3.1 The SU(N) Hamiltonian

As we discussed in Chapter 2, the Fermi-Hubbard Model (FHM) is central to condensed matter physics, as it accounts for many phenomena observed in solid state systems such as the Mott insulating phase, long-range antiferromagnetic order, superconductivity and charge density waves [45–47]. Its generalization, the SU(N) FHM, features larger spins and enhanced symmetry, and it is defined by the grand-canonical Hamiltonian,

$$H = -t \sum_{\langle i,j\rangle,\sigma} \left(c^\dagger_{i\sigma} c_{j\sigma} + c^\dagger_{j\sigma} c_{i\sigma} \right) + \frac{U}{2} \sum_{i,\sigma\neq\tau} n_{i\sigma} n_{i\tau} - \mu \sum_{i,\sigma} n_{i\sigma}, \tag{3.1}$$

where $c^{\dagger}_{i\sigma}(c_{i\sigma})$ is the creation (annihilation) operator for a fermion with spin $\sigma = 1, 2, ..., N$ on site $i = 1, 2, ..., N_s$, and $n_{i\sigma}$ is the number operator. t is the hopping amplitude between nearest-neighbor sites i and j, U is the interaction strength and μ is the chemical potential controlling the fermion density (see Fig. 3.1).

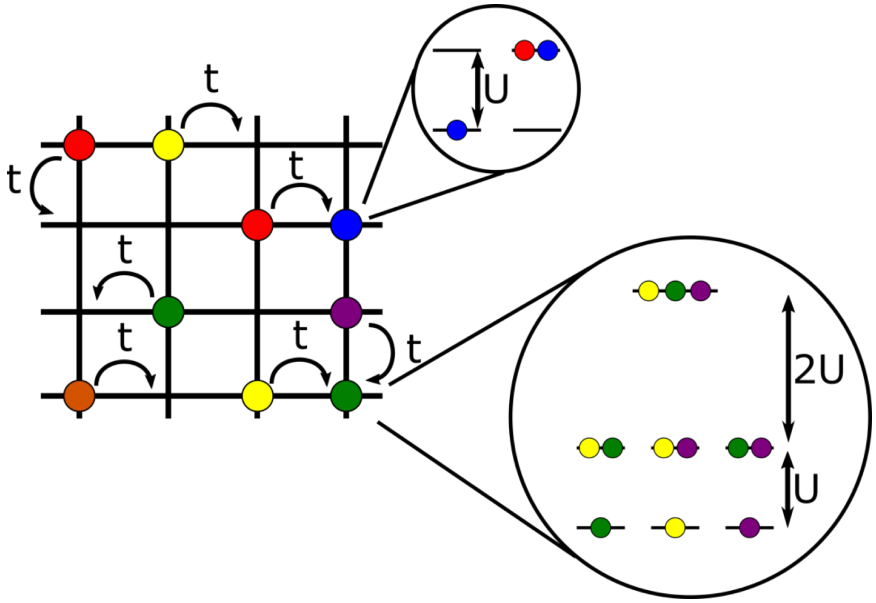

Figure 3.1 : **SU(N) Fermi Hubbard Model**. In its SU(N) symmetric form the Fermi Hubbard Model consists of particles living on a lattice with spin color (denoted by red, blue, green, etc...) that can tunneling to nearest neighboring sites with hopping amplitude t. The number of colors is N. When m atoms of different color occupy the same site, this raises the energy by Um. The filling fraction is controlled by the chemical potential μ.

The SU(N) FHM provides insight into important strongly correlated systems since it is a simple limit of multiorbital models describing transition-metal oxides [72–74], and is an important generalization of the SU(2) FHM since it exhibits the possibility of phenomena such as antiferromagnetism, superconductivity, nematic order, valence bond and the spin-liquid phases [73, 75–79].

3.2 Symmetries of the SU(N) Fermi Hubbard Model

The SU(N) FHM exhibits symmetries similar to its SU(2) counterpart. Similarly to the SU(2) FHM, it has a global U(1) symmetry that reflects a global charge conser-

vation, which means the total particle number $N_{\text{ptcl}} = \sum_{i,\sigma} n_{i\sigma}$ is conserved. It also presents a global SU(N) symmetry that corresponds to the spin isotropy, and the generators of the group are the spin permutation operators,

$$S_\tau^\sigma = \sum_i S_\tau^\sigma(i) = \sum_i c_{i\sigma}^\dagger c_{i\tau}, \tag{3.2}$$

that satisfy the SU(N) algebra,

$$[S_\tau^\sigma, S_\beta^\alpha] = \delta_{\sigma\beta} S_\tau^\alpha - \delta_{\tau\alpha} S_\beta^\sigma. \tag{3.3}$$

All generators of the algebra commute with the Hamiltonian [eq. (3.1)] and therefore the system exhibits and SU(N) symmetry. Similarly to the $N = 2$ case the populations of each spin component are conserved since $S_\sigma^\sigma = N_\sigma = \sum_i c_{i\sigma}^\dagger c_{i\sigma} = \sum_i n_{i\sigma}$.

In a similar fashion to the SU(2) FHM, the SU(N) FHM can be rewritten in a PHS form

$$H = -t \sum_{\langle i,j\rangle,\sigma} \left(c_{i\sigma}^\dagger c_{j\sigma} + c_{j\sigma}^\dagger c_{i\sigma} \right) + \frac{U}{2} \sum_{i,\sigma\neq\tau} \left(n_{i\sigma} - \frac{1}{2} \right) \left(n_{i\tau} - \frac{1}{2} \right) - \mu \sum_{i,\sigma} n_{i\sigma}. \tag{3.4}$$

Under this transformation the shift in the chemical potential is $\mu \to \mu + (U/2)(N-1)$ and the overall additive constant to the energy can be neglected. Under the PHT, the sign of μ gets reversed and one can derive the following relationships.

- Density $\rho = \langle n \rangle = \sum_\sigma \langle n_\sigma \rangle$

$$\rho(\mu) = N - \rho(-\mu), \tag{3.5}$$

  which implies that half-filling, i.e. $\rho = N/2$, occurs at $\mu = 0$ for values of T/t and U/t.

- Number of onsite pairs $\mathcal{D} = \frac{1}{2}\sum_{\sigma\neq\tau}\langle n_{i\sigma}n_{i\tau}\rangle$

$$\mathcal{D}(\mu) = \binom{N}{2} + (1-N)\rho(-\mu) + \mathcal{D}(-\mu). \tag{3.6}$$

- Kinetic energy $K = -t\sum_{\langle i,j\rangle,\sigma}\langle c^\dagger_{i\sigma}c_{j\sigma} + c^\dagger_{j\sigma}c_{i\sigma}\rangle$

$$K(\mu) = K(-\mu). \tag{3.7}$$

And the total energy is given by $E(\mu) = K(\mu) + U\mathcal{D}(\mu)$. With these expressions, one only needs to compute the results for positive values of μ to recover the quantities for $-\mu$ without the need of further calculations.

For further information on the SU(N) group, we refer the reader to Refs. [80, 81].

3.3 Some important limits

3.3.1 The non-interacting limit $U = 0$

The non-interacting limit is one of the useful initial steps to understand the physics of the SU(N) FHM. Not only is it the basis for introducing the interaction as a perturbation, but also allows for debugging numerical techniques. In the non-interacting limit $U = 0$ and the Hamiltonian reads as,

$$H = -t\sum_{\langle i,j\rangle,\sigma}\left(c^\dagger_{i\sigma}c_{j\sigma} + c^\dagger_{j\sigma}c_{i\sigma}\right) - \mu\sum_{i,\sigma} n_{i\sigma}, \tag{3.8}$$

and has a simpler expression in the momentum basis $c_{\mathbf{r}\sigma} = \frac{1}{N_s}\sum_{\mathbf{k}} e^{-i\mathbf{k}\cdot\mathbf{r}}c_{\mathbf{k}\sigma}$, where $\mathbf{k} = \frac{2\pi}{N_s}(n_1, n_2, n_3)$ with $n_i \in 1, \ldots, N_s$. With the previous relations, the Hamiltonian is simply given by,

$$H = \sum_{\mathbf{k},\sigma}(\epsilon_{\mathbf{k}} - \mu)n_{\mathbf{k}\sigma}, \tag{3.9}$$

where the energy dispersion for cubic lattices is,

$$\epsilon_{\mathbf{k}} = -2t \sum_{x_i} \cos(k_{x_i}), \tag{3.10}$$

where i can run from $\{1\}$, $\{1,2\}$ or $\{1,2,3\}$, depending on dimensionality.

In this case, one can write analytic expressions for the observables of interest. Let D be the dimensionality. In this case, thermodynamic quantities in the thermodynamic limit are,

$$\rho = \frac{N}{(2\pi)^D} \int_{-\pi}^{\pi} \frac{1}{1+e^{\beta(\epsilon_{\mathbf{k}}-\mu)}} d^D\mathbf{k}, \tag{3.11}$$

$$E = \frac{N}{(2\pi)^D} \int_{-\pi}^{\pi} \frac{\epsilon_{\mathbf{k}}}{1+e^{\beta(\epsilon_{\mathbf{k}}-\mu)}} d^D\mathbf{k}, \tag{3.12}$$

$$\mathcal{D} = \binom{N}{2} \rho^2, \tag{3.13}$$

$$F = \frac{1}{\beta} \frac{N}{(2\pi)^D} \int_{-\pi}^{\pi} \ln\left[1+1+e^{-\beta(\epsilon_{\mathbf{k}}-\mu)}\right] d^D\mathbf{k} - \mu\rho, \tag{3.14}$$

$$S = \beta E + F, \tag{3.15}$$

which correspond to the density, energy, energy, number of onsite pairs, free energy, and entropy, respectively.

In addition, one can compute correlation functions. Of particular relevance are the spin-spin and density-density correlation functions. The spin-spin correlation function is given by,

$$C_s(\mathbf{x},\mathbf{y}) = \sum_{\sigma\neq\tau} \Big[\langle n_{\mathbf{x}\sigma} n_{\mathbf{y}\sigma} \rangle - \langle n_{\mathbf{x}\sigma} n_{\mathbf{y}\tau} \rangle \Big]. \tag{3.16}$$

Here is useful to note that, assuming translation invariance, if the spin-populations are balanced and therefore the SU(N) symmetry is present, the disconnected part of the correlator, i.e. $\langle n_{\mathbf{x}\sigma}\rangle\langle n_{\mathbf{y}\sigma}\rangle - \langle n_{\mathbf{x}\sigma}\rangle\langle n_{\mathbf{y}\tau}\rangle$ vanishes and therefore it is irrelevant whether it is included.

The density-density correlation function is defined as,

$$C_d(\mathbf{x},\mathbf{y}) = \langle n_\mathbf{x} n_\mathbf{y}\rangle - \langle n_\mathbf{x}\rangle\langle n_\mathbf{y}\rangle = \sum_{\sigma,\tau}\langle n_{\mathbf{x}\sigma} n_{\mathbf{y}\tau}\rangle - \rho^2$$
$$= \sum_{\sigma\neq\tau}\langle n_{\mathbf{x}\sigma} n_{\mathbf{y}\tau}\rangle + \sum_{\sigma}\langle n_{\mathbf{x}\sigma} n_{\mathbf{y}\sigma}\rangle - \rho^2. \tag{3.17}$$

For simplicity we define $\tilde{C}_d = C_d + \rho^2$:

$$\tilde{C}_d = \langle n_\mathbf{x} n_\mathbf{y}\rangle = \sum_{\sigma\neq\tau}\langle n_{\mathbf{x}\sigma} n_{\mathbf{y}\tau}\rangle + \sum_{\sigma}\langle n_{\mathbf{x}\sigma} n_{\mathbf{y}\sigma}\rangle. \tag{3.18}$$

Therefore, in order to access C_s and $\tilde{C}_d$, we need to compute the following expectation values:

$$\begin{aligned}
\langle n_{\mathbf{x}\sigma} n_{\mathbf{y}\sigma}\rangle &= \langle c^\dagger_{\mathbf{x}\sigma} c_{\mathbf{x}\sigma} c^\dagger_{\mathbf{y}\sigma} c_{\mathbf{y}\sigma}\rangle \\
&= \frac{1}{N_s^2}\sum_{\mathbf{pkqs}} e^{i(\mathbf{p}\text{ - }\mathbf{k})\cdot\mathbf{x}} e^{i(\mathbf{q}-\mathbf{s})\cdot\mathbf{y}} \langle c^\dagger_{\mathbf{p}\sigma} c_{\mathbf{k}\sigma} c^\dagger_{\mathbf{q}\sigma} c_{\mathbf{s}\sigma}\rangle, \qquad (3.19)\\
\langle n_{\mathbf{x}\sigma} n_{\mathbf{y}\tau}\rangle &= \langle c^\dagger_{\mathbf{x}\sigma} c_{\mathbf{x}\sigma} c^\dagger_{\mathbf{y}\tau} c_{\mathbf{y}\tau}\rangle \\
&= \frac{1}{N_s^2}\sum_{\mathbf{pkqs}} e^{i(\mathbf{p}\text{ - }\mathbf{k})\cdot\mathbf{x}} e^{i(\mathbf{q}-\mathbf{s})\cdot\mathbf{y}} \langle c^\dagger_{\mathbf{p}\sigma} c_{\mathbf{k}\sigma} c^\dagger_{\mathbf{q}\tau} c_{\mathbf{s}\tau}\rangle, \qquad (3.20)
\end{aligned}$$

where we have explicitly separated the cases $\sigma = \tau$ and $\sigma \neq \tau$.

We can compute the expectation values using Wick's theorem for fermions,

$$\langle ABCD\rangle = \langle AB\rangle\langle CD\rangle - \langle AC\rangle\langle BD\rangle + \langle AD\rangle\langle BC\rangle. \tag{3.21}$$

Therefore,

$$\begin{aligned}
\langle c^\dagger_{\mathbf{p}\sigma} c_{\mathbf{k}\sigma} c^\dagger_{\mathbf{q}\sigma} c_{\mathbf{s}\sigma}\rangle &= \langle c^\dagger_{\mathbf{p}\sigma} c_{\mathbf{k}\sigma}\rangle\langle c^\dagger_{\mathbf{q}\sigma} c_{\mathbf{s}\sigma}\rangle + \langle c^\dagger_{\mathbf{p}\sigma} c_{\mathbf{s}\sigma}\rangle\langle c_{\mathbf{k}\sigma} c^\dagger_{\mathbf{q}\sigma}\rangle \\
&= \langle n_{\mathbf{k}\sigma}\rangle\langle n_{\mathbf{q}\sigma}\rangle\delta_{\mathbf{p},\mathbf{k}}\delta_{\mathbf{q},\mathbf{s}} + \langle n_{\mathbf{p}\sigma}\rangle\big(1-\langle n_{\mathbf{k}\sigma}\rangle\big)\delta_{\mathbf{p},\mathbf{s}}\delta_{\mathbf{q},\mathbf{k}} \qquad (3.22)\\
\langle c^\dagger_{\mathbf{p}\sigma} c_{\mathbf{k}\sigma} c^\dagger_{\mathbf{q}\tau} c_{\mathbf{s}\tau}\rangle &= \langle c^\dagger_{\mathbf{p}\sigma} c_{\mathbf{k}\sigma}\rangle\langle c^\dagger_{\mathbf{q}\tau} c_{\mathbf{s}\tau}\rangle + \langle c^\dagger_{\mathbf{p}\sigma} c_{\mathbf{s}\sigma}\rangle\langle c_{\mathbf{k}\tau} c^\dagger_{\mathbf{q}\tau}\rangle \\
&= \langle n_{\mathbf{k}\sigma}\rangle\langle n_{\mathbf{q}\tau}\rangle\delta_{\mathbf{p},\mathbf{k}}\delta_{\mathbf{q},\mathbf{s}}. \qquad (3.23)
\end{aligned}$$

With these results the $\sigma \neq \tau$ case (σ,τ) is,

$$\begin{aligned}
\langle n_{\mathbf{x}\sigma} n_{\mathbf{y}\tau}\rangle &= \frac{1}{N_s^2}\sum_{\mathbf{pkqs}} e^{i(\mathbf{p}\,-\,\mathbf{k})\cdot\mathbf{x}} e^{i(\mathbf{q}-\mathbf{s})\cdot\mathbf{y}}\langle n_{\mathbf{k}\sigma}\rangle\langle n_{\mathbf{q}\tau}\rangle\delta_{\mathbf{p},\mathbf{k}}\delta_{\mathbf{q},\mathbf{s}} \\
&= \frac{1}{N_s^2}\sum_{\mathbf{kq}}\langle n_{\mathbf{k}\sigma}\rangle\langle n_{\mathbf{q}\tau}\rangle \\
&= \left(\frac{\rho}{N}\right)^2. \qquad (3.24)
\end{aligned}$$

Now the (σ,σ) term is given by,

$$\begin{aligned}
\langle n_{\mathbf{x}\sigma} n_{\mathbf{y}\sigma}\rangle &= \frac{1}{N_s^2}\sum_{\mathbf{pkqs}} e^{i(\mathbf{p}\,-\,\mathbf{k})\cdot\mathbf{x}} e^{i(\mathbf{q}-\mathbf{s})\cdot\mathbf{y}}\left[\langle n_{\mathbf{k}\sigma}\rangle\langle n_{\mathbf{q}\sigma}\rangle\delta_{\mathbf{p},\mathbf{k}}\delta_{\mathbf{q},\mathbf{s}} + \langle n_{\mathbf{p}\sigma}\rangle\big(1-\langle n_{\mathbf{k}\sigma}\rangle\big)\delta_{\mathbf{p},\mathbf{s}}\delta_{\mathbf{q},\mathbf{k}}\right] \\
&= \left(\frac{\rho}{N}\right)^2 + \frac{1}{N_s^2}\sum_{\mathbf{kq}} e^{i(\mathbf{q}\,-\,\mathbf{k})\cdot(\mathbf{x}-\mathbf{y})}\langle n_{\mathbf{q}\sigma}\rangle\big(1-\langle n_{\mathbf{k}\sigma}\rangle\big) \\
&= \left(\frac{\rho}{N}\right)^2 + \frac{\rho}{N}\delta_{\mathbf{r},\mathbf{0}} - \left[\frac{1}{N_s}\sum_{\mathbf{q}} e^{i\mathbf{q}\cdot\mathbf{r}}\langle n_{\mathbf{q}\sigma}\rangle\right]\left[\frac{1}{N_s}\sum_{\mathbf{k}} e^{-i\mathbf{k}\cdot\mathbf{r}}\langle n_{\mathbf{k}\sigma}\rangle\right] \\
&= \left(\frac{\rho}{N}\right)^2 + \frac{\rho}{N}\delta_{\mathbf{r},\mathbf{0}} - \left|\frac{1}{(2\pi)^D}\int_{-\pi}^{\pi}\frac{e^{i\mathbf{k}\cdot\mathbf{r}}}{1+e^{\beta(\epsilon_{\mathbf{k}}-\mu)}}d^D\mathbf{k}\right|^2 \qquad (3.25)
\end{aligned}$$

For all the previous expressions we used the SU(N) spin permutation symmetry and the fact that the correlation functions do not depend on the particular $\mathbf{x}$ and $\mathbf{y}$ but just their difference $\mathbf{r} = \mathbf{x} - \mathbf{y}$.

With these results, C_s and $\tilde{C}_d$ in the non-interacting limit are,

$$C_s^{U=0}(\mathbf{r}) = N(N-1)\left[\delta_{\mathbf{r},\mathbf{0}}\frac{\rho}{N} - \left|\frac{1}{(2\pi)^D}\int_{-\pi}^{\pi}\frac{e^{i\mathbf{k}\cdot\mathbf{r}}}{1+e^{\beta(\epsilon_{\mathbf{k}}-\mu)}}d^D\mathbf{k}\right|^2\right] \tag{3.26}$$

$$\tilde{C}_d^{U=0}(\mathbf{r}) = \rho^2 + \rho\delta_{\mathbf{r},\mathbf{0}} - N\left|\frac{1}{(2\pi)^D}\int_{-\pi}^{\pi}\frac{e^{i\mathbf{k}\cdot\mathbf{r}}}{1+e^{\beta(\epsilon_{\mathbf{k}}-\mu)}}d^D\mathbf{k}\right|^2 \tag{3.27}$$

These results will be useful to diagnose numerical techniques and to understand the effects of introducing interactions. Plots of some of these quantities are presented in Chapter 7 and Appendix C.

3.3.2 The atomic limit $t = 0$

Another useful limit corresponds to the case of a single site or when we set the tunneling to zero ($t = 0$) and the system is a series of independent sites. In this case, the Hamiltonian in its PHS form reduces to,

$$H = \frac{U}{2}\sum_{i,\sigma\neq\tau}\left(n_{i\sigma}-\frac{1}{2}\right)\left(n_{i\tau}-\frac{1}{2}\right) - \mu\sum_{i,\sigma}n_{i\sigma}, \tag{3.28}$$

and its eigenenergies are,

$$\epsilon_0(n) = \frac{U}{2}n(n-1) - \mu n, \tag{3.29}$$

where n is the number of particles on the site [and recall that in the PHS form $\mu \to \mu + (U/2)(N-1)$, which we are omitting for simplicity]. The partition function for the single site is given by,

$$z_0 = \sum_{n=0}^{N}\binom{N}{n}e^{-\beta\epsilon_0(n)} \tag{3.30}$$

For simplicity, let us define $y = e^{-\beta U}$ and $x = e^{\beta\mu}$. Written like this, the partition function is:

$$z_0 = \sum_{n=0}^{N}\binom{N}{n}y^{\frac{1}{2}n(n-1)}x^n, \tag{3.31}$$

and the free energy in the grand canonical ensemble is $\Omega_0 = -\frac{1}{\beta}\ln z_0$. In this limit, thermodynamic quantities are,

$$\rho_0 = \langle n \rangle_0 = \frac{1}{z_0}\sum_{n=0}^{N} n\binom{N}{n} e^{-\beta\epsilon_0(n)}, \tag{3.32}$$

$$\mathcal{D}_0 = \frac{1}{2}\langle n(n-1)\rangle_0 = \frac{1}{z_0}\sum_{n=0}^{N}\binom{N}{2}\binom{N}{n} e^{-\beta\epsilon_0(n)}, \tag{3.33}$$

$$E = U\mathcal{D}, \tag{3.34}$$

$$S = \ln(z_0) + \beta(E - \mu\rho). \tag{3.35}$$

The atomic limit calculation is the zeroth-order high temperature series expansion in t/T and we will discuss corrections to it to second order in $(t/T)^2$ in Chapter 5. Several plots of the atomic limit are presented in Chapters 7 and 10 and in Appendix C.

3.3.3 The Heisenberg limit

Another important limit of the SU(N) FHM is the limit $t/U \ll 1$ and one particle per site $\langle n \rangle = 1$ where the system is effectively described by the quantum spin Heisenberg Hamiltonian. Ref. [82] presents a detailed discussion on how to obtain the spin-1/2 Heisenberg Hamiltonian from the SU(2) FHM. Here we will present the main idea and introduce the concept of superexchange for a two-site system following Ref. [8]. Starting from eq. 3.1, and only focus on the kinetic $\widehat{K}$ and interaction energy terms $\widehat{U}$ in the Hamiltonian. For $U/t \gg 1$, the interaction energy term dominates, and therefore we can use it as our zeroth-order Hamiltonian. The ground state manifold for two sites is 2^N-fold degenerate and we will denote it as,

$$\{GS\} = |\sigma_1, \sigma_2\rangle, \tag{3.36}$$

where σ_i can take one of the spin flavor values, i.e. $\sigma_i = 1, 2, \cdots, N$, and $i = 1, 2$.

The energies of the doubly occupied sites are higher by U than the multiplet state [eq. (3.36)]. When we introduce the tunneling term perturbatively, we have to do it to second order. The first-order term in perturbation theory in $\widehat{K}$ takes one particle from one site and puts it on top of the other one on the other site. This term takes us out of the ground state manifold. When we consider the second-order term in the degenerate perturbation theory, it allows us to construct and effective Hamiltonian,

$$\langle a|H_{\text{eff}}^{(2)}|b\rangle = -\langle a|\widehat{K}\left(\frac{1-\widehat{P}_{GS}}{\widehat{V}}\right)\widehat{K}|b\rangle = -\sum_{m\neq\{GS\}}\langle a|\widehat{K}|m\rangle\frac{1}{\langle m|\widehat{V}|m\rangle}\langle m|\widehat{K}|b\rangle, \quad (3.37)$$

where a, b denote states in the ground state subspace $\{GS\}$, and $\widehat{P}_{GS}$ is the projection operator onto the ground state manifold, which means that states $|m\rangle$ contain higher occupancies. We can visualize the effects of the terms in the sum in Table 3.1 where the allowed paths (first two rows) each yield a contribution $-t^2/U$. Note that there are some paths that are blocked by Pauli exclusion principle (last row).

Initial state	$\widehat{K}$	$1/\widehat{V}$	$\widehat{K}$	Final state
$\|\sigma,\tau\rangle$	$\rightarrow$	$\|\sigma\tau,0\rangle$	$\rightarrow$	$\|\sigma,\tau\rangle$
$\|\sigma,\tau\rangle$	$\rightarrow$	$\|0,\sigma\tau\rangle$	$\rightarrow$	$\|\sigma,\tau\rangle$
$\|\sigma,\sigma\rangle$	$\rightarrow$	0		

Table 3.1 : "Exchange paths" in the Heisenberg model.

The operators that connect these initial and final states can be written in terms of the spin permutation operators $S_\sigma^\tau(i)$. Therefore one can write the effective Hamiltonian in the ground state subspace as an isotropic antiferromagnetic Heisenberg exchange:

$$H_{\text{Heisenberg}} = J\sum_{\langle i,j\rangle}\sum_{\sigma,\tau}S_\sigma^\tau(i)S_\tau^\sigma(j), \quad (3.38)$$

where $J = 4t^2/U$ is the superexchange energy [*]. In the $U/t \gg 1$ limit and one particle

[*]The simplest way of seeing this is the following: The only terms contributing in $\langle m|V|m\rangle$ all have energy U, therefore we can replace this term by U. We are then left with $H_{\text{eff}} = -(1/U)P_{GS}K^2P_{GS}$.

per site on average the system is a Mott insulator where the energy is lowered by the virtual process of double occupation, called superexchange. In the Heisenberg Hamiltonian only spin interactions are present and is a paradigmatic model to study quantum magnetism.

3.3.4 The large-N limit

The last limit worth mentioning is the large-N limit. The $1/N$ (or more adequately $1/S$) expansion technique was first used to understand spin-1/2 systems that exhibit SU(2) spin symmetry [83–86]. In this case, one reduces the role of quantum fluctuations by considering the classical limit of magnets with large spin S. In doing so, the expectation value of the spins acquires a definite value with a small variation around this saddle point and thus the $1/S$ expansion provides a method to therefore obtain mean field theories.

In the $1/S$ expansion, the relevant operators are the raising and lowering operators $S^{\pm}$, which only connect two possible values of the spin projections, and therefore as S increases the variance of the spin projection falls off as $1/S$. In contrast, for the SU(N) case even though $1/N$ is small, the spin permutation operators connect all possible values of the spin projection and therefore quantum fluctuations are relevant and play a major role in the ground state spin structure. For this reason, in the SU(N) case the variance does not go like $1/N$.

The $1/N$ expansion is not a perturbative expansion in the interaction or the tunneling, but instead is a saddle point expansion that preserves the spin symmetry of the Hamiltonian [8,87] [†]. For more information, Ref. [86] provides a comprehensive

Let us now focus on K^2, which for two sites can be written as $t^2 \sum_{\sigma,\tau} c^\dagger_{1\sigma} c^\dagger_{1\tau} c_{1\tau} c_{2\sigma} + \text{h.c.}$ In the case of $N = 2$ this term can be rewritten as $-t^2(n_1 n_2 + 4\mathbf{S}_1 \cdot \mathbf{S}_2)$. Since the number of particles is fixed to $\langle n \rangle = 1$ by the projector operator, the first term is a constant and can be dropped. The effective Hamiltonian is now $(4t^2/U)\mathbf{S}_1 \cdot \mathbf{S}_2$, where the superexchange energy scale $J = 4t^2/U$ naturally arises. It is customary in the literature to work only with the spin permutation operators instead of $\mathbf{S}$, and for that reason we present the Heisenberg Hamiltonian in terms of those in the main text.

[†]For the purposes of this thesis, we consider it useful to make a differentiation between the cases, therefore for the case of SU(N) symmetric models we will used the term $1/N$ expansion, while for

review of the large-N expansion technique.

3.4 SU(N) FHM and Heisenberg models

So far we have discussed important properties and limits of the SU(N) FHM. In this section we will present its application in the condensed matter community and then connect with previous theoretical and numerical results regarding the model.

3.4.1 Wait, aren't electrons spin-1/2?

In our description of the SU(2) FHM we stated it is single orbital model used to describe electrons in a solid, and that electrons are spin-1/2 particles. The SU(N) FHM is a limit of multi orbitals models such as the ones used to describe transition metal oxides [72–74]. In our discussion of the SU(N) FHM, we mentioned we have N spin colors or flavors, which in the context of quantum simulation with alkaline-earth-like atoms correspond to the nuclear spin projections m_I as we will see in Chapter 4. In order to make the connection with the problem of electrons in a solid, we need to take one step back and recall that an electron that is bound to or nearly localized on an specific site has three attributes: charge, spin, and orbital (the shape of the electron cloud in a solid). In the SU(2) FHM case we considered a single orbital and the spin degree of freedom which is invariant under SU(2) rotations. Multi orbital models correspond to models in which higher orbitals are now included and if the Hubbard parameters are independent of the spin and orbital degrees of freedom, then the Hamiltonian is SU(N) symmetric. It is worth noting that such enhanced symmetry is a crude approximation in solid state systems, where interactions between different orbitals may vary over 10% or more [73]. On the other hand, for ultracold atomic experiments the SU(N) symmetry holds down to many orders of magnitude as we will discuss in the next chapter.

the case of SU(2) with enlarged spins, we will refer to it as the $1/S$ expansion to make the underlying spin symmetry explicit and clear.

3.4.2 Previous studies

Historically, the study of SU(N) quantum magnetism was originated from the mathematical technique of large-N expansions [8]. The large-N expansion was used in Ref. [83] to study the Coqblin-Schrieffer Hamiltonian [‡], in Ref. [84] SU(N) antiferromagnetic quantum spin chains, and in Ref. [85] for the Heisenberg model. More recently, an SU(4) spin-valley symmetry was observed in graphene [90] and twisted-bilayer graphene [91–96] which has attracted broader interest to study Hamiltonians with enhanced symmetry.

It has been however, the possibility of exploiting the inherent SU(N) symmetry of alkaline-earth-like atoms what has attracted more attention to the SU(N) FHM [97–101]. In the last decade, a series of theoretical predictions and state-of-the art numerical calculations of the ground state physics have been performed for different values of N.

One of the first pioneering works was Ref. [102, 103], where renormalization group and mean-field theory results of the SU(N) FHM in the two-dimensional square lattice at weak to moderate interactions observe that at half-filling there is a tendency to break the SU(N) symmetry (see Fig. 3.2). For $N = 3$ at half-filling, the SU(3) symmetry breaks by forming a flavor-density wave, in which two flavors prefer one sublattice with equal density, the third flavor goes predominantly on the other sublattice, and the staggered magnetization does not add up to zero. Their results suggest that for $N \leq 6$, there is a strong tendency towards breaking the SU(N) symmetry with staggered two-sublattice real space dependence. On the other hand for $N > 6$ they predict a staggered flux state, in which there are particle currents.

[‡]The Coqblin-Schrieffer model has been used to understand rare-earth solids. In this model, itinerant fermions and an impurity are both N-fold spin degenerate, and thus the Hamiltonian has an SU(N) symmetry [88, 89].

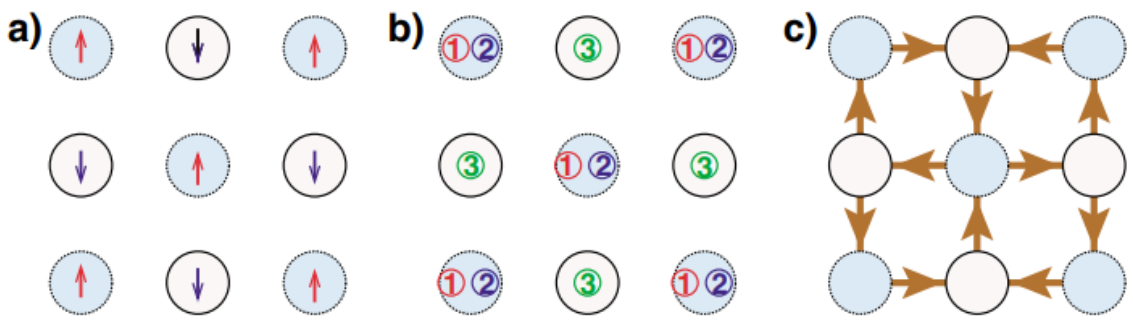

Figure 3.2 : **Half-filling SU(N) FHM states**. a) AFM spin-density wave for $N = 2$. b) Flavor-density wave for $N = 3$. c) Staggered flux state for $N = 6$ (arrows indicate the particle currents). Figure reprinted with copyright permission of Ref. [102].

Since then a series of results of the SU(N) FHM were obtained which predict the existence of a variety of interesting and exotic phases for different values of N, fillings, and interaction strengths. Results for the $N = 3$ FHM are presented in Refs. [104–112] (see Fig. 3.3 as an example). Results for $N = 4$ at quarter filling are given in Refs. [113, 114]. Results for even values of N at half-filling are shown in Refs. [77, 78, 115–122]. Results for one-dimensional chains are displayed in Refs. [123–129] (see Fig. 3.4 as an example). Results in the SU(N) Heisenberg limit are exhibited in Refs. [75, 76, 130–139].

The richness of the model is well illustrated by studies in the Heisenberg limit, where it is predicted to exhibit several phases of matter with novel and difficult-to-explain properties depending on the value of N. For example, Ref. [75] studied Mott insulators in the two-dimensional square lattice and in the large-N limit found a chiral spin liquid ground state with topological order [140]. Furthermore, the dependence of the ground state order with N does not follow a simple pattern as illustrated by Refs. [130–132] (see Fig. 3.5), where $N = 2$ exhibits a checkerboard pattern with 2-sublattice structure [21], the $N = 3$ a 3-sublattice structure [130], the $N = 4$ breaks the translational symmetry and forms dimers [132], the $N = 5$ forms a flavor-ordered pattern [131].

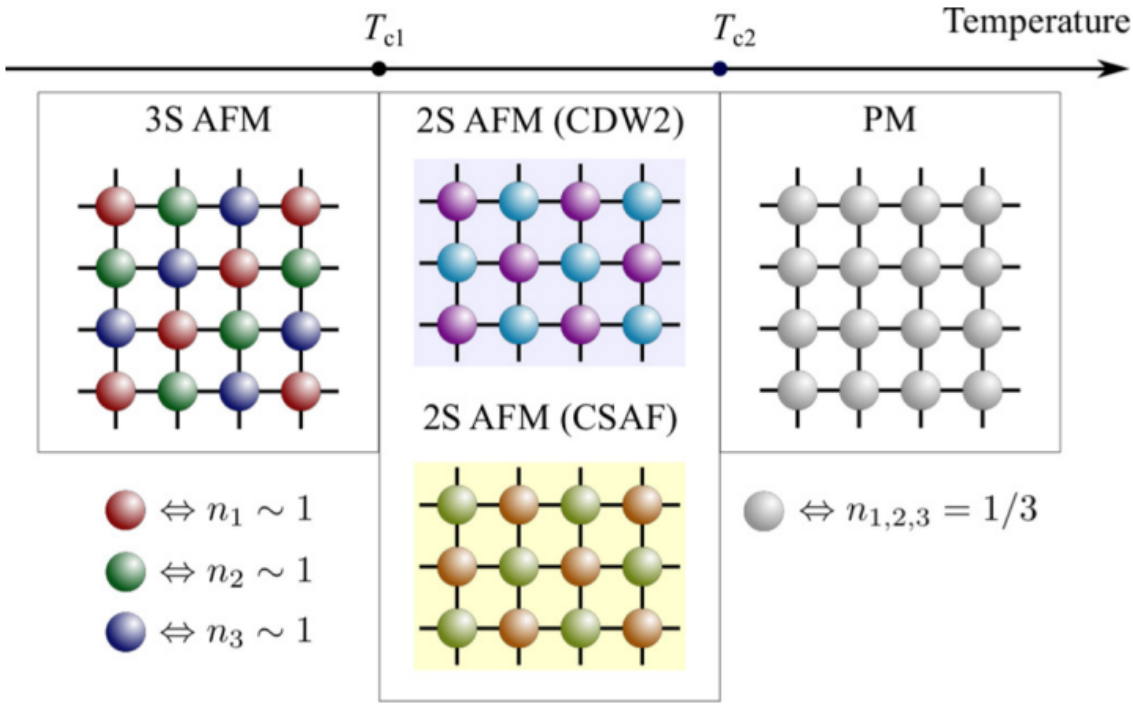

Figure 3.3 : **Magnetic phases at 1/3-filling in the SU(3) FHM**. Schematic of results for a cubic lattice as a function of temperature. As temperature is lowered the system evolves from a paramagnetic phase (PM) to a 2-sublattice antiferromagnetic (AFM) structure which is either a color-density wave (CDW2) or a color-selective antiferromagnetic state (CSAF). As the temperature is lowered even further, a 3-sublattice structure develops. Figure reprinted with copyright permission of Ref. [107].

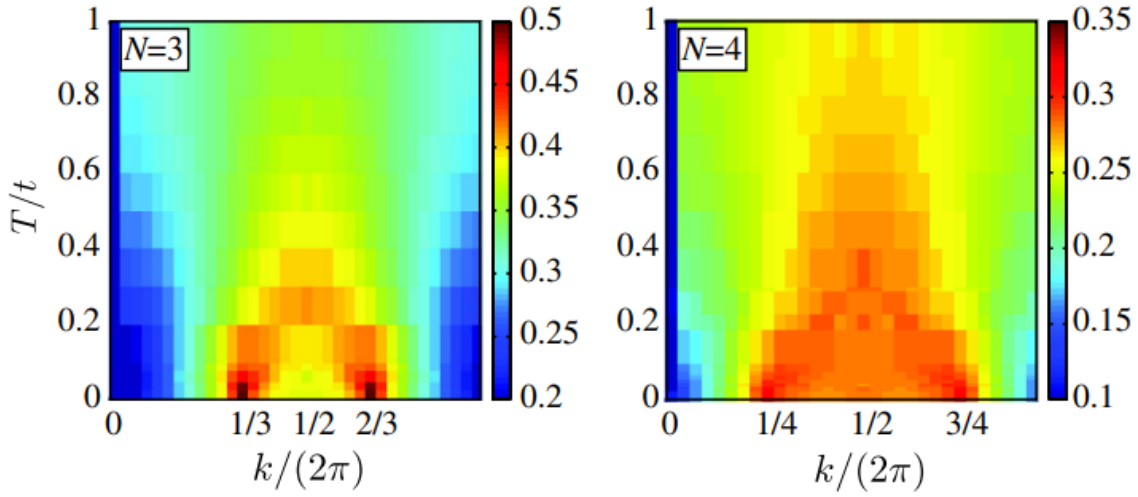

Figure 3.4 : **Spin structure factor in 1D optical lattices for the SU(N) FHM**. Results for $N = 3$ and $N = 4$ are presented as a function of temperature at density $\langle n \rangle = 1$ and $U/t = 8$. As the temperature is lowered magnetic correlations start to develop with an onset of peaks at $2k_F$ (k_F is the Fermi wavevector) at $T/t \lesssim 0.15$. Figure reprinted with copyright permission of Ref. [127].

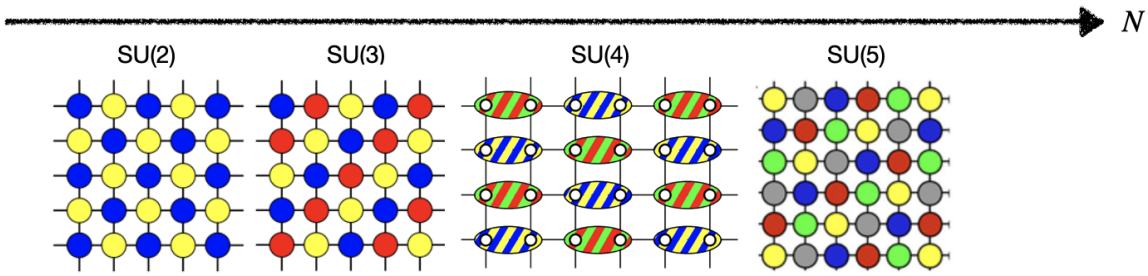

Figure 3.5 : **Ground state dependence on N in the Heisenberg limit**. a) $N = 2$ exhibits a 2-sublattice (2-SL) structure. b) $N = 3$ displays a 3-SL. c) $N = 4$ breaks translational symmetry and froms dimers that teselate the lattice. d) $N = 5$ exhibits a long-ranged flavor ordered pattern. Figures reprinted with copyright permission of Refs. [130–132].

3.5 Quantum simulation of the SU(N) Fermi Hubbard Model

The field of quantum simulation with alkali atoms has yielded numerous important results regarding the SU(2) FHM as we discussed in Chapter 2. In a similar fashion, in recent years state-of-the-art experiments with ultracold ^{173}Yb in 3D optical lattices (OL) have:

- Successfully achieved the SU(6)-symmetric Mott insulator state [71] where experiments compared results for $N = 2$ and $N = 6$. Of particular relevance these results illustrate that the final temperature in the lattice after adiabatic loading (i.e. total number of particles and entropy are conserved) is lower for $N = 6$ than for $N = 2$ (Fig. 3.6b) and that for the lowest temperature achieved in each case, only the $N = 6$ case develops a robust Mott plateau at the center of the trap with an entropy per site close to $\ln(N)$, and the entropy gets pushed onto the metallic state near the edge of the cloud (Fig. 3.6c).

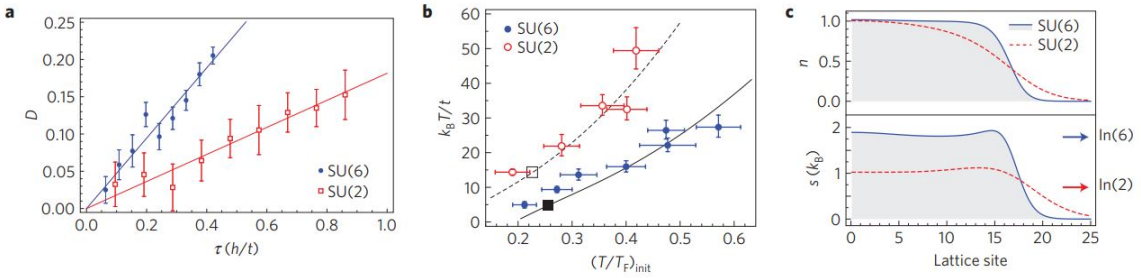

Figure 3.6 : **SU(N) Mott Insulators**. a) Onsite pairs production rate for $N_{\text{ptcl}} = 1.9 \times 10^4$, $U/6t = 10.4$ b) Temperatures of the Fermi gases after adiabatic loading in the lattice as a function of the initial temperature. c) Density and entropy profiles at the lowest temperatures indicated by squares in b). Figure reprinted with copyright permission of Ref. [71].

- Explored the equation of state of the 3D SU(3) and SU(6) FHMs [141]. These experiments measured the density as a function of the chemical potential (Fig. 3.7) for different values of the interaction strength U/t. These results highlight that for $U \ll t$, the system is metallic and can be approximately described by the non-interacting theory (Fig. 3.7a), whereas for $U \gg t$, the single site limit

is a good approximation and can provide a good interpretation of the data (Fig. 3.7b). However, for interactions of the order of the bandwidth $U \sim W$, the system is a strongly correlated many-body state and at the time of publication on 2016 there were no numerical techniques to compare against. As we will see in Chapter 10, we have been collaborating with this group to provide a precise characterization of the equation of state of the SU(N) FHM.

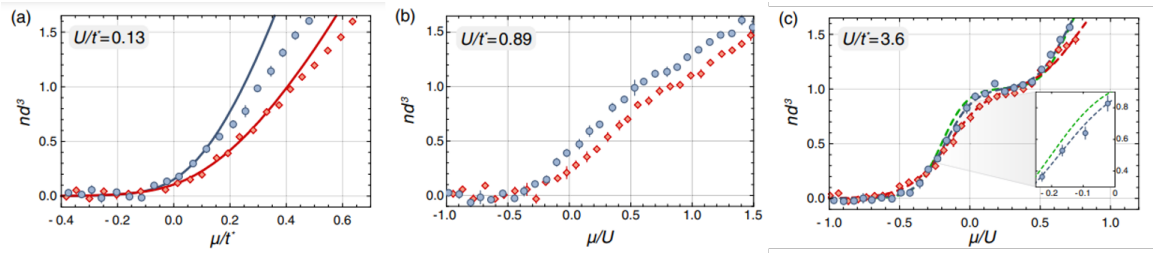

Figure 3.7 : **Equation of State (EoS) of the SU(N) FHM**. Density as a function of the chemical potential for $N = 3$ (red diamonds) and $N = 6$ (blue squares) Fermi gases in a 3D lattice. Here $t^* = W$ the bandwidth of the 3D lattice. a) $U/t^* = 0.128$ b) $U/t^* = 0.89$ c) $U/t^* = 3.6$. Solid lines are fits to the non-interacting Fermi gas EoS for densities below 0.5. Dashed lines are a second-order high temperature series expansion to extract the temperature (in green for $N = 2$ for comparison). Figure reprinted with copyright permission of Ref. [141].

- Observed nearest-neighbor antiferromagnetic (AFM) correlations in a Fermi gas with SU(4) symmetry in a dimerized OL [142] (see Fig. 3.8). The importance of these results are twofold. First, at a fixed entropy per particle AFM nearest-neighbor correlations are enhanced for $N = 4$ compared with $N = 2$; and second, it set up the basis for the experimental technique to measure nearest-neighbor spin correlation functions in lattices with uniform tunnelings. This technique is called singlet-triplet oscillation (STO) and was used for the results we will present in Chapter 8 where we collaborated with this experimental group.

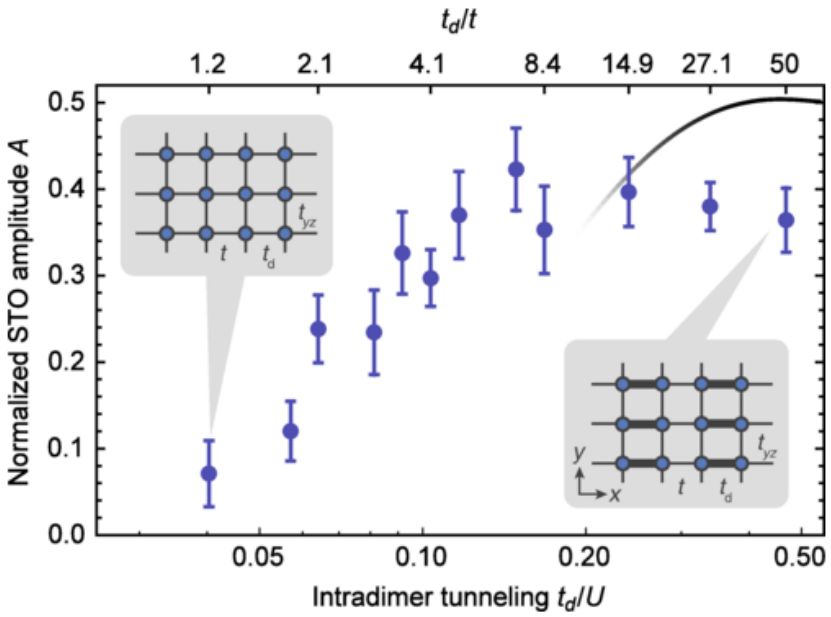

Figure 3.8 : **Nearest-neighbor AFM correlations in a dimerized lattice**. Normalized STO amplitude, which is related to the nearest-neighbor spin correlation function as a function of the intradimer tunneling t_d. $U/h = 3.0$ kHz, $t \in [28.0, 100]$ Hz, and $t_{yz}/t \in [1.7, 1.0]$. Figure reprinted with copyright permission of Ref. [142].

- Detected flavor-selective localization in an SU(3) Fermi gas [143]. These results illustrate that by breaking the SU(3) symmetry using two-photon Raman transitions, the number of on-site pairs is suppressed at as the Raman couplings are introduced, and that the double occupancies are now flavor-dependent (see Fig. 3.9). Exploring the spin-imbalanced SU(N) FHM or the SU(N) FHM under symmetry breaking fields is an immediate question of interest to the field.

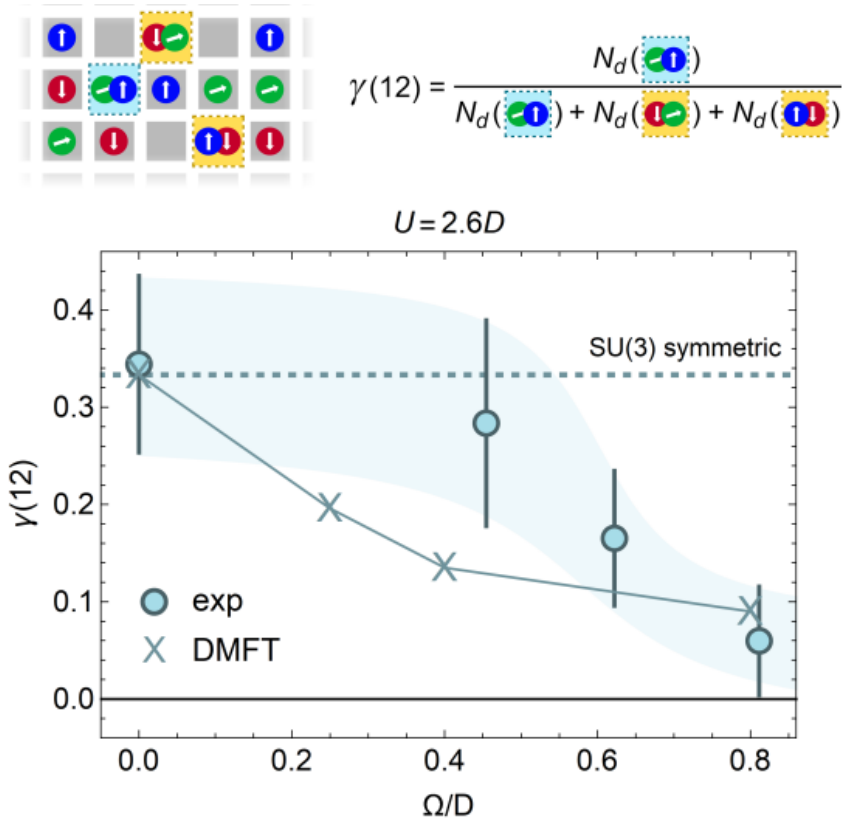

Figure 3.9 : **State selective correlations**. $\gamma(12)$ measures the number of atoms forming doublons in the $|12\rangle$ channel, normalized by the total number of atoms forming doublons. In the absence of Raman couplings ($\Omega = 0$) the results agree with the $N = 3$ symmetric expectation value (dotted line). As Ω is increased, the SU(3) symmetry is broken and $\gamma(12)$ diminishes, approaching zero as $\Omega \approx D = 6t$. Results are presented at $U = 2.6D$. Figure reprinted with copyright permission of Ref. [143].

3.6 Summary

In this chapter we introduced the SU(N) symmetric Fermi-Hubbard model. We discussed its symmetries and important limits such as the non-interacting ($U = 0$), the single-site ($t = 0$), the Heisenberg ($U/t \gg 1$, $\langle n \rangle = 1$), and the large-N limit. Then we presented previous theoretical/numerical results for different values of N to illustrate the richness of the model and we concluded by presenting the major experimental results with quantum simulation with ultracold quantum gases.

Chapter 4

Alkaline-earth-like atoms in optical lattices

> Las vidas no empiezan cuando las personas nacen,
> la vidas empiezan más tarde.
>
> *La balsa de piedra.* José Saramago

In this chapter we discuss why the SU(N) Fermi Hubbard Model (FHM) describes alkaline-earth-like atoms (AEAs) in optical lattices. To do so, we first give a summary on the electronic structure of AEAs, which exhibit a large nuclear spin I and a natural SU($N = 2I + 1$) symmetry in the ground state. Then we provide a derivation of why the SU(N) Fermi Hubbard Model is a good description of AEAs atoms in a optical lattice. This chapter is inspired and adapted from Refs. [51, 144–146].

4.1 A primer on Alkaline-Earth-like atoms

In this section we provide a short introduction to the physics of AEAs, which are used to engineer the SU(N) FHM. First we provide a short discussion of their electronic structure and then comment on why interactions are SU(N) symmetric.

4.1.1 Electronic structure

Alkaline-Earth-like atoms correspond to the elements that exhibit completely full inner shells and have two outer valence electrons in a filled s-shell. Due to the filled inner shells, the two valence electrons are primarily responsible for the chemical and electronic properties of these atoms.

AEAs are the elements that belong to group-II of the periodic table, such as Be, Mg, C, Sr, Ba, and Ra; but also the rare-earth element Yb. Experiments with AEAs have mainly utilized ^{87}Sr ($I = 9/2$) and ^{173}Yb ($I = 5/2$) and for such reason we

will mainly focus only on these two. Given that most of our experimental collaborators work with Yb (Yoshiro Takahashi in Kyoto and Simon Fölling in Münich), all examples given in this section will correspond to Yb, except where explicitly stated.

The electronic configuration of Yb is a filled f- and s-shell. Yb exhibits an electronic structure with spin-singlet ($S = 0$) and spin-triplet ($S = 1$) manifolds. Its level structure is described in the LS-coupling scheme, where coupling between the total orbital angular momentum $\mathbf{L}$ and the total spin of the valence electrons $\mathbf{S}$ gives the total electronic angular momentum $\mathbf{J} = \mathbf{L} + \mathbf{S}$. A detailed scheme of the level structure for Yb with the most relevant optical transitions is shown in Fig. 4.1.

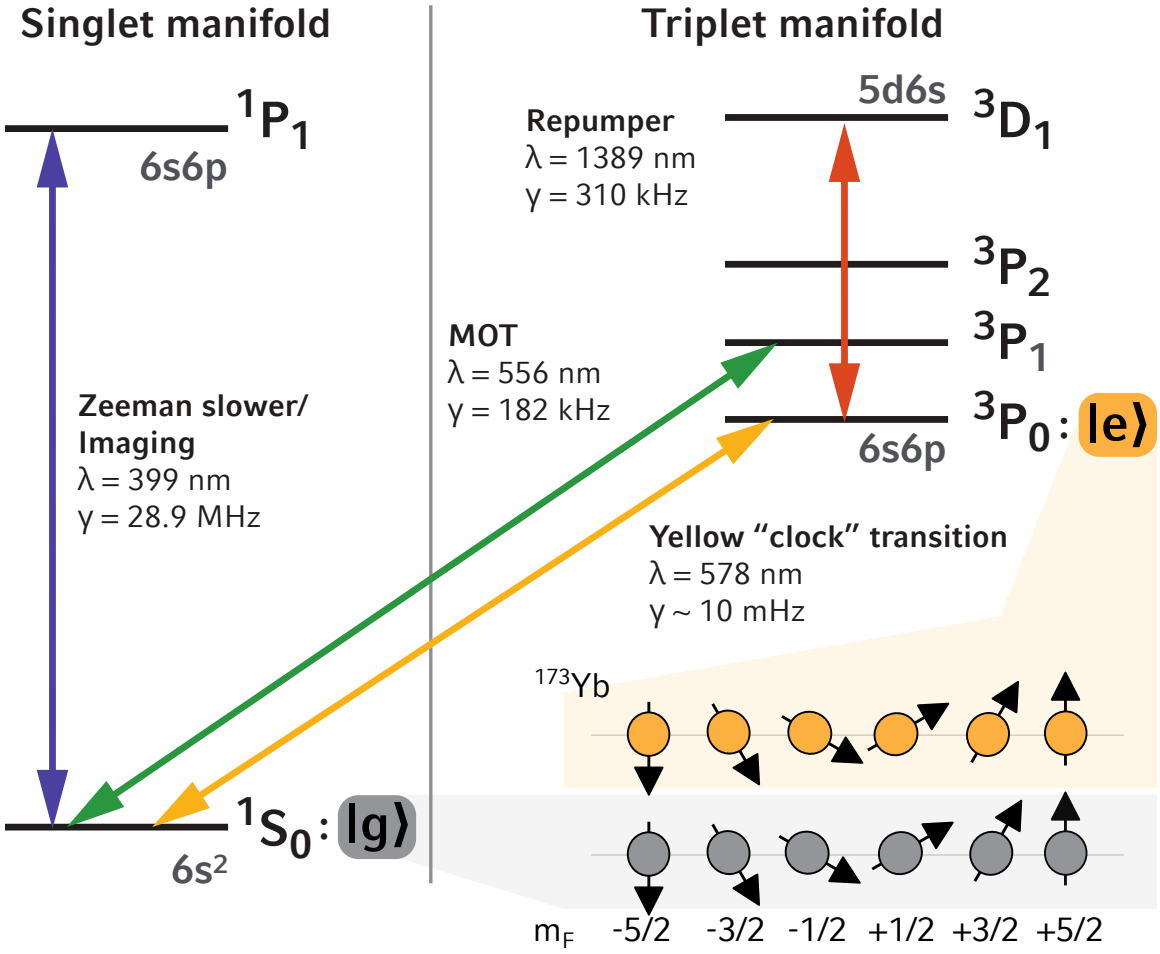

Figure 4.1 : **Electronic structure of Yb**. Most relevant optical transitions to excited states are indicated by solid arrows. Figure kindly shared by the Fölling Group at Ludwig-Maximilians-Universität München.

The ground state of Yb is a spin singlet $^1S_0$ with $J = 0$, i.e. no total electronic angular momentum. This has profound implications on the properties of the ground state, since in this case the total angular momentum of the atom F is given only by the nuclear spin I ($F = I$). As we will see in the next section this decoupling of the nuclear spin degree of freedom from the electronic structures is what gives rise to the SU(N) symmetric nature of interactions for the fermionic isotopes ^{171}Yb and ^{173}Yb, which possess a nuclear spin $I = 1/2$ and $I = 5/2$, respectively. In contrast, their bosonic counterparts ^{168}Yb, ^{170}Yb, ^{172}Yb, ^{174}Yb, and ^{176}Yb have $I = 0$. On the other hand, one immediate consequence appertaining to the electronic structure is that the ground state does not exhibit a hyperfine structure, since $\mathbf{I} \cdot \mathbf{J} = 0$. In addition, given that the only magnetic moment of the ground state steams from the nuclear spin, the Yb atom in the ground state is almost completely insensitive to magnetic fields because fermionic and bosonic isotopes have a weak or zero nuclear magnetic moment, respectively. In the case of fermions, the magnetic moment arising from the nuclear spin is virtually irrelevant since the nuclear magneton μ_N is approximately 2000 times smaller than the Bohr magneton μ_B of the electron, due to the large proton-to-electron ratio. This has relevant consequences in how interactions can be tuned for ^{173}Yb atoms since magnetic Feshbach resonances (which are generally used for tuning the s-wave scattering length between two hyperfine states in alkali-atoms [11]) are experimentally unavailable as they would require extremely high magnetic fields that are not attainable in the laboratories.

One final remark about AEAs is that there are two metastable states, the $^3P_0$ state and the $^3P_2$ state. For Yb, the $^3P_0$ state has a lifetime $\tau \approx 20$ seconds, and also has no total angular momentum ($J = 0$) like the ground state $^1S_0$, which also leads to SU(N) symmetric interactions due to the decoupling of the nuclear spin from the electronic structure. This metastable state can be useful to realize the Kondo lattice model, and, as we will discuss in further chapters, to probe the SU(N) FHM.

4.1.2 SU(N) symmetric interactions

As discussed in the previous section, the ground state $^1S_0$ and the metastable state $^3P_0$ exhibit perfect decoupling of the nuclear spin from the electronic structure because there is no hyperfine structure ($\mathbf{I} \cdot \mathbf{J} = 0$) since $J = 0$. In these states, the spin is protected inside the nucleus and it is not affected by the physics occurring at the electronic cloud distance scales. This has a startling effect on the characteristics of atomic collisions because, aside from Pauli exclusion, nuclei can only influence collisions through hyperfine coupling to the electron angular momentum [*].

In dilute atomic gases at low-temperatures (therefore low-energy collisions), scattering properties are predominantly elastic binary collisions, and are well characterized by the s-wave scattering length. In this case, and for single component bosons or spin-1/2 fermions, is possible to model the collisions with the following pseudo-potential,

$$V(\mathbf{r}) = \frac{4\pi\hbar^2}{m} a\delta(\mathbf{r}) \tag{4.1}$$

named the Fermi contact potential, where $\hbar$ is the reduced Planck's constant, m is the mass of the colliding atoms, and a is the scattering length. For fermionic gases with $N = 2I + 1$ spin components, this expression in generalized to [147],

$$V(\mathbf{r}) = \frac{4\pi\hbar^2}{m} \sum_{F_t=0,2,\ldots}^{N-2} a_{F_t} \delta(\mathbf{r}) \mathcal{P}_{F_t}, \tag{4.2}$$

where $\mathcal{P}_{F_t}$ is the projector on states with even total spin $F_t = 0, 2, 4, \ldots, N-2$ of the atom pair. In s-wave scattering collisions the spatial wave function is symmetric, and because the total wavefunction has to be antisymmetric, the spin wave function has to

[*] One could in principle argue that magnetic dipole-dipole interactions between the nuclear spin of the two atoms should affect collisions. However this coupling is negligible. For example, in Ref. [97] the interaction energy between two magnetic dipole moments as a large as $10\mu_N$ at a distance of 10 nm (substantially smaller that the confinement obtained in an optical lattice site) corresponds to a frequency smaller that one Hertz. In contrast, the on-site interaction energy is of the order of kHz, from the induced dipole-dipole interactions of the electronic clouds.

be antisymmetric only states with even total spin F_t can contribute to the scattering. Because of this, a total of $N/2$ scattering lengths a_{F_t} are needed to characterize all the available s-wave collision channels.

Due to the rotational invariance of the inter-atomic potential, there is an underlying SU(2) symmetry associated with the scattering processes. As we will see, AEAs possess an SU(N) symmetry, which corresponds to a higher symmetry group than the one just arising from rotational invariance.

Let us take a look at the situation when two atoms in states $|F, m_1\rangle$, $|F, m_2\rangle$ and total spin $|F_t, m_t = m_1 + m_2\rangle$ collide. The initial state $|F, m_1\rangle|F, m_2\rangle$ will couple to a different spin combination $|F, m_3\rangle|F, m_4\rangle$ via the pseudopotential

$$\begin{aligned}
&\langle F, m_4; F, m_3|V(\mathbf{r})|F, m_1; F, m_2\rangle = \qquad (4.3)\\
&= \sum_{F_t, F_{t'}=0}^{2F} \sum_{m_{t'}=-F_{t'}}^{F_{t'}} \sum_{m_t=-F_t}^{F_t} C^{F_t m_t}_{F m_1 F m_2} C^{F_{t'} m_{t'}}_{F m_3 F m_4} \langle F_{t'}, m_{t'}|V(\mathbf{r})|F_t, m_t\rangle\\
&= \frac{4\pi\hbar^2}{m}\delta(\mathbf{r}) \sum_{F_{t''}=0,2,\ldots}^{N-2} a_{F_{t''}} \sum_{F_t, F_{t'}=0}^{2F} \sum_{m_{t'}=-F_{t'}}^{F_{t'}} \sum_{m_t=-F_t}^{F_t} C^{F_t m_t}_{F m_1 F m_2} C^{F_{t'} m_{t'}}_{F m_3 F m_4} \langle F_{t'}, m_{t'}|\mathcal{P}_{F_{t''}}|F_t, m_t\rangle,
\end{aligned}$$

where $C^{JM}_{j_1 m_1 j_2 m_2}$ are the clebsh-Gordan coefficients. Since $\mathcal{P}_{F_t} = \sum_{m_t=-F_t}^{F_t} |F_t, m_t\rangle\langle F_t, m_t|$,

$$\langle F_{t'}, m_{t'}|\mathcal{P}_{F_t}|F_t, m_t\rangle = \sum_{m_{t''}=-F_{t''}}^{F_{t''}} \delta_{F_{t'}, F_{t''}} \delta_{F_{t''}, F_t} \delta_{m_{t'}, m_{t''}} \delta_{m_{t''}, m_t} \qquad (4.4)$$

Incorporating this result in eq. (4.3) and simplifying one obtains,

$$\langle F, m_4; F, m_3|V(\mathbf{r})|F, m_1; F, m_2\rangle = \frac{4\pi\hbar^2}{m}\delta(\mathbf{r}) \sum_{F_t=0,2,\ldots}^{N-2} \sum_{m_t=-F_t}^{F_t} a_{F_t} C^{F_t m_t}_{F m_1 F m_2} C^{F_t m_t}_{F m_3 F m_4}. \qquad (4.5)$$

From this expression we notice that momentum conservation ensures that the total spin F_t and its projection m_t are conserved during the collision [†], but the spin

[†]Since $m_t = m_1 + m_2 = m_3 + m_4$.

projection of the individual atoms is not. In other words, in general, when atoms with definite spin projections collide, these couple to all scattering channels with non-vanishing clebsh-Gordan coefficients and other spin states become populated [‡].

For AEAs, since the nuclear spin is decoupled from the electronic structure its influence in the scattering process is simply reduced to Pauli exclusion principle, and in this case $a_{F_t} = a \, \forall F_t$, i.e. the scattering lengths are equal for all possible F_t pairs [97]. Using the orthogonality relationships of the Clebsch-Gordan coefficients $\sum_J \sum_M C^{JM}_{j_1 m_2 j_2 m_2} C^{JM}_{j_1 m_{1'} j_2 m_{2'}} = \delta_{m_1,m_{1'}} \delta_{m_2,m_{2'}}$ one obtains that in contrast to the general case of collisions, for AEAs the spin projection m_F of each colliding atom is preserved and thus spin relaxation to other m_F states is forbidden. Mathematically, this means that the interaction will be SU(N) symmetric, i.e. it will be invariant under SU($N = 2I+1 = 2F+1$) transformations and the interaction pseudopotential will be given by eq. (4.1) for all possible pairs of spin projections.

Theoretical estimates for the SU(N) symmetry breaking of AEAs have been given in Ref [97]. For the ground state $^1S_0$ the variation in the scattering length for different nuclear spins is of the order $\delta a_{gg}/a_{gg} \sim 10^{-9}$, while for the excited metastable state $^3P_0$ these are of order $\delta a_{ee}/a_{ee} \sim \delta a^{\pm}_{eg}/a^{\pm}_{eg} \sim 10^{-3}$ [§], since the perfect decoupling is slightly broken by the admixture with higher-lying P states with $J \neq 0$.

4.2 Ultracold atoms in optical lattices

Most of the results presented in this thesis appertain to the study for fermions in optical lattices. Optical lattices are produced by the interference of off-resonant counter-propagating laser beams, creating a standing wave where atoms are trapped in the resulting periodic potential via the AC Stark shift [148]. Atoms are trapped

[‡]For example, for $F = 3/2$, the collision of two atoms in the state $|m_1, m_2\rangle = |3/2, -3/2\rangle$ couples to both $|3/2, -3/2\rangle$ and $|1/2, -1/2\rangle$. The only exception of spin combinations that are stable during collisions are the states $|m_1, m_2\rangle = |\pm F, \pm F \mp 1\rangle$.

[§]a_{gg} refers to scattering processes between two atoms in the ground state, a_{ee} for atoms in the excited state, and $a^{\pm}_{eg}$ refer to one atom in the excited state and the other one in the ground state in their triplet (+) or singlet (-) configuration. In the gg and ee they must be in the singlet state.

in the maxima of intensity for blue detuned traps and at the minima for red detuned traps. These lattices provide a periodic potential, for which standard procedures discussed in several textbooks [149, 150] are available to treat the non-interacting limit. On the other hand, results for optical tweezers require other tools, since the lack of periodicity hinders the benefits of using Bloch states. We start by considering the one-dimensional case, followed by a discussion of maximally localized Wannier states. Then we proceed to construct the Fermi-Hubbard Hamiltonian in second quantization. We defer the discussion of ultracold atoms in optical tweezers for Chapter 10.

4.2.1 One-dimensional periodic potential

The Hamiltonian that describes a single particle of mass m in a periodic one-dimensional optical lattice is [¶],

$$H_0 = -\frac{\hbar^2}{2m}\frac{\partial^2}{\partial x^2} + V_0 \sin^2(kx), \tag{4.6}$$

where $k = 2\pi/\lambda = \pi/a$, λ is the wavelength of the laser used to generate the optical lattice, and $a = \lambda/2$ is the lattice spacing. It is convenient to introduce the recoil energy $E_R = \hbar^2 k^2/2m$ (which is the natural energy scale for ultracold atom experiments). Defining $v_0 = V_0/E_R$, the Hamiltonian is now rewritten as,

$$H_0 = -\frac{1}{k^2}\frac{\partial^2}{\partial x^2} + v_0 \sin^2(kx). \tag{4.7}$$

Furthermore is useful to express $\sin^2(kx)$ in terms of its Fourier components,

$$H_0 = -\frac{1}{k^2}\frac{\partial^2}{\partial x^2} + \frac{v_0}{4}\left(2 - e^{-2ikx} - e^{2ikx}\right). \tag{4.8}$$

Because of the translational symmetry of the Hamiltonian, the solutions to the Schrödinger equation are the Bloch states, which are written as a product of a plane

[¶] We restrict ourselves to the one-dimensional case, since in higher dimensions the problem for simple cubic lattices can be separated along each axis.

wave and a function that preserves the periodicity of the potential,

$$\phi_{\alpha,q}(x) = e^{iqx} u_{\alpha,q}(x) = e^{iqx} \sum_{\ell \in \mathcal{Z}} c_{\alpha,q,\ell} e^{i2\ell kx} \tag{4.9}$$

where α is called the band index and q is the quasimomentum. The kinetic energy term of the single-particle Hamiltonian is

$$-\frac{1}{k^2}\frac{\partial^2}{\partial x^2}\phi_{\alpha,q}(x) = e^{iqx} \sum_{\ell} \left(2\ell + \frac{q}{k}\right)^2 c_{\alpha,q,\ell} e^{i2\ell kx}, \tag{4.10}$$

and so acting the Hamiltonian on the Bloch states to solve for the stationary states one obtains,

$$\begin{aligned} H_0\phi_{\alpha,q}(x) &= \sum_{\ell} \left[\left(2\ell + \frac{q}{k}\right)^2 + \frac{v_0}{4}\left(2 - e^{-2ikx} - e^{2ikx}\right)\right] c_{\alpha,q,\ell} e^{i2\ell kx} e^{iqx} \\ &= \sum_{\ell} \left(\left[\left(2\ell + \frac{q}{k}\right)^2 + \frac{v_0}{2}\right] c_{\alpha,q,\ell} - \frac{v_0}{4} c_{\alpha,q,\ell-1} - \frac{v_0}{4} c_{\alpha,q,\ell+1}\right) e^{i2\ell kx} e^{iqx} \\ &= \epsilon_{\alpha,q}\phi_{\alpha,q}(x) \\ &= \epsilon_{\alpha,q} \sum_{\ell} c_{\alpha,q,\ell} e^{i2\ell kx} e^{iqx}, \end{aligned} \tag{4.11}$$

which translates into the following set of equations,

$$\left[\left(2\ell + \frac{q}{k}\right)^2 + \frac{v_0}{2}\right] c_{\alpha,q,\ell} - \frac{v_0}{4} c_{\alpha,q,\ell-1} - \frac{v_0}{4} c_{\alpha,q,\ell+1} = \epsilon_{\alpha,q} c_{\alpha,q,\ell}, \tag{4.12}$$

that can be expressed in matrix form as,

$$\sum_{\ell} h_{\ell,\ell'} c_{\alpha,q,\ell} = \epsilon_{\alpha,q} c_{\alpha,q,\ell'}, \tag{4.13}$$

with

$$h_{\ell,\ell'} = \begin{cases} \left(2\ell + \frac{q}{k}\right)^2 + \frac{v_0}{2} & \text{if } \ell = \ell' \\ -\frac{v_0}{4} & \text{if } \ell = \ell' \pm 1 \\ 0 & \text{otherwise} \end{cases} \tag{4.14}$$

This is an infinite linear system of equations which determines the coefficients $c_{\alpha,q,\ell}$. One then truncates the number of equations and numerically calculates the eigenvalues and eigenvectors to obtain the dispersion relationship of the bands. Due to the periodicity of the potential, one only needs to consider the quasimomenta in the first Brillouin zone, i.e. $q \in [-\pi/a, \pi/a]$ for the description of the band structure.

In Fig. 4.2 we present the result of the band structure calculation for the lowest three bands for different lattice depths. In the absence of the lattice potential the dispersion relation corresponds to the free particle one. As one increases the lattice depth, energy gaps open and the band structure emerges.

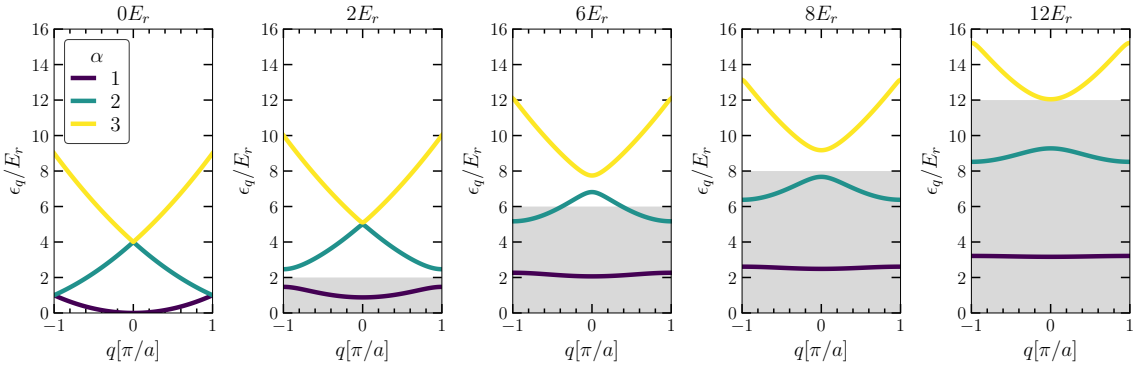

Figure 4.2 : **Band structure in a 1D optical lattice I**. Results for the lowest three energy bands are presented here for different lattice depths, which is indicated by the shaded area. An energy gap opens and increases with lattice depth. Figure obtained adapting the software in Ref. [146].

Fig. 4.3 illustrates that as the lattice depth in increased, the bands become narrower and the energy gaps between the bands increase.

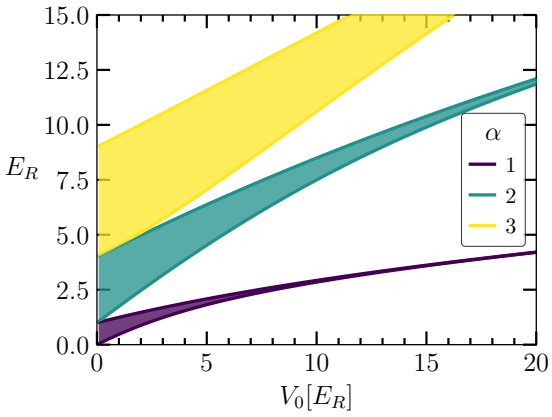

Figure 4.3 : **Band structure in a 1D optical lattice II**. Results for the lowest three energy bands are presented as a function of the strength of optical lattice in units of the recoil energy. Figure obtained adapting the software in Ref. [146].

4.2.2 Wannier states

Although the delocalized Bloch states are solutions to the problem of a particle on a periodic potential, it will be more convenient to describe the physics of the system in a localized basis. Such a basis is formed by the Wannier states. In a lattice with N_s sites, for the α-th band, a localized state centered around the x_j site is given by the Fourier transform of the Bloch states,

$$w^{\alpha}(x - x_j) = w_j^{\alpha}(x) = \frac{1}{\sqrt{N_s}} \sum_q e^{-iqx_j} \phi_{\alpha,q}(x), \tag{4.15}$$

where the sum is over all allowed quasimomenta. Now, since $[H_0, \widehat{\pi}] = 0$, where $\widehat{\pi}$ is the parity operator, the Bloch states have definite parity. In other words, the Bloch states $\phi_{\alpha,q}(x)$ and $\phi_{\alpha,q}(-x)$ have the same eigenenergies, and therefore one can construct symmetric and antisymmetric eigenstates $\phi^{\pm}_{\alpha,q}(x) = \frac{1}{\sqrt{2}} [\phi_{\alpha,q}(x) \pm \phi_{\alpha,q}(-x)]$ and the proper way to construct the maximally localized Wannier functions is to consider the the symmetrized and antisymmetrized Bloch states instead, i.e.

$$w_j^{\alpha}(x) = \frac{1}{\sqrt{2N_s}} \sum_q e^{-iqx_j} \phi^{\pm}_{\alpha,q}(x), \tag{4.16}$$

where in Ref. [151] it is shown that the maximally localized Wannier states are obtained with the antisymmetric term for the odd bands and with the symmetric term for the even bands.

In Fig. 4.4 we present the Wannier states for different lattice depths. We can see that the Wannier states become more localized as the lattice depth increases, resulting in states with smaller common domains between adjacent sites and thus a decrease in the probability amplitude for a particle to tunnel between them. As the Wannier states become more localized, this also implies that the on-site interaction will be larger, since, on average, two particles in the same site will be closer to one another.

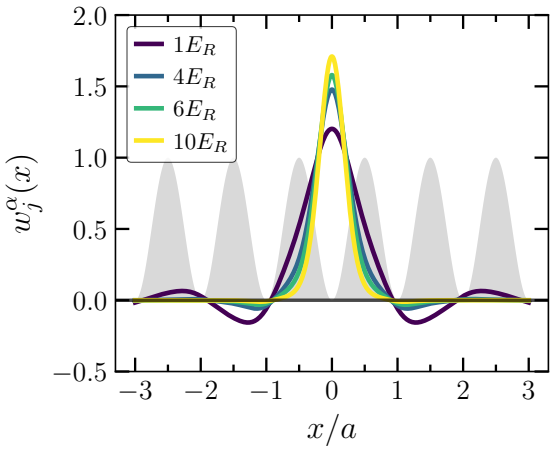

Figure 4.4 : **Wannier states in a 1D optical lattice**. Wannier states for the lowest energy band $\alpha = 1$ of the sinusoidal lattice potential (shaded gray) localized at the origin ($x_j = 0$) are presented for different lattice depths. Figure obtained adapting the software in Ref. [146].

4.2.3 The nearest-neighbor tight-binding model

One can rewrite the Hamiltonian H_0 in second quantization using the Wannier states in the following form,

$$H_0 = -\sum_{i,j} t_{ij} \left(c_i^\dagger c_j + c_j^\dagger c_i \right), \tag{4.17}$$

where the tunneling amplitude t_{ij} between sites i and j is,

$$t_{ij} = -\int dx w_i^*(x) H_0 w_j(x), \tag{4.18}$$

and we only considered the lowest energy band (and therefore dropped the band index). Since the Wannier functions become more and more localized as the lattice depth increases, only the tunneling matrix element between neighboring sites $\langle i, j\rangle$ has a significant contribution [‖]. This can be seen in Fig. 4.5 where we present different tunneling matrix elements as a function of the lattice depth. Beyond nearest-neighbor tunneling amplitudes can be safely ignored for lattice depths $V_0 \gtrsim 5E_R$ [51].

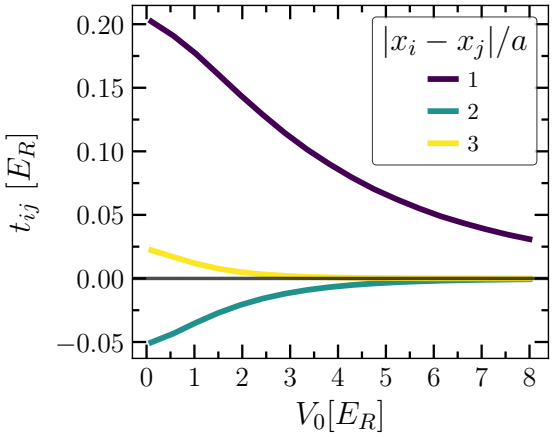

Figure 4.5 : **Tunneling matrix elements in a 1D optical lattice**. Results for nearest-neighbors and beyond nearest-neighbors are presented as a function of lattice depth. Figure obtained adapting the software in Ref. [146].

In this limit, the Hamiltonian simplifies to,

$$H_0 = -t \sum_{\langle i,j\rangle} \left(c_i^\dagger c_j + c_j^\dagger c_i \right). \tag{4.19}$$

Since all spin flavors σ see the same lattice, this last expression is valid for all σ, which can take the values of the different nuclear spin projections m_I. Then the

[‖] The on-site potential $V_i = t_{ii}$ is also relevant, but can be dropped since it corresponds to an overall shift in the chemical potential μ, and therefore can be absorbed in that term.

kinetic energy term of the N flavors can be given as,

$$H_0 = -t \sum_{\langle i,j\rangle,\sigma} \left(c_{i\sigma}^\dagger c_{j\sigma} + c_{j\sigma}^\dagger c_{i\sigma} \right), \tag{4.20}$$

with $\sigma = 1, \ldots, N$.

4.2.4 The interaction term

The interaction between atoms is determined by the 2-body interaction previously described in this chapter. Restricting ourselves to a single band (working under the assumption that the energy gap between the lowest two bands is large compared to the interaction energies) the interaction term in second quantization is,

$$H_{\text{int}} = \sum_{(\sigma,\tau)\neq(\gamma,\beta)} \sum_{i,j,k,m} U_{ijkm} c_{i\sigma}^\dagger c_{j\tau}^\dagger c_{k\gamma} c_{m\beta}, \tag{4.21}$$

where

$$U_{ijkm}^{\sigma,\tau;\gamma,\beta} = \frac{1}{2} \int dx \int dx' w_{i\sigma}^*(x) w_{j\tau}^*(x) V_{\sigma,\tau;\gamma,\beta}(x-x') w_{k\gamma}(x) w_{m\beta}(x'). \tag{4.22}$$

Since $V_{\sigma,\tau;\gamma,\beta}(x-x') = (4\pi\hbar^2 a/m)\delta(x-x')\delta_{\sigma\beta}\delta_{\tau\gamma}$ for AEAs in their ground state, this expression simplifies to

$$U_{ijkm} = \frac{1}{2} \frac{4\pi\hbar^2}{m} a \int dx w_{i\sigma}^*(x) w_{j\tau}^*(x) w_{k\tau}(x) w_{m\sigma}(x), \tag{4.23}$$

which is independent of the (σ, τ) pair. Furthermore, we restrict ourselves to a single site, i.e. $i = j = k = m$ because of the exponentially small overlap of the Wannier functions which are centered on different sites. In this case we only need to consider

the on-site interaction term $U = 2U_{iiii}$,

$$U = \frac{4\pi\hbar^2}{m} a \int dx |w_i(x)|^4, \tag{4.24}$$

where we have dropped the spin label since Wannier functions are independent of σ. Therefore, the interaction Hamiltonian now reads as,

$$H_{\text{int}} = \frac{U}{2} \sum_{\sigma \neq \tau} \sum_{i} c_{i\sigma}^{\dagger} c_{i\tau}^{\dagger} c_{i\tau} c_{i\sigma}, \tag{4.25}$$

or in terms of the number operators $n_{i\sigma} = c_{i\sigma}^{\dagger} c_{i\sigma}$,

$$H_{\text{int}} = \frac{U}{2} \sum_{i, \sigma \neq \tau} n_{i\sigma} n_{i\tau}. \tag{4.26}$$

4.2.5 Hamiltonian describing AEAs in optical lattices

Putting together the results from the last two sections, the Hamiltonian in the grand-canonical ensemble that describes AEAs in their ground state that interact via s-wave scattering in an optical lattice is given by,

$$\begin{aligned} H &= H_0 + H_{\text{int}} - \sum_{\sigma} \mu_\sigma N_\sigma \\ H &= -t \sum_{\langle i,j \rangle, \sigma} \left(c_{i\sigma}^{\dagger} c_{j\sigma} + c_{j\sigma}^{\dagger} c_{i\sigma} \right) + \frac{U}{2} \sum_{i, \sigma \neq \tau} n_{i\sigma} n_{i\tau} - \sum_{i,\sigma} \mu_\sigma n_{i,\sigma}. \end{aligned} \tag{4.27}$$

In the case of spin-balanced mixtures, i.e. $\langle N_\sigma \rangle = N_{\text{ptcl}}/N$, the chemical potentials $\mu_\sigma = \mu \; \forall \sigma$ and the Hamiltonian corresponds to the SU(N) Fermi Hubbard Model,

$$H = -t \sum_{\langle i,j \rangle, \sigma} \left(c_{i\sigma}^{\dagger} c_{j\sigma} + c_{j\sigma}^{\dagger} c_{i\sigma} \right) + \frac{U}{2} \sum_{i, \sigma \neq \tau} n_{i\sigma} n_{i\tau} - \mu \sum_{i,\sigma} n_{i,\sigma}. \tag{4.28}$$

Therefore, when AEAs are loaded into an optical lattice these are well described by the SU(N) FHM.

4.3 Summary

In this chapter we discussed the electronic and scattering properties of alkaline-earth-like atoms (AEAs). We discussed how SU(N) symmetric interactions are a consequence of a shielding of the nuclear spin from the electronic cloud in states with total vanishing electronic angular momentum. Finally, we presented how AEAs in optical lattices are well described by the SU(N) Fermi-Hubbard model.

Chapter 5

Numerical techniques

> No conocían el mar y se les antojó más triste que en la tele, pájaros de Portugal sin dirección ni alpiste ni papeles.
>
> *Pájaros de Portugal.* Joaquín Sabina

Although there are a series of useful techniques in one dimension ($d = 1$) that can be used to gain insight into the SU(N) FHM (such as the Bethe Ansatz [126, 152]), in higher dimensions and in particular for larger N, one has to resort to perturbation theory, mean-field approaches or numerical techniques to gain information about phases and phase transitions in this model. Numerical techniques such as Quantum Monte Carlo (QMC) methods have proven to be crucial in extracting information about strongly correlated fermions. In this section we discuss perturbative approches such as high-temperature series expansions, and numerical methods like Exact Diagonalization, Numerical Linked Cluster Expansion, and Determinant Quantum Monte Carlo, with an emphasis on the last one.

5.1 High-Temperature Series Expansion

Controlled perturbative approaches are a useful tool in understanding the physics of models. For example, the Heisenberg model can be obtained from the Fermi-Hubbard model in the $t/U \ll 1$ limit in a second order expansion in the tunneling, where one realizes that the relevant energy scale that controls the spin interactions is the super-exchange energy $J = 4t^2/U$ [82]. On the other hand, high-temperature series expansions (HTSE) start from the atomic-limit or single site solution, where analytic solutions are available and perturbatively introduce the tunneling in a t/T

expansion [153–155]. The zeroth-order HTSE corresponds to $t = 0$ and the next non-vanishing order is of 2nd order, i.e. $\mathcal{O}(t/T)^2$.

In the HTSE, the unperturbed Hamiltonian is

$$H_0 = \frac{U}{2} n(n-1) - \mu n \tag{5.1}$$

and we treat the kinetic energy term as the perturbation,

$$K = -t \sum_{\langle ij \rangle, \sigma} \left(c^\dagger_{i,\sigma} c_{j,\sigma} + c^\dagger_{j,\sigma} c_{i,\sigma} \right). \tag{5.2}$$

To second order (the first order term vanishes), the partition function is [156]:

$$Z = Z_0 \left[1 + \int_0^\beta d\tau_1 \int_0^{\tau_1} d\tau_2 \langle \tilde{K}(\tau_1) \tilde{K}(\tau_2) \rangle_0 \right] = Z_0 (1 + \chi), \tag{5.3}$$

where $\tilde{K}(\tau) = e^{\tau H_0} K e^{-\tau H_0}$ (i.e. written in the interaction picture). The free energy is,

$$\Omega = -\frac{1}{\beta} \ln Z = -\frac{1}{\beta} \ln \left[Z_0 (1 + \chi) \right] = -\frac{1}{\beta} \ln Z_0 - \frac{1}{\beta} \ln(1 + \chi) \approx \Omega_0 + \Delta\Omega, \tag{5.4}$$

where we used $\ln(1 + \chi) \approx \chi$ if $\chi \ll 1$,

$$\Delta\Omega = -\frac{1}{\beta} \int_0^\beta d\tau_1 \int_0^{\tau_1} d\tau_2 \langle \tilde{K}(\tau_1) \tilde{K}(\tau_2) \rangle_0. \tag{5.5}$$

Now, following Ref. [156] the correction to the free energy is therefore given by,

$$-\beta \Delta\Omega = \sum_{\mathbf{q},\mathbf{p}} e^{-\beta E_\mathbf{q}} \langle \mathbf{q}|K|\mathbf{p}\rangle \langle \mathbf{p}|K|\mathbf{q}\rangle I(\Delta) = \sum_{\mathbf{q},\mathbf{p}} e^{-\beta E_\mathbf{q}} K_{\mathbf{qp}} K_{\mathbf{pq}} I(\Delta), \tag{5.6}$$

where $\Delta = E_{\mathbf{q}} - E_{\mathbf{p}}$,

$$I(\Delta) = \int_0^\beta d\tau_1 e^{\Delta\tau_1} \int_0^{\tau_1} d\tau_2 e^{-\Delta\tau_2} = \begin{cases} \frac{1}{2}\beta^2, & \Delta = 0 \\ \frac{1}{\Delta^2}\left(e^{\beta\Delta} - 1 - \beta\Delta\right), & \Delta \neq 0. \end{cases}, \tag{5.7}$$

and $\mathbf{q}$ corresponds to the basis of the unperturbed Hamiltonian, in this case, the product of single-site terms.

Working out all the terms in eq. (5.6) (which are not many since the perturbation only couples nearest-neighboring sites and the matrix elements are of the form $K_{qp}K_{pq}$ imposing constraints on the sums over nearest-neighbor sites), one arrives to the following expression [71, 141]:

$$-\beta\Delta\Omega = zN\left(\frac{\beta t}{z_0}\right)^2 \left[\frac{1}{2}\sum_{n=1}^{N}\binom{N-1}{n-1}^2 x^{2n-1}y^{(n-1)^2} - \frac{1}{\beta U}\sum_{n\neq m}\binom{N-1}{n-1}\binom{N-1}{m-1}\frac{x^{n+m-1}y^{\frac{1}{2}[n(n-1)+(m-1)(m-2)]}}{n-m}\right]. \tag{5.8}$$

For simplicity and in order to keep the following calculations tidy, we define $F[f(n,m)]$, and $G[f(n,m)]$ as,

$$F[f(n,m)] = \frac{1}{2}\sum_{n=1}^{N}\binom{N-1}{n-1}^2 x^{2n-1}y^{(n-1)^2} f(n,m) \tag{5.9}$$

$$G[f(n,m)] = -\frac{1}{\beta U}\sum_{n\neq m}\binom{N-1}{n-1}\binom{N-1}{m-1}\frac{x^{n+m-1}y^{\frac{1}{2}[n(n-1)+(m-1)(m-2)]}}{n-m} f(n,m) \tag{5.10}$$

Using this notation we get can rewrite the correction to the free energy as,

$$-\beta\Delta\Omega = zN\left(\frac{\beta t}{z_0}\right)^2 \Big(F[1] + G[1]\Big). \tag{5.11}$$

And the corrections to the density $\langle \Delta n \rangle$ and the number of on-site pairs $\langle \Delta \mathcal{D} \rangle$ are given by,

$$\langle \Delta n \rangle = zN \left(\frac{\beta t}{z_0} \right)^2 \left(-2\langle n \rangle_0 \Big(F[1] + G[1] \Big) + F[2n-1] + G[n+m-1] \right), \quad (5.12)$$

$$\langle \Delta \mathcal{D} \rangle = zN \left(\frac{\beta t}{z_0} \right)^2 \left(-2\langle \mathcal{D} \rangle_0 \Big(F[1] + G[1] \Big) + F[(n-1)^2] + G\left[\frac{n(n-1) + (m-1)(m-2)}{2} \right] \right). \quad (5.13)$$

where $\langle n \rangle_0$, and $\langle \mathcal{D} \rangle_0$ correspond to the atomic limit solution ($t = 0$).

HTSE have been used to study the SU(N) FHM in the square lattice [157], the honyecomb lattice [158], and the infinite-U limit to explore the SU(N) Nagaoka-Thouless ferromagnet [159]*. In this work, we compute thermodynamic observables with zeroth- and second-order HTSE to understand their behavior in the $T \gtrsim t$ regime and test the convergence of other numerical techniques. Results of HTSE are presented in Chapters 7 and 10 where we derive and plot expressions for different thermodynamic observables of interest.

5.2 Exact Diagonalization

Ideally, in the absence of analytic solutions to the FHM, one would like to be able to construct the Hamiltonian matrix and then diagonalize it. However exact diagonalization (ED) of the SU(2) FHM is not easy due to the Hilbert space explosion: it grows as 4^{N_s}, where N_s is the number of lattice sites. This problem aggravates for the SU(N) FHM, since the Hilbert space grows as 2^{NN_s} (see Table 5.1).

State of the art calculations with Exact Diagonalization can solve the SU(2) FHM in a lattice with 12-14 sites. For 10 sites, the $N = 2$ Hilbert space contains 10^6 states, in contrast for $N = 6$ the Hilbert space contains 10^{12} more states, rendering

*Other studies that rely on perturbative approaches to study itinerant ferromagnetism in dilute SU(N) Fermi gases are presented in Refs. [160, 161].

N	N_s	Hilbert space
2	10	10^6
3	10	10^9
4	10	10^{12}
6	10	10^{18}

Table 5.1 : Hilbert space explosion

it almost impossible to perform those calculations. However, we have implemented and performed ED calculations in small lattices over a reduced Hilbert space and perform finite-size scaling to gain information the physics of the SU(N) FHM. For computational efficiency, we exploit two aspects of the SU(N) symmetry. Particle number conservation for each spin flavor

$$[N_\sigma, H] = 0, \tag{5.14}$$

with $N_\sigma = \sum_j n_{j\sigma}(j)$ where $n_{j\sigma} = c^\dagger_{j\sigma} c_{j\sigma}$ and the translation symmetry (in the case of periodic boundary conditions) allow us to block-diagonalize the Hamiltonian. Furthermore, the method exploits the spin permutation symmetries,

$$[S^\sigma_\tau, H] = 0 \qquad \forall \sigma, \tau = 1, \ldots, N. \tag{5.15a}$$

with

$$S^\sigma_\tau = \sum_i S^\sigma_\tau(i) = \sum_i c^\dagger_{i\sigma} c_{i\tau}. \tag{5.15b}$$

which relate many of the sectors of the Hamiltonian, and therefore one needs to diagonalize each sector only once (see Fig. 5.1).

In addition to the exact symmetries, we employ a physically motivated basis state truncation, which we systematically converge and works best for large U/t. First, the Hilbert space only includes states with total particle number lesser or equal to a fixed

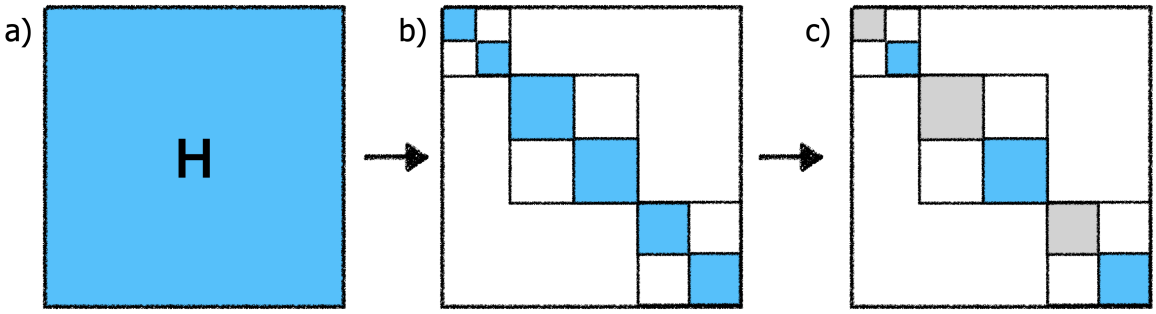

Figure 5.1 : **Exact Diagonalization**. a) The SU(N) FHM corresponds to a matrix (blue colors correspond to non-vanishing matrix elements). b) Applying the spin particle conservation and translation invariance the matrix is now block diagonal. c) Exploiting the spin permutation symmetry, different sectors of the Hamiltonian are identical, so one only needs to diagonalize each sector once (the gray block is related to the blue one by spin permutation). By employing these symmetries, larger system sizes can be considered. For example, in the case of SU(6), the largest system size we can solve considering the full Hilbert space is 4 sites. In contrast, using the symmetries we can solve for 6 sites.

particle number $N_{\max}$. Second, it omits states where the on-site energy of the cluster is larger than E_{cut}. Results at large U/t for densities $\langle n \rangle \lesssim 1$ are well converged since the number of doublons and higher occupancies are very small in such regime. This for example, allows us to solve the SU(6) FHM for 8 sites. We will present ED results in Chapters 7 and 8.

It is worth mentioning that if one is only interested in the ground state and low energy states of the model (or only a particular subset of the eigenstates), one can use the Lanczos method rather than diagonalizing all sectors of the Hamiltonian [162,163].

5.3 Numerical Linked Cluster Expansion

Thermodynamic properties of the SU(N) FHM can be evaluated with Numerical Linked Cluster Expansions (NLCE) [164]. In the NLCE extensive properties in a lattice are evaluated by performing a weighted sum of their value in all possible

clusters c embeddable in the lattice; specifically,

$$P(\mathcal{L})/N_s = \sum_{c\in\mathcal{L}} L(c)W_P(c) \tag{5.16}$$

where $P(\mathcal{L})$ is the property evaluated on the entire lattice $\mathcal{L}$, N_s is the number of lattice sites, $L(c)$ is the number of ways that the cluster c can be embedded in the lattice (up to translation invariance), and $W_P(c)$ is defined as

$$W_P(c) = P(c) - \sum_{s\subset c} W_P(s). \tag{5.17}$$

Because eq. (5.16) is an infinite sum over all clusters, the key idea of the NLCE is to truncate this sum to clusters of small size and evaluate properties on each cluster using ED (see Fig.5.2). We then truncate the sum over clusters based on the number of sites, performing calculations up to n-site clusters (n-th order NLCE).

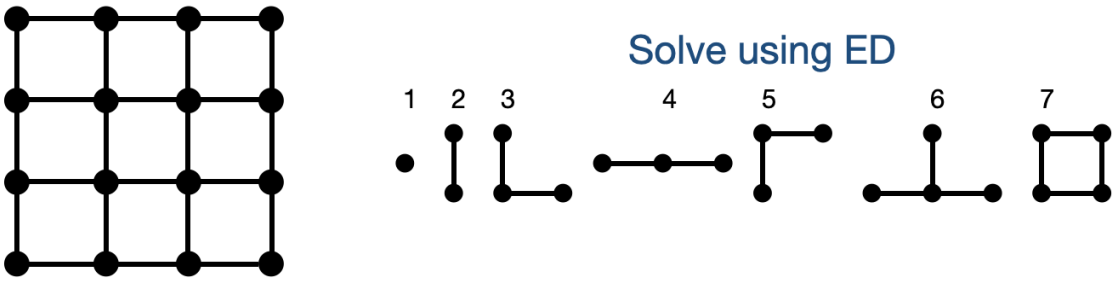

Figure 5.2 : **Numerical Linked Cluster Expansion**. In NLCE one solves the SU(N) FHM in clusters of different sizes that are embeddable in the lattice of interest. Results of thermodynamic observables are then obtained as a weighted sum of the observables measured in each cluster. Figures reprinted with copyright permission of Ref. [164].

The convergence of the ED/NLCE with system size/order of the calculation can be understood by thinking of the procedure as a perturbation series in the correlation length ζ/L: If the correlation length is smaller than the length of the system with N_s sites ($\zeta < L$) an L-order ED/NLCE calculation will be able to capture the ther-

modynamic properties of the system. In contrast, when long-range order develops in the system and $\zeta \gtrsim L$, results from the ED/NLCE are not reliable. It has been demonstrated that NLCE is much more accurate than an exact diagonalization (ED) that uses the same number of (or even more) sites [164] [†]. In addition, the NLCE self-diagnoses its accuracy, with converged results expected when adjacent orders give nearly the same answer.

Using NLCE with the ED procedure described in Sec. 5.2 allows for the exploration of thermodynamic quantities in larger system sizes and works best in the large U/t limit, where the Hilbert space truncation can be applied in the ED method. We will present NLCE results in Chapters 7 and 10.

5.4 Determinant Quantum Monte Carlo

One of the most useful numerical techniques to study strongly correlated matter has been Determinant Quantum Monte Carlo (DQMC) [54, 165–170]. In particular, for $d > 1$ in SU(2) FHM, where it is not exactly solvable, DQMC has provided useful information about the different phases this model exhibits [171,172]. Moreover, DQMC also allows for the exploration of relatively large systems, in comparison with ED and NLCE. To demonstrate its importance, DQMC has provided key input in the interpretation of experiments and is extensively used for precise thermometry of the SU(2) FHM using ultracold atoms in OLs [20], compare spin correlations [68], and calculate transport properties [22], amongst other examples.

Monte Carlo methods rely on performing importance sampling of configurations weighted by a given probability distribution [173]. This importance sampling can be implemented with algorithms such as Metropolis-Hastings [174]. For a given system or Hamiltonian $\mathcal{H}$, the main task is to importance sample $\exp(-\beta\mathcal{H})$, where

[†]The faster rate of convergence of the NLCE can be understood in the sense that by performing a weighted average, one can mitigate finite-size effects more efficiently. However, it is worth mentioning that even though ED is less accurate than NLCE in the temperature regime in which it converges, below this temperature the ED can reproduce the correct qualitative trends while the NLCE diverges.

$\beta = 1/k_B T$, k_B is the Boltzmann constant and T is the temperature. In this section we first describe the basics of DQMC for the SU(2) FHM and then discuss how we generalized it for $N > 2$. For more in-depth details on Monte Carlo methods such as the Metropolis-Hastings algorithm, properties and Markov chain and detailed balance, we refer the reader to Refs. [173–176]. For further details on Quantum Monte Carlo methods we refer the reader to [167]. It is important to mention that most of my knowledge of DQMC I learned it from Richard Scalettar and the following section describing DQMC for the SU(2) FHM is inspired from some of his notes on the subject [168–170].

5.4.1 DQMC for $N = 2$

For the SU(2) FHM given in eq. (2.1), the kinetic and chemical potential terms are bilinear in fermion operators and can be easily diagonalized; however the interaction term, quartic in fermion operators, cannot be diagonalized in the single particle basis. The standard way of computing the partition function is to discretize β in L imaginary time slices $\beta = L\Delta\tau$ via the Trotter-Suzuki decomposition [54],

$$Z = \mathrm{Tr}\left[e^{-\beta\mathcal{H}}\right] \approx \mathrm{Tr}\left[\prod_{\ell=1}^{L} e^{-\Delta\tau K} e^{-\Delta\tau V}\right], \tag{5.18}$$

where K contains the kinetic and chemical potential terms, while V is the interaction term; and introduce, for each imaginary time slice ℓ and each lattice site i, a discrete Hubbard Stratonovich (HS) transformation that replaces the on-site interaction by a fluctuating Ising field $s_i(\ell)$ coupled to the magnetization [54],

$$e^{-U\Delta\tau\left(n_{i\uparrow}-\frac{1}{2}\right)\left(n_{i\downarrow}-\frac{1}{2}\right)} = \frac{1}{2} e^{-U\Delta\tau/4} \sum_{s_i(\ell)=\pm 1} e^{\lambda s_i(\ell)\left(n_{i\uparrow}-n_{i\downarrow}\right)}, \tag{5.19}$$

where $\cosh\lambda = \exp(U\Delta\tau/2)$. By doing so, now Z is a product of exponentials of bilinear terms in the fermion operators and can be traced out, leaving us with

a partition function expressed as the product of two determinants where the trace needs to be taken over the auxiliary Ising fields $\{s\}$:

$$Z = \mathrm{Tr}_{\{s\}} C_1 \det\left[M_\uparrow(\{s\})\right] \det\left[M_\downarrow(\{s\})\right], \tag{5.20}$$

where C_1 is a constant and will be irrelevant for the Monte Carlo method and

$$\begin{aligned} M_\sigma(\{s\}) &= 1 + B_1^\sigma B_2^\sigma \ldots B_{L-1}^\sigma B_L^\sigma, & (5.21)\\ B_\ell^\sigma &= e^{-\Delta\tau K_\sigma} e^{-V_\sigma(\ell)}, & (5.22)\\ G_{ij}^\sigma(\ell = L) &= \langle c_{i\sigma} c_{j\sigma}^\dagger \rangle = \left[M_\sigma(\{s\})\right]_{ij}^{-1}. & (5.23) \end{aligned}$$

Here G^σ is the single particle Green's function for fermion with spin σ, and K_σ and $V_\sigma(\ell)$ are the kinetic and potential energy terms given by,

$$\begin{aligned} K_\sigma &= \sum_{i,j} c_{i\sigma}^\dagger k_{ij} c_{j\sigma}, & (5.24)\\ V_\sigma(\ell) &= \sigma \sum_i \lambda n_{i\sigma} s_i(\ell), & (5.25) \end{aligned}$$

where k_{ij} has the shape,

$$k_{ij} = \begin{pmatrix} -\mu & -t & 0 & \ldots \\ -t & -\mu & -t & \ldots \\ 0 & -t & -\mu & \ldots \\ \vdots & \vdots & \vdots & \ddots \end{pmatrix}. \tag{5.26}$$

We have then expressed the grand partition function as a sum over Ising spins of a product of determinants. If the quantity under the trace were positive definite, it could be used as a Boltzmann weight to perform importance sampling over the Ising

configurations:

$$\rho(\{s\}) = \frac{1}{Z} C_1 \det\left[M_\uparrow(\{s\})\right] \det\left[M_\downarrow(\{s\})\right]. \tag{5.27}$$

In other words, if $\prod \det > 0$, it is a probability distribution that we can sample from. This is the underlying principle of DQMC. There are, however, cases where $\prod \det < 0$. In these cases, DQMC faces a significant challenge known as the *fermion sign problem* [55]: Let's define $c = \{s\}$ and $p(c) = \det\left[M_\uparrow(\{s\})\right] \det\left[M_\downarrow(\{s\})\right]$. If we write $p(c) = \text{sign}(c)|p(c)|$, where $\text{sign}(c) = \pm 1$ to keep track of the sign of $p(c)$, the expectation value of an observable A is replaced by an average weighted by $|p(c)|$ [54],

$$\langle A \rangle_p = \frac{\sum_c p(c) A(c)}{\sum_c p(c)} = \frac{\sum_c \text{sign}(c)|p(c)|A(c)}{\sum_c \text{sign}(c)|p(c)|} = \frac{\langle \text{sign} A \rangle}{\langle \text{sign} \rangle}_{|p|}. \tag{5.28}$$

If the average sign is small, longer runs are necessary in order to compensate for the strong fluctations in $\langle A \rangle_p$. We need at least $\langle \text{sign} \rangle^{-2}$ more runs in order to obtain similar statistical accuracy as for $\langle \text{sign} \rangle \approx 1$ [54]. It is important to mention that most of the great successes of DQMC have been in special cases where the algorithm is *sign problem* free. One of this cases is at half-filling ($\langle n \rangle = 1$), where one can prove using the particle-hole transformation that $\det[M_\uparrow(\{s\})] = \exp[-\lambda \sum_{i,\ell} s_i(\ell)] \det[M_\downarrow(\{s\})]$, and therefore $\rho(\{s\}) \geq 0$ for $U \geq 0$, rendering the calculation free of the *sign problem* and thus allowing to perform calculations down to very low temperatures [54].

5.4.1.1 The algorithm

In the previous section we discussed how in DQMC one can construct a *probability distribution* one can importance sample and mentioned how the *sign problem* arises. Here we briefly describe how the algorithm is used to generate Hubbard-Stratonovich configurations and how are observables computed in the method.

Steps of the algorithm

- Initialize the Hubbard-Stratonovich field $\{s\}$, that is a $N_s \times L$ matrix, with entries ± 1 set to randomly (recall N_s is the number of lattice sites and L is the number of imaginary time slices).

- Monte Carlo Loop

  (a) Set $(\ell, i) = (L, 1)$

  (b) Perform the (ℓ, i) loop

  1. Propose a new configuration $\{s'\}$ by flipping the Ising spin at site i.
  2. Compute the Metropolis-ratio

$$r_{\ell,i} = \frac{\rho(\{s'\})}{\rho(\{s\})} = \frac{\det\left[M_\uparrow(\{s'\})\right] \det\left[M_\downarrow(\{s'\})\right]}{\det\left[M_\uparrow(\{s\})\right] \det\left[M_\downarrow(\{s\})\right]} \tag{5.29}$$

  3. Define the Metropolis acceptance-ratio $\alpha(\{s\} \to \{s'\}) = \min(1, r_{\ell,i})$.
  4. Accept or reject the configuration with probability α.

  If the new configuration is accepted the Green's function for the time slice needs to be updated, not just the ii element. One can

  – Iterate the "old" Green's function via the formula,

$$G^\sigma_{jk} \to G^\sigma_{jk} - b^\sigma_j c^\sigma_k, \tag{5.30}$$

  where

$$b^\sigma_j = \frac{G^\sigma_{ji}}{1 + c^\sigma_i} \tag{5.31}$$

$$c^\sigma_k = -\left(e^{-2\sigma\lambda s_i(\ell)} - 1\right) G^\sigma_{ik} + \delta_{ik}\left(e^{-2\sigma\lambda s_i(\ell)} - 1\right) \tag{5.32}$$

– Or compute it from scratch (generally this has to be done after several iterations, to reduce systematic errors).

5. Update the interaction energy matrix $V_\sigma(\ell)$
6. Go the next site in the same imaginary-time slice, until all sites have been visited $(\ell, i) = (L, i+1)$. After all spatial sites i of the imaginary time slice $\ell = L$ have been updated, change the Green's functions via:

$$G^\sigma(L-1) = B_{\sigma,L} G^\sigma(L) [B_{\sigma,L}]^{-1} \tag{5.33}$$

(c) Go to the next imaginary time slice $(\ell, i) = (L-1, 1)$.

- Repeat steps (a)-(c) for the desired number of warm-up steps (i.e. number of sweeps needed to equilibrate to the probability distribution).
- After warm up steps, repeat (a)-(c) for the desired number of measurement steps. During these sweeps, perform physical measurements.

The algorithm as previously stated scales in CPU time as $N_s^4 L$. This is due to reevaluating $\det[M(\{s\})]$ that takes N_s^3 operations, and we have to do it $N_s L$ times. However we can reduce the scaling to $N_s^3 L$, since we are only flipping one Ising spin at a time, and therefore we can calculate a simpler expression that relates to the Green's functions [‡]:

$$r_{\ell,i} = \frac{\det[M_\uparrow(\{s'\})] \det[M_\downarrow(\{s'\})]}{\det[M_\uparrow(\{s\})] \det[M_\downarrow(\{s\})]} = R^\uparrow_{\ell,i} R^\downarrow_{\ell,i}, \tag{5.34}$$

$$R^\sigma_{\ell,i} = 1 + (1 - G^\sigma_{ii}(\ell)) \left(e^{-2\sigma\lambda s_i(\ell)} - 1\right) \tag{5.35}$$

Computing observables

The expectation value of operators is obtained by sampling the corresponding Green's function over the Hubbard-Stratonovich configurations. Here is important to

[‡]This simplification is an application of the "Sherman–Morrison" formula.

highlight that in the present approach the fermionic particles only interact with the auxiliary fields, so that Wick's theorem holds for a fixed configuration of the Ising fields. This means that, all expectation values of interest can be calculated in terms of the single-particle Green's functions. Some observables of interest are

- The occupation number $\langle n_{i\sigma} \rangle = 1 - G^{\sigma}_{ii}$
- The double occupancy $\langle n_{i\uparrow} n_{i\downarrow} \rangle = \left(1 - G^{\uparrow}_{ii}\right)\left(1 - G^{\downarrow}_{ii}\right)$
- The spin-spin correlation function $\langle S^{+}_{i} S^{-}_{j} \rangle = -G^{\uparrow}_{ji} G^{\downarrow}_{ij}$

5.4.1.2 Non-ergodicities (*sticking*) and numerical instabilities

Besides the existence of the *sign problem* as previously discussed, we need to pay attention to a series of other subtleties:

- At low temperatures the product of matrices required in constructing the Green's functions becomes numerically unstable at low temperatures (and gets worse at strong couplings). This issue arises from the fact that the product of matrices involved in computing M has a very high ratio of largest to smallest eigenvalue, so computing its inverse $G = M^{-1}$ requires numerical stabilization procedures. Such instability can be overcome by using the "Space-Time Formulation" or by performing a "Matrix-Decomposition Stabilization" [54].

  When numerical instabilities arise, the "wrapping" process to update the Green's function after all the sites in a single imaginary time slice ℓ have been updated [see eq. (5.33)] becomes less reliable and carries larger systematic errors. So in addition to having to incorporate more complex methods to numerically multiply matrices on a machine of finite precision, one has to compute from scratch the Green's function at every imaginary time slice.

- At large couplings, DQMC exhibits ergodicity problems, which generally translate into something known as *sticking*: states with fixed occupation numbers

for each spin flavor break the SU(2) symmetry, i.e. $\langle n_\uparrow \rangle \neq \langle n_\downarrow \rangle$. *Sticking* is a major issue for quantities such as the spin-spin correlation function and the structure factor. This problem is overcome for the SU(2) FHM by performing a global move that flips the Ising spin on site i for all imaginary time slices [177]. This global move effectively permits sampling the different regions of the phase space with the largest Boltzmann weights, but that are separated by regions of small weights, which makes it hard for a Monte Carlo trajectory to cross them.

5.4.2 DQMC for $N \geq 2$

Having set up the basics of the DQMC algorithm for $N = 2$ we now proceed to explain how we generalized it to $N > 2$. Our approach was to introduce $N(N-1)/2$ real auxiliary fields, one for each interaction term (see Fig. 5.3),

$$e^{-U\Delta\tau\left(n_{i\sigma}-\frac{1}{2}\right)\left(n_{i\sigma'}-\frac{1}{2}\right)} = \frac{1}{2}e^{-U\Delta\tau/4}\sum_{s_i^{\sigma\sigma'}(\ell)=\pm 1} e^{\lambda s_i^{\sigma\sigma'}(\ell)(n_{i\sigma}-n_{i\sigma'})}. \tag{5.36}$$

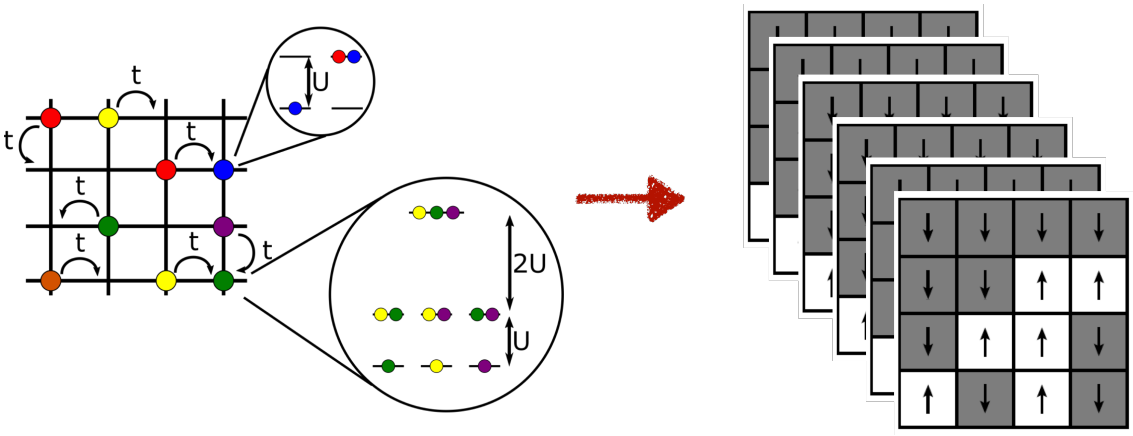

Figure 5.3 : **Determinant Quantum Monte Carlo**. In this technique one maps the Quantum Mechanical problem into a classical one via the Hubbard-Stratonovich configuration. Then one stochastically samples the Ising fields configurations and compute observables of interest. This mapping has the drawback know as the *sign problem* that arises from the fermionic nature of the original Hamiltonian. In the case of $N > 2$, in our current approach, we introduce $N(N-1)/2$ auxiliary fields, one for each interaction term.

It is important to mention that the choice of decoupling is not unique. In previous work performed by Congjun Wu and Fakher Assaad's groups [77, 78, 178, 179], they apply DQMC to the half-filled SU(4) and SU(6) FHM by using an exact discrete complex HS decomposition. Here a single complex auxiliary field is coupled to the charge channel rather than the *magnetization* channel. This complex decomposition has the benefit of being sign-problem free at half-filling, i.e. $\langle n \rangle = N/2$, but its performance for odd values of N has not yet been explored.

Our choice of decoupling has advantages and disadvantages. First of all it allows us to immediately generalize a previous SU(2) DQMC code. Second, we can study, in principle, the SU(N) FHM for any value of N. One question of importance corresponds to how the efficiency of the algorithm is affected by the choice in the decoupling, in particular at experimentally relevant densities $\langle n \rangle \lesssim 1$. For our choice of decoupling, no one has yet explored the efficiency of the algorithm around the experimentally accessible fillings, while for the complex decoupling all results are at half-filling, except Ref. [178] where authors explored the quarter-filling case for even N [§].

On the other hand, a couple of caveats are present. For our choice of decoupling the partition function is now a product of N determinants (see Appendix A for more details). Although the Metropolis-Hastings algorithm can handle this by introducing one extra loop that goes through all the HS fields $s_i^{\sigma\sigma'}(\ell)$, there are two issues to address. First, having more determinants increases the chances of having combinations that will yield a negative product, therefore aggravating the *sign problem*. Second, despite the fact our HS transformation decouples each interaction term by pairs, the $N(N-1)/2$ auxiliary Ising fields couple asymmetrically to the spin flavors. Such asymmetry can have consequences in the efficiency of the global moves and *sticking* [¶]

[§]For large N, like 6, the half-filled case is out of reach experimentally due to three-body losses. For $N = 4$ the half-filled case can be of interest experimentally, but three-body losses might start to become relevant too.

[¶]For SU(N), the global move used for $N = 2$ is not as efficient due to the asymmetry in the

(see Appendix B for more details). For details on the tests we performed to diagnose the convergence of the DQMC method, these are presented in Appendix C.

5.5 Summary

In this chapter we presented the different analytical and numerical techniques we used in the study of the SU(N) FHM. Such techniques have their own benefits and drawbacks, which also determine the regions where they all perform best (see Table 5.2) and provide a way not only to compare techniques where possible (which is a good way to test convergence and look for systematic and/or coding errors), but also provide complimentary strengths to study the model in different temperature, interaction and filling regimes.

Technique	Abbrv	Dimension	U/t
Exact Diagonalization	ED	1D	$\gtrsim 8$
Numerical Linked Cluster Expansion	NLCE	2D/3D	$\gtrsim 8$
Determinant Quantum Monte Carlo	DQMC	2D/3D	$\lesssim 8$

Table 5.2 : Parameter space where different numerical techniques perform best.

Before we summarize the numerical techniques discussed in this chapter, we mention, for completeness, that other numerical techniques exist. One of them is Diagrammatic Quantum Monte Carlo which has been previously used to explore the SU(2) FHM [180–182], but has not been applied to the SU(N)-symmetric version. For $N = 2$ although low temperatures $T/t \sim 0.025$ can be achieved with Diagrammatic QMC, only small interaction strengths can be reached $U/t \sim 4$ [181]. Another technique is Projector QMC which has been applied to one dimensional systems [127] and two dimensional square lattices at half-filling [77, 78], but only provides $T = 0$ results and is a variational approach. In addition, there is single-site Dynamical Mean

quadratic interaction decoupling, but in practice we found it works fairly well. As a future project, finding the most efficient global moves for SU(N) will improve the performance of our code and further mitigate the *sticking* problem.

Field Theory (DMFT) which can provide insight to the physics, but breaks down around $T/t \sim 1$ [183, 184].

Coming back to the methods here presented, in general, ED results perform best in small lattices, making it the ideal choice for 1D systems. In addition, the system sizes that can be computed can be increased if one works in the large U/t limit and considers $\langle n \rangle \lesssim 1$, where the Hilbert space can be truncated.

Then one can build upon the ED to perform NLCE calculations, which allows one to consider larger system sizes and with more accurate results in the regime where it is converged. NLCE will be most powerful, i.e. higher orders will be accessible, when one works in the large U/t limit.

On the other hand, HTSE allow for the analytical exploration of results in the $T \gtrsim t$ limit, where relevant physics already develops, such as the Mott-Insulator transition. These results have been used to diagnose when higher-order processes in the tunneling become relevant, and as a way to gain insight of the physics and benchmarking results.

Finally, we presented DQMC, which allows for the the exploration of relatively large systems, in comparison with ED and NLCE. This method is exact in the non-interacting limit $U = 0$ and although the *sign problem* and the *sticking* worsen as U/t is increased, a wide range of interactions strengths can still be explored $U \in [0, 12]$ to $T \sim 0.5t$ [‖] in different geometries.

[‖] Or even lower temperatures in special cases, for example some cases at half-filling where particle-hole-symmetry (PHS) is present and there is no *sign problem* [55].

Chapter 6

Thermodynamics and magnetism in the 2D-3D crossover of the Hubbard model

The truth of the story lies in the details.

The Brooklyn Follies. Paul Auster

This chapter is adapted from publication:

Thermodynamics and magnetism in the 2D-3D crossover of the Hubbard model, **Eduardo Ibarra-García-Padilla**, Rick Mukherjee, Randall G. Hulet, Kaden R. A. Hazzard, Thereza Paiva, and Richard T. Scalettar, Phys. Rev. A **102**, 033340 (2020) *.

The realization of antiferromagnetic (AFM) correlations in ultracold fermionic atoms on an optical lattice is a significant achievement. Experiments have been carried out in one, two, and three dimensions, and have also studied anisotropic configurations with stronger tunneling in some lattice directions. Such anisotropy is relevant to the physics of cuprate superconductors and other strongly correlated materials. Moreover, this anisotropy might be harnessed to enhance AFM order. In this Chapter we numerically investigate, using Determinant Quantum Monte Carlo, a simple realization of anisotropy in the 3D Hubbard model in which the tunneling between planes, $t_\perp$, is unequal to the intraplane tunneling t. This model interpolates between the three-dimensional isotropic ($t_\perp = t$) and two-dimensional ($t_\perp = 0$) systems. We show that at fixed interaction strength to tunneling ratio (U/t), anisotropy can enhance the magnetic structure factor relative to both 2D and 3D results. However, this enhancement occurs at interaction strengths below those for which the Néel

*Complete article, including text, figures, and tables reprinted with copyright permission of Ref. [43].

temperature $T_{\text{Néel}}$ is largest, in such a way that the structure factor cannot be made to exceed its value in isotropic 3D systems at the optimal U/t. We characterize the 2D-3D crossover in terms of the magnetic structure factor, real space spin correlations, number of doubly-occupied sites, and thermodynamic observables. An interesting implication of our results stems from the entropy's dependence on anisotropy. As the system evolves from 3D to 2D, the entropy at a fixed temperature increases. Correspondingly, at fixed entropy, the temperature will decrease going from 3D to 2D. This suggests a cooling protocol in which the dimensionality is adiabatically changed from 3D to 2D.

6.1 Introduction

Quantum simulation uses engineered quantum systems, such as ultracold atoms in lattices, to realize many-body models of interest in ways that offer powerful control over the system and probes of its physics [12,16,17]. A prototypical example is using fermions in an optical lattice as an optical lattice emulator (OLE) to realize the Fermi-Hubbard model [14,15,18,20,185–188]. Such simulations allow experiments to flexibly tune the kinetic and interaction energies, lattice geometry, and lattice filling, and in principle use this control to study antiferromagnetism (AFM), superconductivity, pseudogap, and strange metal behavior, for example.

AFM is intriguing in its own right and is a natural first step to more exotic phases [22, 69, 189]. AFM in cold atoms has been studied in bosonic atoms [190], spin-1/2 ions [191, 192], in highly anisotropic lattices [60, 67, 142, 193], and in other more recent theoretical work [172, 194–198]. In a fermion OLE, spin-selective Bragg scattering observed AFM correlations at temperatures down to $1.4\,T_{\text{Néel}}$ in a three-dimensional (3D) cubic lattice [20], where $T_{\text{Néel}}$ is the Néel temperature (the critical temperature for AFM ordering), with an accompanying characterization of the Mott insulator equations of state [19]. In addition, quantum gas microscopy [199–206]

has provided direct observation of correlations beyond nearest-neighbors, through real-space imaging of AFM order in one [59] and two [21, 62, 63] dimensions. As we will elaborate on later, dimensionality plays an important role in the transition temperature to the antiferromagnetic phase, being equal to zero in 2D, but finite in 3D.

Although OLEs are giving us new insights into quantum matter, there are also significant challenges. Of particular relevance here is that, although experiments have achieved spin correlations which extend across the finite 2D lattice [21], so far experiments have not reached sufficiently low temperatures or entropies to observe a long-range ordered AFM phase in a regime where $T_{\text{Néel}} > 0$, i.e. where correlations would persist to long range as the system size is increased arbitrarily. In order to achieve this goal, several cooling protocols exist. One that has received a lot of attention from both theory and experiment is to use spatial subregions as repositories for excess entropy, allowing for lower temperatures in other regions [21,37,38,67,207], but reaching the Néel temperature, and below, remains an outstanding challenge.

Anisotropic systems that have larger tunneling rates in some directions than others offer potentially richer varieties of physics than simple 1D, 2D, or 3D cubic lattices. Anisotropic systems are relevant to real materials, as discussed below, while also suggesting a route to achieving longer-range AFM order. Specifically, it is known that 2D systems offer stronger nearest neighbor correlations for a given entropy than 3D systems [67, 193], making them favorable to search for short-ranged AFM. However, true long-range order cannot develop at $T > 0$ in 2D due to the Mermin-Wagner theorem, in contrast to 3D. Thus a potential scenario for anisotropic lattices that interpolate between 2D and 3D is that they retain the strong AFM correlations associated with 2D planes, while being able to develop long-range order by virtue of the interplane tunnelings.

This Chapter explores the evolution of AFM correlations in the half-filled repulsive

Hubbard model across the 2D-3D crossover using Determinant Quantum Monte Carlo (DQMC) [165,166]. DQMC [19–22,63,68,172,208–210] and other numerical solutions of the Hubbard model [such as numerical linked-cluster expansion (NLCE) [20,63,68], dynamic mean-field theory (DMFT) [22, 211–213], density matrix renormalization group (DMRG) [126], and diagrammatic QMC [214, 215]] have provided key input in the interpretation of experiments and, in particular, in the determination of temperature. In this Chapter, the evolution of AFM correlations is characterized as a function of both temperature T and entropy S, to allow for a deeper understanding of the optimization of AFM at fixed S.

An important conclusion is that, for interaction strength U less than (roughly) the 2D bandwidth, the long-range AFM correlations at a given temperature or entropy, measured by the magnetic structure factor at the $\vec{k} = (\pi, \pi, \pi)$ wavevector, are maximized in lattices which straddle dimensionality. Although anisotropy can increase the structure factor at small U, it never exceeds the value in the isotropic 3D system evaluated at the optimal U. Similar conclusions were reached in Ref. [60] for the 1D-3D crossover using a dynamical cluster approximation (DCA).

In addition to the possibility of achieving AFM in OLE, an understanding of dimensional crossover is relevant to strongly correlated materials [216]. Perhaps the most important example is the cuprate superconductors, layered materials for which the superexchange coupling $J_\perp = 4t_\perp^2/U$ between planes is several orders of magnitude lower than the in-plane superexchange $J = 4t^2/U$ [217, 218]. Despite this large anisotropy, $J_\perp$ is crucial to the physics, since in a purely 2D geometry $T_{\text{Néel}} = 0$.

The remainder of this Chapter is organized as follows: Section 6.2 presents the Hubbard Hamiltonian and defines the observables we consider. Section 6.3 presents the details of the DQMC simulation. Section 6.4 presents the main results. Section 6.5 concludes.

6.2 The anisotropic Fermi-Hubbard model

In this study we numerically investigate using DQMC a simple realization of an anisotropic SU(2) half-filled FHM, in which the tunneling between two-dimensional (2D) planes $t_\perp$ is different from the intraplane tunneling t. This model interpolates between the 2D ($t_\perp = 0$) and the three-dimensional (3D, $t_\perp/t = 1$) systems. This anisotropic Hamiltonian is depicted in Fig. 6.1 and is given by,

$$H = -t \sum_{\langle i,j\rangle_\parallel,\sigma} \left(c^\dagger_{i\sigma} c_{j\sigma} + c^\dagger_{j\sigma} c_{i\sigma} \right) - t_\perp \sum_{\langle i,j\rangle_\perp,\sigma} \left(c^\dagger_{i\sigma} c_{j\sigma} c^\dagger_{j\sigma} c_{i\sigma} \right) + U \sum_i \left(n_{i\uparrow} - \frac{1}{2} \right) \left(n_{i\downarrow} - \frac{1}{2} \right), \tag{6.1}$$

where $t_\perp/t \in [0, 1]$, and $\langle i, j\rangle_\parallel$ ($\langle i, j\rangle_\perp$) denote in-plane (out-of-plane) nearest-neighbors. We have set $\mu = 0$ which ensures half-filling, i.e. $\langle n_i\rangle = \langle n_{i\uparrow}\rangle + \langle n_{i\downarrow}\rangle = 1$ occurs for all values of U/t, T/t, $t_\perp/t$. We set Boltzmann's constant $k_B = 1$ throughout.

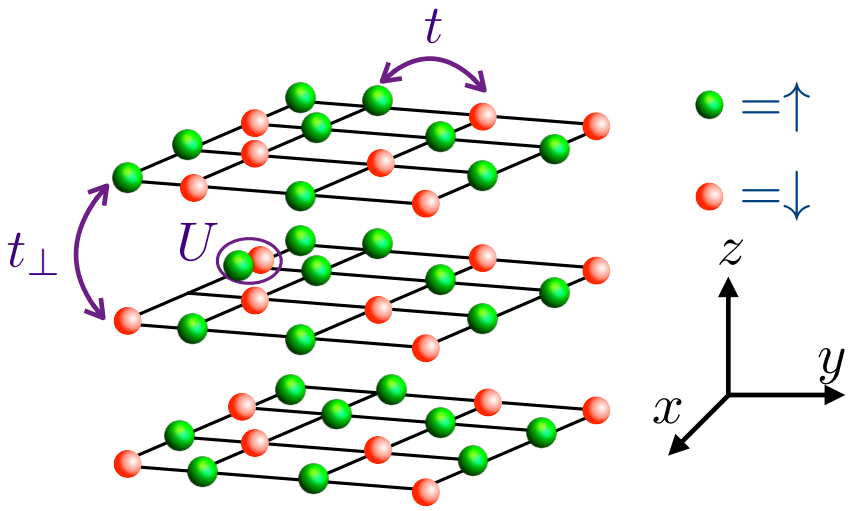

Figure 6.1 : **Anisotropic Fermi-Hubbard Model setup**. Red and green spheres denote fermionic atoms in different spin-1/2 projections in a 3D anistropic lattice. Atoms can be in either $|\uparrow\rangle, |\downarrow\rangle$ states using two different hyperfine states of ultracold atoms. The intraplane nearest-neighbor tunneling is t, the interplane hopping amplitude is $t_\perp$, and the on-site interaction is U. By controlling $t_\perp/t$ the 2D-3D crossover is achieved.

We are interested both in the thermodynamics, e.g. energy and entropy, how the temperature T changes with $t_\perp$ at fixed entropy S, and also with the behavior of the real space spin-spin correlation function $c(\vec{r}) = c(\rho, z)$ (where ρ is the magnitude of the in-plane components of $\vec{r}$), in particular the in-plane $c_{||}(\rho)$ and out-of-plane $c_\perp(z)$ correlation functions, as well as the magnetic structure factor $S(\vec{q})$:

$$\begin{aligned} c(\vec{r}) &= \left\langle \left(n_{\vec{r}_0+\vec{r},\uparrow} - n_{\vec{r}_0+\vec{r},\downarrow}\right)\left(n_{\vec{r}_0,\uparrow} - n_{\vec{r}_0,\downarrow}\right)\right\rangle, \\ c_{||}(\rho) &= c(\rho, z=0), \\ c_\perp(z) &= c(\rho=0, z), \\ S(\vec{q}) &= \sum_{\vec{r}} e^{i\vec{q}\cdot\vec{r}}\, c(\vec{r}), \end{aligned} \tag{6.2}$$

where these averages are taken in thermal equilibrium at fixed temperature T and chemical potential $\mu = 0$. The structure factors can diagnose long range order. At half-filling, the Fermi surface is nested for any $t_\perp$, so that the ordering wavevector is always (π, π, π) regardless of the degree of anisotropy. For that reason we focus on the AF structure factor $S\big(\vec{q} = (\pi, \pi, \pi)\big)$, which we denote S_π. In addition, Ref. [219] contains a mean field theory study of the crossover from 3D to 2D considered here, including careful treatment of finite-size and shell effects to ensure the correct ordering wavevector is captured at all densities.

6.3 Details of the DQMC

The averages of thermal equilibrium observables of Eq. (6.1) are evaluated with DQMC [171] in 10×10 (for $t_\perp = 0$) and $6 \times 6 \times 6$ (for $t_\perp > 0$) lattices. In addition we also computed results in $4 \times 4 \times 4$ and $8 \times 8 \times 8$ lattices to analyze finite-size effects in the structure factor. In this method, the introduction of a space- and imaginary time-dependent auxiliary field allows tracing over the fermion degrees of freedom analytically. The auxiliary field is then sampled stochastically. To achieve accurate

results, we obtain DQMC data for 20-50 different random seeds for $T/t \leq 1$ and for 1-10 different random seeds for $T/t > 1$. In each realization, 500 sweeps updating the auxiliary field at every lattice site and imaginary time are performed for equilibration and 5000 sweeps for measurements. For each Monte Carlo trajectory measurements of the $\langle S^z S^z \rangle$ and $\langle S^x S^x \rangle$ correlation functions are made. These are equal on average by the SU(2) symmetry, and both are included in the statistics. The inverse temperature interval $(0, \beta)$ is discretized in steps of $\Delta\tau$ with a Trotter step $\Delta\tau = 0.05/t$ for $U/t = 4, 8$ and $\Delta\tau = 0.04/t$ for $U/t = 12$. The number of global moves per sweep, which update all the imaginary time slices at a given lattice site, to mitigate possible ergodicity issues [177], is set to 2 for $U/t = 4, 8$ and to 4 for $U/t = 12$.

Estimates of other systematic errors – Trotter and finite-size error – show that the predominant error is statistical, arising from the finite number of measurements. In the following section, error bars are reported as the standard error of the mean for all results. For $U/t = 12$, where the inverse temperature discretization error is expected to be worst, we can gain insight into the magnitude of this error by considering the difference of the results obtained with Trotter steps $\Delta\tau = 0.04/t$ and $\Delta\tau = 0.05/t$. This difference is below 2.5% for all observables of interest, comparable to the statistical error in many cases. This discretization error is even smaller for the other two values of U/t considered. Finite-size errors for thermodynamic quantities and nearest-neighbor correlations are estimated by taking the difference between results obtained in cubic lattices with sides of length $L = 4$ and $L = 6$ in 3D. These differences are $\lesssim 5\%$. At high temperatures and away from the optimal anisotropies, i.e. well above the Néel temperature, the error in the structure factor is similar, but for $T \lesssim T_{\text{Néel}}$, the structure factor is sensitive to longer-ranged correlations, including those between sites separated by distances comparable to L. Here, finite-size effects can be more significant, $\sim 50\%$ in our calculations. (Indeed, below $T_{\text{Néel}}$, the difference in S_π in a finite and infinite system is infinitely large, and a different extrapolation scheme

would be necessary to infer the $L = \infty$ results.). Results for the structure factor at low temperatures where it has become independent of temperature should therefore be interpreted with some care. However, we expect the conclusions of this Chaper to remain. A detailed study of finite-size effects in the structure factor can be found in Refs. [215, 220], where careful finite-size scaling techniques are used to extract the Néel temperature in 3D. For more discussion of the finite-size effects in the 2D-3D crossover, see section 6.5.2.

6.4 Results

This section shows the main results of this Chapter. We calculate several observables as functions of T/t, U/t, and $t_\perp/t$: the spatial correlation functions $c_{||}(\rho)$ and $c_\perp(z)$, the AFM structure factor S_π, the double occupancy $\mathcal{D} = \langle n_{i,\uparrow} n_{i,\downarrow} \rangle$, the contributions to the specific heat $C(T)$ from the interaction and kinetic energies, and the entropy per site S/N – where N denotes the number of sites. All of these observables contain important information about the physics and can be measured in experiments with ultracold atoms. The double occupancy is a key measure of the Mottness and insulating nature of the system, and the correlations and structure factor give information about the magnetic phase diagram. The thermodynamic observables give information about the ordering of the state – its spatial coherence (kinetic energy) and to what extent degrees of freedom are capable of fluctuating (the entropy and specific heat). The entropy is usually obtained by ramping from a weakly interacting gas near-adiabatically, and the entropy of the weakly interacting gas can be determined by thermometry. As the temperature is often not directly experimentally accessible in strongly interacting systems, understanding the dependence of observables on S is crucial.

6.4.1 Spin correlations

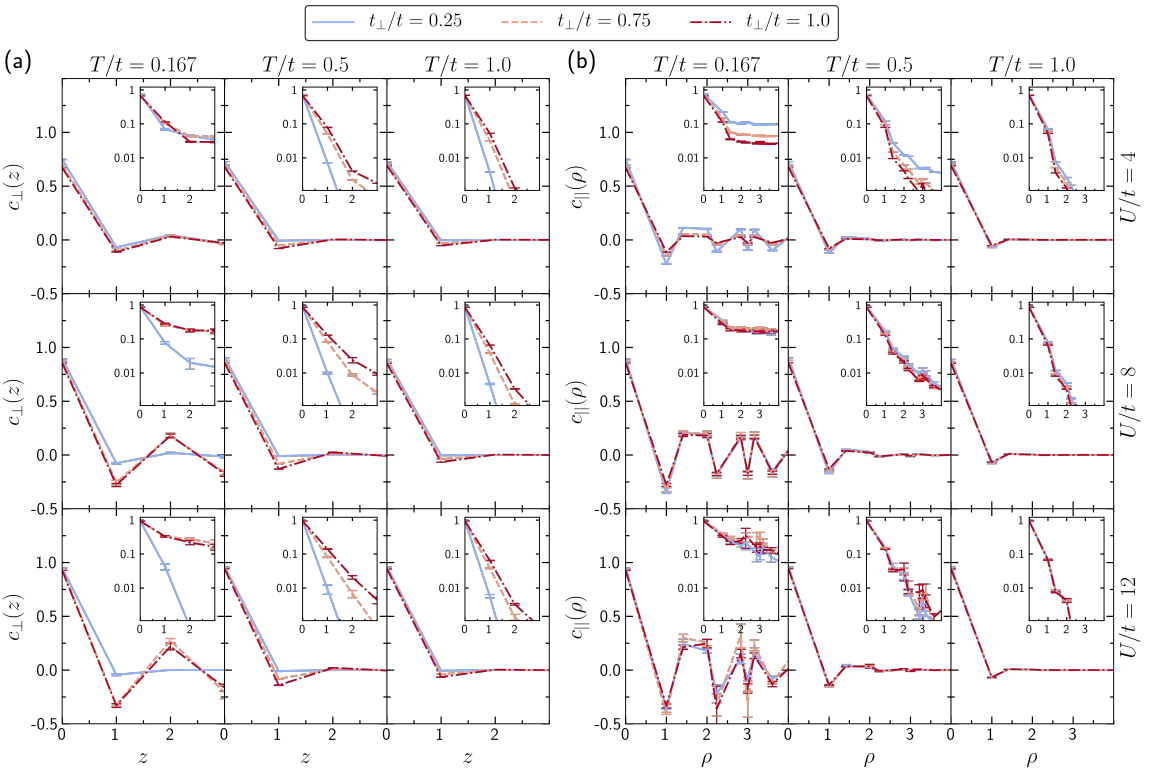

Figure 6.2 : **Spin correlations of the anisotropic FHM**. (a) Interplane $c_\perp(z)$ and intraplane $c_{||}(\rho)$ spin correlations as a function of distance for different values of the interaction strength U/t and the anisotropy $t_\perp/t$. Insets show the same plot on a log scale.

Figure 6.2 shows the out-of-plane and in-plane spatial correlations for different values of U/t, T/t and $t_\perp/t$. First, let's focus on the first row of panels (a) and (b), which corresponds to $U/t = 4$. The spatial correlations are larger at small T/t, showing clear in- and out-of-plane AF oscillations as a function of distance. At the lowest T/t considered in Fig. 6.2, $T/t = 0.167$, both $c_{||}(\rho)$ and $c_\perp(z)$ indicate a strong antiferromagnetic ordering extending to several lattice sites. The insets, which present the correlations on a log scale, demonstrate that for the two high temperature sets both $c_{||}(\rho)$ and $c_\perp(z)$ have an exponential decay associated with a correlation length ξ, while the low temperature data reaches a constant value, an indicator of larger correlation length ξ and the onset of long-range order. As one might expect, the

strength of the correlations increases as the correlation length increases. All of these trends are similar for the $U/t = 8$ and $U/t = 12$ data, but both spatial correlations exhibit stronger AF correlations than for $U/t = 4$.

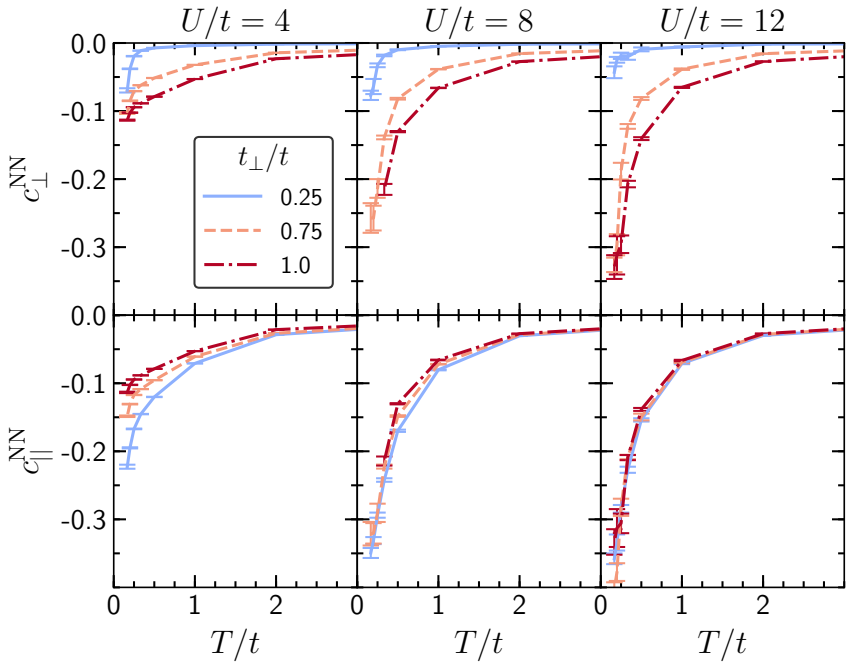

Figure 6.3 : **Nearest-neighbor spin correlations of the anisotropic FHM**. $c_{\perp}^{\mathrm{NN}} = c_{\perp}(z = 1)$ and $c_{\parallel}^{\mathrm{NN}} = c_{\parallel}(\rho = 1)$ as functions of temperature for different values of the interaction strength U/t and the anisotropy $t_{\perp}/t$.

Now let's focus on how the the low temperature data for panels (a) and (b) evolves with $t_{\perp}/t$. As $t_{\perp}/t$ increases, the between-plane correlations get stronger while the in-plane correlations get slightly weaker. The effect on in-plane correlations is strongest for $U/t = 4$ and nearly negligible for $U/t = 8, 12$.

In Fig. 6.3 we plot the in-plane and out-of-plane nearest-neighbor spatial correlations, $c_{||}^{\mathrm{NN}}$ and $c_{\perp}^{\mathrm{NN}}$, as functions of temperature T/t at various $t_{\perp}/t$. Both correlation functions get enhanced at small T/t and large U/t. Similar to the trends of longer-ranged correlations shown in Fig. 6.2, we see that at large U/t, the in-plane correlations weakly depend of $t_{\perp}$, but diminish as $t_{\perp}$ is increased at weak couplings, while the out-of-plane correlations strongly depend on the anisotropy for all interac-

tion strengths. As expected $c_{\perp}^{\mathrm{NN}} \to 0$ when $t_{\perp} \to 0$, indicating that the 2D planes are decoupled.

6.4.2 Structure factor I

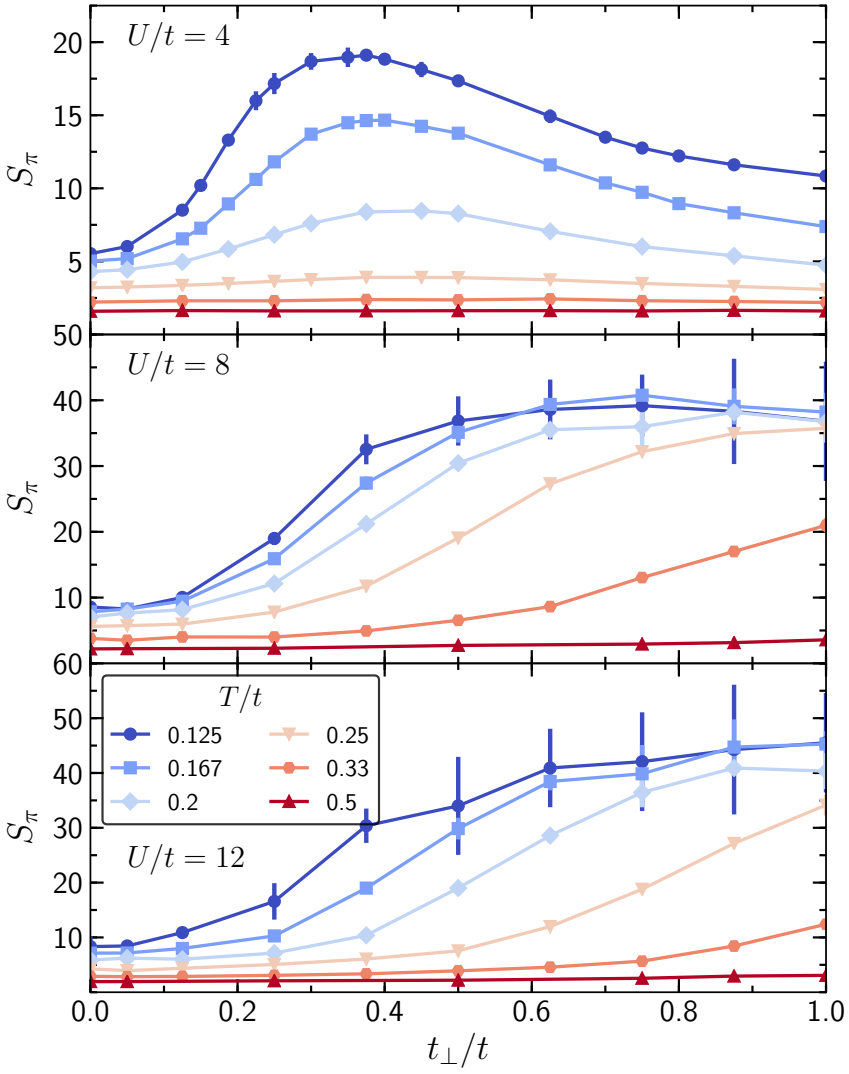

Figure 6.4 : **AFM structure factor of the anisotropic FHM**. S_π as a function of interplane hopping $t_\perp/t$ for different temperatures T/t at $U/t = 4$ (top panel), $U/t = 8$ (middle panel), and $U/t = 12$ (bottom panel). At weak coupling, the structure factor increases with anisotropy, i.e. as $t_\perp/t$ decreases from 1.

Figure 6.4 presents the structure factor S_π vs $t_\perp/t$ at various temperatures. The $U/t = 4$ data clearly show that at each temperature, S_π is largest between 2D and 3D.

In contrast, for $U/t = 8$ and 12, the largest S_π occurs at the isotropic point $t_\perp = t$. Although the $U/t = 8$ data is consistent with S_π being maximized at $t_\perp/t = 1$, it is rather independent of $t_\perp/t$ for $t_\perp/t \in (0.5, 1.0)$ at the lowest temperatures considered, $T/t \leq 0.167$. Moreover, the maximal S_π at $U/t = 4$ is smaller than the isotropic S_π for $U/t = 8$; if one's goal is simply to maximize S_π – irrespective of U/t – there is no advantage to using anisotropy.

The behavior of S_π as a function of $t_\perp/t$ at different interaction strengths, as displayed in Fig. 6.4, has a simple explanation. In a 3D cubic lattice, S_π is maximized around $U/t \sim 10$ [221]. One effect of anisotropy is to change the average tunneling to be somewhere between t and the smaller $t_\perp$, and thus one would expect anisotropy to decrease the effective tunneling, t_{eff}, and increase the effective U/t_{eff} compared to U/t. This change qualitatively explains why S_π is maximized around $t_\perp/t \sim 0.4$ for $U/t = 4$, while is maximized near the isotropic point at $U/t = 8, 12$.

Figure 6.5 shows the AF structure factor S_π versus temperature T/t at different $t_\perp/t$. Structure factors at all values of $t_\perp/t$ and U/t grow as temperature is lowered. Generally, the onset of growth of the structure factor begins at the largest temperature for $U/t = 8$, although this U/t at which growth onsets can depend on anisotropy. For example, for small $t_\perp/t$, $U/t = 4$ has a similar temperature for the onset of correlations.

6.4.3 Thermodynamics

Figure 6.6 plots the double occupancy $\mathcal{D} = \langle n_{i,\uparrow} n_{i,\downarrow} \rangle$ as a function of temperature, and displays three essential parts. Imagine starting at high temperature and cooling the system down. As the temperature is lowered, first the double occupancy $\mathcal{D}$ goes down. Then, as the temperature is lowered further, it increases (in every case except the 2D $U/t = 4$). Finally, as the temperature is lowered even further, $\mathcal{D}$ saturates, or in some cases, such as $U/t = 4$, it begins to decrease.

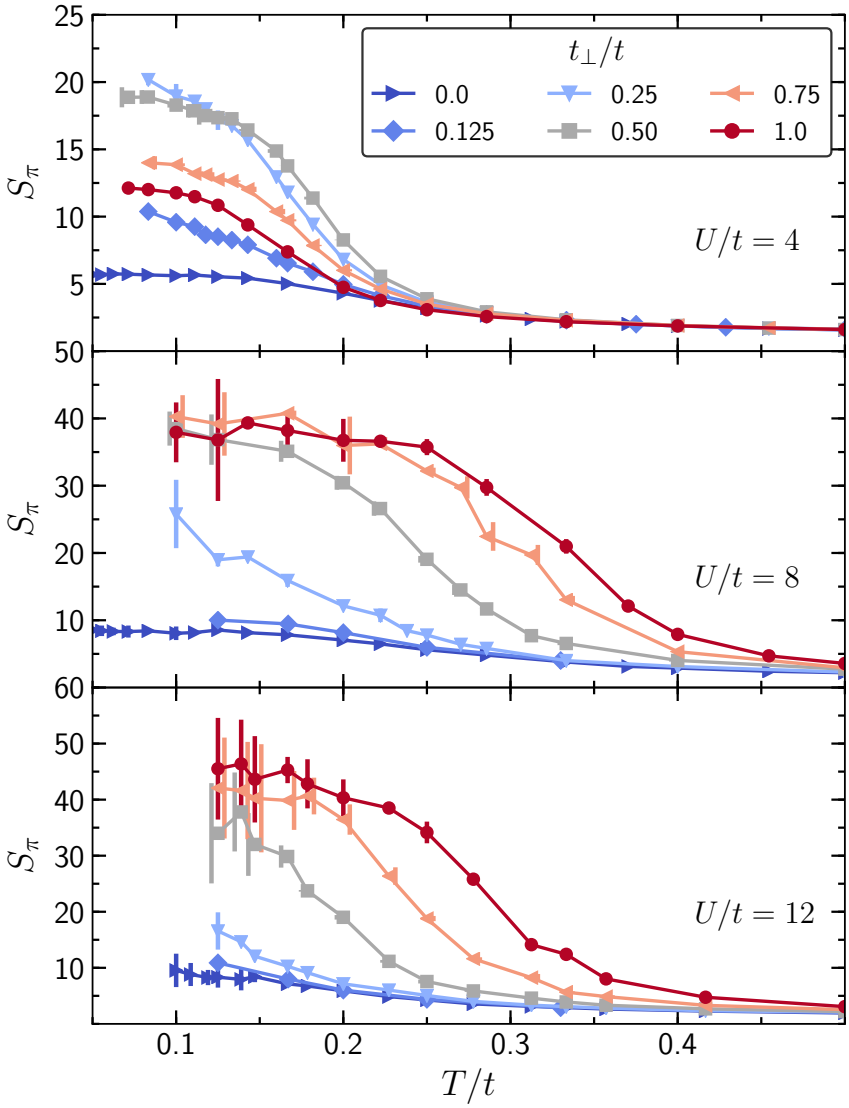

Figure 6.5 : **AFM structure factor of the anisotropic FHM**. S_π as a function of temperature T/t for different interplane hopping $t_\perp/t$. For $U/t = 4$ at low T/t, as anisotropy is introduced, S_π grows by almost a factor of two down to $t_\perp/t = 0.25$. For very strong anisotropy, $t_\perp/t = 0.125$, S_π comes down and approaches the 2D limit. For $U/t = 8, 12$, S_π decreases with anisotropy. This decrease will overwhelm the benefits of adiabatic cooling (described later; see e.g. Fig. 6.10).

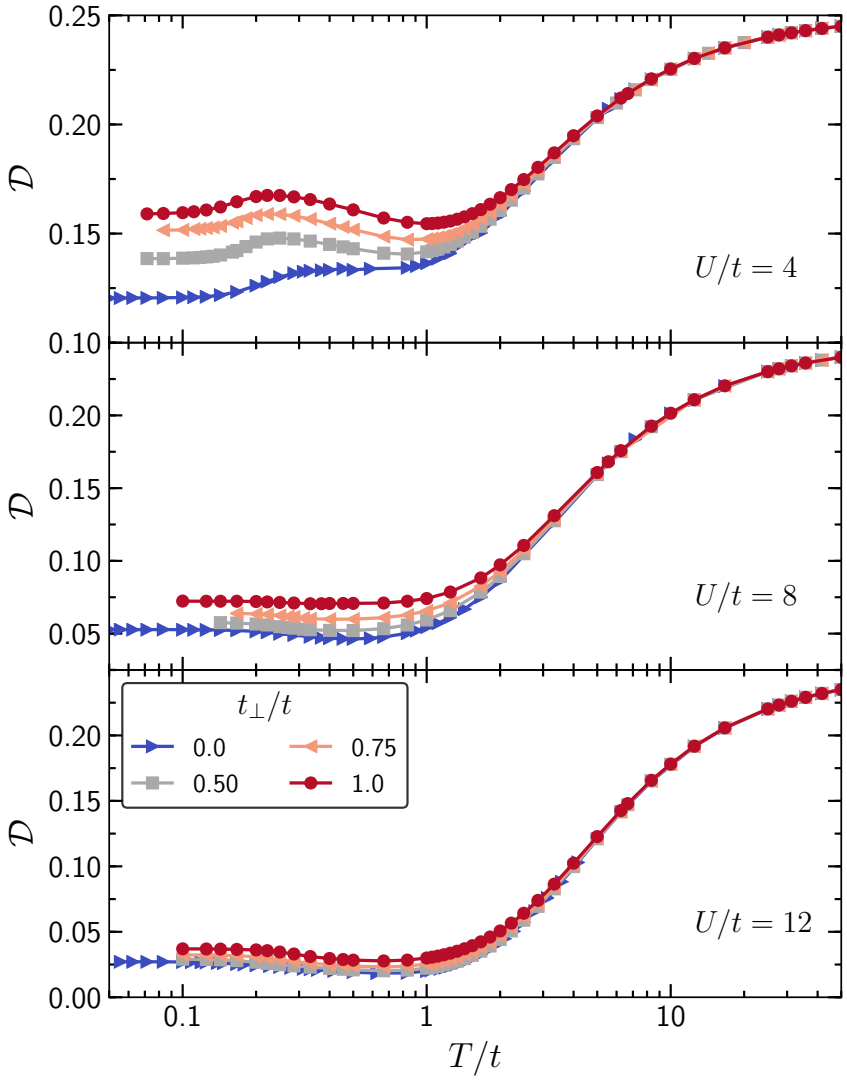

Figure 6.6 : **Double occupancy of the anisotropic FHM**. $\mathcal{D}$ as a function of temperature for $U/t = 4, 8, 12$ at different values of $t_\perp/t$.

The first feature, the high temperature decrease of $\mathcal{D}$ upon cooling, is straightforward to understand. At temperatures $T \gtrsim U$, eigenstates with significant numbers of double occupancies will be created, while at temperatures below this, the eigenstates relevant to the $\mu = 0$ state will have only a small admixture of doublons, at least for reasonably strong interactions.

The second feature is more interesting, and arises from spin-ordering. We can gain a simple understanding of this starting from the $U \gg t$ limit. For temperatures $T \ll U$, we can think of the states as essentially having a single particle per site with small admixtures of other states. The relevant states in the relevant sector are just determined by their spin configurations. AFM aligned spin configurations will have energy $\propto -t^2/U$ per site lower energy than FM aligned spins. Therefore, as the temperature is lowered below $T \lesssim -t^2/U$, the AFM aligned states become favored. Now consider the doublon content of these two classes of states. The number of doublons in the state with FM aligned spins is small (zero if all the spins are exactly aligned) since Pauli exclusion prevents tunneling. In contrast, there is an admixture $\propto (t/U)^2$ of doublons in the AFM state; it is precisely this admixture which allows some delocalization of particles that lowers the energy of the AFM states relative to the FM ones. Therefore, as the temperature is lowered, the AFM states are increasingly favored and the number of doublons increases by an amount $\propto (t/U)^2$. (This is why, in general at low temperature, the increase in $\mathcal{D}$ is accompanied by a lowering of the kinetic energy.) We note that a simple place to check this argument is in a two-site system, where the calculation can be done analytically.

These arguments provide an understanding of the decrease in $\mathcal{D}$ as T is lowered below U and its small increase (in almost all cases) when $T \lesssim t^2/U$. This also explains some of the dependences on parameters. For example, the low-temperature value of $\mathcal{D}$ decreases as U/t increases, and increases with $t_\perp$. However, some features remain unexplained: Why does $\mathcal{D}$ at $U/t = 4$ decrease again with decreasing temperature

at sufficiently low temperatures? And why is there no (visible) increase in $\mathcal{D}$ with decreasing temperature for the one set of parameter values ($U/t = 4$ for $t_\perp = 0$). A simple theory capturing these more refined features and dependences could provide powerful insights into the Hubbard model's physics, and our data will be an excellent test for any candidate theories.

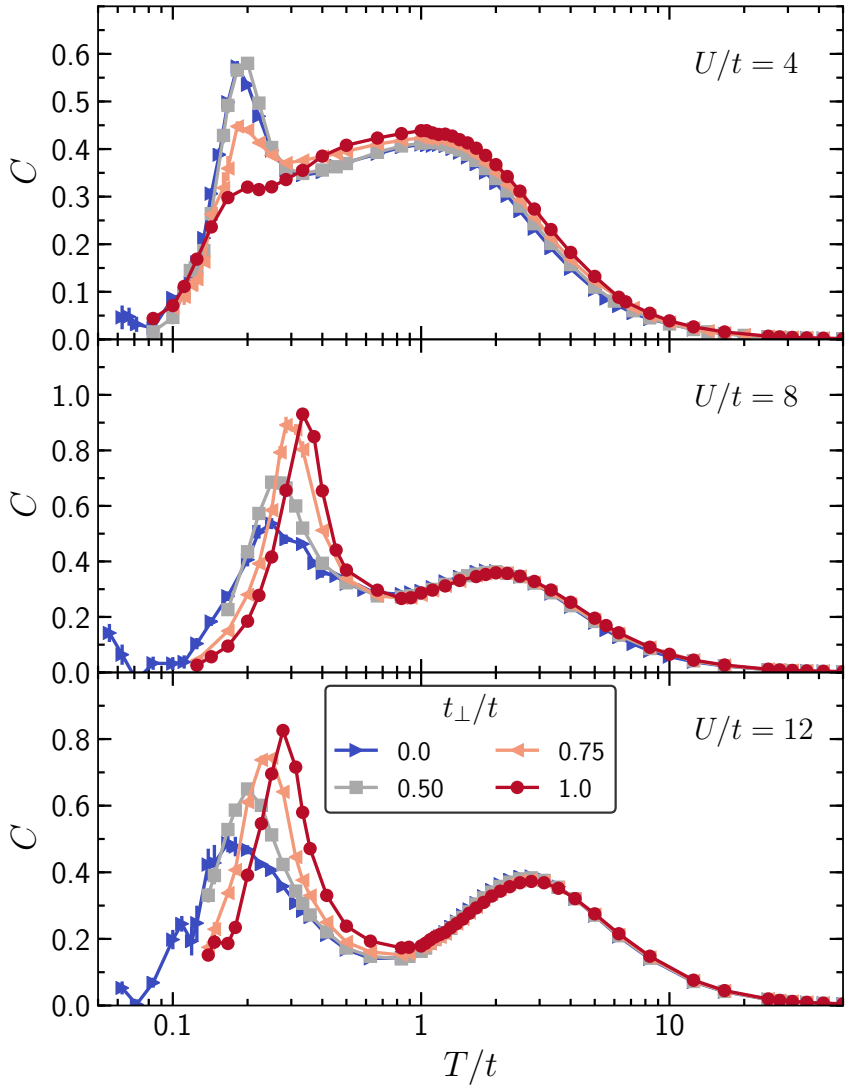

Figure 6.7 : **Specific heat of the anisotropic FHM**. $C = dE/dT$ for $U/t = 4, 8, 12$ at different values of $t_\perp/t$. For $U/t = 8, 12$ the low temperature peak associated with spin degrees of freedom is reduced by anisotropy, while $U/t = 4$ shows the opposite effect.

The specific heat as a function of temperature is a useful thermodynamic observable, showing peaks that characterize the entropy reduction as degrees of freedom reorganize and cease to fluctuate. In particular, there is a two-peak structure, shown in Fig. 6.7, where at large U/t one peak is associated with the charge (i.e. density) and the other with the spin degree of freedom. It is even more informative to break its contributions into the interaction energy ($P = U\mathcal{D}$) and kinetic energy (K) contributions.

Reference [222] examined the contributions dP/dT and dK/dT to the specific heat in the 2D Hubbard model. One reason this is useful is that the interaction energy directly captures the charge fluctuations of freedom, while the kinetic energy is closely related to the spin degree of freedom (at least at large U/t). For $U/t = 10$, the high T charge peak originated in dP/dT (moment formation) and the low T spin peak in dK/dT was related to moment ordering. However, although the two peak structure in C was clearly evident at $U/t = 2$, the high T peak came from dK/dT and the low T peak from dP/dT. (The designation of these peaks as charge and spin thus clearly becomes inappropriate as U gets small.) At $U/t = 10$, in addition to the high T peak, dP/dT also had a negative dip at lower T. This has also been observed in the 1D Hubbard model [223] and dynamical mean field studies [224].

We show a similar decomposition of the specific heat into dP/dT and dK/dT in Figs. 6.8 and 6.9 [†]. Figure 6.8 shows the interaction energy contribution to the specific heat, dP/dT. The $U/t = 8$ and the $U/t = 12$ data have a high temperature charge peak and a negative dip at lower T/t, associated with the increase in interaction

[†]In order to take derivatives in an unevenly spaced dataset, we have used three-point differentiation rule with a $\mathcal{O}(h^2)$ error, where h is the spacing between the variable differentiated with respect to:

$$f'(x) = \left[\frac{x_i - x_{i+1}}{(x_{i-1} - x_i)(x_{i-1} - x_{i+1})}\right] f(x_{i-1}) + \left[\frac{2x_i - x_{i-1} - x_{i+1}}{(x_i - x_{i-1})(x_i - x_{i+1})}\right] f(x_i) + \left[\frac{x_i - x_{i-1}}{(x_{i+1} - x_{i-1})(x_{i+1} - x_i)}\right] f(x_{i+1}).$$

Error bars are obtained by error propagation and treating the errors in quadrature.

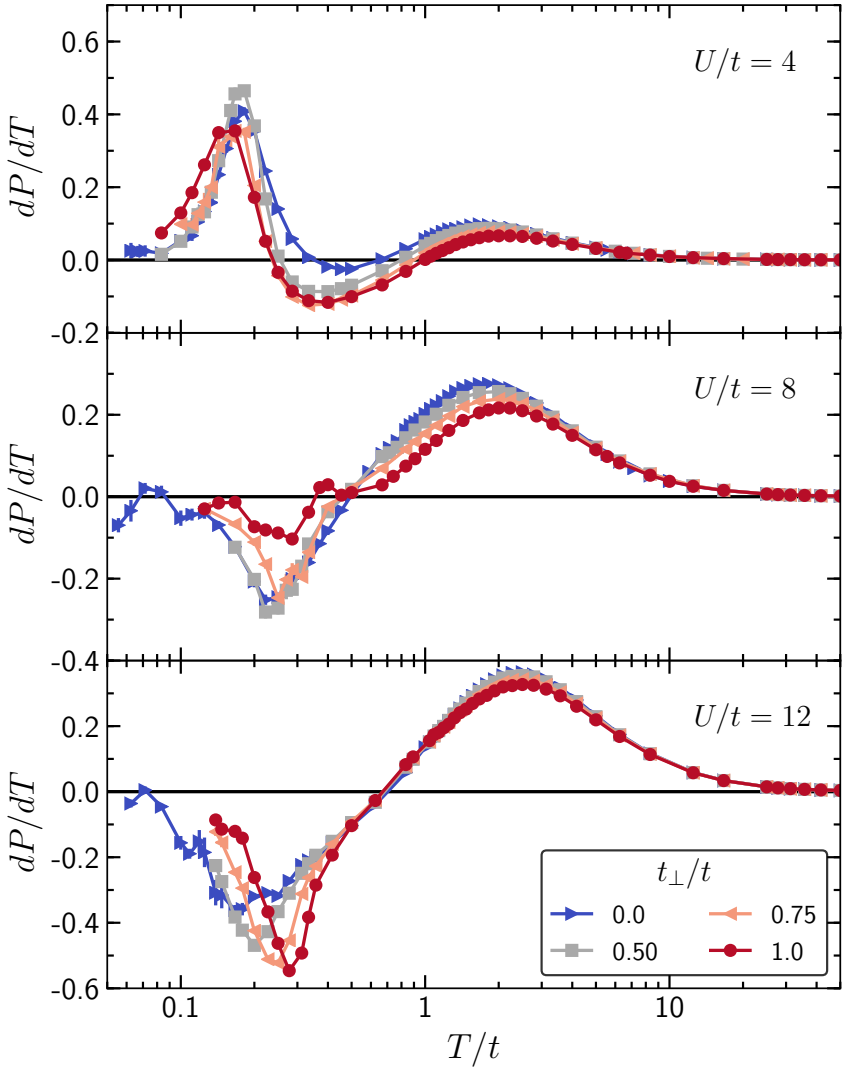

Figure 6.8 : **Potential energy contribution to the specific heat of the anisotropic FHM**. dP/dT with $P = U\mathcal{D}$ the interaction energy as a function of temperature for $U/t = 4, 8, 12$ at different values of $t_\perp/t$.

energy which occurs with the formation of AF order. For $U/t = 8$ the negative dip increases by more than a factor of two moving away from 3D, while for $U/t = 12$ the magnitude of the dip decreases moving away from 3D, and the dip shifts to lower T/t as the system becomes more 2D. Although U/t is constant, $U/t_\perp$ increases as $t_\perp$ decreases; the more pronounced dip can thus be explained by an increase in the effective interaction strength. Finally, for $U/t = 4$ the low temperature peak in dP/dT leads to the low temperature peak in the specific heat.

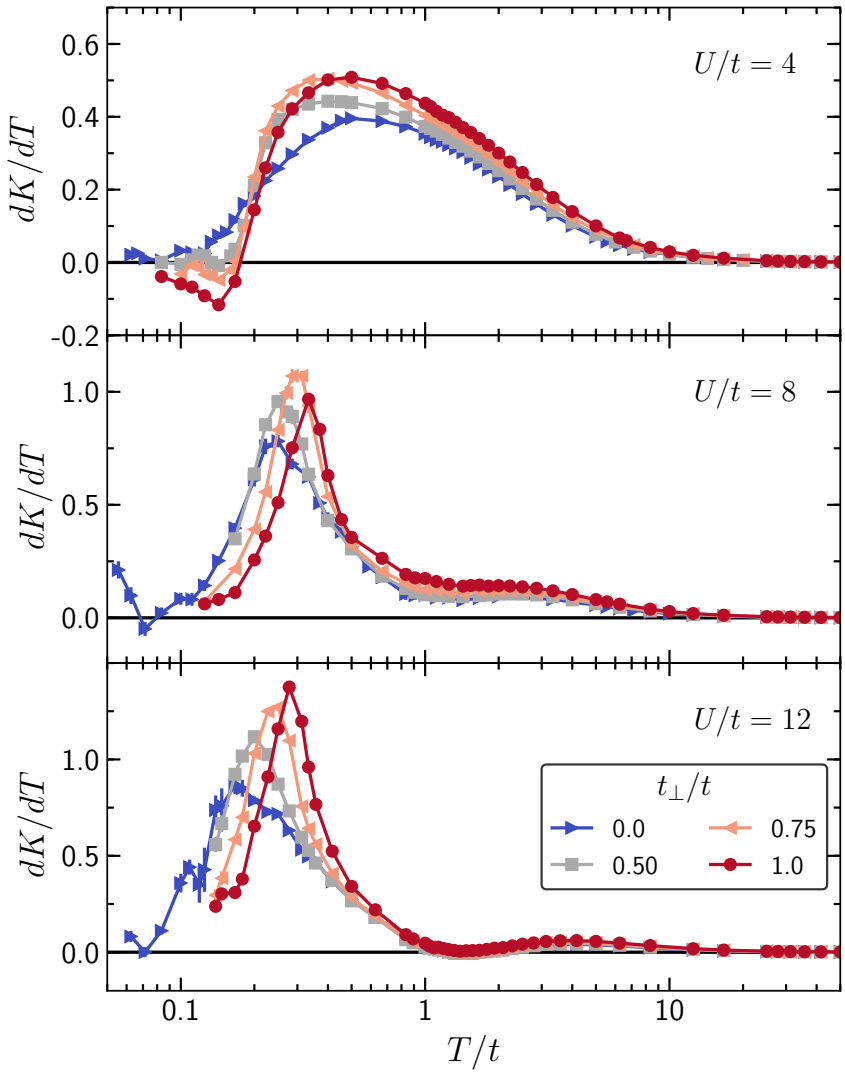

Figure 6.9 : **Kinetic energy contribution to the specific heat of the anisotropic FHM**. dK/dT with K the kinetic energy as a function of temperature for $U/t = 4, 8, 12$ at different values of $t_\perp/t$.

The low temperature spin peak in dK/dT can be seen in Fig. 6.9 for $U/t = 8$ and $U/t = 12$. It is mostly independent of $t_\perp/t$ although the peak position moves down in T/t as the system becomes more 2D. For $U/t = 4$ the peak is replaced by a broader bump that moves to higher T/t as $t_\perp/t$ decreases.

Together, dK/dT and dP/dT combine to form the characteristic two peak structure of the specific heat seen in Fig. 6.7. For strong couplings $U/t = 8, 12$ the low T peak in the specific heat comes from the kinetic energy peak, and the role of the interaction energy is to reduce the height of the peak. For $U/t = 4$ we can see that both dP/dT and dK/dT give a positive contribution to the low T peak in the specific heat.

The interpretation of the multi-peak structure of the specific heat data is complicated by the possibility that the spin-ordering peak might itself be split owing to the presence of two distinct superexchange energy scales, J and $J_\perp$. For $J_\perp < J$ stochastic series expansion (SSE) studies of the 2D-3D crossover of the spin-1/2 Heisenberg model [225] have shown the existence of a broad peak from short range 2D order, as well as a sharper 3D ordering peak whose height diminishes as $J_\perp/J$ decreases. Resolving these structures is already challenging for the spin model, even though the SSE approach scales linearly with the number of spins N and system sizes as large as $N = 3 \times 10^4$ were investigated, and is not possible for the more challenging itinerant Hubbard model studied here.

The entropy as a function of temperature has, in principle, similar information to the specific heat, but the physics is less directly apparent, as seen in Fig. 6.10. We compute the entropy by integrating $dS = dQ/T = C/T\, dT$, with $C = dE/dT$ the specific heat. Integrating by parts, that integral can be rewritten in terms of the energy E,

$$S(T) = 2\log(2) + \frac{E(T)}{T} - \int_T^\infty \frac{E(T')}{T'^2} dT'. \tag{6.3}$$

In practice, we obtain DQMC results up to a temperature cutoff $T_{\text{cut}} = 250t$ and use

the leading order high temperature series term ($t = 0$) in the integral in Eq. (6.3) for $T > T_{\rm cut}$ to accelerate convergence [‡].

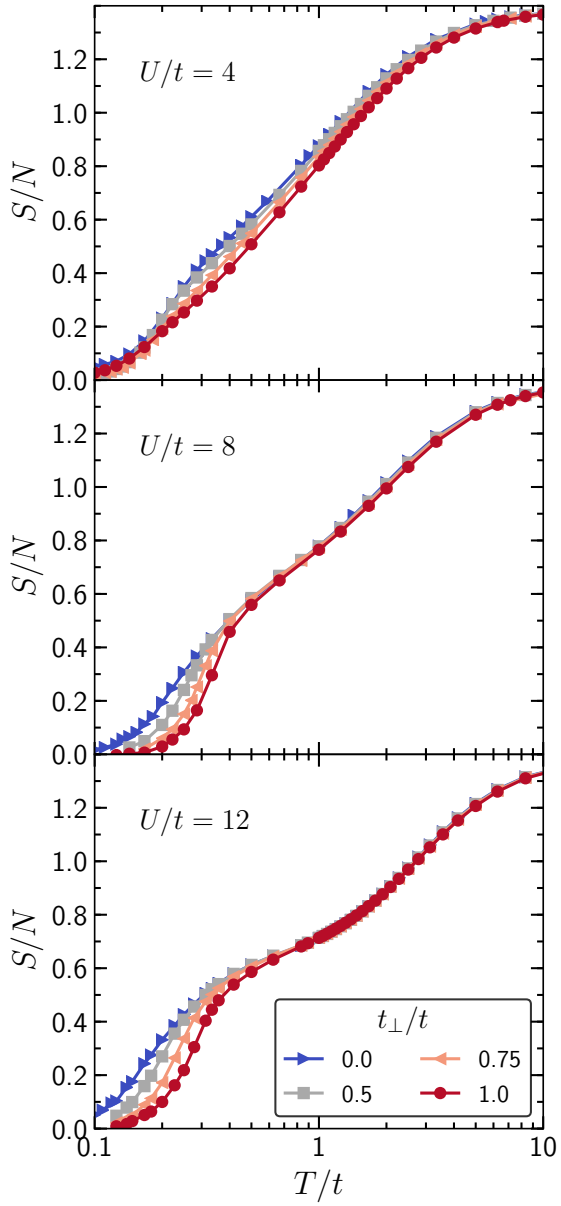

Figure 6.10 : **Entropy of the anisotropic FHM**. S versus temperature for different interplane hopping $t_\perp$. Adiabatic cooling is observed as $t_\perp$ is decreased for all values of the interaction strength.

[‡]The error in the entropy calculation due to the finite value of the temperature cutoff $T_{\rm cut}$ was estimated by comparing the results obtained with $T_{\rm cut}/t = 100, 250$. The difference between those two is below 3.5×10^{-4} for all interaction strengths, temperatures, and values of $t_\perp$ considered in this manuscript.

Figure 6.10 shows the entropy per site S/N versus T/t for different $t_\perp/t$ at $U/t = 4, 8, 12$. Systems with small $t_\perp/t$ have larger S for a given T/t. For $U/t = 4$, $S(T)$ for different values of $t_\perp/t$ begins to become distinct at $T/t \lesssim 5$, and then again become independent of $t_\perp$ at $T/t \lesssim 0.1$. For $U/t = 8, 12$, the dependence on $t_\perp/t$ is negligible until $T/t \lesssim 0.5$. Decreasing $t_\perp/t$ at fixed entropy lowers the temperature.

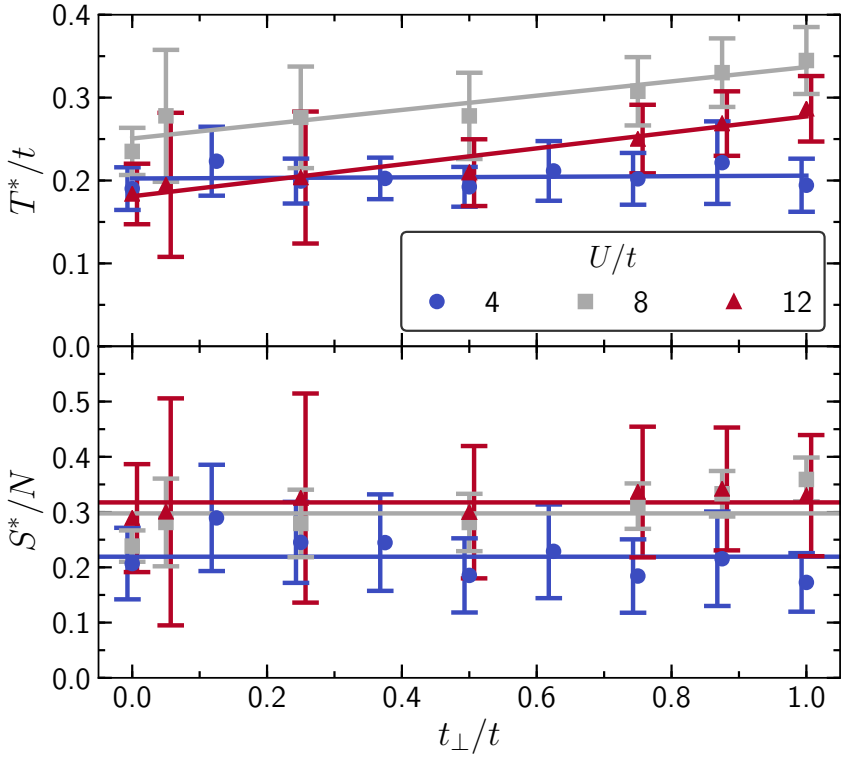

Figure 6.11 : **Low-T peak location in the anisotropic FHM**. Top panel: T^*, defined as the position of the small-temperature peak in C; lower panel $S^* = S(T^*)$ as a function of $t_\perp/t$. Lines in the upper panel are linear fits to the data, while lines in the lower panel are the average of the datasets.

We define the temperature for the low-T peak in $C(T)$ as T^*. For $t_\perp/t = 1$ and $U/t = 8$, T^* closely coincides with the Néel temperature; while for $U/t = 4$, T^* is nearly in agreement with the upper bound given by Ref. [215]. For $U/t = 12$, we do not know of literature where finite-size scaling is done to extract $T_{\text{Néel}}$. For the 2D system, $T_{\text{Néel}} = 0$ due to the Mermin-Wagner theorem, but in contrast $T^* \neq 0$. It is also useful to define $S^* = S(T^*)$. Figure 6.11 shows T^* and S^* as functions of $t_\perp/t$.

For $U/t = 8$ and $U/t = 12$, T^* increases with $t_\perp/t$, signaling that the formation of strong AF correlations moves to lower T as $t_\perp/t$ is decreased. For $U/t = 4$, on the other hand, T^* is almost independent of $t_\perp/t$.

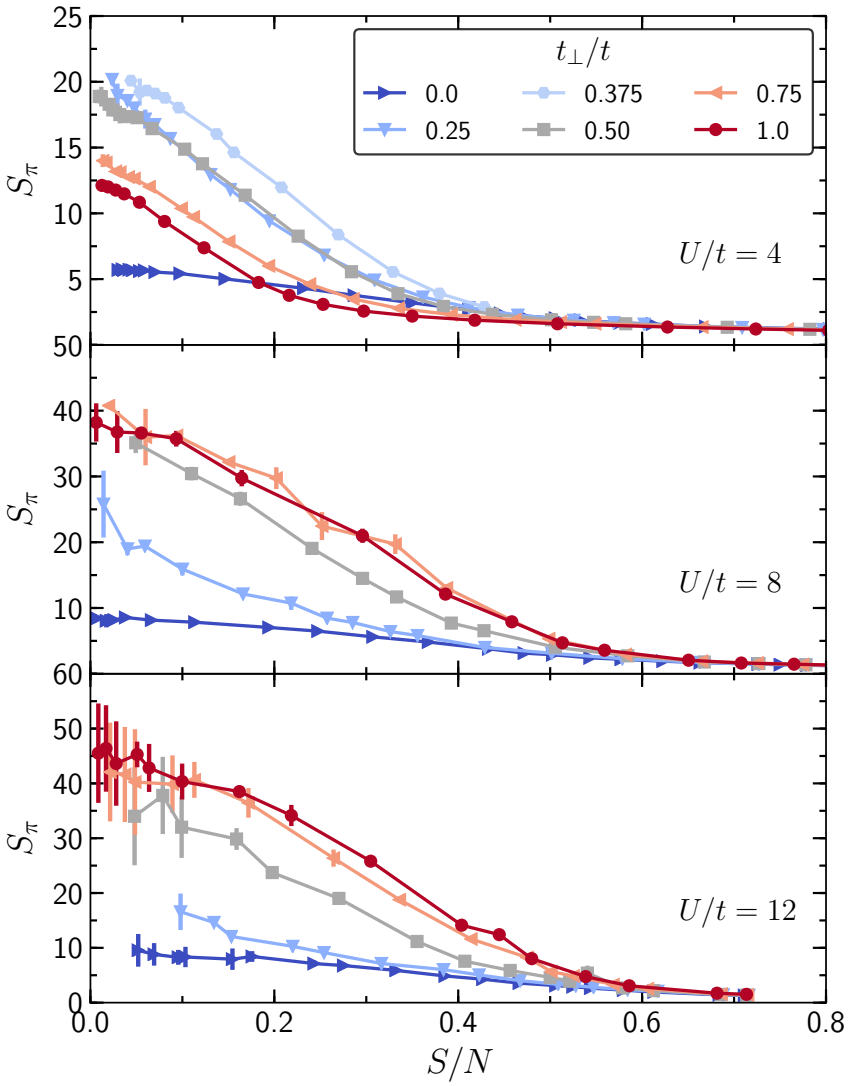

Figure 6.12 : **AFM structure factor of the anisotropic FHM**. S_π as a function of entropy S for different interplane hopping $t_\perp/t$. At weak coupling S_π grows as one moves adiabatically away from the isotropic 3D limit down to $t_\perp/t = 0.375$ and then comes back down.

In the strong-coupling (Heisenberg) limit of the 2D-3D crossover, $T_{\text{Néel}}/J$ is known [217] to go as $T_{\text{Néel}} \sim -1/\ln\alpha$ for $\alpha \ll 1$, with $\alpha = J_\perp/J$. The isotropic case, $\alpha = 1$, has the highest transition temperature $T_{\text{Néel}}/J \sim 0.946$ [226]. $T_{\text{Néel}}$ decreases slowly

with α over most the range from 0 to 1, then rapidly drops to zero as $\alpha \to 0$. Similar trends are observed for T^* in Fig. 6.11 for large U/t, where the results indicate that although T^* is on the same order as the 3D value at weak $t_\perp/t$, it still reaches is largest value at the isotropic point $t_\perp = t$. On the other hand, this strong coupling behavior does not extend to weaker coupling, as the $U/t = 4$ data demonstrate in Fig. 6.11, where T^* is nearly independent on anisotropy. A possible explanation for this behavior is that for small U/t band structure effects such as the van Hove singularity in the 2D density of states become relevant.

6.4.4 Structure factor II

Previous work [184] examined short-range magnetic order in different dimensions and concluded that for strong couplings their onset occurs at a common (dimension independent) entropy, roughly $S/N \sim \ln 2$. This result is in agreement with Fig. 6.12 for $U/t = 8, 12$, where the onset of growth of the structure factor begins around $S/N \sim \ln 2$. That trend, however, does not extend to smaller U/t, as the $U/t = 4$ panel in Fig. 6.12 shows.

The reduction in S_π with anisotropy at $U/t = 8, 12$ overwhelms the benefits of adiabatic cooling, as seen in Fig. 6.12. At fixed entropy, S_π is reduced by anisotropy. In contrast, at $U/t = 4$, Fig. 6.12, S_π can be enhanced by more than a factor of two by reducing $t_\perp/t$ away from the 3D limit. As discussed previously, however, the value is never as large as the maximum attained for $U/t = 8$ in the isotropic case at the same entropy.

6.5 Conclusions

Although anisotropy enhances magnetism at $U/t = 4$, the structure factor is smaller than it is for larger U/t at the isotropic point $t_\perp = t$. Furthermore, despite some adiabatic cooling when reducing $t_\perp$ for large U/t, S_π remains roughly the same for

$t_\perp/t \in (0.5, 1.0)$ for $U/t = 8$, and diminishes with anisotropy for $U/t = 12$, so there is no benefit in using anisotropy.

The study of anisotropy in the tunneling of the Hubbard model, and its strong-coupling Heisenberg limit, is of interest beyond OLE. QMC simulations of bilayer Hubbard [227] and Heisenberg [228] models in which $t_\perp \neq t$ or $J_\perp \neq J$ have explored quantum phase transitions between AF and singlet phases relevant to heavy fermion magnetism, as well as studied $s\pm$-wave superconductivity [229–231]. Similarly, the possibility of enhanced transition temperatures to magnetic order at the 2D surface of bulk 3D materials has been investigated [232, 233]. Finally, analogous issues concerning the effect of inhomogeneous intersite tunneling occur in the context of optimizing d-wave pairing in the 2D Hubbard Hamiltonian. In that case, a model of 2×2 plaquettes [234] with internal hopping t and coupled by interplaquette hopping t' was suggested to have an optimal tunneling for pairing which occurs at $t' < t$, away from the isotropic limit [235–242]. The interest in anisotropic tunnelings also extends to the attractive Hubbard model as well. For example, in Ref. [243] a layer of disconnected attractive Hubbard sites coupled to a metallic layer shows that although the superconducting critical temperature T_c exhibits a maximum as function of the interlayer tunneling, the highest T_c is still smaller than the maximal T_c of the uniform 2D attractive Hubbard model. The results presented in the present paper provide additional information in this broader context, both by quantifying how AF evolves for layered materials, and also by providing further insight into how the strong correlation physics interplays with anisotropy.

6.5.1 Anisotropy as a mean to cool

Finally, a possible application of our results is to design a cooling protocol, relying on the results of Fig. 6.10 that show a system at a fixed entropy will get colder as $t_\perp/t$ is reduced, specially for strong interactions. By exploiting inhomogeneity, this effect can

be used to cool systems with an arbitrary $t_\perp/t$, even isotropic 3D systems, as follows. First, load the atoms into a 3D lattice. Now adjust the lattice depth of the system in a carefully constructed inhomogeneous way; for simplicity think of two regions: R, an entropy reservoir we will sacrifice to cool the system, and S, the system we want to cool and study. In R, we adiabatically lower the z-direction lattice depth V_z. This spatially inhomogeneous lattice depth could be engineered using, for example, a spatial light modulator (however, implementing the spatially-modulated anisotropy will be more challenging than a spatially-modulated trapping potential). The now-anisotropic R can carry extra entropy at a given temperature, as per Fig. 6.10, so entropy will transport to this region from S as the system reaches thermal equilibrium at a new temperature. At the temperatures plotted for $U/t = 12$, the entropy per particle in region S can be reduced by a factor of 2. Finally, one can cool and study S with an arbitrary $t_\perp/t$ this way by applying an optical barrier to turn transport off between S and R, and then adiabatically change V_z in the S region to give the desired $t_\perp/t$. This cooling method bears similarities to other entropy redistribution protocols [21, 37, 38, 207, 244–253] but overcomes some difficulties. In particular, schemes that rely on metal reservoirs created by changing the local potential, rather than lattice anisotropy, suffer at large U/t from the fact that the metals created this way are bad metals, therefore they carry significantly less entropy, than, e.g., a non-interacting metal. Our protocol also has some similarities to the conformal cooling suggested in Ref. [254], but allows one to cool the full Fermi-Hubbard model in a practical way, rather than just the Heisenberg limit.

6.5.2 Finite-size effects

As mentioned in Section 6.3, for the energy, kinetic energy, interaction energy (number of doublons), nearest neighbor spin correlations, and entropy, finite size errors (as measured by the difference between $L = 4$ and $L = 6$ calculations) are $\lesssim 5\%$. It is

the correlations at distances comparable to the system size that are affected; other than these, S_π is thus the only observable that is affected, and only when the system is near or below the Néel temperature so that the correlations at separations comparable to the system size are appreciable.

In order to give an estimate of the finite-size effects for the different values of $t_\perp/t$ and U/t, we present $S_\pi^{(L)}$ and $\tilde{S}_\pi^{(L)} = S_\pi^{(L)}/L^3$ as a function of U/t, $t_\perp/t$ and T/t in $L \times L \times L$ cubic systems. We note that for $T > T_{\text{Néel}}$ we have $S_\pi \to$ constant $\neq 0$ as $L \to \infty$ and $\tilde{S}_\pi \to 0$, while for $T < T_{\text{Néel}}$ we have $S_\pi \to \infty$ and $\tilde{S}_\pi \to$ const.

Fig. 6.13 presents S_π at $T/t = 0.2$ as a function of $t_\perp/t$ for different system sizes, while Tables 6.1 and 6.2 report $\tilde{S}_\pi$ for two T/t presented in Fig. 6.4. The $U/t = 8, 12$ panels exhibit the same behavior seen in Fig. 6.4, i.e. S_π is maximized when $t_\perp \sim t$. For $t_\perp/t \gtrsim 0.5$, S_π grows roughly proportional to L^3, suggesting that the system is below $T_{\text{Néel}}$, and that the numerics provides a reasonable estimate of $\tilde{S}_\pi$. In contrast, the $U/t = 4$ panel demonstrates that S_π is maximized at the 2D-3D crossover, in agreement with the results presented in Fig. 6.4 although the location of the maximum depends significantly on the system size. The scaling looks neither like a the simple L-independent S_π expected in large systems for temperature above the Néel temperature, nor the L-independent $\tilde{S}_\pi$ expected for large systems below the Néel temperature. Previous results in the $t_\perp/t \ll 1$ limit [255], and in 3D [215], place $T_{\text{Néel}} \lesssim 0.2$ for $U/t = 4$; therefore this absence of a simple scaling on L is expected at $T/t = 0.2$. A detailed study of finite-size effects, as was done in [215, 220] in 3D, and for larger system sizes than in the present Chapter is required to precisely determine $T_{\text{Néel}}$ in the 2D-3D crossover. This task is out of the scope of the Chapter, but our results will provide a useful starting point for such calculations.

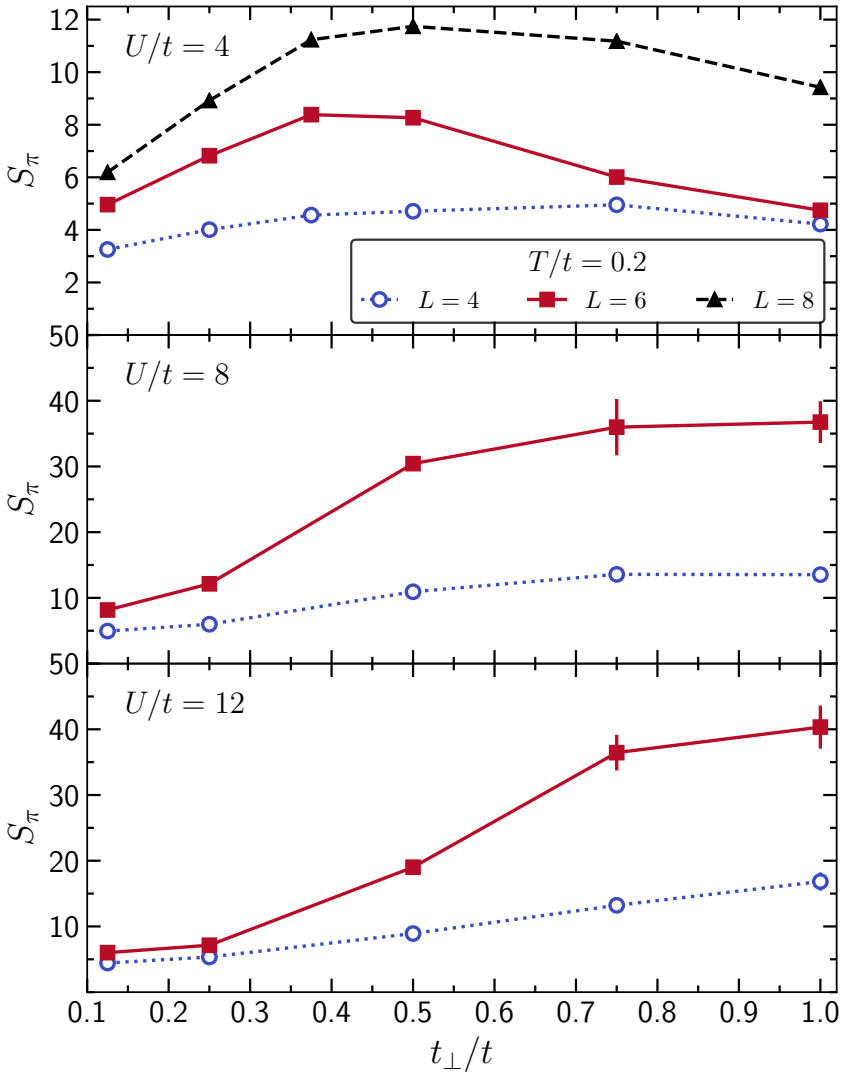

Figure 6.13 : **Finite size effects in the anisotropic FHM**. AFM structure factor S_π as a function of interplane tunneling $t_\perp/t$ at $T/t = 0.2$ for different cubic lattices with sides of length L. We note that the $L = 8$ calculations are substantially more computationally expensive because – defining $N_{\text{sites}} = L^3$ to be the number of sites – the computational cost scales as $O(N_{\text{sites}}^3) = O(L^9)$.

U/t	$t_\perp/t$	$\tilde{S}_\pi^{(4)}$	$\tilde{S}_\pi^{(6)}$	$\lvert\tilde{S}_\pi^{(6)} - \tilde{S}_\pi^{(4)}\rvert$
4	0.125	0.06	0.04	0.03
	0.25	0.10	0.08	0.02
	0.375	0.11	0.09	0.02
	0.5	0.11	0.08	0.03
	0.75	0.11	0.06	0.05
	1	0.09	0.05	0.04
8	0.125	0.09	0.05	0.04
	0.25	0.12	0.09	0.03
	0.5	0.20	0.17	0.03
	0.75	0.22	0.18	0.04
	1	0.21	0.17	0.04
12	0.125	0.09	0.05	0.04
	0.25	0.11	0.08	0.03
	0.5	0.20	0.16	0.04
	0.75	0.26	0.19	0.06
	1	0.25	0.21	0.04

Table 6.1 : **Finite-size effects in the structure factor I**. Structure factor $\tilde{S}_\pi^{(L)}$ in cubic lattices with sides of length L at $T/t = 0.125$.

U/t	$t_\perp/t$	$\tilde{S}_\pi^{(4)}$	$\tilde{S}_\pi^{(6)}$	$\tilde{S}_\pi^{(8)}$	$\lvert\tilde{S}_\pi^{(6)} - \tilde{S}_\pi^{(4)}\rvert$	$\lvert\tilde{S}_\pi^{(8)} - \tilde{S}_\pi^{(6)}\rvert$
4	0.125	0.05	0.02	0.01	0.03	0.01
	0.25	0.06	0.03	0.02	0.03	0.01
	0.375	0.07	0.04	0.02	0.03	0.02
	0.5	0.07	0.04	0.02	0.04	0.02
	0.75	0.08	0.03	0.02	0.05	0.01
	1	0.07	0.02	0.02	0.04	0.00
8	0.125	0.08	0.04		0.04	
	0.25	0.09	0.06		0.04	
	0.5	0.17	0.14		0.03	
	0.75	0.21	0.17		0.05	
	1	0.21	0.17		0.04	
12	0.125	0.07	0.03		0.04	
	0.25	0.08	0.03		0.05	
	0.5	0.14	0.09		0.05	
	0.75	0.21	0.17		0.04	
	1	0.26	0.19		0.08	

Table 6.2 : **Finite-size effects in the structure factor II.** Structure factor $\tilde{S}_\pi^{(L)}$ in cubic lattices with sides of length L at $T/t = 0.2$.

Chapter 7

Universal thermodynamics of an SU(N) Fermi-Hubbard model

> Se trabaja con imaginación, intuición y una verdad aparente; cuando esto se consigue, entonces se logra la historia que uno quiere dar a conocer. Creo que eso es, en principio, la base de todo cuento, de toda historia que se quiere contar.
>
> Juan Rulfo

This chapter is adapted from publication:

Universal thermodynamics of an SU(N) Fermi-Hubbard Model, **Eduardo Ibarra-García-Padilla**, Sohail Dasgupta, Hao-Tian Wei, Shintaro Taie, Yoshiro Takahashi, Richard T. Scalettar, and Kaden R. A. Hazzard, Phys. Rev. A **104**, 043316 (2021) [Editors' Suggestion] *.

The SU(2) symmetric Fermi-Hubbard model (FHM) plays an essential role in strongly correlated fermionic many-body systems. In the one particle per site and strongly interacting limit $U/t \gg 1$, it is effectively described by the Heisenberg Hamiltonian. In this limit, enlarging the spin and extending the typical SU(2) symmetry to SU(N) has been predicted to give exotic phases of matter in the ground state, with a complicated dependence on N. This raises the question of what — if any — are the finite-temperature signatures of these phases, especially in the currently experimentally relevant regime near or above the superexchange energy. We explore this question for thermodynamic observables by numerically calculating the thermo-

*Complete article, including text, figures, and tables reprinted with copyright permission of Ref. [44].

dynamics of the SU(N) FHM in the two-dimensional square lattice near densities of one particle per site, using determinant Quantum Monte Carlo and Numerical Linked Cluster Expansion. Interestingly, we find that for temperatures above the superexchange energy, where the correlation length is short, the energy, number of on-site pairs, and kinetic energy are universal functions of N. Although the physics in the regime studied is well beyond what can be captured by low-order high-temperature series, we show that an analytic description of the scaling is possible in terms of only one- and two-site calculations.

7.1 Introduction

The Fermi-Hubbard model (FHM), in its original spin-1/2, SU(2) symmetric form [24, 47–49], plays a central role in the understanding of strongly correlated fermionic many-body systems. This is in part because it is one of the simplest models that captures essential features of real materials, and in part because it exhibits a variety of canonical correlated phases of matter. In the two-dimensional (2D) square lattice, it displays a metal-to-insulator crossover as well as magnetic order, and it is widely studied in the context of d-wave superconductivity [46, 50, 52, 171, 256].

Its generalization, the SU(N) FHM, features larger spins and enhanced symmetry, and it provides insight into important strongly correlated systems. First, it is a simple limit of multi-orbital models such as those used to describe transition metal oxides [72–74], graphene's SU(4) spin-valley symmetry [90], and twisted-bilayer graphene [91–96]. Second, the SU(N) FHM is predicted to display a variety of interesting and exotic phases even in very special limits, such as: the conventional $N = 2$ FHM, the $N = 3$ FHM [102–111], the $N = 4$ FHM at quarter filling [113, 114], even values of N at half-filling [77, 78, 115–121], special $N \to \infty$ limits [8, 83–86], 1D chains [123–129], and the Heisenberg limit for $N = 3, 4, 5$ [73, 75, 76, 102, 130–136]. This richness is well illustrated by numerical studies of the Heisenberg limit, which

describes the situation where the average number of particles per site is $\langle n \rangle = 1$ and the interactions dominate the kinetic energy ($U \gg t$, with notation discussed below). Already in this simple limit and additionally in the simple 2D square lattice, the model is predicted to exhibit several phases of matter with novel and difficult-to-explain properties depending on the value of N. The dependence of the ground state order with N does not follow a simple pattern. This raises the question of whether and how this complicated N-dependence manifests in the finite-temperature properties.

Although the SU(N) FHM is a crude approximation to real materials, it has been realized to high precision by loading alkaline earth-like atoms (AEAs) into an optical lattice (OL). Fermionic AEAs (such as ^{173}Yb and ^{87}Sr) feature an almost perfect decoupling of the nuclear spin I from the electronic structure in the ground state, which gives rise to SU($N = 2I + 1$) symmetric interactions with deviations predicted to be of order $\mathcal{O}(10^{-9})$ [97, 98, 257–259]. For that reason, by selectively populating nuclear spin projection states m_I of AEAs and loading them into an OL, experiments can engineer the SU(N) FHM with N tunable, from $2, 3, \ldots, 10$.

In recent years, experiments with ^{173}Yb in OLs have probed the SU(N) FHM's interesting physics: The Mott insulator state for SU(6) in three dimensions [71], the equation of state for SU(3) and SU(6) in three dimensions [141], nearest-neighbor antiferromagnetic (AFM) correlations in an SU(4) system with a dimerized OL [142], nearest-neighbor SU(6) AFM correlations in OLs with uniform tunneling matrix elements in one, two, and three dimensions [41], and recently a flavor-selective Mott insulator for SU(3) [143]. Furthermore, employing quantum gas microscopy [12, 16, 17, 21, 62, 65, 66] to discriminate finite temperature analogs of the variety of proposed ground states [75–78, 130–133] via direct observation of long-ranged correlations [41, 205, 206, 260] is expected to reveal a wealth of physics. All of these experimental efforts make an understanding of the 2D square lattice thermodynamics

urgent.

In contrast with most previous work that focused on the Heisenberg limit, in this work we study the SU(N) FHM at finite temperature and for a range of interaction parameters, including far from the Heisenberg limit, a regime that is both interesting and experimentally important. We calculate and analyze thermodynamic properties of the model as a function of N, the interaction strength U, and the temperature T. We numerically explore the evolution of the energy, number of on-site pairs [†], and kinetic energy, as well as their derivatives in the 2D square lattice SU(N) FHM at $1/N$ filling, i.e., one particle per site on average.

Some of the quantities we compute, such as the number of on-site pairs are immediately measurable in experiment, while others such as the kinetic energy and total energy are of fundamental importance and also may also become accessible. For example, Ref. [261] experimentally determined the energies of a Bose-Hubbard model. In that work the kinetic energy was measured by analyzing time-of-flight images and the interaction energy was measured by site-resolved high-resolution spectroscopy. These techniques can be also used for the FHM. Additionally, in a quantum gas microscope the number of on-site pairs can be spatially resolved by generalizing the technique used in Ref. [262] to AEAs. This would require employing an optical (rather than magnetic) Stern-Gerlach technique to split the different spin flavors into different layers, followed by detection by single-site fluorescence. Additionally, access to total density fluctuations in a bilayer quantum gas microscope, as done in Refs. [263, 264], provides a route to realize thermometry without the need to comparison with numer-

[†]The number of on-site pairs and the double occupancy are equivalent in the SU(2) Fermi-Hubbard model due to Pauli exclusion principle. However, for $N > 2$ this is not the case. The number of on-site pairs $\mathcal{D}$ counts the pairs of particles per site and is what controls the interaction energy $U\mathcal{D}$, while the double occupancy most naturally refers to the probability of configurations with exactly two particles per site, or to summing probabilities of all configurations with two or more particles per site. Either one of these is distinct from the number of on-site pairs $\mathcal{D}$. Computing the number of double occupancies thus requires the calculation of density fluctuations, i.e., terms of the order $\langle n^x \rangle$ with $x \in [2, N]$, which are computationally more expensive and experimentally harder to access.

ical simulations.

We also present some selected results as a function of chemical potential μ. Results are obtained using the determinant Quantum Monte Carlo (DQMC) and Numerical Linked Cluster Expansion (NLCE) methods. Here and throughout we set Boltzmann's constant to $k_B = 1$.

Although the ground state has a complicated N-dependence, we find that for temperatures above the superexchange energy $T \gtrsim J = 4t^2/U$, the energy, the number of on-site pairs, and the kinetic energy depend on N in a particularly simple way, obeying a simple, analytic dependence on N.

Even though a simple scaling at very high temperatures would be unsurprising — since a low-order high-temperature series expansion (HTSE) would be expected to be accurate and to produce analytic expressions that plausibly would show simple N-dependence — such expansions are insufficient to explain our findings. The HTSE is accurate only for $T \gtrsim 4t$, while the universal scaling persists to temperatures $T \gtrsim 4t^2/U$ that are much lower when $U \gg t$. At such temperatures the HTSE is not only inaccurate, but diverges.

Despite the failure of the HTSE to fully explain the observations, a simple explanation is possible by recognizing that correlations are short-ranged in this temperature regime. We show that in this limit, the second order NLCE accurately reproduces the results and the N scaling relation. Furthermore, under controlled approximations in the $J \ll T \ll U$ regime one can analytically evaluate the pertinent contributions based on the NLCE, and with this explain the observed universal scaling with N to zeroth order in βJ. This demonstrates the utility of the NLCE framework for analytic calculations, beyond its typical application in numerical calculations. These observations show that the one- and two-site correlations control the physics deep in this regime.

The remainder of this Chapter is organized as follows: Section 7.2 presents the

SU(N) Hubbard Hamiltonian, defines the observables we consider, and presents details of the numerical and analytical methods used. Section 7.3 presents the main results, and Section 7.4 concludes.

7.2 Model and Methods

7.2.1 The SU(N) Hubbard Hamiltonian and observables

The SU(N) FHM is defined by the grand canonical Hamiltonian

$$H = -t \sum_{\langle i,j\rangle,\sigma} \left(c^{\dagger}_{i\sigma} c_{j\sigma} + \text{h.c.} \right) + \frac{U}{2} \sum_{i,\sigma\neq\tau} n_{i\sigma} n_{i\tau} - \mu \sum_{i,\sigma} n_{i\sigma}, \tag{7.1}$$

where $c^{\dagger}_{i\sigma}$ ($c_{i\sigma}$) is the creation (annihilation) operator for a fermion with spin flavor $\sigma = 1, 2, ..., N$ on site $i = 1, 2, ..., N_s$ in a 2D square lattice, N_s denotes the number of lattice sites, $n_{i\sigma} = c^{\dagger}_{i\sigma} c_{i\sigma}$ is the number operator for flavor σ, t is the nearest-neighbor hopping amplitude, U is the interaction strength, and μ is the chemical potential that controls the fermion density.

We are interested in thermodynamic quantities such as the number of on-site pairs

$$\mathcal{D} = \frac{1}{N_s} \sum_{i} \left[\frac{1}{2} \sum_{\sigma\neq\tau} \langle n_{i\sigma} n_{i\tau} \rangle \right], \tag{7.2}$$

the kinetic energy per site

$$K = \frac{1}{N_s} \Big\langle -t \sum_{\langle i,j\rangle,\sigma} \left(c^{\dagger}_{i\sigma} c_{j\sigma} + c^{\dagger}_{j\sigma} c_{i\sigma} \right) \Big\rangle, \tag{7.3}$$

the energy per site $E = \langle H/N_s + \mu n \rangle$ (where $n = \sum_{\sigma} n_{i\sigma}$), and the entropy S. We present these observables and the derivatives dE/dT, dK/dT, and $U d\mathcal{D}/dT$ as functions of T/t for different values of the interaction strength U/t either as a function of chemical potential μ/t or at fixed density $\langle n \rangle = (1/N_s) \sum_{i,\sigma} \langle n_{i\sigma} \rangle = 1$. We also

show the compressibility $\kappa = d\langle n\rangle/d\mu$ as a function of μ for various T/t, U/t, and N. These observables provide valuable knowledge about the physics: the number of on-site pairs is a useful measure of the Mott insulating nature of the system, the kinetic energy of its spatial coherence, and the entropy and specific heat provide information about the temperature scales at which various degrees of freedom cease to fluctuate.

7.2.2 Numerical methods

To calculate the thermodynamic observables, we employ two numerical techniques, DQMC [165, 166] and NLCE [164, 265], which have complementary strengths, and compare in some cases with low-order analytic HTSE and the non-interacting limit. The DQMC and NLCE are often the numerical methods of choice for the SU(2) FHM in the finite-temperature regime studied in ultracold matter [20, 22, 63, 67, 68], and we use our extensions of these methods to SU(N) systems [41]. Generally speaking, the DQMC will perform best at weak to intermediate interactions, while the NLCE performs best at strong interactions; we present both methods where both are viable.

7.2.2.1 Determinant Quantum Monte Carlo (DQMC)

Averages of the thermal equilibrium observables are evaluated with DQMC on 6×6 lattices by introducing $N(N-1)/2$ auxiliary Hubbard-Stratonovich fields, one for each interaction term [‡]. In this method, the inverse temperature β is discretized in steps of $\Delta\tau$ with a Trotter step $\Delta\tau = 0.05/t$ for $U/t = 4, 8$ and $\Delta\tau = 0.04/t$ for $U/t = 12$. In order obtain accurate results, we obtain DQMC data for $40-60$ different random seeds for $T/t \leq 4$ and for $2-10$ different random seeds for $T/t > 4$. For each Monte Carlo trajectory we perform 2000 warm up sweeps and 8000 sweeps for measurements [§]. In addition, the number of global moves per sweep to mitigate possible ergodicity

[‡]Previous work applied Determinant Quantum Monte Carlo for the SU($2N$) Fermi-Hubbard model at half-filling, i.e. $\langle n\rangle = N/2$, using an alternative Hubbard-Stratonovitch decomposition. This alternative decomposition is free of the sign problem at half-fillling for SU($2N$) [77, 78, 178, 179]

[§]A sweep updates all the auxiliary fields at every lattice site and imaginary time slice.

issues [177] is set to 2 for $U/t = 4, 8$ and to 4 for $U/t = 12$. These global moves update, at a given lattice site, all the imaginary time slices that couple two spin flavors. DQMC results presented in this Chapter are obtained by computing the weighted average and weighted standard error of the mean of the results obtained by using different random seeds. We use the inverse squared error of each measurement as their weight. Results obtained using a uniform weight for all measurements yield consistent results but with larger error bars (∼2-4 times larger). Estimates of systematic errors are obtained for $N = 6$ at $U/t = 12$ (Trotter) and $N = 6$ at $U/t = 4$ (finite-size), where they are expected to be worst. We estimate the Trotter error by comparing the results obtained with $\Delta\tau = 0.04/t$ and $\Delta\tau = 0.05/t$. Their difference is below 4% for all observables of interest at $T/t = 0.5$. This discretization error is even smaller at higher temperatures and for the other two values of U/t considered. Finite-size errors are estimated by comparing results for different thermodynamic quantities in 4×4 and 6×6 lattices. At $T/t = 0.5$ their differences are $\lesssim 6.5\%$ for $U/t = 4$ and $\lesssim 5.7\%$ for $U/t = 12$.

7.2.2.2 Calculation of specific heat and entropy in DQMC

For DQMC data we evaluate the specific heat and entropy in two ways. In the first approach, we numerically differentiate the energy to obtain the specific heat [¶], and we compute the entropy by integrating $dS = dQ/T = C/T\, dT$, with $C = dE/dT$ the

[¶] We used the three-point differentiation rule

$$f'(x) = \left[\frac{x_i - x_{i+1}}{(x_{i-1} - x_i)(x_{i-1} - x_{i+1})}\right] f(x_{i-1}) + \left[\frac{2x_i - x_{i-1} - x_{i+1}}{(x_i - x_{i-1})(x_i - x_{i+1})}\right] f(x_i) + \left[\frac{x_i - x_{i-1}}{(x_{i+1} - x_{i-1})(x_{i+1} - x_i)}\right] f(x_{i+1}),$$

with error $\mathcal{O}(h^2)$ where h is the maximum spacing of adjacent x_i. Statistical error bars are obtained by error propagation.

specific heat. Integrating by parts, S can be rewritten in terms of the energy E,

$$S(T) = S_\infty + \frac{E(T)}{T} - \int_T^\infty \frac{E(T')}{T'^2} dT', \tag{7.4}$$

where S_∞ is the entropy at fixed density in the limit when $T \to \infty$ (see Appendix 7.4.1 for more details).

The DQMC becomes unreliable at T below the superexchange scale J. In this regime the statistical noise increases due to the sign problem, severely limiting calculations. In addition to presenting the DQMC calculations directly, we also show results obtained from fitting and from differentiating this smooth fit function, which can reduce the noise at the cost of potentially biasing the data. For the energy, we fit to the simple functional form [222, 266],

$$E(T) = E(0) + \sum_{k=1}^{M} c_k e^{-\beta k \Delta}, \tag{7.5}$$

with fitting parameters c_k, Δ, and $E(0)$. The number of parameters c_k, M, is chosen to be around 6-12 (slightly less than one-third of the data points to be fit), which is similar to Refs. [222, 266]. We smooth the 10 lowest temperature data points using a moving average with a three-point window fitted with a local first-order polynomial (Savitzky–Golay filter). Then the data are fit with Eq. (7.5), by choosing the fitting parameters that minimize

$$\Xi^2 = \frac{1}{N_p + 1} \left(\sum_{n=1}^{N_p} \left[E(T_n) - E_n \right]^2 + \left[S_\infty - \sum_{k=1}^{M} \frac{c_k}{k\Delta} \right]^2 \right), \tag{7.6}$$

where N_p is the number of data points, and E_n is the DQMC energy at T_n. The first term ensures a good fit of the data, while the second term regularizes the fit and ensures that $S \to 0$ as $T \to 0$ by enforcing the constraint $S_\infty = \int_0^\infty \frac{C(T')}{T'} dT' =$

$\sum_{k=1}^{M} \frac{c_k}{k\Delta}$ [‖]. A similar procedure is used to obtain fits for the number of on-site pairs and the kinetic energy: Each dataset is fit using the same form as Eq. (7.5), subject to the constraint that the derivative of their sum obeys the specific heat sum rule.

Results obtained from fitting remove the noise providing smooth guides to the eye. By construction they also satisfy important physical features such as sum rules. However, fitting necessarily biases the results and should be interpreted with caution. Care is especially warranted in the high-noise regimes (mainly occurring in the derivative data at the lowest temperatures presented) where the fits are used to extrapolate the data. Nevertheless, the fits suggest interesting features and trends that may help guide future low-temperature calculations and experiments.

7.2.2.3 Numerical Linked Cluster Expansion (NLCE)

Thermodynamic observables are computed using a fifth-order site expansion NLCE. We briefly derive and present this algorithm, which is reviewed in Ref. [164]. Extensive properties in a lattice are evaluated by performing a weighted sum of their value in all possible clusters c embeddable in the lattice; specifically,

$$P(\mathcal{L})/N_s = \sum_{c \in \mathcal{L}} L(c) W_P(c) \tag{7.7}$$

where $P(\mathcal{L})$ is the property evaluated on the entire lattice $\mathcal{L}$, N_s is the number of lattice sites, $L(c)$ is the number of ways that the cluster c can be embedded in the lattice (up to translation invariance), and $W_P(c)$ is defined as

$$W_P(c) = P(c) - \sum_{s \subset c} W_P(s). \tag{7.8}$$

[‖] An equal weight on regularization and fitting terms is enough to ensure that $S \to 0$ as $T \to 0$ with an error $\lesssim 10^{-2}$ for all N and U/t.

Eq. (7.7) follows directly from the definition of the $W_P(c)$. Eq. (7.7) is an infinite sum over all clusters, and the key idea of the NLCE is to truncate this sum to clusters of small size (different variants use different measures of size) and evaluate properties on each cluster using exact diagonalization (ED). Here we truncate the sum over clusters based on the number of sites, performing calculations up to five site clusters, which shows good convergence (see Appendix 7.4.2).

The Hilbert space dimension increases rapidly with N, limiting the size of clusters that can be included in the expansion, and we use multiple methods to reduce the computational cost in order to reach five-site clusters for SU(6). The most straightforward is to account for the SU(N) symmetry, in particular its abelian symmetries (the N conserved flavor numbers) and the flavor permutation symmetry. Additionally, for $N = 6$, we truncate the Hilbert space in the Fock basis using two criteria: (1) We include only basis states with a number of particles below a cutoff value (chosen to be six, which is one larger than the number of sites in the largest cluster), and (2) We include only basis states whose interactions energy is less than a cutoff value (chosen to be $3U$). These choices provide highly accurate (several decimal places) results over the temperature and density ranges of interest in this Chapter, though at high temperatures or densities they can break down. Appendix 7.4.3 provides details of these truncations and the calculations' convergence.

The NLCE is much more accurate than an exact diagonalization (ED) that uses the same number of (or even more) sites. At all temperatures considered, the five-site NLCE calculations are dramatically more accurate than 3×2 ED calculations in either periodic or open boundary conditions to quite low temperatures. In fact, at least for temperatures where the NLCE is convergent and the density $\langle n \rangle = 1$ case that is our main focus, even a two-site NLCE calculation outperforms the 3×2 ED, despite requiring enormously fewer computational resources. We note that this is, to our knowledge, the first application of NLCE to the SU(N) FHM. The convergence

with expansion order and comparisons with ED are discussed in Appendix 7.4.2.

The NLCE self-diagnoses its accuracy, with converged results expected when adjacent orders give nearly the same answer. Results in this Chapter are presented for the highest order computed and the NLCE data are cutoff at temperatures where the three highest consecutive orders deviate more than 2%.

7.2.2.4 Low-order high-temperature series expansions (HTSE)

It is useful to compare computed observables against simple analytic zeroth- and second-order high temperature series in t/T [155]. The region of validity of the HTSE to any order is $T \gtrsim t$, yielding unphysical results for $T \lesssim t$.

7.3 Results

This section presents our main results, the calculation of several thermodynamic observables and analysis of features observed in them, especially their striking universal N-dependence. Specifically, we calculate the number of on-site pairs $\mathcal{D}$, the kinetic energy K, the energy E, the entropy S, the specific heat C and the contributions to it from the interaction and kinetic energies $Ud\mathcal{D}/dT$, and dK/dT, respectively, all defined previously. Mostly we focus results at a density $\langle n \rangle = 1$, but some results are also presented as a function of chemical potential μ/t which causes the density to vary.

This section is organized as follows: Section 7.3.1 presents the μ/t-dependence of $\langle n \rangle$, $\mathcal{D}$, the compressibility $\kappa = \partial \langle n \rangle / \partial \mu$, and the determinantal sign. The following subsections present the U/t, T/t, and N dependence of $\mathcal{D}$ (Section 7.3.2), K (Section 7.3.3), and E (Section 7.3.4). Section 7.3.5 presents the scaling collapse demonstrating the universal N-dependence of E, $\mathcal{D}$, and K. Section 7.3.6 presents the temperature derivatives. Finally Section 7.3.7 presents the U/t, T/t, and N dependence of S. Results in Sections 7.3.2 to 7.3.7 are all at unit density.

7.3.1 Density, number of on-site pairs, compressibility, and determinantal sign dependence on chemical potential μ/t

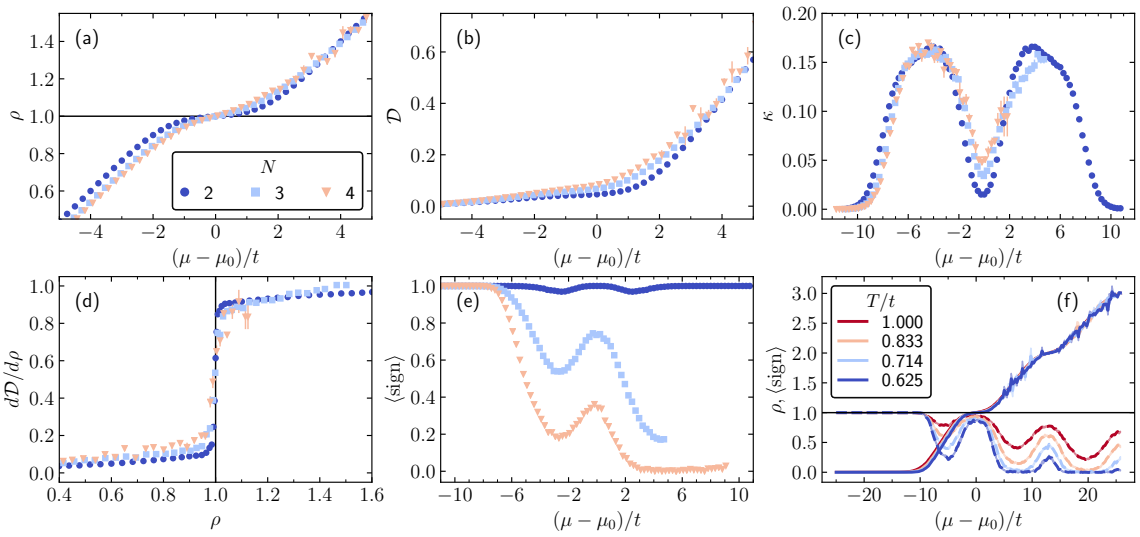

Figure 7.1 : **Density's, number of on-site pairs', compressibility's, and determinantal sign's dependence on chemical potential**. Panels (a-e) compare observables for $N = 2, 3, 4$ for $U/t = 8$ at $T/t = 0.5$ as functions of the chemical potential $(\mu - \mu_0)/t$, where $\rho(\mu_0) = 1$. (a) Density; there is a clear softening of the Mott plateau as N increases. (b) Number of on-site pairs. (c) Compressibility. (d) Derivative of the number of on-site pairs with respect to the density as a function of density. (e) Average sign. (f) Density (solid) and average sign (dashed) vs $(\mu - \mu_0)/t$ for different values of T/t for $N = 6$ at $U/t = 12$. Shaded regions correspond to error bars.

Figs. 7.1(a-b) show the dependence of density $\rho = \langle n \rangle$ and number of on-site pairs $\mathcal{D}$ on the chemical potential. These are particularly important quantities because typical experiments on ultracold atoms use smooth traps, and the μ-dependence of the observables is related to their spatial dependence by the local density approximation [11]. These are also among the most straightforward observables to measure, and have been explored experimentally as a function of U/t, N, μ/t, and T/t in Refs. [71, 141].

The density as a function of chemical potential shows a Mott plateau – a region of μ over which the density is nearly constant – when the temperature is $T \lesssim U$, as shown in Fig. 7.1(a), signaling the incompressible and insulating nature of the system.

At fixed temperature, the Mott region becomes less sharply defined as N increases. This is expected, as increasing N allows for more density fluctuations at a given energy and thus a more compressible system at a fixed temperature [as corroborated by Fig. 7.1(c)]. This behavior is also observed for $U/t = 12$ at the same temperature (not shown here as to not overcrowd Fig. 7.1). The general trend is already seen in the second order HTSE [155] and was observed experimentally in Ref. [141].

Although the Mott plateau softens with increasing N, appearing only as a subtle shoulder for $N = 4$ at $U/t = 8$ and $T/t = 0.5$, if one plots $d\mathcal{D}/d\rho$ as a function of ρ, there is a quite sharp and clear signature of the Mott plateau for all cases, as shown in Fig. 7.1(d).

We also show the average determinantal sign, which characterizes the sign problem, one of the fundamental limitations to quantum Monte Carlo calculations of interacting fermions [55, 267, 268]. For the type of Hubbard-Stratonovich decomposition used in the current study for DQMC, we find the average sign decreases (i.e. the sign problem worsens) overall as N increases and as the temperature is lowered [see Figs. 7.1(e-f)]. On top of this, the sign problem is worse for the metallic phase than the Mott insulating phase at a fixed temperature. Figures 7.2(a) and 7.3(a) show that at fixed T/t, increasing U/t worsens the sign problem in the metal, but improves it in the insulator in the currently studied temperature regime. The $N = 2$ case is free of the sign problem at half-filling, and therefore $\langle \text{sign} \rangle = 1$ when $\langle n \rangle = 1$ for all values of U/t.

Finally, the U/t dependence of κ for different N is displayed in Figs. 7.2(b) and 7.3(b). As the U/t increases, the system becomes more incompressible where $\langle n \rangle = 1$, highlighting the insulating nature of the system. Our results are in agreement with qualitative trends identified in previous dynamical mean-field theory (DMFT) results [269].

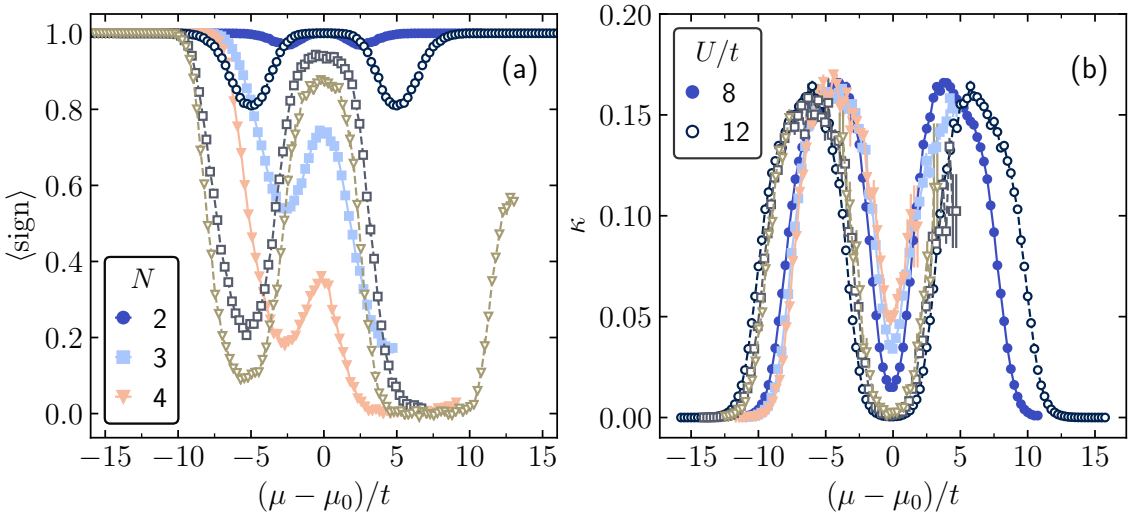

Figure 7.2 : **Determinantal signs' and compressibility's dependence on interaction strength I**. (a) Average sign (b) Compressibility vs $(\mu - \mu_0)/t$, where $\rho(\mu_0) = 1$ for $U/t = 8$ (full markers) and $U/t = 12$ (open markers) for $N = 2, 3, 4$ at $T/t = 0.5$.

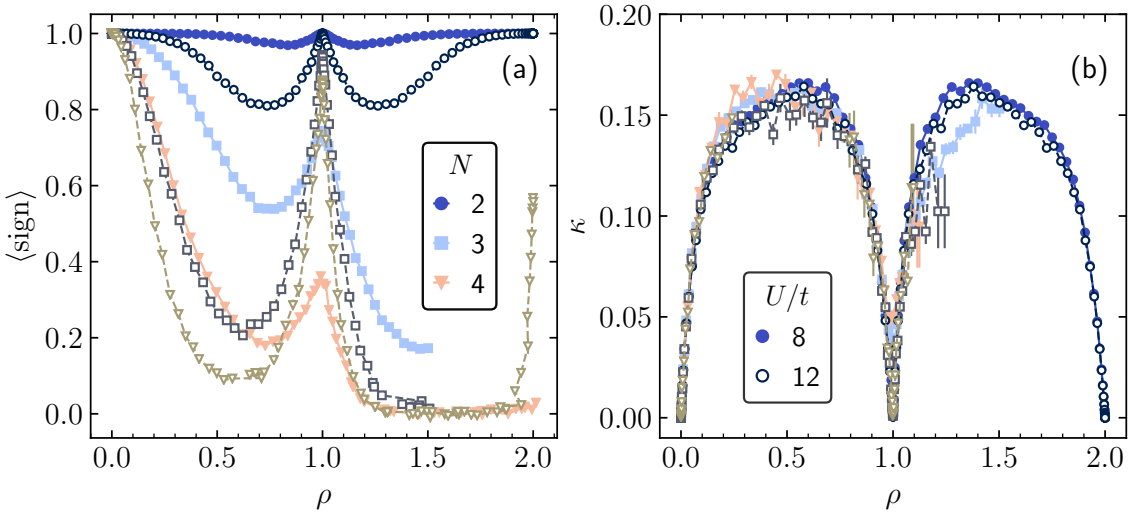

Figure 7.3 : **Determinantal signs' and compressibility's dependence on interaction strength II**. (a) Average sign (b) Compressibility vs ρ, for $U/t = 8$ (full markers) and $U/t = 12$ (open markers) for $N = 2, 3, 4$ at $T/t = 0.5$.

7.3.2 Number of on-site pairs at unit density: dependence on U/t, T/t, and N

The number of on-site pairs $\mathcal{D}$ decreases as temperature is lowered, almost always followed by an increase at the lowest temperatures. These features show clear trends with U/t and N as shown in 7.4. The trends with U/t are that, as the temperature is lowered, (1) $\mathcal{D}$ is suppressed from its high-temperature value at a temperature scale $T \sim U$, and (2) $\mathcal{D}$ increases at a much lower temperature that decreases with increasing U/t. Also, as expected, overall larger U/t leads to smaller $\mathcal{D}$, most strongly in the temperature window between the two features discussed previously. The trends with N are also clear: (1) as N increases, $\mathcal{D}$ increases, (2) the temperature at which the low-T increase of $\mathcal{D}$ occurs is roughly independent from N except for $U/t = 8$, where is higher for larger N, and (3) the increase of $\mathcal{D}$ as the temperature is decreased through the lower temperature feature is larger for larger N. For sufficiently large U/t, the dependence on N is weaker, as shown in Fig. 7.4(a). These features will be explained below.

Although the temperatures are not extremely low, $T \gtrsim 0.1t$, the qualitative features are not captured with a low-order HTSE, as shown in Fig. 7.4(a), which diverges from the true results at $T/t \sim 3$ or larger. Furthermore, for the temperature regions where NLCE and DQMC are well converged, both methods are in good agreement, supporting the validity and convergence of the different approaches.

The T, N, and U dependence of $\mathcal{D}$ can be qualitatively understood by considering the two-site, two-particle (TSTP) system, which was employed to understand similar features in the $N = 2$ anisotropic lattice calculations of Ref. [43]. We begin by describing the T dependence. For $T \gtrsim U$, eigenstates with energy $\sim U$ and a large fraction of double occupancies are occupied. As the temperature is lowered below U, the eigenstates dominated by one-particle-per-site configurations have the largest Boltzmann weight and have small admixture of doublons, thus explaining the

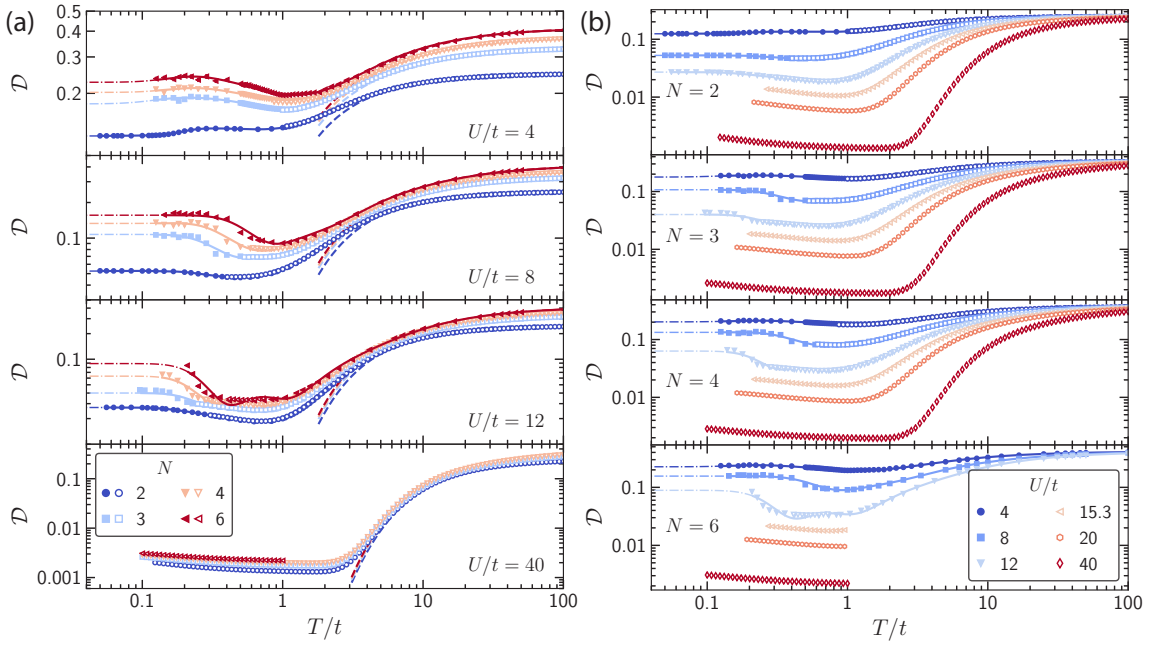

Figure 7.4 : **Number of on-site pairs $\mathcal{D}$ versus temperature**.(a) Each panel compares $\mathcal{D}$ for $N = 2, 3, 4, 6$ for a fixed U/t at $\langle n \rangle = 1$. (b) Each panel compares $\mathcal{D}$ for $U/t = 4, 8, 12, 15.3, 20, 40$ for a fixed N. Solid markers are DQMC, open markers are NLCE, dashed lines are the zeroth order HTSE, and solid lines are fits of Eq. (7.5) to the DQMC data down to the lowest T_n point. Thinner dash-dotted lines come from the fit in the extrapolated regime $T < \min(T_n)$, where $\{T_n\}$ is the data set of temperatures where DQMC results are obtained.

high-temperature decrease of $\mathcal{D}$ upon cooling. The more interesting low-temperature increase of $\mathcal{D}$ is explained by considering the physics in this sector dominated by one-particle-per-site configurations. In this sector, these low-energy eigenstates are approximately "SU(2) singlets" on the two sites [$\propto (|\sigma, \tau\rangle - |\tau, \sigma\rangle)$ with $\sigma \neq \tau$] or "SU(2) triplets" [$\propto (|\sigma, \tau\rangle + |\tau, \sigma\rangle)$ where τ and σ may be equal]. The "singlet" states include an admixture $\propto (t/U)^2$ of doublons, which allows for some delocalization, lowering the kinetic energy and therefore lowering the energy of singlet states relative to the triplet ones, which have no admixture of doublons. Therefore, as the temperature is lowered below the energy scale splitting the singlet and triplet configurations, the system populates the singlet states and the number of double occupancies increases until it saturates. This low-temperature population of SU(2) singlets also leads to

the antiferromagnetic correlations observed in Ref. [41].

The dependence of $\mathcal{D}$ on N can also be understood in this picture, by considering the number of available ways to form double occupancies. Since the number of possible configurations of m particles on a single site is $\binom{N}{m}$, the number of on-site pairs is enhanced for $N > 2$ for all values of the interaction strength and temperature due to thermal fluctuations and quantum fluctuations (tunneling) **.

This argument provides an understanding of the overall trends of $\mathcal{D}$ with T and N, but the $U = 4t$, $N = 2$ curve is worth further consideration as the sole curve that does not show the low-temperature increase. The reason for this is not obvious: that a low-temperature rise would be smaller for small N is explained above, but that it actually turns from a rise to a decrease is not. We note that this is likely a special feature of not only $N = 2$ and small U/t, but also 2D systems, as when the system is perturbed away from 2D a low-temperature rise in $\mathcal{D}$ appears [43]. As such, it is natural to conjecture it is related to Fermi surface nesting (see Fig. 7.5), which is most important at small U/t, and which is perfect only for $N = 2$.

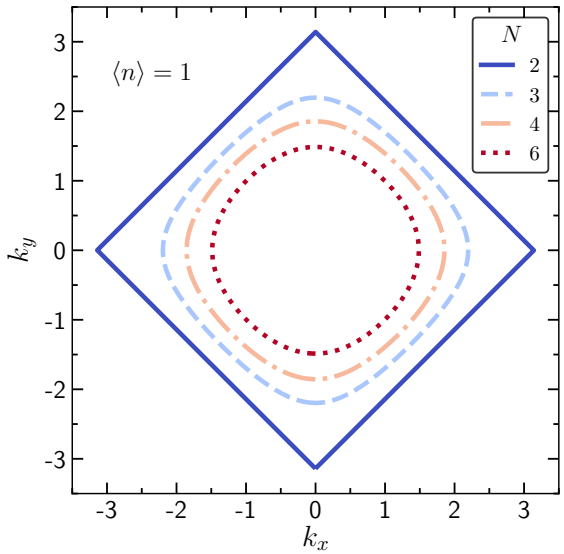

Figure 7.5 : **Fermi surface for $N = 2, 3, 4, 6$ in the 2D square lattice at $\langle n \rangle = 1$.**

**In the $T \to \infty$ limit, at $\langle n \rangle = 1$, the number of on-site pairs is given by $\mathcal{D}_\infty = \frac{1}{2} \sum_{\sigma \neq \tau} \langle n_\sigma \rangle \langle n_\tau \rangle = \binom{N}{2} \frac{1}{N^2} = \frac{1}{2}\left(1 - \frac{1}{N}\right)$, where we used that $\langle n_\sigma \rangle = \langle n \rangle / N$ because of the SU(N) symmetry.

7.3.3 Kinetic energy at unit density: dependence on U/t, T/t, and N

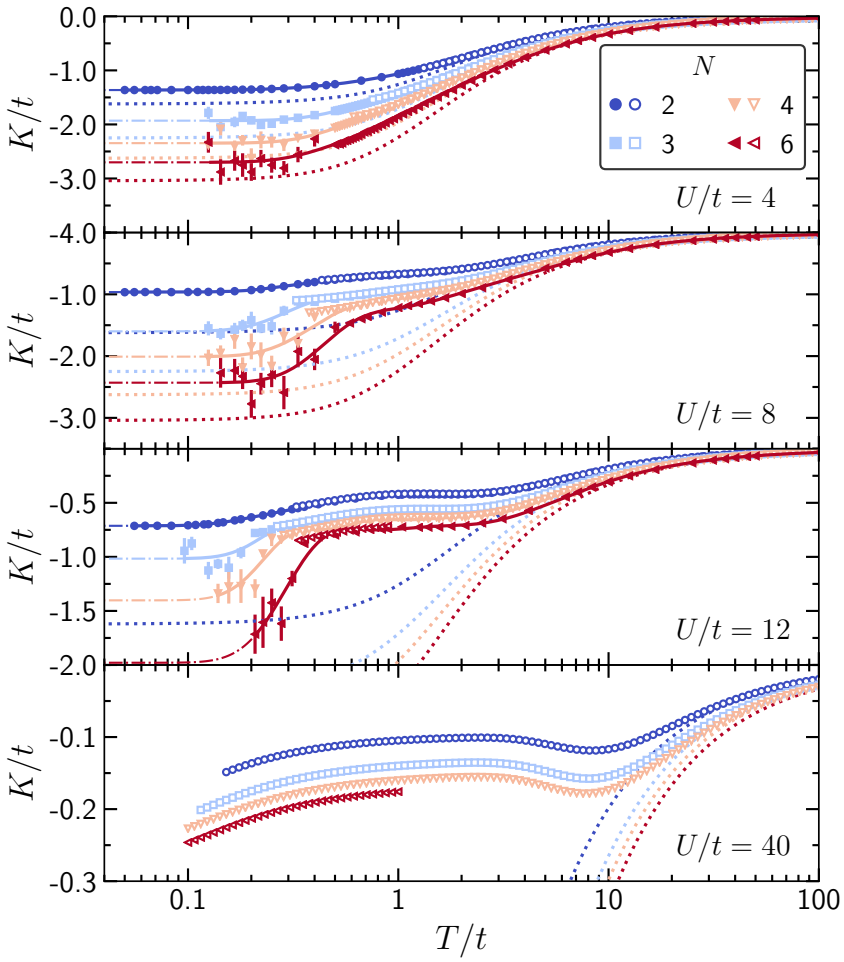

Figure 7.6 : **Kinetic energy vs temperature**. Each panel compares K for $N = 2, 3, 4, 6$ for a fixed U/t at $\langle n \rangle = 1$. Solid markers are DQMC, open markers are NLCE, dotted lines correspond to the non-interacting limit, and solid lines are fits of Eq. (7.5) to the DQMC data down to the lowest T_n point. Thinner dash-dotted lines come from the fit in the extrapolated regime $T < \min(T_n)$, where $\{T_n\}$ is the data set of temperatures where DQMC results are obtained.

The kinetic energy K shows features at similar energy scales as $\mathcal{D}$, as shown in Fig. 7.6. At high temperatures, the kinetic energy vanishes, and decreases as the temperature is lowered, in close agreement with the non-interacting calculations (described momentarily) until $T \sim U$. At $T \lesssim U$ the kinetic energy becomes smaller in magnitude than the non-interacting limit by an amount that increases with U.

Finally, at the lower temperature scale on which $\mathcal{D}$ rises again, the kinetic energy drops significantly, signaling the same tunneling processes that create doublons, explained at the end of Sec. 7.3.2.

The non-interacting limit's behavior is straightforward to understand: for $N = 2$ and $\langle n \rangle = 1$, the Fermi surface is a perfect square (Fig. 7.5), and as N is increased this shrinks and becomes circular. Thus the kinetic energy decreases as N increases. Fig. 7.6 shows the non-interacting limit results (dotted lined)

$$K = \frac{1}{(2\pi)^2} \int_{\mathrm{BZ}} \frac{\epsilon_{\vec{k}} d^2k}{e^{\beta(\epsilon_{\vec{k}} - \mu)} + 1}, \tag{7.9}$$

where the integral is over the Brillouin zone and $\epsilon_{\vec{k}} = -2t(\cos k_x + \cos k_y)$ is the non-interacting dispersion (setting the lattice constant to unity). The chemical potential μ is determined numerically to give $\langle n \rangle = 1/(2\pi)^2 \int_{\mathrm{BZ}} d^2k/(e^{\beta(\epsilon_{\vec{k}} - \mu)} + 1) = 1$.

7.3.4 Total energy at unit density: dependence on U/t, T/t, and N

The total energy $E = U\mathcal{D} + K$ (Fig. 7.7) shows features simply related to D and K. However, a new and surprising feature appears in E: the curves for different N cross at a temperature and energy (T^*, E^*) with $t < T^* < U$. Fig. 7.8 shows that T^* first decreases then increases as a function of U/t, while E^* first increases, then decreases. In Section 7.3.5, we will see that this crossing is a consequence of an even more dramatic phenomena — a universal collapse upon rescaling over a broad temperature range.

The existence and qualitative trends of the crossing can be understood again by the system with two sites and two particles (TSTP), and can be quite accurately described by the second order NLCE, whose only inputs are the one- and two-site exact diagonalization calculations (a point we will revisit in Sec. 7.3.5).

Within the TSTP, the crossing occurs when $E^* = 0$, indicating that for all N's,

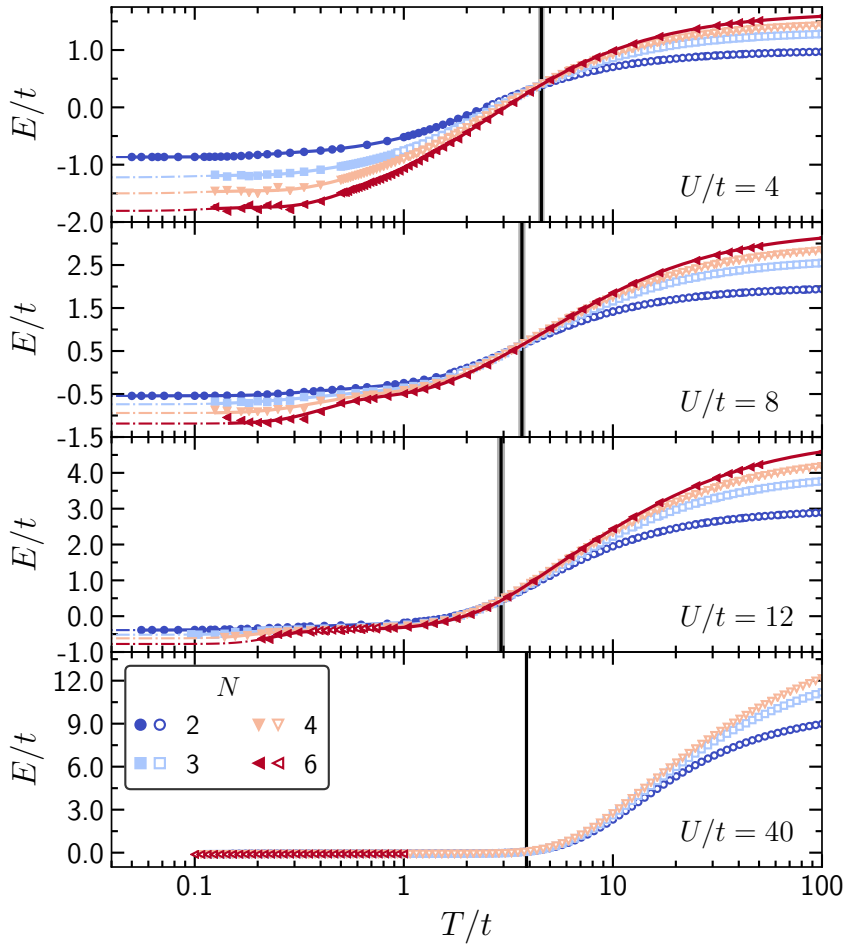

Figure 7.7 : **Energy vs temperature**. Each panel compares E for $N = 2, 3, 4, 6$ for a fixed U/t at $\langle n \rangle = 1$. Solid markers are DQMC, open markers are NLCE, solid lines are fits of Eq. (7.5) to the DQMC data down to the lowest T_n point. Thinner dash-dotted lines come from the fit in the extrapolated regime $T < \min(T_n)$, where $\{T_n\}$ is the data set of temperatures where DQMC results are obtained. Vertical regions in black indicate the temperature window where the different N curves intersect.

their kinetic and interaction energies cancel each other at the same T^* (see Appendix 7.4.3 for details). When we include higher particle numbers in the two-site problem, there is a small contribution to the energy from eigenstates that present multiple double occupancies and/or higher-than-double occupancies. Their contribution accounts for a constant positive shift in the energy for all N's, implying that the crossing occurs at $E^* > 0$. The second order NLCE is a linear combination of the one-site and two-site results. The one-site result contributes another constant positive shift for all N's to E. Together, the second order NLCE clearly reproduces the trends displayed in Fig. 7.8, where we present E^* and T^* as a function of the interaction strength.

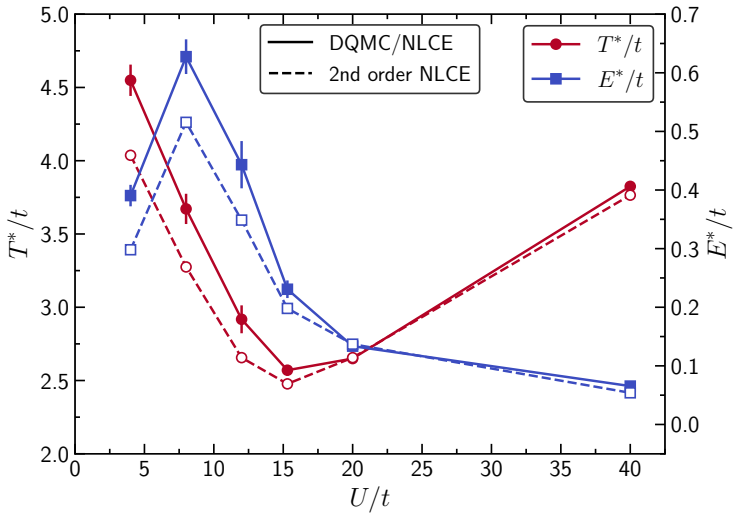

Figure 7.8 : **Interaction dependence of the energy crossing**. Temperature (red circles) and energy (blue squares) where the curves for different N cross in Fig. 7.7. Error bars correspond to the width of the crossings. Dashed lines correspond to the second order NLCE.

7.3.5 Universal N-dependence of energy, number of on-site pairs, and kinetic energy

In this section, we show that the crossing point of E vs T for all N in Fig. 7.7 is actually a consequence of a much stronger universal scaling relation that determines the N-dependence of all the observables studied here to temperatures well below the

crossing temperature (though not arbitrarily low), down to a temperature comparable to the superexchange energy $4t^2/U$. We find that the energy satisfies

$$E(T, N) = E(T, \infty) + (1/N)E_1(T) \tag{7.10}$$

for some $E_1(T)$ independent of N over a broad range of temperature. This is shown in Fig. 7.9 by a universal collapse of appropriately constructed quantity $\tilde{E}$, and we will discuss the features of this collapse more momentarily. First, to understand $\tilde{E}$'s construction, note that Eq. (7.10) is equivalent to

$$\tilde{E}(T, N) \equiv E(T, N) - (1/N)E_1(T) \tag{7.11}$$

being independent of N, since the right hand side is simply $E(T, \infty)$. Fig. 7.9 plots this $\tilde{E}$, taking

$$E_1(T) = \frac{E(T, N_1) - E(T, N_2)}{(1/N_1) - (1/N_2)} \tag{7.12}$$

for $N_1 = 2$ and $N_2 = 3$. When Eq. (7.10) is satisfied, the $E_1(T)$ obtained would be the same for all choices of N_1 and N_2; we choose $N_1 = 2$ and $N_2 = 3$ as they are the least noisy datasets and span the largest range of temperatures, but the overall collapse is observed independent of this choice. The analysis of scaling is inspired by similar scalings discovered in the spectra of strongly correlated materials in Ref. [270]. We observe that Eq. (7.10) has the form of a first order Taylor expansion of $E(T, N)$ in $1/N$; from this point of view, the remarkable aspect of the data collapse is that (in an appropriate temperature window) it accurately describes the physics even when $1/N$ is not small (e.g. for $N = 2$).

Figure 7.9 shows that $\tilde{E}$ is independent of N at temperatures $T \gtrsim J \equiv 4t^2/U$ for all U studied here, and therefore $E(T, N)$ has the simple N-dependence given by Eq. (7.10). Below $T \sim J$, $\tilde{E}$ no longer collapses, signaling a more complicated

N-dependence. One consequence of the universal scaling is that the thermodynamics in this temperature regime can be obtained for any N from the results for $N = 2$ and 3 (or any two N). This is convenient for several reasons: The Hilbert space of SU(2) is more manageable for numerical calculations, and because numerical methods such as DQMC are free of the sign problem at $\langle n \rangle = 1$ for SU(2).

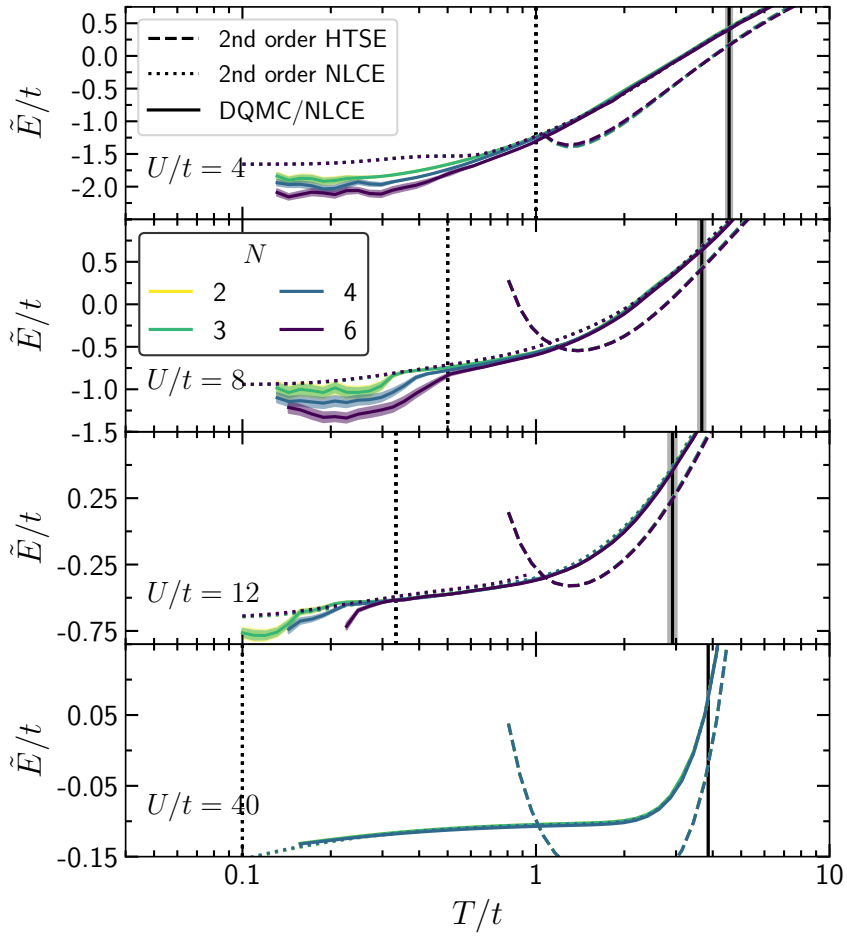

Figure 7.9 : **Universal dependence of energy on** N. $\tilde{E}$ vs temperature for several N at fixed $U/t = 4, 8, 12$ at $\langle n \rangle = 1$. Solid lines correspond to numerical data: DQMC for $U/t = 4, 8, 12$ and NLCE for $U/t = 40$. Shaded regions correspond to error bars obtained by error propagation in Eq. (7.11). Dashed lines correspond to second-order HTSE calculations and dotted lines correspond to second-order NLCE. Solid vertical lines indicate the temperature where the different N curves intersect, and dotted vertical lines indicate the superexchange energy J.

One natural attempt to explain the observed scaling would be the HTSE, since this is expected to be accurate at high temperatures; however, although $\tilde{E}$ calculated

with the second-order HTSE collapses, it deviates strongly from the data at $T \lesssim 5t$ [Fig. 7.9], so it cannot explain the collapse to the lowest temperatures observed ($0.1t$ to t, depending on the value of U). In contrast, as Fig. 7.9 shows, the second-order NLCE's $\tilde{E}$ not only collapses, but accurately reproduces the numerical results for all temperatures where the collapse occurs, thus providing a simple and effectively complete calculational tool to obtain the scaling, albeit not an analytic one. That the second-order NLCE reproduces the data in the scaling regime allows us to infer characteristics of the physics. The first thing to notice is that the second-order NLCE can capture one- and two-site nearest-neighbor correlations, but no longer-ranged correlations. Thus, one-site physics and nearest-neighbor correlations suffice to capture the physics in the regime where collapse occurs. This provides interesting insight into the physics, and explains why the collapse occurs at $T \gtrsim J$: this is the characteristic energy scale for correlations in the $\langle n \rangle = 1$ system (at least when U/t is large) and thus longer range correlations only develop at temperatures below J. Note that this also lets us understand why the collapse is not captured by the second-order HTSE: this misses two-site correlations that are $\mathcal{O}(\beta t)^3$ or higher. Such non-perturbative effects are strong in the regime $4t^2/U \lesssim T \lesssim t$ and not easily captured at any order of the HTSE, which diverges for $T \lesssim t$.

By examining the second order NLCE and simplifying it by taking advantage of the range of temperatures being considered, we can also arrive at an analytic explanation of the scaling phenomena. Although NLCE is typically used as a numerical method, at low-enough order and in simplified limits, it may provide simple analytic expressions. Indeed, in the present case, we show in Appendix 7.4.4 that the energy in the second-order NLCE in the temperature range $4t^2/U \ll T \ll U$ is given, to zeroth order in βJ, by

$$E(T, U, N) \approx -J + \frac{1}{N} J. \tag{7.13}$$

We note the additional condition that $T \ll U$ not previously noted; indeed, there

are small deviations of the data from collapsing in the $T \sim U$ regime. Finally, when $T \gg U$ the collapse is again recovered, since $K \to 0$ and $D \propto 1/N$ in that regime. In summary, the parametrically accurate collapse for the two separate regimes $4t^2/U \ll T \ll U$ and $T \gg U$ is interpolated to a quite accurate collapse, though not parametrically so, for all $T \gg 4t^2/U$, as seen in the data.

Although we only analytically show the scaling of Eq. (7.10) to leading order in J/T and T/U (i.e., deep in the $J \ll T \ll U$ regime), numerics seems to indicate the collapse holds beyond this. Explaining this is an open problem. Despite lacking a simple analytic formula, the second order NLCE reproduces all of the behavior, offering a simple predictive theory for the thermodynamics in the $T \gtrsim J$ regime.

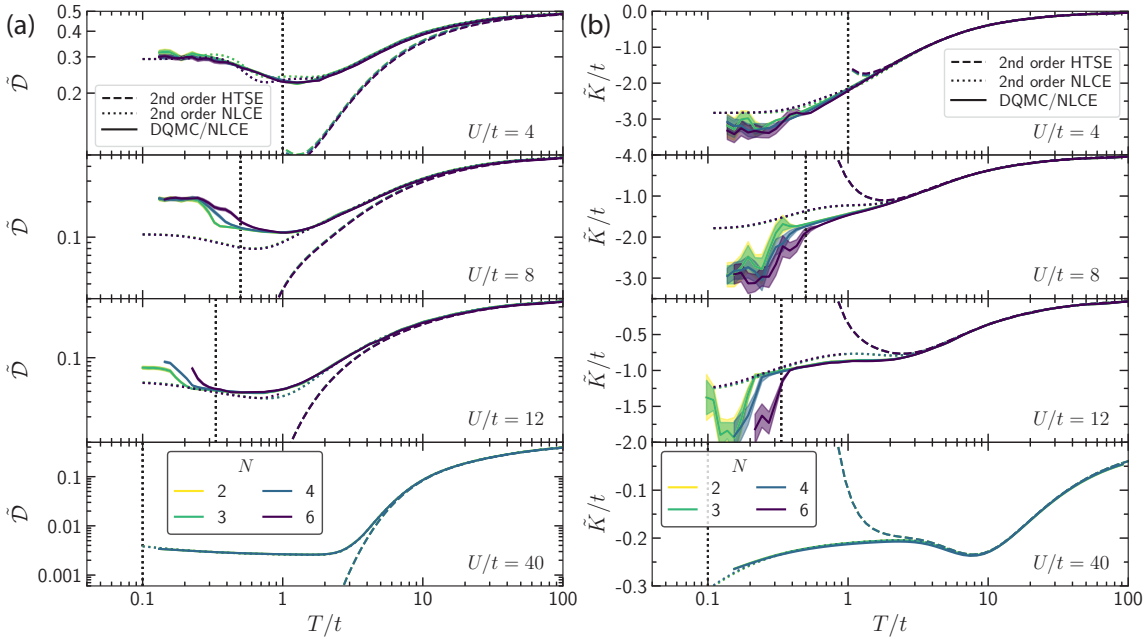

Figure 7.10 : **Universal dependence of number of on-site pairs and kinetic energy on** N. (a) $\tilde{\mathcal{D}}$ (b) $\tilde{K}$ vs temperature for several N at fixed $U/t = 4, 8, 12$ at $\langle n \rangle = 1$. Solid lines correspond to numerical data: DQMC for $U/t = 4, 8, 12$ and NLCE for $U/t = 40$. Shaded regions correspond to error bars obtained by error propagation in analogs of Eq. (7.11). Dashed lines correspond to second-order HTSE calculations and dotted lines correspond to second-order NLCE. Dotted vertical lines indicate the superexchange energy J.

The observables $\mathcal{D}$ and K show a similar universal N-dependence, satisfying analogs of Eq. (7.10), as demonstrated in Fig. 7.10(a-b) by showing the collapse of $\tilde{\mathcal{D}}$ and $\tilde{K}$ defined analogously to $\tilde{E}$. These are also reproduced by the second order NLCE and its analytic simplifications in the temperature window of interest. The $U/t = 4$ results exhibit a window around $T = t$ where the second-order NLCE weakly breaks the collapse ($< 4\%$), but is then recovered at lower temperatures around $T/t = 0.2$, where the DQMC data collapse too. Why the $U/t = 4$ results collapse even for $T \lesssim 4t^2/U$ remains an open question and merits further exploration.

7.3.6 Temperature derivatives at unit density: $C = dE/dT$, UdD/dT, and dK/dT

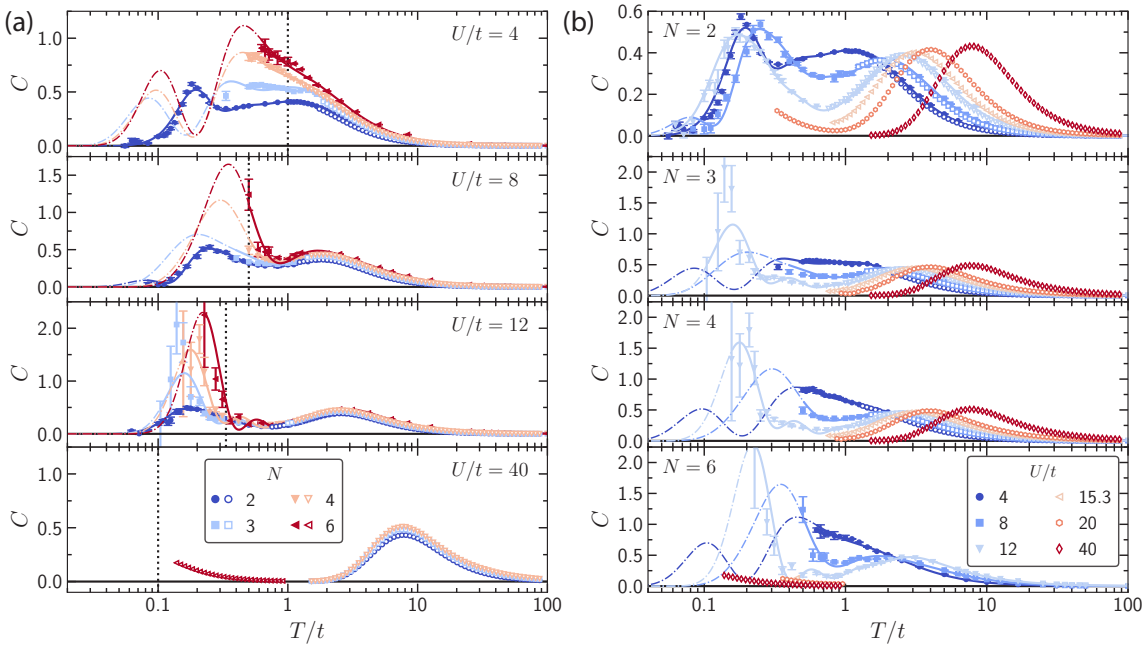

Figure 7.11 : **Specific heat versus temperature**. (a) Each panel compares C for $N = 2, 3, 4, 6$ for a fixed U/t. (b) Each panel compares C for $U/t = 4, 8, 12, 15.3, 20, 40$ for a fixed N. Solid markers are DQMC, open markers are NLCE, dotted lines correspond to the non-interacting limit, dashed lines are the zeroth-order HTSE, and solid lines come from the fit (7.5) to the DQMC data in Fig. 7.7 down to the lowest T_n point. Thinner dash-dotted lines come from the fit in the extrapolated regime $T < \min(T_n)$, where $\{T_n\}$ is the data set of temperatures where DQMC results are obtained. Dotted vertical lines indicate the superexchange energy J.

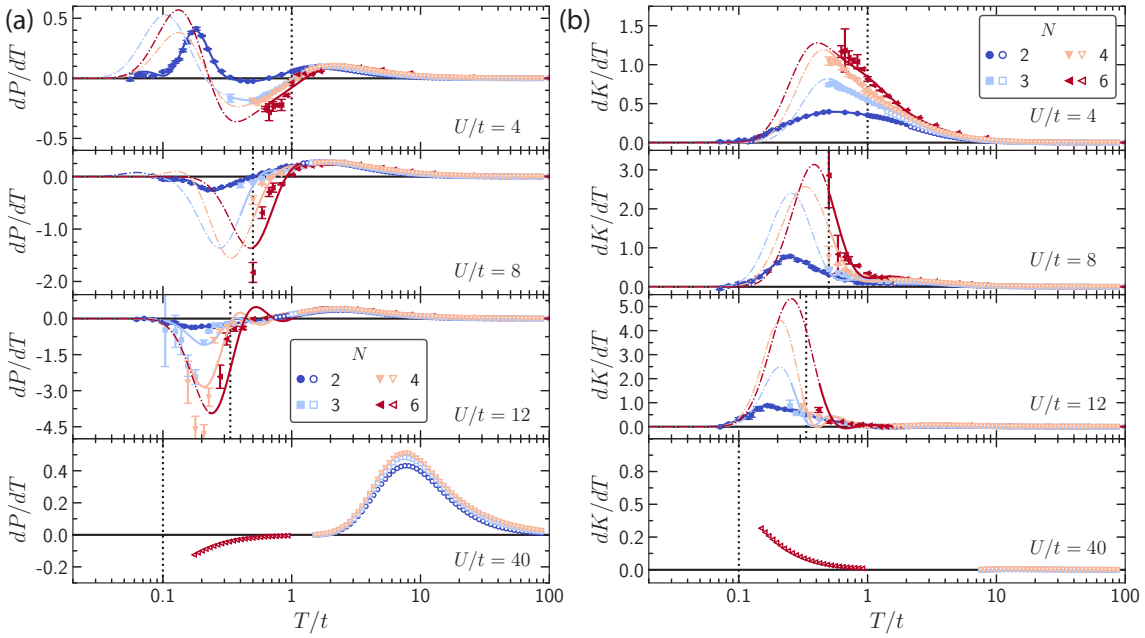

Figure 7.12 : **Contributions to the specific heat vs temperature**. Each panel compares (a) dP/dT (b) dK/dT for $N = 2, 3, 4, 6$ for a fixed U/t. Solid markers are DQMC, open markers are NLCE, and solid lines come from the fit (7.5) to the DQMC data in Figs. 7.4(a) and 7.6 down to the lowest T_n point. Thinner dash-dotted lines come from the fit in the extrapolated regime $T < \min(T_n)$, where $\{T_n\}$ is the data set of temperatures where DQMC results are obtained. Dotted vertical lines indicate the superexchange energy J. Dotted vertical lines indicate the superexchange energy J.

We now present the derivatives of the energy E, interaction energy $P = U\mathcal{D}$, and the kinetic energy K. The specific heat (dE/dT) as a function of temperature is a valuable thermodynamic observable since its peaks indicate temperatures below which the entropy is significantly reduced as degrees of freedom reorganize and cease to fluctuate.

The specific heat as a function of temperature [see Fig. 7.11(a)] presents a two-peak structure for $N = 2$; for other N a high-temperature peak is present in all cases, and in most an upturn occurs at lower temperatures, necessitating a second peak at lower temperatures beyond the range of our calculations since $C \to 0$ as $T \to 0$. At least at large U/t, the origin of the high-temperature peak is associated with freezing of the charge fluctuations as the temperature is lowered, while the low-temperature peak is

associated with the onset of spin correlations, as has been shown for $N = 2$ [43, 222] and will be evident from our results on $d\mathcal{P}/dT$ and dK/dT. For strong interactions, the high-temperature peak is closely in agreement with the results of the zeroth-order HTSE and is roughly independent of N, with just small changes of amplitude at small U/t. The upturn of C as T/t is lowered towards a presumable low-temperature peak (though not directly accessible in the data for $N \geq 3$) depends on N and U/t. The upturn seems to grow with N, and it generally decreases with U/t, although at the lowest temperatures, there may be a complicated non-monotonic dependence. The extent to which the trends of the upturn are either a reflection of the temperature at which the low-T peak occurs or result from changes in the amplitude of the low-T peak cannot be assessed with the current data, and is an interesting question for future theory and experiment.

The final feature of the specific heat that we analyze is motivated by the finding in Ref. [222] that the specific heat versus temperature curves cross around $T/t \approx 1.6$ for all $U/t \in [1, 10]$ for $N = 2$. Fig. 7.11(b) shows that this remains true for other values of N, with nearly the same value of the crossing temperature. However, we note that this crossing only occurs for $U/t \lesssim 10$, and fails for $U = 15.3t$ and larger. The physical significance of this crossing is unclear. Several Refs. [222, 271–275] have seen this crossing in two dimensions (in square, honeycomb, and asymmetric $[t_\uparrow \neq t_\downarrow]$ Hubbard models) at $(C^*, T^*) \approx (0.34, 1.6t)$ but all are at relatively small U/t. For small U/t Ref. [272] shows that the presence of such high-T crossing arises if one approximates two parameters as small: $1/d$ (where d is the dimension) and the integral over the deviation of the density of states from a constant value [270].

Examining the contributions dP/dT and dK/dT to the specific heat helps disentangle the contributions to the specific heat of the charge and spin degrees of freedom. In Fig. 7.12(a) the dP/dT data for $U/t \geq 8$ exhibit a high-T charge peak and a negative dip at lower T/t for all N. For such interactions, the high-T peak in the specific

heat comes from dP/dT. For $U/t = 4$ and $N = 2$ there is a low-T peak in dP/dT, which gives rise to the low-T peak in the specific heat. For $U/t = 4$ and $N > 2$, the fits suggest the existence of a dip and then a peak as temperature is lowered; however drawing firm conclusions here requires further studies.

In Fig. 7.12(b), the dK/dT data for all values of the ineraction strength are positive and exhibit a low-T peak, or a low-T upturn which implies the existence of a peak since $dK/dT \to 0$ as $T \to 0$. The magnitude of the upturn or peak increases with N. For $U/t \geq 8$ the low-T peak (or upturn) in the specific heat arises from the spin degree of freedom, seen in dK/dT [Fig. 7.12(b)]. Together dP/dT and dK/dT give Fig. 7.11(a). These results complement the ones presented in Refs. [43, 222], which demonstrate that for $N = 2$, at small U/t the low-T peak arises from dP/dT as opposed to dK/dT in the large U/t limit. The results presented here imply the same conclusion for all N studied in this work: at large U/t the low-T peak arises from dK/dT and the high-T peak from dP/dT, while at small U/t the low-T peak comes from dP/dT and the high-T peak from dK/dT.

7.3.7 Entropy at unit density: dependence on U/t, T/t, and N

Figure 7.13(a) shows the N-dependence of the entropy per site as a function of T for each U/t studied. For all values of the interaction strength we observe that for temperatures above the superexchange energy, at fixed entropy, the system with larger N is at a lower temperature. These results are in agreement with [155, 276], highlighting that gases adiabatically loaded into an optical lattice in this regime will have a significantly lower temperature as N is increased. For $U/t = 4$ this cooling seems to occur for all values of T/t and N. However, for $U/t \geq 8$, the curves roughly collapse below $T \lesssim 4t^2/U$, at least for $N > 2$, suggesting that for 2D square lattices, the dramatic benefits in cooling to the superexchange energy scale will be less effective when cooling well below this scale. We note that this doesn't rule out the cooling

with increasing N persisting to arbitrarily low temperatures in other geometries, for example as been shown in 1D chains [127].

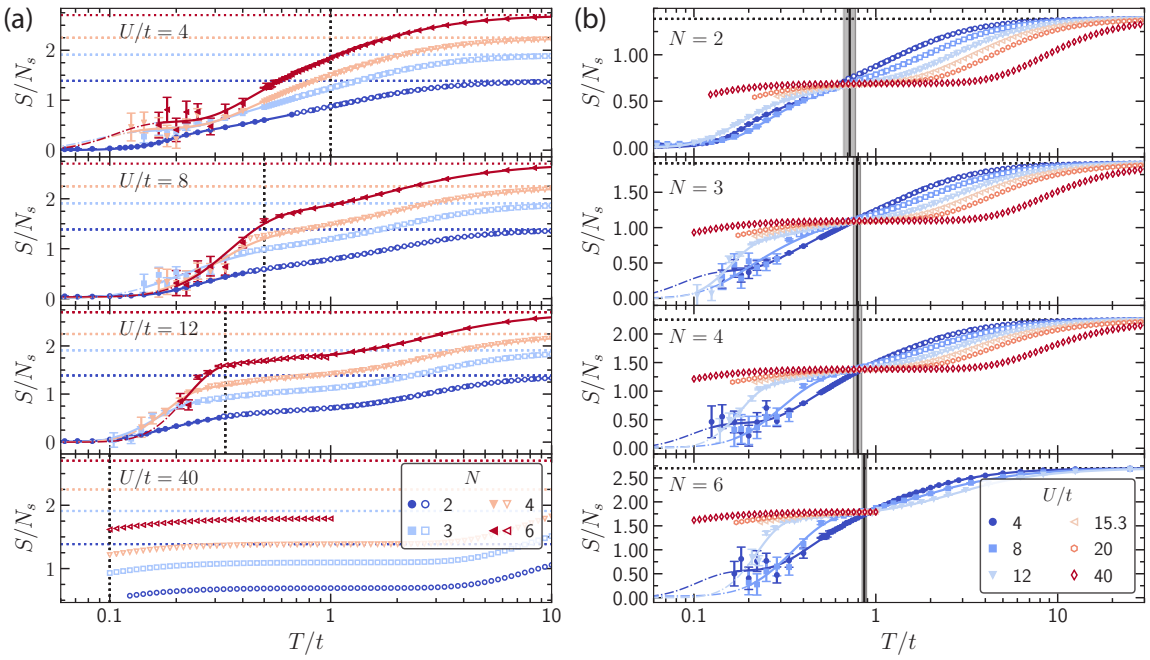

Figure 7.13 : **Entropy per site vs temperature**. (a) Each panel compares S/N_s for $N = 2, 3, 4, 6$ for a fixed U/t. (b) Each panel compares S/N_s for $U/t = 4, 8, 12, 15.3, 20, 40$ for a fixed N. Solid markers are DQMC, open markers are NLCE, and solid lines come from the fit Eq. (7.5) to the DQMC data in 7.7 down to the lowest T_n point. Thinner dash-dotted lines come from the fit in the extrapolated regime $T < \min(T_n)$, where $\{T_n\}$ is the data set of temperatures where DQMC results are obtained. Dotted vertical lines indicate the superexchange energy J and solid vertical lines indicate the temperature where the different U/t curves intersect.

Figure 7.13(b) shows the same entropy per site's U-dependence as a function of T for each N studied. For each N there is a crossing at finite temperature for all U/t. The location of this crossing occurs at higher entropy and T for larger N. The existence of a crossing in the entropy curves for different U/t for $N = 2$ follows from the presence of a crossing in the specific heat [222, 271–275], given that $C(T, U) = T[\partial S(T, U)/\partial T]$. Our results demonstrate that such behavior is still present for $N > 2$.

7.4 Conclusions

We have explored the evolution of thermodynamic observables of the SU(N) Fermi-Hubbard model as a function of temperature T, interaction strength U/t, and the number of flavors N at $\langle n \rangle = 1$. DQMC and NLCE provide accurate results over a wide range of temperatures, including temperatures roughly an order of magnitude below the tunneling t, with the exact value depending on N and U/t. Neither method is able to access arbitrarily low-temperatures, but the obtained results are far beyond what is accessible to low-order HTSE methods or ED, which have serious inaccuracies even at $T \gtrsim 5t$. The DQMC and NLCE agree where their regimes of convergence overlap, further boosting confidence in the accuracy of the numerics. Some results were also presented in Fig. 7.1 for the dependence of $\langle n \rangle$, $\mathcal{D}$, and average determinantal sign as a function of μ/t, as well as quantities derived from these.

A striking finding is the existence of a simple scaling law with N for $T \gtrsim J$ for E, $\mathcal{D}$ and K. We show that this observed scaling can be reproduced by the second-order NLCE, which takes as input only one- and two-site correlations and information about the lattice geometry, and in the appropriate regime this provides analytic expressions for the observed results. Furthermore, we show that this regime is well beyond the second-order HTSE. Although the numerics cannot provide accurate results to arbitrarily low temperature, accurate results for E, K, and $\mathcal{D}$ are attained for all N studied to temperatures where strong correlations are present. For example, the temperatures reached for all N are slightly lower than recent experiments on the 2D SU(2) FHM [21] that observed correlations that spanned the entire ($\sim$ 15-site wide) system. Short-ranged correlations in the SU(6) FHM have been observed in Ref. [41], and longer-ranged correlations will be an interesting subject for future work. For example, Ref. [138] found a unifying pattern for all N in the Heisenberg limit at high temperatures: spin correlations are organized in shells of equal Manhattan distance and for $N = 3$, they evolve from a two sublattice structure to a three

sublattice structure as temperature is lowered. The thermodynamic results provided here provide a foundation for studying such phenomena.

Furthermore, the exploration of the specific heat and its contributions provided additional information about the N dependence of the degrees of freedom that fluctuate in the temperature regime studied, and the specialness of the $N = 2$ case, possibly due to the perfect nesting. Our results show that the behavior of C, $Ud\mathcal{D}/dT$, and dK/dT are all qualitatively similar for all N, with only the location and height of peaks shifting. The high temperature peaks (at $T \propto U$) are roughly independent of N, while the low-temperature behavior shows a dependence on N. The details of the latter are difficult to resolve with current numerical capabilities, and point to interesting future numerical and experimental directions.

Finally, the results for the entropy have important implication for the observed dramatic cooling of SU(N) FHM systems as N is increased at fixed entropy [71, 127, 155, 276], which has been designated Pomeranchuk cooling. This has been important for achieving the lowest temperatures in Fermi-Hubbard models by using SU(6) gases [41]. Although this effect was shown theoretically at $T \gtrsim t$ using a HTSE [155] and experimentally [41, 71] and theoretically in 1D down to much lower temperatures [127], our results here indicate that as one reaches very low temperatures, the cooling as N increases becomes less pronounced in 2D square lattices. In particular, Fig. 7.13(a) suggests that when in the regime with T well below the superexchange energy $4t^2/U$, the temperature may be nearly independent of N at fixed entropy. However, this conclusion is reached in a regime where the noise in the numerical results is large and systematic effects may not be fully under control, so further work will be important to settle this question. Moreover, this is a lattice- and parameter-dependent phenomenon, as it is known in 1D chains that the cooling with increasing N persists to arbitrarily low temperatures [127].

7.4.1 Chemical potential and entropy at fixed density when $T \to \infty$

In order to compute the entropy using the results from DQMC at fixed density $\langle n \rangle$ using Eq. (7.4), we need to know a priori what is the entropy when $T \to \infty$. This depends on the chemical potential at $T \to \infty$, which we can analytically determine from the condition that $\langle n \rangle$ is fixed. As $T/t \to \infty$, the zeroth-order HTSE captures the behavior of $\langle n \rangle$ and it can be used with the condition $\langle n \rangle = \rho$ to determine the chemical potential. When $T \gg U$, the density is $\rho = \frac{1}{Z} \sum_n n \binom{N}{n} e^{\beta \mu n}$, defining $Z = \sum_n \binom{N}{n} e^{\beta \mu n}$. Then

$$\rho = \frac{d \log Z}{d(\beta\mu)} \tag{7.14}$$

$$= \frac{d}{d(\beta\mu)} \left[\log \left[(1 + e^{\beta\mu})^N \right] \right] \tag{7.15}$$

$$= N \frac{e^{\beta\mu}}{1 + e^{\beta\mu}}. \tag{7.16}$$

Solving for $\beta\mu$, we obtain

$$\beta\mu(N, \rho) = \ln \left(\frac{\rho}{N - \rho} \right). \tag{7.17}$$

Using this result in the zeroth-order HTSE for S gives the $T \to \infty$ entropy per site $S_\infty(N, \rho)$:

$$S_\infty(N, \rho) = \ln \left[\sum_{n=0}^{N} \binom{N}{n} \left(\frac{\rho}{N - \rho} \right)^n \right] - \rho \ln \left(\frac{\rho}{N - \rho} \right), \tag{7.18}$$

$$= N \ln \left(\frac{N}{N - \rho} \right) - \rho \ln \left(\frac{\rho}{N - \rho} \right). \tag{7.19}$$

7.4.2 Convergence of NLCE as number of sites increases, and comparison with ED

We investigate the convergence of the NLCE with expansion order, and we demonstrate that it is significantly more accurate than ED, even when the ED is performed on larger clusters (and therefore requires more computational resources) than the NLCE. We focus on two cases: $U/t = 0$ which offers an analytic solution for comparison [Fig. 7.14(a)] and $U/t = 15.3$ [Fig. 7.14(b)], both for $\langle n \rangle = 1$. Fig. 7.14(a) shows that the six-site (3×2) ED calculations for $U = 0$, whether with open-boundary or periodic boundary conditions, has noticeable deviations from the exact analytic result at temperatures $T/t \lesssim 20$. Even the very low-order two-site NLCE converges accurately to much lower temperature, $T/t \lesssim 3$. Increasing the order of the NLCE calculation leads to results that converge down to still lower temperature. Note that the NLCE calculation is self-diagnosing: even without appealing to the analytic result, the NLCE demonstrates its accuracy when adjacent NLCE orders agree with each other. For example, when the order four and order five results closely agree with each other, then they also agree with the analytic result. This is consistent with earlier findings in other models [164, 277]. It is worth mentioning that ED results may still provide valuable information: at low-T the NLCE fails dramatically, and while the ED may not be quantitatively accurate, it may still reproduce qualitative features.

Now we show similar results for $U/t = 15.3$ where no analytic result is available. The self-diagnosis of the NLCE demonstrates the convergence of two-site NLCE to $T \sim 0.4t$, and lower temperatures upon increasing the order. Again, the NLCE converges down to a much lower temperature than the ED, which shows significant deviations due to finite-size effects already at $T/t \gtrsim 2$. These results show that even numerically inexpensive NLCE calculations (two or three sites) accurately converge to much lower temperatures than the much more expensive six-site ED.

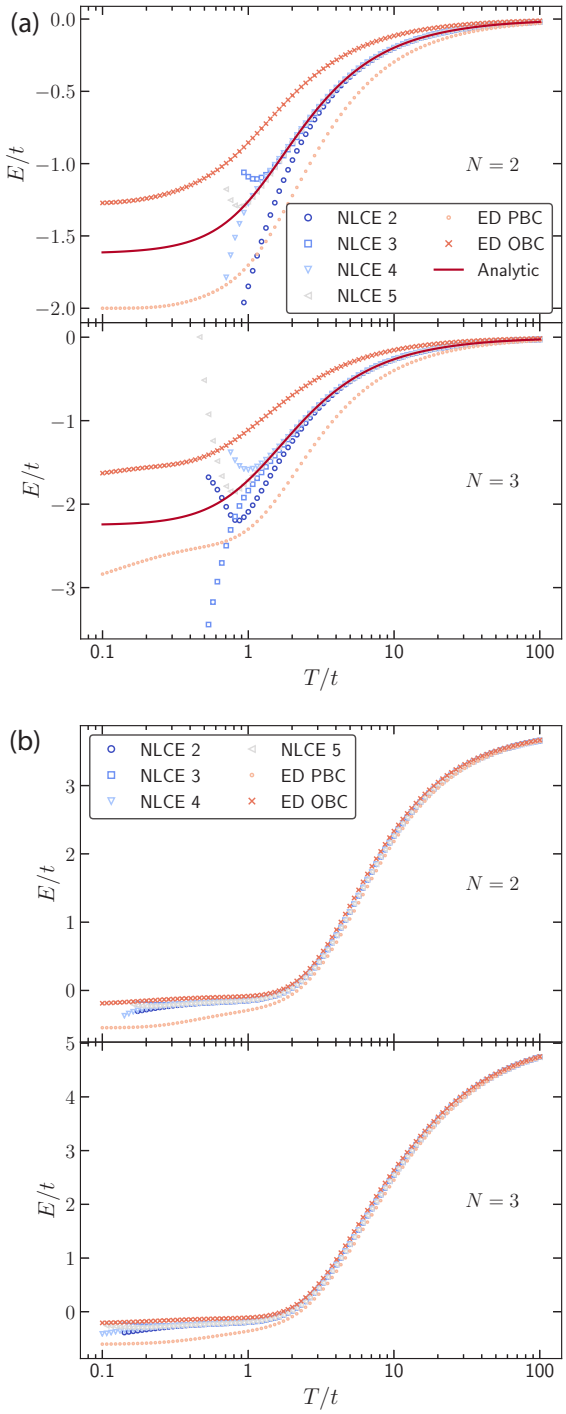

Figure 7.14 : **Convergence of NLCE with expansion order vie and comparison with ED**. Energy vs T/t at $\langle n \rangle = 1$ for (a) $U = 0$ (b) $U = 15.3t$ for SU(2) and SU(3). The ED is evaluated in a 3×2 lattice for both open and periodic boundary conditions. (a) The NLCE converges to the analytic result (the solid line) to much lower T/t than either of the ED results. (b) The NLCE curves converge to each other at much lower temperatures than the ED curves collapse on each other or on the NLCE results, signaling that the NLCE converges to significantly lower temperatures than the ED.

7.4.3 Basis truncation in the NLCE

The Hilbert space dimension for the SU(N) system imposes a severe limit on ED and NLCE if implemented naively, and this difficulty increases dramatically with N: the Hilbert space dimension is 2^{NN_s}, where N_s is the number of lattice sites, reaching a nearly intractable dimension of 2^{24} already for SU(6) at four sites. Accounting for the SU(N) symmetries ameliorates this considerably, but the basic difficulty remains.

To alleviate these problems for $N = 6$ where the difficulties are worst, we employ a basis truncation scheme for the ED used in the NLCE; this truncation was first introduced for ED in Ref. [41], and it can provide accurate results with negligible truncation error in the physical regime we consider, $\langle n \rangle \lesssim 1$, $U/t \gtrsim 1$, and T/U not too large. To understand this scheme, note that eigenstates with significant weight on flavor-number basis states with large interaction energy will be highly suppressed in the thermal average by the Boltzmann factor for that eigenstate. Thus we restrict the basis states to those with interaction energy less than or equal to pU for a constant p that we choose to obtain sufficient accuracy while remaining computationally feasible. In addition, by a similar logic, we restrict the maximum number of particles in the cluster. In this Chapter, we choose $p = 3$ and a maximum particle number of six (one more particle than the maximum number of sites used in the NLCE), and the truncation error is negligible at low-T but increases as T increases (details below).

Fig. 7.15 illustrates the accuracy of NLCE with maximum particle number restriction, and also the new numerical issues the truncation introduces, by comparing results for maximum number of particles equal to six, eight and ten and the unrestricted result for SU(3) at $U/t = 15.3$ and $\langle n \rangle = 1$. Results are plotted to temperatures a bit past where the truncations are accurate so that the effects of this restriction are visible. The feature apparent from the truncation is that as the temperature is increased, the results with particle number restriction deviate from the correct answer. This is expected: as temperature is increased, the Boltzmann weight on basis states with

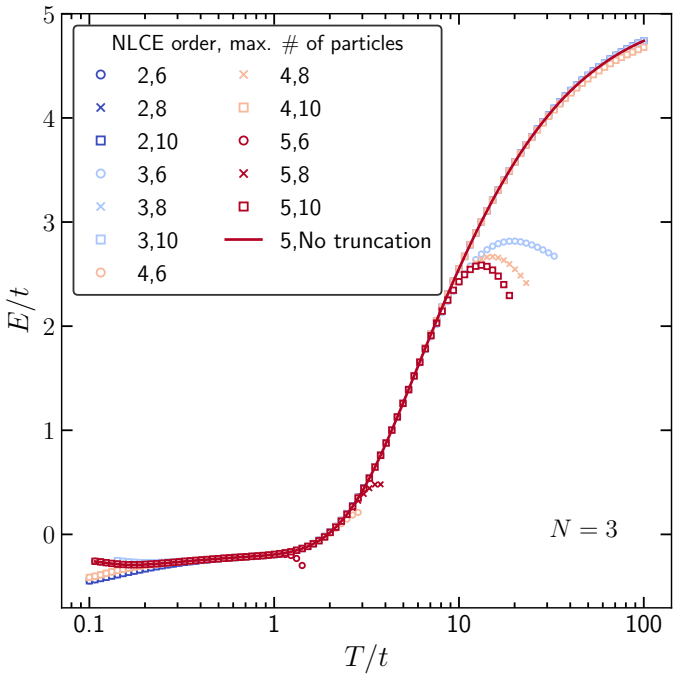

Figure 7.15 : **Convergence of NLCE with restriction of maximum number of particles**. Energy vs T/t plot at $U = 15.3t$ for SU(3). Different curves are different NLCE orders from two to five, and restriction of maximum number of particles to six, eight and ten, as indicated in the legend. The divergence of NLCE at low temperature is due to the finite order of the expansion, while the divergence at high temperature is due to particle number truncation.

more particles increases. A less obvious feature is that the temperature above which the restriction fails to be accurate actually decreases as the NLCE order increases. This is because the NLCE relies on cancellation of finite-size errors when combining results from many clusters to obtain accurate results, and the number of clusters used increases with NLCE order, and thus so does the required level of cancellation. The truncation of maximum number of particles interferes with the exact cancellation, and is magnified by the NLCE procedure by an amount that grows with the number of contributing clusters. Thus, there is a finite window over which the NLCE results are highly converged: the particle number truncation constrains the results to being accurate below some temperature, while the finite-size clusters used in the NLCE constraint the results to being accurate above some temperature. For the SU(3) results [Fig. 7.15] this window is roughly from $T/t = 0.2$ to 1 for maximum number of particles of six and five-site NLCE, as seen through comparison to the results without the restriction. We also observe that the NLCE self-diagnoses its failure due to this restriction similar to how it diagnosed the failure due to the finite number of clusters used: when results with different particle number truncations agree, the calculation is accurately converged.

Fig. 7.16 illustrates the effects of the interaction-energy-based basis truncation on top of maximum particle number restriction to six by comparing the results for $p = 3$ and $p = 4$ truncations to the nontruncated result for SU(3) at $U/t = 15.3$. The additional effects are negligible for NLCE orders four and five. This is not surprising since for a five-site cluster a particle number restriction of six already discards most states with highly occupied sites (doublons and higher) and a further restriction of basis states with interaction energy $< 3U$ serves mainly to discard triplon and and higher states which have very small Boltzmann weights in the region of interest. Thus, this additional truncation significantly reduces computational time, while introducing negligible additional numerical errors. The self-diagnosis of the NLCE is apparent

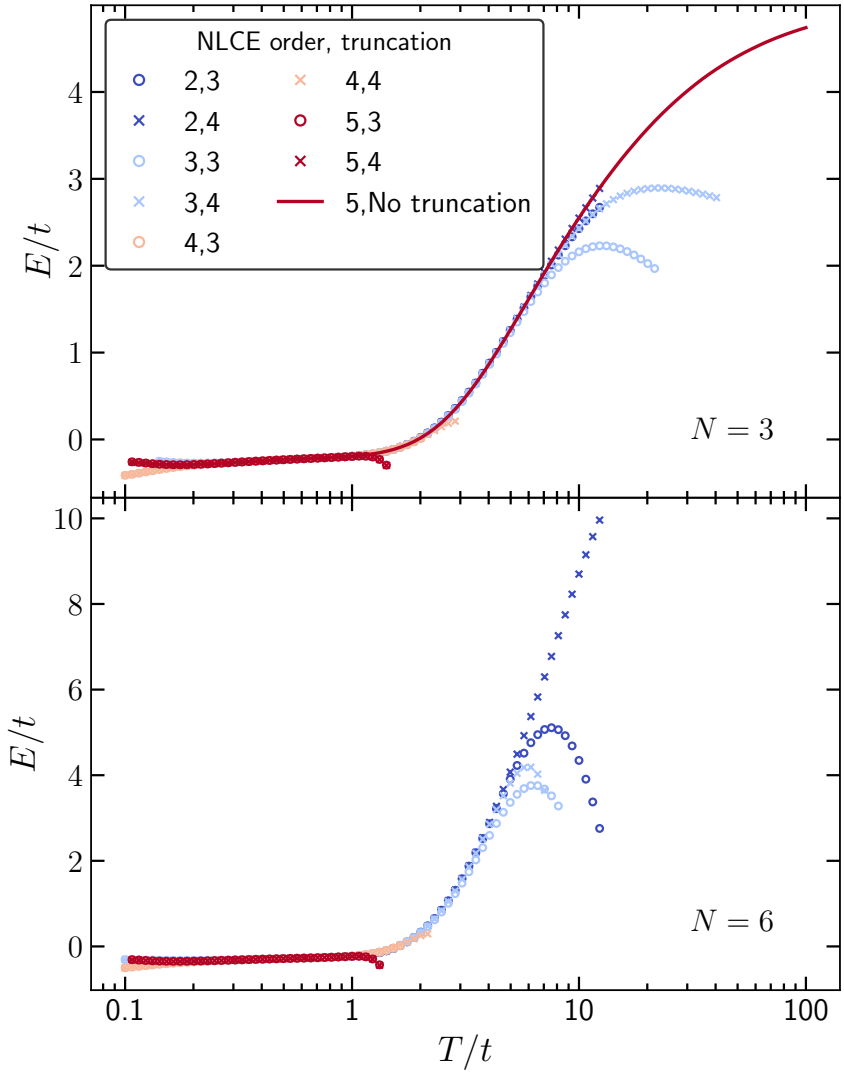

Figure 7.16 : **Convergence of NLCE with Hilbert space truncation.** Energy vs T/t plot at $U = 15.3t$ for SU(3) [top] and SU(6) [bottom]. The total number of particles in the cluster was restricted to six or less and basis states with interaction energy $U\mathcal{D}$ greater than pU were discarded. Different curves are different NLCE orders from two to five, and truncations $p = 3$ and 4, as indicated in the legend. The divergence of NLCE at low temperature is due to the finite order of the expansion, while the divergence at high temperature is due to the basis truncation.

here as well, which we use to analyze the $N = 6$ results, where results without truncation are unavailable [Fig. 7.16 (bottom)]. When adjacent orders and different truncations agree, the NLCE is converged. We see the same trends for $N = 6$ as for $N = 3$, and a similar region of convergence for the five-site NLCE. The results in this Chapter thus use $p = 3$ and particle number restricted to six in the results for $N = 6$. Naturally, the value of U affects the region of convergence significantly. The size of the temperature region of convergence increases with U. For $U \leq 8t$, there is barely any region of convergence for these choices of the truncation parameters, and hence we cannot get converged results for the SU(6) system from the fifth-order NLCE with our truncation.

7.4.4 Second order NLCE calculation for $J \ll T \ll U$. Energy crossing and $1/N$ dependence

In this section we focus on two things: explaining the existence of an energy crossing (as seen in Fig. 7.7) and demonstrating the $1/N$ scaling observed in the limit $J \ll T \ll U$. As mentioned in previous sections in this Chapter, the second order NLCE captures such behavior, but this does not admit a general analytic formula. However, analytic formulas can be obtained in the $J \ll T \ll U$ regime.

The second order NLCE in the square lattice is $E = 4E^{(2)} - 3E^{(1)}$, where $E^{(x)}$ is the energy per site in an x-site system. First we demonstrate that for $J \ll T \ll U$ the one-site problem does not contribute to the energy, then we calculate the energy in the relevant particle sectors in the two-site problem, and finally we present results for their linear combination, i.e. the second order NLCE.

7.4.4.1 One-site problem

In the one-site problem, the partition function is given by

$$Z^{(1)} = \sum_{n=0}^{N} \binom{N}{n} e^{-\beta\epsilon_0(n)}, \tag{7.20}$$

where $\epsilon_0(n) = U\binom{n}{2} - \mu n$. The density $\rho^{(1)}$ is

$$\rho^{(1)} = \langle n \rangle = \frac{1}{Z^{(1)}} \sum_{n=0}^{N} n \binom{N}{n} e^{-\beta\epsilon_0(n)}, \tag{7.21}$$

while the energy $E^{(1)}$ is

$$E^{(1)} = \langle H + \mu n \rangle = \frac{1}{Z^{(1)}} \sum_{n=0}^{N} U \binom{n}{2} \binom{N}{n} e^{-\beta\epsilon_0(n)}. \tag{7.22}$$

Because $T \ll U$, we can obtain an analytical approximate expression for the chemical potential $\mu_0(T, U, N)$ that fixes the density to $\rho = 1$ by only considering the zero-, one-, and two-particle sectors. This expression is exact for $N = 2$, but is only true to leading order in T/U for $N > 2$, since it truncates eigenstates with triplons and higher occupancies. The solution for μ_0 is given by

$$\mu_0(T, U, N) = \frac{U}{2} + \frac{1}{2} T \ln \left[\frac{2}{N(N-1)} \right], \tag{7.23}$$

and the energy in this limit is

$$E^{(1)} = \frac{U e^{-\beta U/2}}{2 + \sqrt{\frac{2N}{N-1}}} \approx 0. \tag{7.24}$$

Therefore we have shown that in the $\beta U \gg 1$ limit the second-order NLCE in the square lattice is determined by the two-site result, $E = 4E^{(2)}$.

7.4.4.2 Two-site problem

The Hilbert space of the two-site problem is 4^N, and analytically diagonalizing such matrix — even if exploiting particle number conservation for each spin component and spin permutation symmetry — is not possible. However, not all particle sectors need to be considered since $\beta U \gg 1$ and $\langle n \rangle = 1$. Under these two conditions, and to leading order in βJ, we can use the chemical potential from Eq. (7.23) in the two-site calculation. This ensures that at $\langle n \rangle = 1$ only the two-site two-particle sector (TSTP) contributes, since all other sectors are $\propto e^{-\beta U}$, and therefore negligible.

In the TSTP, there are N states where two particles of the same flavor sit on sites 1 and 2. Since these are Pauli blocked from hopping, and there is no U contribution, they constitute N independent one dimensional subspaces of energy $\epsilon = 0$, giving rise to a contribution N in the partition function. Furthermore, there are $\binom{N}{2}$ choices where the flavors of the two particles are different. Since the hopping conserves flavor, these form independent four-dimensional subspaces with levels identical to the usual $N = 2$ spectrum in the one spin-up and one spin-down sector. Therefore, in the TSTP the partition function $Z^{(2)}$ and energy per site $E^{(2)}$ are given by:

$$Z^{(2)} = N + \binom{N}{2} Z_2, \tag{7.25}$$

$$E^{(2)} = \frac{1}{2}\binom{N}{2} E_2, \tag{7.26}$$

$$Z_2 = \sum_{n=1}^{4} \exp(-\beta \epsilon_n), \tag{7.27}$$

$$E_2 = \frac{1}{Z} \sum_{n=1}^{4} \epsilon_n \exp(-\beta \epsilon_n), \tag{7.28}$$

where ϵ_n are the eigenvalues of the two-particle sector with different spin component, i.e. $\sigma \neq \tau$. These eigenvalues are $\epsilon_n = \{0, U, U/2 \pm \sqrt{16t^2 + U^2}\}$.

First, an energy crossing for different values of N as a function of T/t at a fixed U/t in the TSTP occurs when Eq. (7.26) is equal to zero, i.e. $E_2 = 0$, to demand the

N-independence of the energy. The temperature at which the crossing occurs is the solution to the following trascendental equation:

$$0 = Ue^{-\beta U} + \frac{U}{2}\left[1+\sqrt{1+\left(\frac{4t}{U}\right)^2}\right] e^{-\beta\frac{U}{2}\left[1+\sqrt{1+\left(\frac{4t}{U}\right)^2}\right]} + \frac{U}{2}\left[1-\sqrt{1+\left(\frac{4t}{U}\right)^2}\right] e^{-\beta\frac{U}{2}\left[1-\sqrt{1+\left(\frac{4t}{U}\right)^2}\right]}. \tag{7.29}$$

That this equation has solutions demonstrates the existence of a crossing point, and it qualitatively explains the trends of T^*/t with U/t, although it deviates quantitatively from the results in Fig. 7.8.

Now we demonstrate the $1/N$ scaling for $J \ll T \ll U$, where the second-order NLCE shows unconditionally that the collapse occurs in this regime. We present results for E, but analogous results can be obtained for $\mathcal{D}$ and K. The energy in the TSTP is given by Eq. (7.26),

$$E^{(2)}(T,U,N) = \frac{1}{2}\frac{\binom{N}{2}\sum_{n=1}^{4}\epsilon_n \exp(-\beta\epsilon_n)}{N+\binom{N}{2}\sum_{n=1}^{4}\exp(-\beta\epsilon_n)}. \tag{7.30}$$

Since $U \gg t$, the ϵ_n have simple expressions $\epsilon_n = \{0, U, U+J, -J\}$. Because $\beta U \gg 1$, $E^{(2)}$ is given to leading order by

$$\begin{aligned} E^{(2)}(T,U,N) &\approx \frac{1}{2}\frac{\binom{N}{2}\left(-Je^{\beta J}\right)}{N+\binom{N}{2}\left(1+e^{\beta J}\right)}, \\ &= \frac{1}{2}\frac{-Je^{\beta J}}{\frac{N+1}{N-1}+e^{\beta J}}. \end{aligned} \tag{7.31}$$

Finally, since in the $J \ll T \ll U$ limit $E = 4E^{(2)}$, the second order NLCE to zeroth order in $\beta J \ll 1$ is

$$E(T,U,N) \approx -J + \frac{1}{N}J. \tag{7.32}$$

This demonstrates that the scaling Eq. (7.10) holds in the regime $4t^2/U \ll T \ll U$, when $t/U \ll 1$ to zeroth order in βJ.

Chapter 8

Observation of antiferromagnetic correlations in an ultracold SU(N) Hubbard model

> The superiority of the symmetrical flower is reflected in a greater production of nectar, and that nectar has a higher sugar content. Symmetry tastes sweet.
>
> *Symmetry: A Mathematical Journey.*
> Marcus Du Sautoy

This chapter is adapted from publication:

Observation of antiferromagnetic correlations in an ultracold SU(N) Hubbard model, Shintaro Taie*, **Eduardo Ibarra-García-Padilla***, Naoki Nishizawa, Yosuke Takasu, Yoshihito Kuno, Hao-Tian Wei, Richard T. Scalettar, Kaden R. A. Hazzard, and Yoshiro Takahashi, arXiv:2010.07730 (accepted at Nat. Phys). *This authors contributed equally to this work [*].

Mott insulators are paradigmatic examples of strongly correlated physics from which many phases of quantum matter with hard-to-explain properties emerge. Extending the typical SU(2) spin symmetry of Mott insulators to SU(N) is predicted to produce exotic quantum magnetism at low temperatures. In this work, we experimentally observe nearest-neighbor spin correlations in a SU(6) Hubbard model realized by ytterbium atoms in optical lattices. We study one-dimensional, two-dimensional square, and three-dimensional cubic lattice geometries. The measured SU(6) spin correlations are enhanced compared to the SU(2) correlations, due to strong Pomer-

*Complete article, including text, figures, and tables reprinted with copyright permission of Ref. [41].

anchuk cooling. The experimental data for a one-dimensional lattice qualitatively agrees with our theoretical calculations, with an error of at most 30%, without any fitting parameters. Detailed comparison between theory and experiment allows us to infer the temperature to be the lowest achieved for a cold atom Fermi-Hubbard model. For two- and three-dimensional lattices, the experiments reach entropies below the regime where our calculations converge, highlighting the importance of these experiments as quantum simulations.

8.1 Introduction

A recurring question in many-body quantum systems is how the competition of kinetic and interaction energies determines ground state quantum phases. The quantum fluctuations play an essential role in determining the ground state spin structure, which may differ drastically from the mean-field prediction. The SU(2) Hubbard model has long been a prototypical system to study these effects, and Hubbard models with an enlarged SU(N) symmetry have attracted great interest.

The study of SU(N) quantum magnetism historically originated from the mathematical technique of large-N expansions [8, 83, 84, 86]. More recently, understanding $N > 2$ systems has attracted broader interest, due to the expectation that such systems will display a wide array of exotic physics [76, 130–134, 138]. Although N can be large, quantum fluctuations remain important since SU(N) symmetry prevents spins from becoming classical [8, 257].

Although theoretical models with SU(N) symmetry also have been discussed in connection with real physical systems such as transition metal metal oxides [72, 73] and graphene's SU(4) spin-valley symmetry [90], the introduction of the symmetry is just a rough approximation. In contrast, an intrinsic SU(N) nuclear spin symmetry [97, 98, 257, 258] is realized in fermionic isotopes of alkaline-earth-metal-like atoms (AEAs), providing unique opportunities for quantum simulation experiments of the

SU(N) Fermi-Hubbard Model (FHM) [75, 85, 102, 143, 178, 278]. The SU($N = 2I + 1$) FHM can be implemented by loading an AEA with nuclear spin I in an optical lattice. This model is given by the Hamiltonian

$$H = -t \sum_{\langle i,j \rangle, \sigma} c_{i\sigma}^{\dagger} c_{j\sigma} + \frac{U}{2} \sum_{i, \sigma \neq \tau} n_{\sigma}(i) n_{\tau}(i) - \mu \sum_{i,\sigma} n_{\sigma}(i), \tag{8.1}$$

where $c_{i\sigma}$ ($c_{i\sigma}^{\dagger}$) denotes the fermionic annihilation (creation) operator for site i, $n_{\sigma}(i) = c_{i\sigma}^{\dagger} c_{i\sigma}$ is the number operator and μ is the chemical potential that controls the density. The flavor index σ labels the projection quantum number of the nuclear spin m_I. Here we employ ^{173}Yb, and m_I is $-5/2, -3/2, \ldots, +5/2$. The tunneling amplitude t and the on-site interaction U do not depend on σ, giving rise to the SU(N) symmetry.

An important characterization of strongly correlated states is provided by their spin correlation functions. For the SU(2) Hubbard model, antiferromagnetic (AFM) correlations were first observed in dimerized lattices [67], in un-dimerized three-dimensional (3D) lattices using Bragg spectroscopy [20], and in one- and two-dimensional (1D and 2D) lattices using quantum gas microscopy [21, 59]. However, correlations in a uniform SU(N) Hubbard model have not been previously observed. Although observing long-ranged correlations would be essential to characterize phases of matter and their phase transitions, nearest-neighbor spin correlations are already of great interest. In many models, the most rapid change of nearest neighbor correlations with temperature can be a proxy for the critical temperature, and short-ranged correlations are a key ingredient in pairs formations in cuprate and iron-pnictide superconductors, where short-ranged magnetic correlations appear to be essential for the pairing. In this work, we observe the nearest-neighbor AFM spin-correlations in an SU(6) ^{173}Yb Fermi gas loaded in 1D, 2D, and 3D optical lattices, and measure them as a function of initial entropy in a harmonic trap. These experimental results are compared with the theoretical calculations with no fitting parameters.

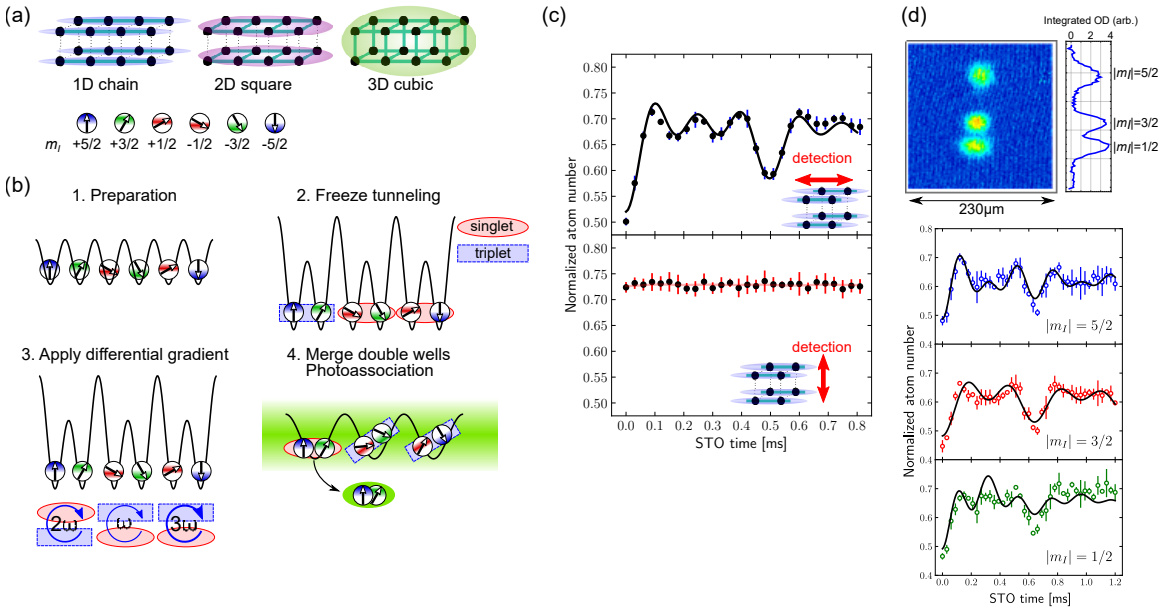

Figure 8.1 : **Experimental setup**. (a) SU(6) Hubbard systems realized in various configurations of a 3D optical lattice. Spin components are labeled by the nuclear spin projection quantum number m_I. (b) Schematic of the experiment. After preparing the equilibrium state and freezing all the tunneling processes, a spin-dependent potential gradient is applied to drive STOs. Subsequently, every two adjacent lattice sites are merged into single sites of the detection lattice, followed by photoassociation which removes atom pairs in antisymmetric spin states. (c) Typical examples of SU(6) STO signal measured for the 1D chain lattice. The spin-correlation signal for the nearest-neighbors along the chain axis and along the inter-chain direction are shown in the upper and lower graphs, respectively. Atom numbers are normalized by the total atom number without molecular association processes, and the deviation from unity represents the fraction of singlet states at each time. The initial entropy per particle is $1.45k_B \pm 0.05k_B$, and the interaction strength is $U/t = 15.3(5)$. The error bars represent the standard deviation for the 6 independent measurements. (d) STO measurement with optical Stern-Gerlach (OSG) spin separation. Top: Absorption image of the OSG experiment. The image is taken after 5ms time-of-flight. Bottom: Time evolution of the spin population during STO. The solid lines are the fits with the two-frequency model in Eq. (8.10). A spin imbalance of 3% is evaluated from the independent measurement with full 6-spin separation. The error bars represent the standard error of the mean for the 3 independent measurements.

8.2 Experimental setup

Figure 8.1(a) depicts our physical system. The SU(6) Fermi gas of ^{173}Yb with atom number $N_{\mathrm{ptcl}} = 2.4(1) \times 10^4$ is adiabatically loaded into 1D chain, 2D square, and 3D cubic lattices that are constructed by a primary optical lattice operating at 532 nm (see Methods). The 1D chain and 2D square lattices are created by introducing strong tunneling anisotropy into the cubic lattice. The inter-lattice tunneling is less than 5% of intra-lattice tunneling t, and is much smaller than the other energy scales in the system. In our previous work [142] we measured the spin correlation of SU(4) fermions loaded into a double-well system in which the nearest-neighbor correlation is artificially enhanced by strong dimerization. However, in the present work, the SU(6) fermions are loaded into uniform lattices in 1D, 2D, and 3D in which there is no trivial enhancement of spin correlations due to dimerization.

One can utilize the technique of singlet-triplet oscillations (STO) [67, 279] in an optical superlattice to measure the nearest-neighbor correlations, including for SU(N) Fermi gases [142]. The principle of the STO measurement is illustrated in Fig. 8.1(b). Tunneling is frozen except between pairs of adjacent lattice sites along the measurement axis, which are merged into single sites of a detection lattice which has twice the lattice spacing. Here we utilize the fact that s-wave photoassociation (PA) only associates pairs of atoms with a spatially symmetric wavefunction, and thus is only sensitive to spin antisymmetric states in each detection site since the total wavefunction is antisymmetric. Associated molecules quickly escape from the trap, resulting in atom loss. Application of a spin dependent potential gradient before the merging process drives oscillations of spin symmetry, enabling us to also detect spin symmetric states. In this way, we measure the fraction of both "singlet" and "triplet" states formed within nearest-neighbor lattice sites. The detected SU(N) counterpart of the SU(2) double-well singlet is a $\binom{N}{2}$-fold multiplet with the form $(|\sigma,\tau\rangle - |\tau,\sigma\rangle)/\sqrt{2}$ ($\sigma \neq \tau$ represents one of the N flavors). Similarly, the double-well triplet is extended to a

$\left[\binom{N}{2}+N\right]$-fold multiplet, among which $\binom{N}{2}$ states with the form $(|\sigma,\tau\rangle+|\tau,\sigma\rangle)/\sqrt{2}$ ($\sigma\neq\tau$) are detected by our scheme while $\sigma=\tau$ is not. In the following, we represent the fraction of atoms forming these "singlet" and detectable "triplet" by P_s and P_{t0}, respectively. These are not to be confused with SU(N) singlets and triplets, which are N-body entangled states [72]. The STO measurement is valid only if the contribution from multiple occupancies can be neglected. For that reason, we set the central density to unit filling and the interaction to be sufficiently strong to suppress double occupancies in the primary lattice. This also maximizes the Pomeranchuk cooling effect because the maximum spin entropy $\ln N$ can be realized only in singly occupied sites. The presence of holes results in double wells containing only a single atom and does not affect STOs.

As a measure for the nearest-neighbor spin correlation, we consider a singlet-triplet imbalance defined as

$$I=\frac{P_s-P_{t0}}{P_s+P_{t0}}. \tag{8.2}$$

In addition, we consider a normalized STO amplitude

$$A=P_s-P_{t0} \tag{8.3}$$

as an alternative measure. As long as the SU(N) symmetry holds, A is proportional to the spatial integration of the SU(N) spin correlation function C_{NN} [126] (see Methods),

$$C_{NN}=\sum_{\sigma\neq\tau}\Big[\langle n_\sigma(i)n_\sigma(i+1)\rangle-\langle n_\sigma(i)n_\tau(i+1)\rangle\Big], \tag{8.4}$$

where $n_\sigma(i+1)$ is a shorthand we use throughout for number operators at a nearest-neighbor of i. In the trap, A will be significantly reduced compared to the uniform unit filled case because of the low density at the edge of the sample, and incorporating the effect of the harmonic confinement is important to compare calculations of A with

experiments. Note that the singlet and triplet fractions can be determined if we know both I and A.

Figure 8.1(c) shows a typical STO signal measured in a 1D chain lattice. To create the spin dependent potential gradient, we utilize linearly polarized laser light close to the ${}^1S_0 \rightarrow {}^3P_1$ resonant frequency (see Methods). As a result, STOs are driven for the spin pairs with different $|m_I|$ (= 1/2, 3/2, and 5/2), resulting in three different STO frequencies. The ratio of these frequencies $\omega_{\frac{1}{2}-\frac{3}{2}} : \omega_{\frac{3}{2}-\frac{5}{2}} : \omega_{\frac{5}{2}-\frac{1}{2}} = 1 : 2 : 3$ is determined by the Clebsch-Gordan coefficients and does not depend on detuning (see Methods). We analyze the STO signal assuming the SU(N) symmetry, namely, that all spin combinations equally contribute to correlations. Along the chain axis, we obtain a singlet-triplet imbalance of $I = 0.674 \pm 0.052$, indicating the large AFM correlation ($C_{NN} < 0$). On the other hand, correlations between chains are zero within the error bar ($I = 0.01 \pm 0.01$) as expected from the negligible inter-chain tunneling.

To verify the expected SU(6) symmetry, we observe the time evolution of each nuclear spin component during STOs. After the standard STO process (driving STO, merging double-wells, and applying PA), lattice potentials are adiabatically ramped down in 6 ms to suppress momentum spread. Then we turn off the optical trap, followed by the application of the optical Stern-Gerlach (OSG) beam for 0.2 ms. The OSG light source is identical with that for the gradient beam for driving STO, with nearly 3 times higher intensity. Therefore the OSG beam is π-polarized and distinguishes only spin components with different $|m_I|$. Figure 8.1(d) shows analysis of the spin distribution. The behavior is well reproduced by the two-frequency model (see Methods), indicating that the STO scheme is working as designed. The fit to oscillations of the $|m_I| = 1/2$ cloud seem slightly worse than the others. This is due to the stronger deformation of the cloud and possibly spin-flips caused by the photon scattering from the OSG laser. We confirm that the deviation of each spin population

from the balanced mixture is about 3% and this does not affect the following results.

8.3 Results

8.3.1 Antiferromagnetic nearest-neighbor spin correlations

Figures 8.2(a) and (b) show the nearest-neighbor correlations for 1D and 3D lattices as a function of entropy per particle, with a dramatic enhancement of SU(6) spin correlations compared to the SU(2) correlations in the 1D system. The total entropy S is inferred from a time-of-flight measurement of the weakly interacting gas before lattice loading. The on-site interaction is fixed to $U/t = 15.3(5)$ for all lattice configurations, which is determined from the band calculation with measured lattice depths. In this strongly interacting regime, an important scale is the maximum spin entropy per particle for a singly-occupied site, given by $s_{\mathrm{spin}}^{(N)} = k_B \ln N$. Naïvely, ignoring the spatial inhomogeneity of the trap, a sample with $S/N_{\mathrm{ptcl}} < s_{\mathrm{spin}}^{(N)}$ is expected to reach the temperature regime where the spin-correlations emerge. For SU(6), $s_{\mathrm{spin}}^{(6)} = 1.79 k_B$, while for SU(2), $s_{\mathrm{spin}}^{(2)} = 0.69 k_B$, and $N = 6$ systems are therefore expected to show significantly enhanced correlations, which is interpreted as the enhancement of the Pomeranchuk effect due to large spin [71, 127, 128]. Our microscopic theory confirms this simple picture, and the observed data show reasonable agreement with theoretical predictions by exact diagonalization (ED) for 1D and determinantal quantum Monte Carlo (DQMC) for 3D, without any fitting parameters.

Here, we suggest a possible origin of the small observed deviation between the theory and experiment. Given the extensive tests we have done on our codes and experiments, we consider an actual error in the calculations or the experiments unlikely. The remaining possibility is the fundamental differences between the model being simulated and the atomic system being measured. On the computational side, we have carefully investigated Trotter errors, finite size effects, and the use of the local density approximation (Methods). Calculations assume that loading is adiabatic,

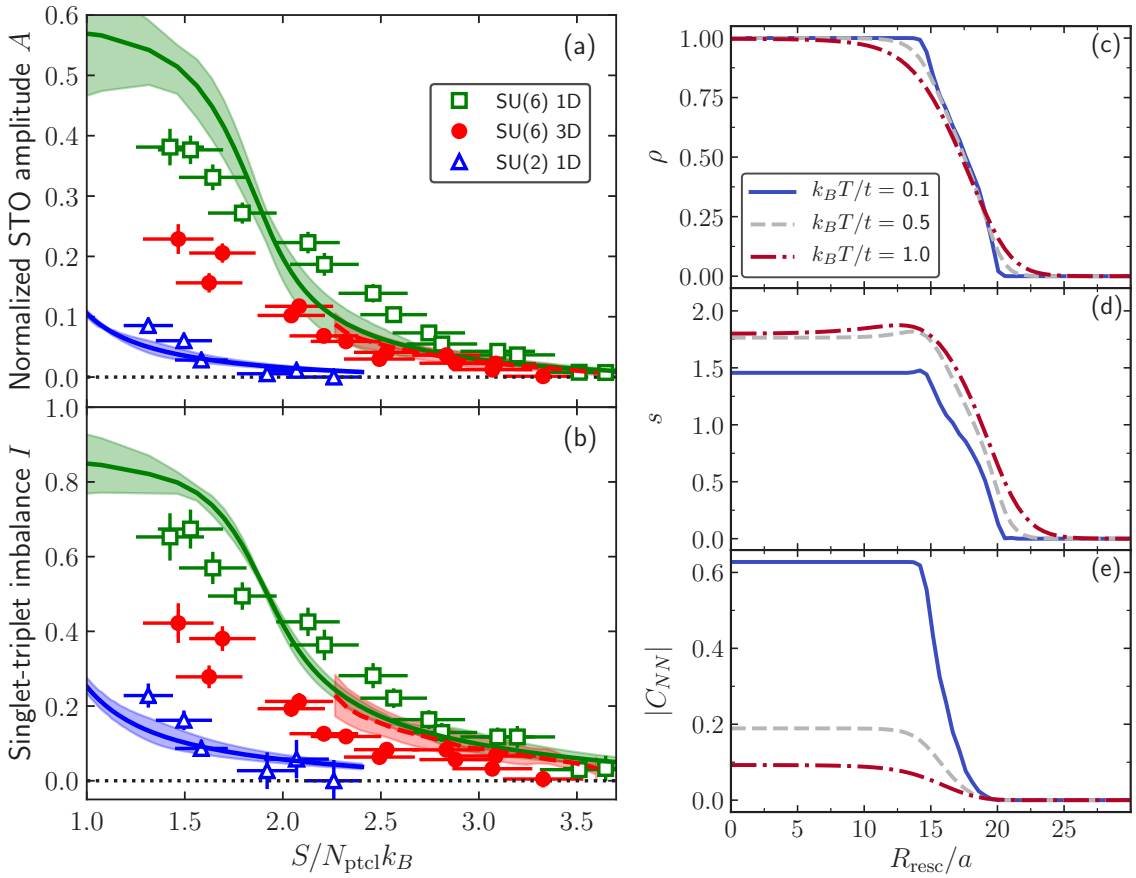

Figure 8.2 : **Entropy dependence of the nearest-neighbor correlations of the SU(N) FHM at** $U/t = 15.3$. Entropy dependence of (a) the normalized STO amplitude A and (b) the singlet-triplet imbalance I in 1D and 3D lattices are shown. Green squares, red circles, and blue triangles represent the experimental data for SU(6) 1D, SU(6) 3D, and SU(2) 1D systems, respectively. Solid (dashed) lines are the result of ED (DQMC) calculations. The horizontal error bars represent standard deviation of the 10 entropy measurements, and the vertical error bars are extracted from the fitting errors in the analysis of the STO signal. Shaded areas represent uncertainty from systematic and statistical errors of the numerical methods (for more details, see Methods), and the possible systematic error (20%) in the total atom number measurement, summed linearly . (c)-(e) Observables as a function of distance to the center of the trap for the 1D system with trap parameters as in the experiments calculated by ED. (c) Particle number per site, (d) entropy per site, and (e) nearest-neighbor spin correlation per site as a function of $R_{\rm resc}/a$, where the rescaled radii are $R_{\rm resc} = \sqrt{\sum_{a=x,y,z}(\omega_a r_a/\overline{\omega})^2}$, $a = 266$ nm is the lattice constant, and $\overline{\omega} = (\omega_x\omega_y\omega_z)^{1/3}$ is the geometric mean of the trapping frequencies, for $N = 6$ at $U/t = 15.3$ in an $L = 8$ site chain at $k_BT/t = 0.1$, 0.5, and 1.0. These temperatures correspond to $S/N_{\rm ptcl}k_B = 1.75$, 2.17, and 2.54, respectively.

while non-adiabatic loading of the atoms to the lattice may play some role in the experiments. For the 1D SU(6) case, measured correlations in the low entropy region are smaller than the theoretical curve by $\sim 30\%$, and it is plausible the main source of the discrepancy is the non-adiabaticity of the lattice loading. We estimate the amount of heating to be $0.2k_B$ around the lowest temperature (Methods). For the higher entropy region in 1D SU (6) case, on the other hand, measured correlations are larger than the theory predictions. Although experiments start with a weakly interacting gas, it is possible that some of the initial correlations are frozen during lattice loading, which could be a source of small remaining discrepancies between the experimental results and theory.

Figures 8.2(c)-(e) show theoretically calculated trap profiles of atom number, entropy, and nearest-neighbor spin correlations per site for a 1D system. A rigid Mott plateau is well-developed at $k_BT/t \sim 0.5$, and spin correlation rapidly develops for lower temperature. Estimation of the temperature obtained in our experiment is discussed in the next section.

8.3.2 Extracting temperature in an optical lattice by theory-experiment comparison

The present experiments cannot directly measure the temperature at the very low entropies studied here. However, for the 1D systems, the temperature can be inferred by comparing experiment and theory. In 1D, the lowest temperature achieved in the experiments is $k_BT/t = 0.096 \pm 0.054 \pm 0.030$, obtained from the experimentally-measured singlet-triplet imbalance I at $S/N_{\mathrm{ptcl}}k_B = 1.45 \pm 0.05$ (see Fig. 8.5). The first error bar is an estimate of the finite-size error given by the difference between the finite-size extrapolation to the thermodynamic limit and the 8-site result. The second error bar comes from the experimental uncertainty on the correlations. This is lower than the state-of-the-art temperatures reported in cold atom FHM systems

[20, 21, 62, 63, 141]. Estimates based on A rather than I are similar (see Methods). The theory and experiment agreement in 1D suggests the reliability of the experiment in higher dimensions where numerics fail and quantum simulation via experiment is crucial.

For comparison, at the same entropy, the SU(2) system is at $k_B T/t = 1.008 \pm 0.073 \pm 0.001$, or to obtain the same singlet-triplet imbalance, the SU(2) system should be at $S/N_{\mathrm{ptcl}} k_B = 0.499 \pm 0.136 \pm 0.120$. Since the state-of-the-art averaged entropy per particle for SU(2) experiments with alkali atoms is around $1 k_B$ [21], this suggests an experimental advantage for SU(N) systems in obtaining highly correlated states in optical lattices.

8.3.3 Dependence on lattice dimensionality

In addition to the dependence on N, the correlations significantly depend on dimensionality, with the 1D case exhibiting the largest correlations as shown in Figs. 8.3(a) and (b). This behavior is similar to previous studies in an SU(2) system [43, 60, 193] and can be understood at sufficiently high-temperatures. In this regime, correlations depend only on temperature, not dimension (this intuitive result can be proved with a high temperature expansion), and decrease with increasing temperature. Additionally, decreasing dimension decreases the bandwidth and thus at fixed entropy decreases the temperature [as seen in Fig. 8.3(b)]. Together, these imply that correlations decrease as the dimensionality is increased. The situation at lower temperatures is expected to be more complicated, but the numerics indicate that this simple conclusion remains true. Constructing simple arguments for the low temperature regime remains an interesting challenge.

In Fig. 8.3(a), we plot the singlet-triplet imbalance measured through 1D-2D and 2D-3D crossovers with the same initial condition. We measure the correlations along the z axis and change the ratio of t_z to the tunneling $t_\perp$ of the initially weak link.

At both the maximum and minimum $t_z/t_\perp$ and at the intermediate point $t_z/t_\perp = 1$, we set $U/t_z = 15.3$. Lattice geometry is smoothly changed between the above three points (see also Methods). We find that spin correlations monotonically decrease as the lattice is deformed from 1D to 2D. For the 2D-3D crossover, the difference is smaller but the trends of decreasing correlations with increasing dimensionality are still visible. The correlation quickly drops for $t_z/t_\perp < 1$ and becomes undetectable, as expected.

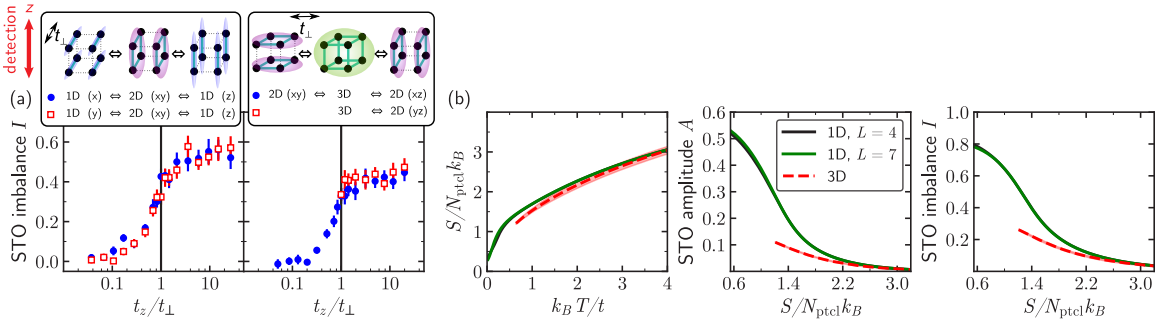

Figure 8.3 : **Dimension dependence of the spin correlations**.(a) Left: Spin correlations of an SU(6) Fermi gas as the lattice dimensionality is tuned by lattice anisotropy from 1D to 2D. Correlations along the z axis are measured. Lattices are deformed from x-chains (blue circles) and y-chains (red squares) to z-chains with $U/t = 15.3$, via the 2D square lattice with same U/t. Right: Measurement in 2D-3D crossover. Three possible 2D square lattices are connected via the isotropic 3D cubic lattice at $U/t = 15.3$. The initial entropy is $S/N_{\rm ptcl}k_B = 1.4 \pm 0.1$ for both experiments. (b) Entropy per particle, normalized STO amplitude, and singlet-triplet imbalance for $N = 3$ in L-site chains and a $4 \times 4 \times 4$ cubic lattice for $U/t = 8$. Note that the results for 1D $L = 4$ and $L = 7$ are nearly identical.

Numerical calculations show a similar trend. Although DQMC has difficulty in obtaining reliable results for 3D systems at the low temperatures where significant correlations develop for $U/t = 15.3$ and $N = 6$, it can calculate the properties of 3D systems for $U/t = 8$ and $N = 3$ to low temperature where significant correlations develop. Because we are considering a smaller N we calculate ED results without using the basis state truncation for 1D L-sites chains with $L = 4$–7. Figure 8.3(b) presents the computed entropy per particle and the spin correlations. Although these are not directly the conditions in the experiments, they do show the same trend of

correlations decreasing with increasing dimension.

DQMC results for $N = 6$ are only presented at temperatures above $T/t = 1$, owing to a strong sign problem below this temperature, as well as the onset of nonergodicities in the Monte Carlo sampling in this region. The sign problem is particularly strong in the metallic region, where large errors in the observables appear for several values of the chemical potential. Ref. [44] provides more details on how the sign problem depends on U/t and μ/t.

8.4 Discussion

We find that the measured nearest-neighbor AFM correlations agree broadly with the theory with no fitting parameters for all temperatures in 1D, and at temperatures where converged theoretical results can be obtained in 3D. In our work for 3D lattices, we have entered the region where converged theoretical calculations are unavailable and quantum simulation manifests its usefulness.

While we successfully demonstrate the lowest temperature achieved in the FHM in our 1D optical lattice experiment, there is still room for reaching even lower temperatures, for example by engineering spatial redistribution of entropy [21].

The STO measurement presented here is also applicable to spin imbalanced cases by introducing proper oscillation functions. On the other hand, the spin structures measured in this work are limited to the SU(2)-type nearest-neighbor singlets and triplets. In general SU(N) systems, more nontrivial spin states arise. For example, the SU(N) singlet given by the fully antisymmetric combination of N spins plays an essential role in SU(N) antiferromagnets. Probing such multi-spin entanglement will be an important experimental challenge. Measuring the long range correlations is also of interest. One of the most important questions that has not been uncovered yet is whether the long-range ordering persists in the SU(N) system. Measuring long range correlations will be feasible by using a quantum gas microscope with spin-

selective detection technique. State-of-the-art numerical and analytic calculations, with the use of approximations, have proposed a variety of possible ground states such as flavor-ordered patterns and valence bond solids, among others [76, 130–134, 138]. Experiments are now poised to discriminate finite temperature analogs of such proposed states.

8.5 Methods

8.5.1 Sample preparation

A degenerate Fermi gas of ^{173}Yb is prepared by evaporative cooling in a crossed dipole trap operating at 532 nm. The optical lattice also has the wavelength 532 nm and the simple cubic geometry. The additional detection lattices at 1064nm along the z and x axes are used only for STO measurement. In the main result obtained in Fig. 8.2, the optical lattices are ramped up to $\mathbf{s} = (s_x, s_y, s_z) = (7.0, 7.0, 7.0)$ for the 3D cubic lattice, $(6.1, 20.0, 6.1)$ for the 2D (xz-) square lattice, and $(20.0, 20.0, 5.0)$ for the 1D (z-)chain lattice. Here, $s_{x,y,z}$ are the lattice depths in units of the recoil energy $E_{\mathrm{R}} = \hbar^2(2\pi/\lambda)^2/2m$ with atomic mass m and the wavelength of the lattice laser beams $\lambda = 532$ nm. In the dimensional crossover experiment shown in Fig. 8.3, the lattice geometry is smoothly changed in the form $\mathbf{s} = (1-p)\mathbf{s}_1 + p\mathbf{s}_2$ $(0 < p < 1)$, where $\mathbf{s}_1$ and $\mathbf{s}_2$ take the values given above for definite dimensionalities, as well as $(6.1, 6.1, 20)$ for 2D (xy-) square and $(5.0, 20.0, 20.0)$ for 1D (x-) chain lattices. The dipole trap together with the optical lattice creates an overall harmonic potential for the sample, whose trap frequencies are $(\omega_{x'}, \omega_{y'}, \omega_z) = 2\pi \times (102, 44, 155)$ Hz for the 3D lattice, $2\pi \times (105, 49, 158)$ Hz for the 2D lattice, and $2\pi \times (107, 54, 162)$ Hz for the 1D lattice. The principal axes of the trap x' and y' are tilted by 45 degrees from the lattice axes x and y, within the horizontal plane. For the experiment shown in Fig. 8.6, the trap frequency weakly depends on U/t with the variations within 10%.

Entropies of atomic gases are numerically calculated using the temperature ob-

tained by fitting Thomas-Fermi distribution to time-of-flight images of harmonically trapped samples. The effect of the repulsive interaction is evaluated within mean-field theory, which predicts entropies up to 6% higher than that the non-interacting gases. The effect of interaction during cloud expansion causes an additional systematic error in entropy, which is estimated to be smaller than 10%. Trap anharmonicity is also evaluated and we conclude that the correction is no more than 5% of the pure harmonic value.

Non-adiabatic heating is observed during the lattice loading process. We compare the spin correlations after the normal loading and the "round-trip" process in which we once decrease the lattice down to the minimum depth where evaporation is negligible, followed by ramping up again. This results in the decrease of singlet-triplet imbalance by 50-60% for all lattice configurations, corresponding one-way heating of $0.2k_B$ per atom in the 1D case. This is consistent with the widely used method of measuring the entropy increase after the gas loaded to and released from the lattice potential, which in our case implying the heating is 0.15-0.35k_B.

8.5.2 SU(6) singlet-triplet oscillations

To generate a spin-dependent potential gradient, we apply an optical Stern-Gerlach laser beam close to the ${}^1S_0 \rightarrow {}^3P_1$ resonance. The detuning of +2.6 GHz from the $F = 5/2 \rightarrow 7/2$ transition is selected to minimize the ratio of the photon scattering rate to the differential light shifts.

The STO signal is analyzed by comparing the total atom number with the number of atoms remaining after removing singlets by photoassociation via the resonance that is located at -812 MHz from the ${}^1S_0 \rightarrow {}^3P_1$ ($F = 7/2$) transition [142]. Assuming that the SU(6) symmetry is not broken, the functional form of the time evolution of

remaining atom number is

$$N(t) = -a\exp(-t/\tau)\left[\cos\omega t + \cos 2\omega t + \cos 3\omega t\right] + b, \tag{8.5}$$

with fitting parameters a, b, τ and ω. The oscillation frequency ω is determined from the differential light shift of each spin pair. In general, a differential light shift of a pair (m_I, m_I') is of the form $\sum_{F'} f(\delta_{F'})[C(F', m_I) - C(F', m_I')]$, where f is a function of the detuning $\delta_{F'}$ from the excited hyperfine states F' and $C(F', m_I)$ is the transition strength. The constant frequency ratio (ω, 2ω, 3ω) follows from the fact that, for linear polarization, $[C(F', m_I) - C(F', m_I')]$ can be reduced to the separated form $C'(F')R(m_I, m_I')$. Photon scattering and inhomogeneity of the gradient due to the Gaussian shape of the OSG beam with intensity $\sim 15\mathrm{W/cm}^3$ cause a decay of STO signal, which is described by the exponential decay term in Eq. (8.5). The gradient beam propagates along the y axis and the measurement along the z axis is chosen to suppress the effect of inhomogeneity.

Among the $\binom{6}{2} = 15$ spin combinations relevant to STO, linearly polarized light gives rise to the differential light shifts for 12 combinations with different absolute values of m_I. The remaining 3 combinations with the same $|m_I|$ do not show STO. Therefore the singlets formed by these pairs are always removed by PA during STOs and the corresponding triplets always remain in the trap. Taking this fact into account, the singlet and triplet fractions in the SU(6) case are expressed as

$$P_s = \frac{1}{N_{\mathrm{ptcl}}}\left[N_{\mathrm{ptcl}} - D + 3a - b\right], \tag{8.6}$$

$$P_{t0} = \frac{1}{N_{\mathrm{ptcl}}}\left[N_{\mathrm{ptcl}} - D - \frac{9a}{2} - b\right]. \tag{8.7}$$

where N_{ptcl} is the total atom number without PA and D is the number of atoms on doubly occupied sites (typically less than 3% of N_{ptcl}) which are independently

measured without merging and STO processes. Multiple occupancies higher than double are negligibly small. PA light causes also one-body loss induced by photon scattering, which gives rise to an overestimate of two-body PA loss. In the presence of one-body loss, the substitution $N(t) \to e^{\gamma\tau_{\rm PA}}N(t)$ is required in analyzing STO, where γ is the one-body loss rate and $\tau_{\rm PA}$ is PA pluse duration. In our experiment, γ is found to be 0.3% of the PA rate and the correction to $N(t)$ is typically 1%. In the SU(2) case the STO is a simple sinusoid, and the analogous expressions are

$$P_s = \frac{1}{N_{\rm ptcl}}\left[N_{\rm ptcl} - D + a - b\right], \tag{8.8}$$

$$P_{t0} = \frac{1}{N_{\rm ptcl}}\left[N_{\rm ptcl} - D - a - b\right]. \tag{8.9}$$

An atom with specific $|m_I|$ can show STOs with two possible frequencies. With OSG separation, the time evolution of the atom number in each separated cloud $N_{|m_I|}$ is described by the two-frequency oscillation

$$N_{|m_I|}(t) = -a\exp(-t/\tau)\left[\cos\omega_{|m_I|,1}t + \cos\omega_{|m_I|,2}t\right] + b, \tag{8.10}$$

with oscillation frequencies

$$(\omega_{|m_I|,1}, \omega_{|m_I|,2}) = \begin{cases} (\omega, 3\omega) & |m_I| = 1/2 \\ (\omega, 2\omega) & |m_I| = 3/2 \\ (2\omega, 3\omega) & |m_I| = 5/2. \end{cases} \tag{8.11}$$

Figure 8.1(d) in the main text agrees well with these behaviors of Eq. (8.10), confirming the validity of the present analysis of STO.

8.5.3 Numerical calculations for homogeneous systems

Determinantal Quantum Monte Carlo (DQMC) and exact diagonalization (ED) calculations are used to obtain the values of the thermodynamic quantities, including the density, entropy, and nearest-neighbor spin correlation function for homogeneous systems. These results are used to compute the properties for the trapped system using the local density approximation (LDA), which is described below.

ED results were obtained in L-site chains by performing full diagonalization over a reduced Hilbert space (described below) and using finite-size scaling. For computational efficiency, we exploit two aspects of the SU(N) symmetry. Particle number conservation for each spin flavor $[N_\sigma, H] = 0$ with $N_\sigma = \sum_j n_\sigma(j)$ and the translation symmetries allow us to block-diagonalize the Hamiltonian. Furthermore, we exploit the spin permutation symmetries $[S^\sigma_\tau, H] = 0 \qquad \forall \sigma, \tau = 1, \ldots, N$ with $S^\sigma_\tau = \sum_i S^\sigma_\tau(i) = \sum_i c^\dagger_{i\sigma} c_{i\tau}$ which relate many of the sectors of the Hamiltonian, and therefore one needs to diagonalize only one representative from each sector.

In addition to the (exact) symmetries, we employ a basis state truncation, which we systematically converge. First, the Hilbert space only includes states with total particle number lesser or equal to a fixed particle number $N_{\max}$. Second, it omits states if the total on-site energy (the energy associated with the presence of multiple occupancies in the cluster) is larger than E_{cut}. We present results obtained from $N_{\max} = L + 1$ and $E_{\text{cut}} = U$ for $L = 5$–7 and $N_{\max} = L$ for $L = 8$. Figure 8.7 shows that the results for the STO amplitude versus entropy with these truncations are converged to $\sim 10^{-5}$.

DQMC results for 4×4 square and $4 \times 4 \times 4$ cubic lattices were obtained by introducing $N(N-1)/2$ auxiliary Hubbard-Stratonovich fields, one for each interaction term $n_{i\sigma} n_{i\tau}$. It is noted that previous works applied DQMC to the half-filled SU($2N$) FHM using a different, discrete complex Hubbard-Stratonovich decomposition [77, 78]. Following our new approach, DQMC calculations for fillings below 1.5

particles per site at $U/t = 15.3$ can be obtained reliably for temperatures $k_B T \geq t$. At lower temperatures, correlation functions become inaccessible to DQMC owing to sign and ergodicity problems. DQMC data were obtained for 5 different random seeds, each with 8000 sweeps through the lattice and the $N(N-1)/2$ auxiliary fields for equilibration and 10000 sweeps for measurements. The inverse temperature was discretized as $\beta = L\Delta\tau$ with a Trotter step of $\Delta\tau = 0.025/t$. Results are obtained in $\mu - T$ grids with $d\mu = 0.25$ and dT given by the Trotter step for all integers $L \geq 2$. These results are linearly interpolated prior to computing the entropy and using the local density approximation. The entropy per site is computed as the integral of the specific heat, which by thermodynamic relations can be rearranged to

$$s(\mu, T) = N \log(2) + \frac{f(\mu, T)}{T} - \int_T^\infty \frac{f(\mu, T')}{T'^2} dT', \tag{8.12}$$

where $f = \epsilon - \mu n$, and ϵ and n are the energy and particle number per site, respectively. In order to accelerate convergence, we obtain DQMC results up to a temperature cutoff T_{cut} and use the leading order high temperature series term ($t = 0$) in the integral in Eq. (8.12) for $T > T_{\text{cut}}$.

8.5.4 Local density approximation

Local values of thermodynamic quantities and correlation functions are obtained using the local density approximation (LDA), which replaces intensive observables at a spatial location $\mathbf{r}$ with their value in a homogeneous system with chemical potential $\mu(\mathbf{r}) = \mu_0 - V(\mathbf{r})$, where μ_0 is the global chemical potential and $V(\mathbf{r})$ is the external confinement. Applied to the total particle number and to total entropy, this gives

$$N_{\text{ptcl}} = \int \frac{d^3 r}{a^3}\, n(\mu_0 - V(\mathbf{r}), T) \tag{8.13}$$

$$S = \int \frac{d^3 r}{a^3}\, s(\mu_0 - V(\mathbf{r}), T) \tag{8.14}$$

where n/a^3 and s/a^3 are the density and entropy density calculated for the homogeneous system. The variables that can be measured experimentally are $N_{\rm ptcl}$ and S rather than μ_0 and T, but, given the homogeneous functions $n(\mu, T)$ and $s(\mu, T)$, the μ_0 and T can be obtained from $N_{\rm ptcl}$ and S by numerically solving Eqs. (8.13)-(8.14).

As derived below, the singlet-triplet oscillation (STO) amplitude A and imbalance I are related to the correlation C_{NN}, defined in Eq. (8.4), and to the correlation $\langle n(i)n(i+1)\rangle$ by

$$A = -\frac{1}{N_{\rm ptcl}}\left[C_{NN}\right]_{\rm tot}, \tag{8.15}$$

$$I = \frac{2A}{\frac{1}{N_{\rm ptcl}}\left[n(i)n(i+1)\right]_{\rm tot} + A} \tag{8.16}$$

in the LDA, where we define

$$\left[\mathcal{O}\right]_{\rm tot} = \int \frac{d^3r}{a^3}\langle \mathcal{O}(\mu(\mathbf{r}), T)\rangle. \tag{8.17}$$

In practice we calculate plots of observable versus T or S as follows. First, we calculate a list of points (T, μ_0) where μ_0 is obtained by solving Eq. (8.13) for given T and the particle number $N_{\rm ptcl}$ measured in experiment. Then for each such obtained (T, μ_0), we calculate S and other trap-summed observables of interest. In this way, we plot trap-summed observables as a function of T. Details on the grid used and discretization error introduced are given below.

8.5.5 Trap geometry

Due to the large atomic mass of Yb, the effect of gravity is severe for our optical trap, especially in the final stage of evaporative cooling [see Fig. 8.4 (a)]. To include the anharmonic effect in our LDA calculation, we evaluate the density of state (DOS)

defined as

$$D(E) = \frac{\partial \Sigma}{\partial E}, \quad \Sigma(E) = \sum_{\text{lattice sites } i} \Theta\left(E - \tilde{V}(\mathbf{r}_i)\right), \tag{8.18}$$

where $\tilde{V}(\mathbf{r}_i)$ is the full external potential at the site i except the periodic part forming optical lattices. Note that this DOS function becomes exact only in the atomic limit $t \to 0$, but is always valid for the use in the LDA integral described below. Trap-summed observables are calculated using Eqs. (8.13-8.17). These integrals over space are then rewritten as integrals over energy with the DOS,

$$[\mathcal{O}]_{\text{tot}} = \int \mathrm{dE}\, D(E) \langle \mathcal{O}(\mu_0 - E, T) \rangle. \tag{8.19}$$

In the harmonic approximation, the DOS is given by

$$D(E) = \frac{2\pi}{a^3} \left(\frac{2}{m\bar{\omega}^2}\right)^{3/2} E^{1/2} \tag{8.20}$$

where $\bar{\omega}$ is the geometric mean of the trap frequencies.

In Fig. 8.4(b), we plot the evaluated DOS for the 3D cubic lattice. In calculating Eq. (8.18), we exclude the spatial region outside the potential barrier, where $\tilde{V}$ becomes a uniformly decreasing function along the direction of gravity [see Fig. 8.4(a)]. In the low energy region the DOS is well reproduced by the harmonic approximation. As energy increases, the DOS starts to exceed the harmonic prediction due to the nearly flat potential where the optical potential gradient is competing with the gravitational one. For even higher energies, the DOS falls below the harmonic approximation because the contribution is limited only from the upper half of the trap. The difference between the results calculated in the harmonic approximation and using the full potential is small, never larger than 2.4×10^{-2} for the normalized STO amplitude and imbalance in the range of entropies presented in the main text.

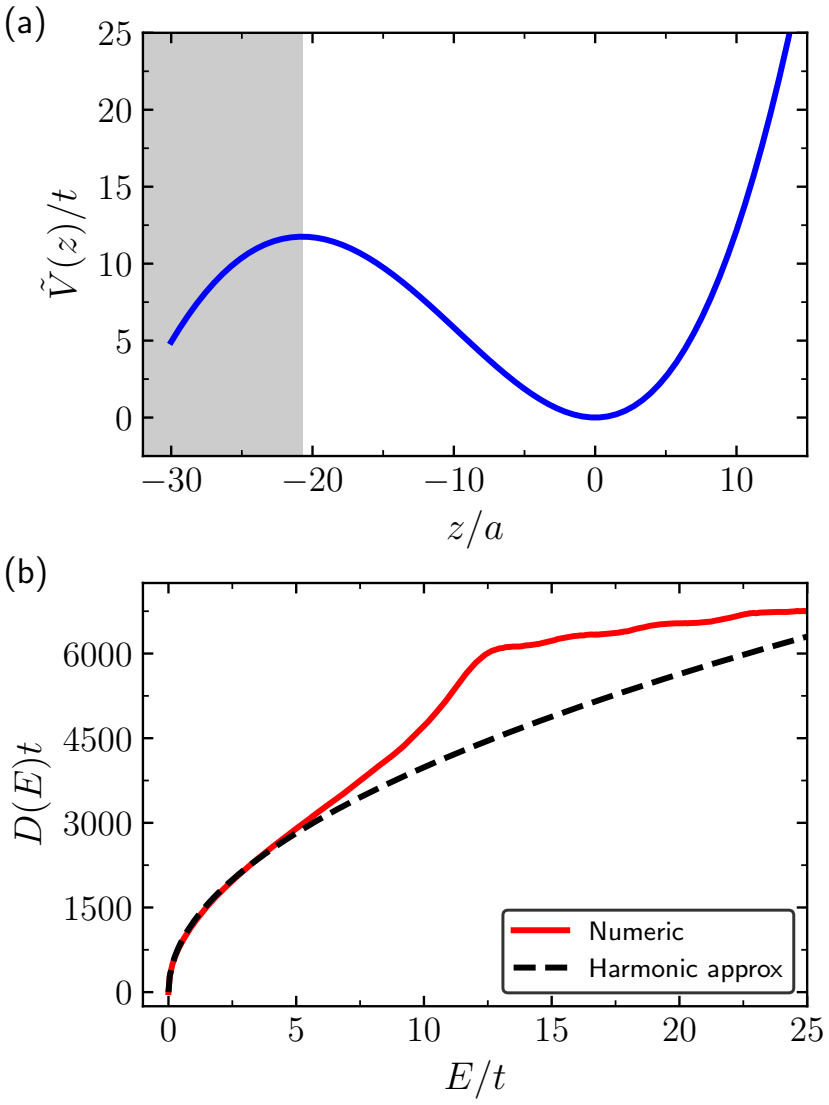

Figure 8.4 : **Trap anharmonicity**. (a) Full external potential (optical + gravity) profile along the direction of gravity z. The shaded region is excluded from the calculation of DOS. (b) Density of states calculated from the external potential for the 3D cubic geometry. The corresponding harmonic approximation is also shown. The atoms are sensitive only to the density of states for $E/t \lesssim 10$.

8.5.6 Singlet-triplet oscillation amplitude and imbalance

In the limit where there are no multiple occupancies, the populations in the singlet and triplet states $p^s_{\sigma\tau}(i)$ and $p^{t0}_{\sigma\tau}(i)$ for an STO with spin components σ and τ in the dimer located on sites i and $i+1$ are given by the expectation value of the projection operators,

$$\widehat{P}^s_{\sigma\tau}(i) = \frac{1}{2}\left(c^\dagger_{i,\sigma}c^\dagger_{i+1,\tau} - c^\dagger_{i,\tau}c^\dagger_{i+1,\sigma}\right) \times \left(c_{i+1,\tau}c_{i,\sigma} - c_{i+1,\sigma}c_{i,\tau}\right), \tag{8.21}$$

$$\widehat{P}^{t0}_{\sigma\tau}(i) = \frac{1}{2}\left(c^\dagger_{i,\sigma}c^\dagger_{i+1,\tau} + c^\dagger_{i,\tau}c^\dagger_{i+1,\sigma}\right) \times \left(c_{i+1,\tau}c_{i,\sigma} + c_{i+1,\sigma}c_{i,\tau}\right). \tag{8.22}$$

Note that these refer to SU(2) singlets involving components σ and τ rather than SU(N) singlets. It is useful to introduce spin-1/2 operators $S^z_{\sigma\tau}(i) = [n_\sigma(i) - n_\tau(i)]/2$ for the pair of states σ and τ. By the SU(N) symmetry the population difference and sum are equal to [67]

$$p^s_{\sigma\tau}(i) - p^{t0}_{\sigma\tau}(i) = -4\langle S^z_{\sigma\tau}(i)S^z_{\sigma\tau}(i+1)\rangle, \tag{8.23}$$

$$p^s_{\sigma\tau}(i) + p^{t0}_{\sigma\tau}(i) = +\frac{1}{2}\langle n(i)n(i+1)\rangle - 2\langle S^z_{\sigma\tau}(i)S^z_{\sigma\tau}(i+1)\rangle. \tag{8.24}$$

The fractions of atoms forming singlets $P_s = N_s/N_{\rm ptcl}$ and triplets $P_{t0} = N_{t0}/N_{\rm ptcl}$ are obtained from a sum over each dimer in the lattice, or equivalently $(1/2)\sum_i \cdots$, and all the possible σ-τ spin pairs,

$$P_s = \frac{2}{N_{\rm ptcl}}\left[\frac{1}{2}\sum_i\left(\frac{1}{2}\sum_{\sigma\neq\tau} p^s_{\sigma\tau}(i)\right)\right], \tag{8.25a}$$

$$P_{t0} = \frac{2}{N_{\rm ptcl}}\left[\frac{1}{2}\sum_i\left(\frac{1}{2}\sum_{\sigma\neq\tau} p^{t0}_{\sigma\tau}(i)\right)\right]. \tag{8.25b}$$

Therefore the global STO amplitude is

$$A = P_s - P_{t0} = \sum_i \sum_{\sigma \neq \tau} \left[\frac{-4\langle S^z_{\sigma\tau}(i) S^z_{\sigma\tau}(i+1) \rangle}{2N_{\text{ptcl}}} \right], \tag{8.26}$$

which in terms of the $n_\sigma(i)$ is

$$\begin{aligned} A &= -\sum_i \sum_{\sigma \neq \tau} \left[\frac{\langle n_\sigma(i) n_\sigma(i+1) \rangle - \langle n_\sigma(i) n_\tau(i+1) \rangle}{N_{\text{ptcl}}} \right] \\ &= -\frac{1}{N_{\text{ptcl}}} \sum_i C_{NN}(i). \end{aligned} \tag{8.27}$$

The STO imbalance I is defined as

$$I = \frac{P_s - P_{t0}}{P_s + P_{t0}} \tag{8.28}$$

so

$$I = \frac{2A}{\frac{1}{N_{\text{ptcl}}} \sum_i \langle n(i) n(i+1) \rangle + A}, \tag{8.29}$$

where $\langle n(i) n(i+1) \rangle$ is the density-density correlation function. Eqs. (8.27-8.29) directly yield Eqs. (8.15) and (8.16).

8.5.7 Thermometry in 1D

In Fig. 8.5 we present how we determine the lowest temperature achieved in the 1D experiments ($k_B T/t = 0.096 \pm 0.054 \pm 0.030$). Estimates based on A rather than I give similar result. The estimate based on the lowest entropy prior to lattice loading predicts somewhat lower temperature, although still consistent within error bars. A small increase in temperature could result from non-adiabatic effects during the lattice loading. In Fig. 8.6, we show the interaction dependence of the spin correlations. The tendency toward larger discrepancy between theory and measurement with larger interactions (equivalent to deeper lattice depths) suggests that heating is important

for deeper lattices.

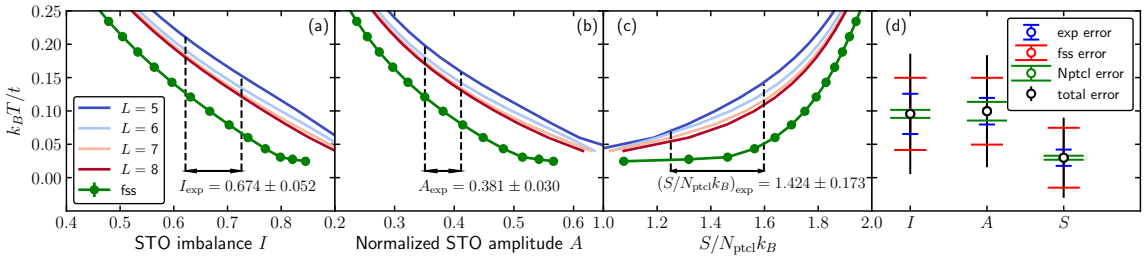

Figure 8.5 : **Temperature of a 1D SU(6) Fermi gas at** $U/t = 15.3$. The vertical dashed lines indicate the range of the largest experimentally measured STO imbalance in 1D that is consistent with error bars. The temperature of this datapoint is inferred from the finite-size scaling curves and the results are summarized in panel (d). The fss error is a conservative estimate of the finite-size error, the difference between the finite-size scaled results and the $L = 8$ site chain. The exp error comes from the experimental uncertainty on the correlations.

8.5.8 Exact diagonalization error estimates

Errors for the exact diagonalization results arise from two sources: finite-size error and truncation of the Hilbert space using the on-site energy and maximum particle number criteria. Figure 8.8 presents the normalized STO amplitude and imbalance for SU(2) and SU(6) in 1D for different system sizes $L = 5, \ldots, 8$, as well as the finite-size extrapolation. Results in the main text are presented after finite-size scaling at fixed entropy per particle, which is performed by fitting the results for $L = 5, \ldots, 8$ to $\mathcal{O}_L = \mathcal{O}_\infty + m/L$ with $\mathcal{O}_\infty$ and m as fitting parameters. Validity of the Hilbert space truncation is tested by varying the energy cutoff $E_{\rm cut}$ as well as the maximum particle number $N_{\rm max}$. Figure 8.7 demonstrates that for the interaction strengths considered herein, the truncation is extremely accurate, with no visible differences for any parameters.

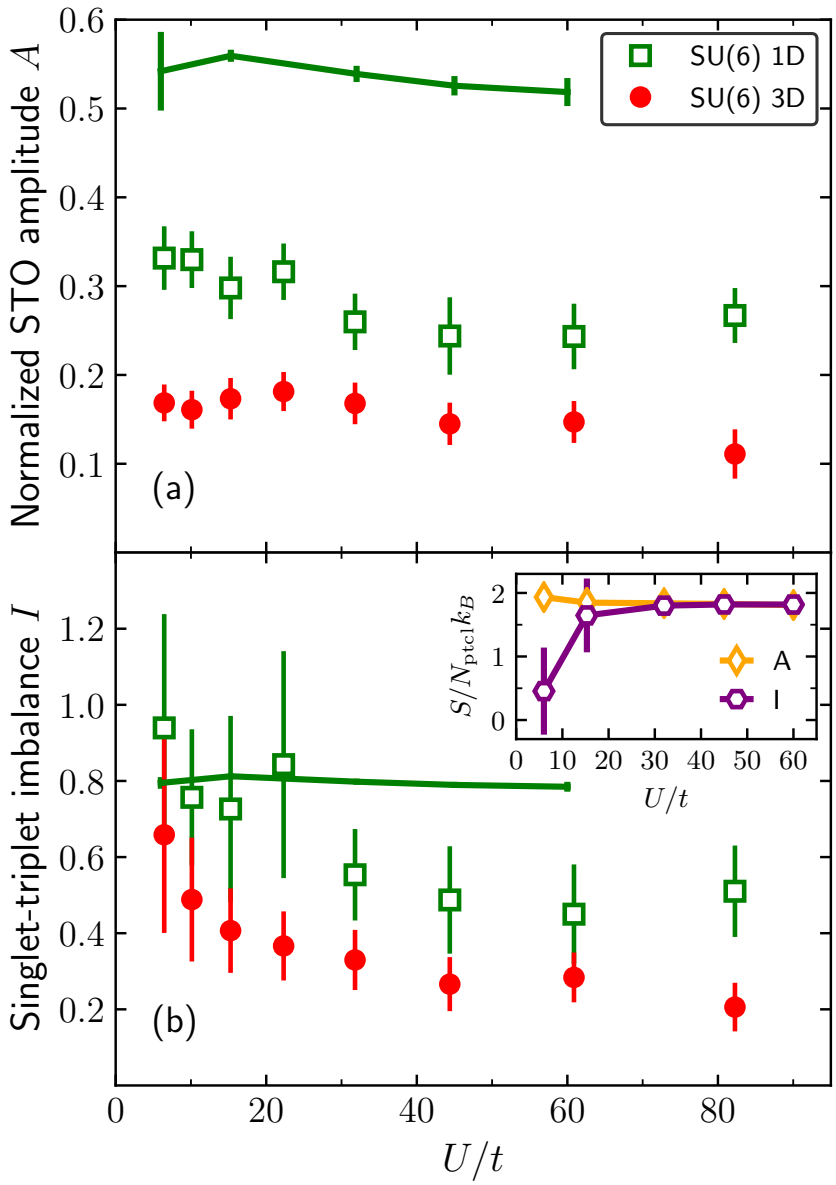

Figure 8.6 : **Interaction dependence of the nearest neighbor correlations**. Behavior of (a) STO amplitude and (b) singlet-triplet imbalance in 1D and 3D lattices are shown. Experimental data is shown for SU(6) systems with initial entropy $S/N_{\rm ptcl}k_B = 1.4 \pm 0.1$. The error bars are extracted from the error of fit in the analysis of the STO signal. Solid lines are the result of exact diagonalization calculations for $S/N_{\rm ptcl}k_B = 1.4$, and the error bars correspond to the sum in quadrature of the finite-size error and the basis-state truncation error. The inset presents the entropy per particle extracted by fitting it to reproduce the experimentally measured spin correlations. Results saturate at $S/N_{\rm ptcl}k_B = 1.818 \pm 0.005$. Error bars in the inset come from the experimental uncertainty on the correlations.

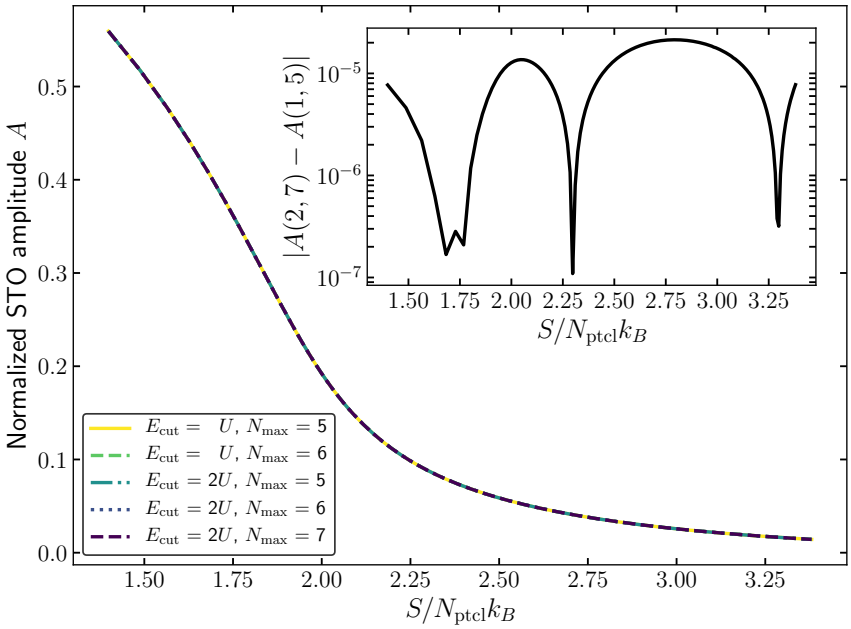

Figure 8.7 : **Normalized STO amplitude for an SU(6) Fermi gas in an $L = 5$ site chain with $U/t = 15.3$ for different truncations of the Hilbert space**. Basis states with an on-site energy larger than the energy cutoff E_{cut}, as well as those that exceed the maximum particle number N_{max} are disregarded. There is no visible difference between calculations. The inset shows the absolute value of the difference between the $E_{\mathrm{cut}} = 2U, N_{\mathrm{max}} = 7$ and $E_{\mathrm{cut}} = U, N_{\mathrm{max}} = 5$ curves.

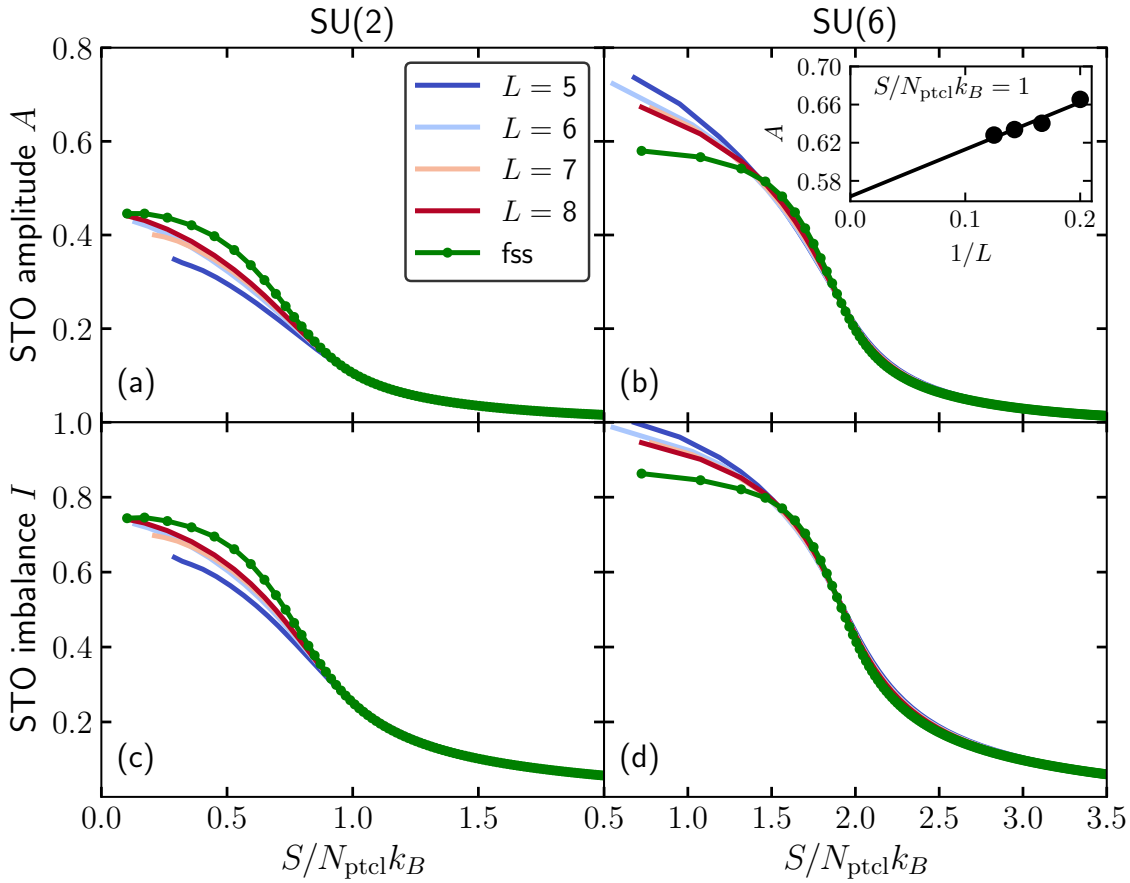

Figure 8.8 : **Finite-size scaling in 1D**. Normalized STO amplitude and imbalance for SU(2) and SU(6) Fermi gases in L-site chains and the results after finite-size scaling (fss) for $U/t = 15.3$. The inset in panel (b) illustrates the finite-size scaling procedure.

8.5.9 Determinantal Quantum Monte Carlo error estimates

DQMC results have several sources of error, which are estimated and presented in Table 8.1 for SU(6) and $U/t = 15.3$, and for SU(3) at $U/t = 8$ in Table 8.2. All error estimates are presented after the adiabatic loading calculation obtained by calculations for a $4 \times 4 \times 4$ lattice at $k_B T/t = 1$ unless explicitly stated otherwise. In this section we will briefly discuss how each error source was estimated.

The largest and most-difficult to quantify error comes from finite-size effects. As a proxy, we estimate finite-size effects in two different ways. Our first estimate is a spot-check comparison between the $3\times3\times3$ and $4\times4\times4$ systems at fixed T/t and density. We obtain $C_{NN}(4 \times 4 \times 4) = -0.096 \pm 0.004$ and $C_{NN}(3 \times 3 \times 3) = -0.125 \pm 0.005$ at the lowest temperature $T/t = 1$ for a homogeneous system at $\langle\rangle = 1$, and this error rapidly decreases with increasing temperature. We note that this error may be dominated by the error of the smaller $3 \times 3 \times 3$ system rather than reflecting the smaller error in the $4 \times 4 \times 4$ system. Our second estimate is by studying 2D, and taking the difference between the 4×4 results and the 6×6 results for the full computations of LDA-averaged observables. Larger system sizes, in particular in 3D, remain inaccessible at present.

The inverse temperature discretization error is estimated as the difference of the results obtained with Trotter steps $\Delta\tau = 0.025$ and $\Delta\tau = 0.05$.

The entropy per site s at temperature T is given by Eq. (8.12). Errors in the calculation of s arise from by the finite value of the temperature cutoff T_{cut}. This error was estimated in the homogeneous case by comparing the results obtained with $k_B T_{\mathrm{cut}}/t = 500$, 800, 1000.

Errors in numerical integration procedures such as the local density approximation summing of observables in the trap and the computation of the entropy are estimated by varying the coarseness of the μ-T integration grids. Such estimations were obtained by coarsening them by a factor of two and comparing the results.

Statistical errors are presented for both the homogeneous case and after adiabatic loading for 5 different random seeds. These errors are presented as the standard error of the mean.

Error source (homogeneous)	S vs T	A vs T	I vs T
Finite T_{cut}	1.3×10^{-4}	–	–
Statistical	1.2×10^{0}	1.8×10^{-1}	8.6×10^{-2}
Error source (in the trap)	S vs T	A vs S	I vs S
Finite size (2D)	1.8×10^{-2}	1.1×10^{-2}	2.4×10^{-2}
Trotter-step	1.8×10^{-2}	4.6×10^{-3}	9.5×10^{-3}
μ grid coarseness	6.9×10^{-3}	7.2×10^{-3}	1.5×10^{-2}
T grid coarseness	1.4×10^{-2}	2.4×10^{-3}	5.3×10^{-3}
Statistical (adiabatic loading)	1.0×10^{-2}	1.6×10^{-3}	3.2×10^{-3}

Table 8.1 : **Error estimates for the DQMC calculation at U/t = 15.3.** Errors are presented at $k_B T/t = 1$. Most errors decrease with increasing temperature. Results in the homogeneous case correspond to the worst case over all μ and T.

Error source	S vs T	A vs S	I vs S
Trotter-step	3.2×10^{-2}	7.8×10^{-4}	2.1×10^{-3}
μ grid coarseness	7.8×10^{-4}	1.6×10^{-4}	5.2×10^{-4}
T grid coarseness	1.3×10^{-1}	1.8×10^{-3}	4.9×10^{-3}
Statistical (adiabatic loading)	2.0×10^{-4}	5.0×10^{-5}	1.2×10^{-4}

Table 8.2 : **Error estimates for the different error sources involved in the DQMC calculation for U/t = 8**. We report the largest error in the whole range of temperatures/entropies considered. The T grid coarseness error for S vs T monotonically increases from 2.0×10^{-2} at $k_B T/t = 0.64$ to the value reported in the table, 1.3×10^{-1}, at $k_B T/t = 4$.

Chapter 9

A two-dimensional programmable tweezer array of fermions

> En los ojos de la gente puede verse lo que verán,
> no lo que han visto
>
> *Novecento.* Alessandro Baricco

This chapter is adapted from publication:

A two-dimensional programmable tweezer array of fermions, Zoe Z Yan, Benjamin M Spar, Max L Prichard, Sungjae Chi, Hao-Tian Wei, **Eduardo Ibarra-García-Padilla**, Kaden R. A. Hazzard, and Waseem S Bakr, arXiv:2203.15023 (under review at Phys. Rev. Lett.) *.

We prepare high-filling two-component arrays of tens of fermionic ^{6}Li atoms in optical tweezers, with the atoms in the ground motional state of each tweezer. Using a stroboscopic technique, we configure the arrays in various two-dimensional geometries with negligible Floquet heating. Full spin- and density-resolved readout of individual sites allows us to post-select near-zero entropy initial states for fermionic quantum simulation. We prepare a correlated state in a two-by-two tunnel-coupled Hubbard plaquette, demonstrating all the building blocks for realizing a programmable fermionic quantum simulator.

9.1 Introduction

Ultracold atoms in optical tweezer arrays have become a popular platform for quantum simulation, computation, and metrology [280]. The tweezer platform has re-

*Complete article, including text, figures, and tables reprinted with copyright permission of Ref. [40].

cently witnessed rapid breakthroughs, ranging from the development of precise optical clocks [281,282] to the demonstration of entangling operations [283–286]. The realization of defect-free arbitrary geometries [287,288], in particular in two dimensions, has paved the way for studying rich quantum many-body physics with localized Rydberg atoms, including frustrated spin models on a triangular lattice [289,290], topological phases in a zig-zag chain [291], and quantum spin liquids with atoms placed on the links of a kagome lattice [292].

The versatility of tweezer arrays has also been extended to systems of itinerant atoms where quantum statistics play a role [39,293–297]. In particular, tunnel-coupled arrays have been realized for small systems of bosonic [293] and fermionic [39,294–296] atoms in one dimensional arrays. If these experiments can be scaled, they would constitute a bottom-up approach toward quantum simulation that complements optical lattice experiments with quantum gas microscopes, which currently lie at the forefront of studying one- and two-dimensional Hubbard models [22–24,59,62,63,65,68,298,299]. The difficulty of reconfiguring microscope experiments has led to an almost exclusive focus on physics in square lattices (Ref. [300] is a recent exception). Programmable Hubbard tweezer arrays would allow the extension of site-resolved studies to arbitrary lattice geometries that bring additional ingredients into play, including frustration, topology, and flat-band physics.

Hubbard tweezer arrays may also provide a route to address another major challenge for optical lattice experiments: the preparation of low-entropy phases of fermions. In optical lattice experiments, the entropy of the gas is limited by evaporative cooling, which is hindered by poor efficiencies at low temperatures. Entropy redistribution schemes relying on the flow of entropy away from gapped phases have been proposed [245,301] and experimentally explored [38], but they have not resulted in significant reduction of achieved temperatures for correlated phases.

Here we show that stroboscopic optical tweezer arrays can be used to prepare

fermionic systems with arbitrary two-dimensional (2D) geometry and entropies comparable to those achieved in optical lattices, with the additional advantage of being able to further reduce the entropy through post-selection. This is possible due to several features particular to this platform. First, in loading a tweezer from a degenerate Fermi gas, the tweezer acts as a "dimple trap," wherein the local Fermi temperature (T_F) is significantly higher than in the bulk gas. Since the fraction of atoms loaded into the tweezers is low, the temperature of the system remains approximately fixed to the bulk gas's temperature, but the tweezers' phase space density is enhanced. Furthermore, the occupancy of the lowest level of each tweezer (given by the Fermi-Dirac distribution) is close to unity. This enables the preparation of a state with two atoms in the ground motional state (one per spin state) on every tweezer with high fidelity, as first demonstrated in Ref. [302]. Second, the system can be evolved from the band insulator into a correlated state via an adiabatic ramp-on of additional sites, taking advantage of independent tunability of each lattice site. We have previously shown that this technique can be used to prepare a state with antiferromagnetic correlations in an eight-site Fermi Hubbard chain [39]. We extend this approach to 2D and show that any pre-ramp entropy in the system can be effectively eliminated by post-selection on the atom number in each spin state. Post-selection is enabled by spin- and density-resolved readout [59, 262], which we implement in a bilayer imaging scheme.

9.2 Experimental setup

The experimental cycle, including tweezer loading, is the same as detailed in Ref. [39]. Tweezers are loaded from a bulk Fermi gas at $T/T_\mathrm{F} \approx 0.2$ that is a balanced mixture of the lowest and third lowest hyperfine ground states ($|\uparrow\rangle$, $|\downarrow\rangle$, respectively). Our scheme for generating 2D arrays uses two crossed acousto-optical modulators [Fig. 9.1(a)]. The tweezers are produced using light with a wavelength of 780 nm, and their waist

at the atoms is 1000^{+180}_{-140} nm. Radiofrequency tones for both AOMs are generated by a two-channel arbitrary waveform generator, with a tone separation of 8 MHz corresponding to a tweezer spacing of 1350 nm in the atom plane. The aperture size and bandwidth of the modulators currently limit us to ~ 9 tweezers in each direction. The beat frequency of neighboring tweezers is > 100 times larger than typical tweezer depths, leading to negligible parametric heating.

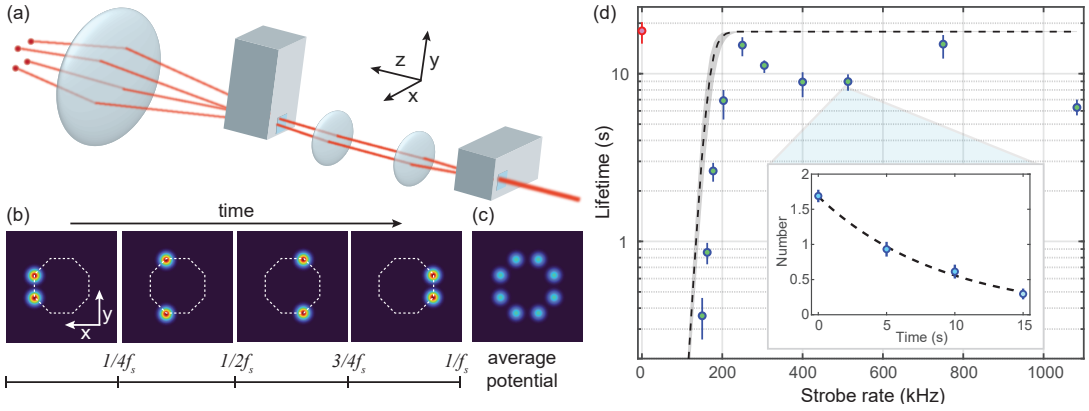

Figure 9.1 : **2D stroboscopic tweezer technique and lifetimes**. (a) Two crossed acousto-optic modulators spaced in a $4f$ configuration generate the array. (b) Illustration of the principle of stroboscopic array generation of an 8-site ring. For a strobe frequency f_s, each column of the array is turned on for a quarter of the period $1/f_s$, generating a time-averaged potential shown in (c). (d) Lifetime of an atom in the ground vibrational state of a tweezer versus strobe frequency, with the red point at 0 kHz indicating the non-strobed lifetime. The dashed line shows the theoretical prediction, and grey shading indicates the systematic uncertainties on the tweezer waist. The inset shows an example of a decay curve of population in the ground state for $f_s = 513$ kHz with an exponential fit.

Homogenizing the tweezer depths is particularly challenging for 2D arrays generated using crossed AOMs. A common approach used in Rydberg tweezer experiments is to apply a static set of frequencies consisting of n_x and n_y tones for the x- and y- directional AOMs, respectively. This generates a rectangular array of $n_x n_y$ sites; however, the $n_x + n_y$ degrees of freedom from the signal strength of each tone are insufficient to independently tune the depth of each tweezer. Better homogeneity can be achieved by tuning the relative phases of the tones, but the typical resultant inho-

mogeneity still exceeds 1%. Tunnel-coupled arrays have more stringent requirements for homogeneity, since the energy offsets in tweezers of typical depth $\sim h\times 50\,\mathrm{kHz}$ must be controlled to within tunneling energies of $\sim h\times 250\,\mathrm{Hz}$, or better than 0.5%.

To homogenize arrays to within this precision and produce arrays with arbitrary geometry, we introduce a stroboscopic tweezer technique. We generate the array one column at a time, with different $y-$directional tones applied in every timestep [Fig. 9.1(b)]. Effectively, the atoms experience a time-averaged potential of concatenated 1D arrays, as long as the strobe rate f_s far exceeds the tweezers' harmonic trap frequencies. As the typical axial (radial) trap frequencies are around $2.5\,(15)\,\mathrm{kHz}$, we need strobe rates over an order of magnitude higher to avoid significant Floquet heating of the atoms.

We verify that the stroboscopic scheme is compatible with long lifetimes in the tweezer ground vibrational state with the following study. We measure the dependence of the lifetime in the lowest vibrational state on f_s in a two-site strobed array, varying the strobe rate from 163-1083 kHz (see Section 9.4.1). Higher frequencies are inaccessible due to limitations on the AOM response rate, set by the speed of sound and beam size in the crystal. We also compare the lifetimes to that of a static (non-strobed) tweezer, which is limited by background gas collisions and off-resonant photon scattering due to the trapping light. Consistent with expectations, the lowest strobe rates give the shortest lifetimes in the ground state [Fig. 9.1(d)]. Measurements and numerics using a discrete variable representation (DVR) method [303,304] (see Section 9.4.2) both indicate that Floquet heating decreases exponentially with increasing f_s and is negligible for $f_s \gtrsim 250\,\mathrm{kHz}$, although the numerics underestimate the threshold frequency range below which severe heating occurs by $\sim 18\%$.

9.3 Results

We demonstrate loading the arrays with band insulators of fermions with high fidelity using the stroboscopic method. These band insulators serve as low entropy initial states for fermionic quantum simulation. As proofs-of-principle, we implement a rectangular 5×5 array, 21-site Lieb plaquette, triangular 4×5 array, and an 8-site octagonal ring (Fig. 9.2, see more details in Section 9.4.3). The tweezers are homogenized using a density balancing algorithm where the number of required experimental shots is almost independent of the array size [39]. In these examples, the sites are not tunnel-coupled due to the large separations. Readout is accomplished by transferring the atoms into a 2D lattice of 752 nm spacing, which oversamples the tweezer array, and performing Raman sideband cooling on the $|\uparrow\rangle$ atoms after removal of the $|\downarrow\rangle$ atoms [39, 68] with a detection fidelity of 98.5%. Throughout these different geometries, the loading fidelity of a single spin averages to 92%/site, corrected for imaging infidelity, indicating a low entropy of loading in the array. As in previous work [39, 302], the tweezer depths are chosen so the predominant type of defect in each tweezer is a missing particle rather than an extra one in a higher motional state. In these data, we only measure one of the spin states in a given experimental shot, due to the problem of light-assisted collisions, which necessitates the removal of the other spin state before imaging [25].

To circumvent this problem and obtain full density- and spin-resolution, we adopt a high-fidelity bilayer imaging scheme [262, 264, 305, 306], which also allows the reduction of entropy upon post-selection. Bilayer density- and spin-readout was first accomplished in fermionic quantum gas microscope experiments in a superlattice charge-pumping scheme [262]. Our method is conceptually similar but involves no superlattice (Fig. 9.3). Starting with tweezer-trapped atoms, we adiabatically turn off the tweezer and turn on a 2D lattice of 1064 nm to 60 E_R and a vertical trap frequency of 1.2 kHz in 5 ms. The magnetic field is brought to 572 G, where we perform

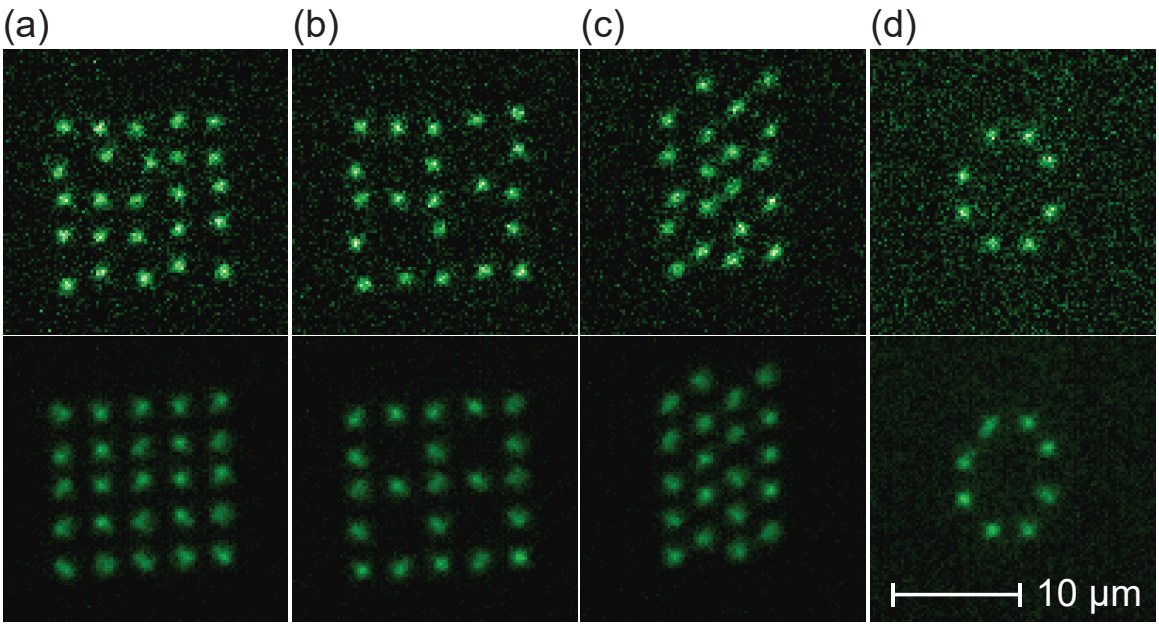

Figure 9.2 : **Examples of band insulators of different geometries**. Showing (a) rectangular 5×5, (b) 21-site Lieb plaquette, (c) 4×5 triangular, and (d) octagonal ring arrays. Only $|\uparrow\rangle$atoms are imaged and the sites here are not tunnel-coupled. The top row shows single shots with perfect filling of the $|\uparrow\rangle$ state, and the bottom row shows average images. Deviations of the atom positions in the single-shot images are due to quantization onto the lattice for imaging. Average fillings of $|\uparrow\rangle$ are (93, 92, 91, 89)%, accounting for imaging fidelity of 98.5%, out of (411, 254 , 275, 100) shots.

a spin-flip of $|\uparrow\rangle$ to the second-lowest hyperfine state, $|\tilde{\uparrow}\rangle$, with an efficiency exceeding 99%, and then decrease the field to near 0 G. Atoms in $|\tilde{\uparrow}\rangle$ and $|\downarrow\rangle$ have a greater differential magnetic moment than those in $|\uparrow\rangle$, enabling the Stern-Gerlach separation of these populations to $\sim 9\mu$m using a z-magnetic gradient of 168 G/cm in the 2D lattice at a depth of $280\,E_R$. We turn on two lightsheet potentials [68]–highly anisotropic beams, each with z-directional trap frequencies of 26 kHz–and linearly ramp their vertical separation to $25\,\mu$m for imaging. We measure a combined transport and spin identification fidelity of 98.7%. Finally, we image the atoms using Raman sideband cooling simultaneously in both layers, with the 2D lattice depth at $2500\,E_R$ and the two lightsheet z-trap frequencies at 70 kHz. Resulting fluorescence is collected by a high numerical aperture objective with atoms in the two planes focused onto two different active areas of a CCD camera. Imaging fidelity is 98% (97%) for the layer

of $|\tilde{\uparrow}\rangle$ ($|\downarrow\rangle$) atoms.

Bilayer imaging enables reduction of the effective entropy associated with the initial state of the tweezer array (the band insulator) through post-selection. The initial entropy per particle of the tweezer ensemble, assuming independent tweezers and single-band occupation, is given by

$$\frac{S}{\langle N\rangle} = -\frac{k_{\mathrm{B}}}{p}\big(p\log p + (1-p)\log(1-p)\big). \tag{9.1}$$

where p is the probability to load one spin on a site. With a typical loading efficiency of $p = 0.907(3)$, the array starts with $0.34(1)\,k_B$ per particle, with entropy entering from microstates with undesired holes. By selecting only images with the population per spin state equal to the number of loading tweezers, we can effectively choose a subsample with $S = 0$. Importantly, this post-selection criterion eliminates the initial state entropy even after changing the filling of the system (by introducing additional tweezers) to prepare a correlated state. The post-selection criterion can be relaxed to use more images from the experiment at the cost of introducing additional initial state entropy. This tradeoff is illustrated in Figs. 9.3(g-h) for a 3×5 array in which $|\uparrow\rangle$ and $|\downarrow\rangle$ had average $p = 0.914(3)$ and $0.900(3)$, respectively (not accounting for imaging fidelity). Out of 972 images, 12% had perfect filling of 15 fermions of each species. However, even keeping images with up to two holes, or over 50% of shots, still results in a low entropy of $0.17(1)\,k_B$ per particle, which is favorable compared to state-of-the-art optical lattice experiments that range from 0.25-0.5 k_B per particle [21,22,38,307].

While post-selection can be used to reduce the effective entropy of the initial state to near zero, subsequent ramps to correlated states will inevitably introduce additional entropy. Numerical simulations of the dynamical ramps in small systems indicate this extra entropy should be low for defect-free initial configurations. For example, for the ramp used in our previous work with an eight-site chain [39], the

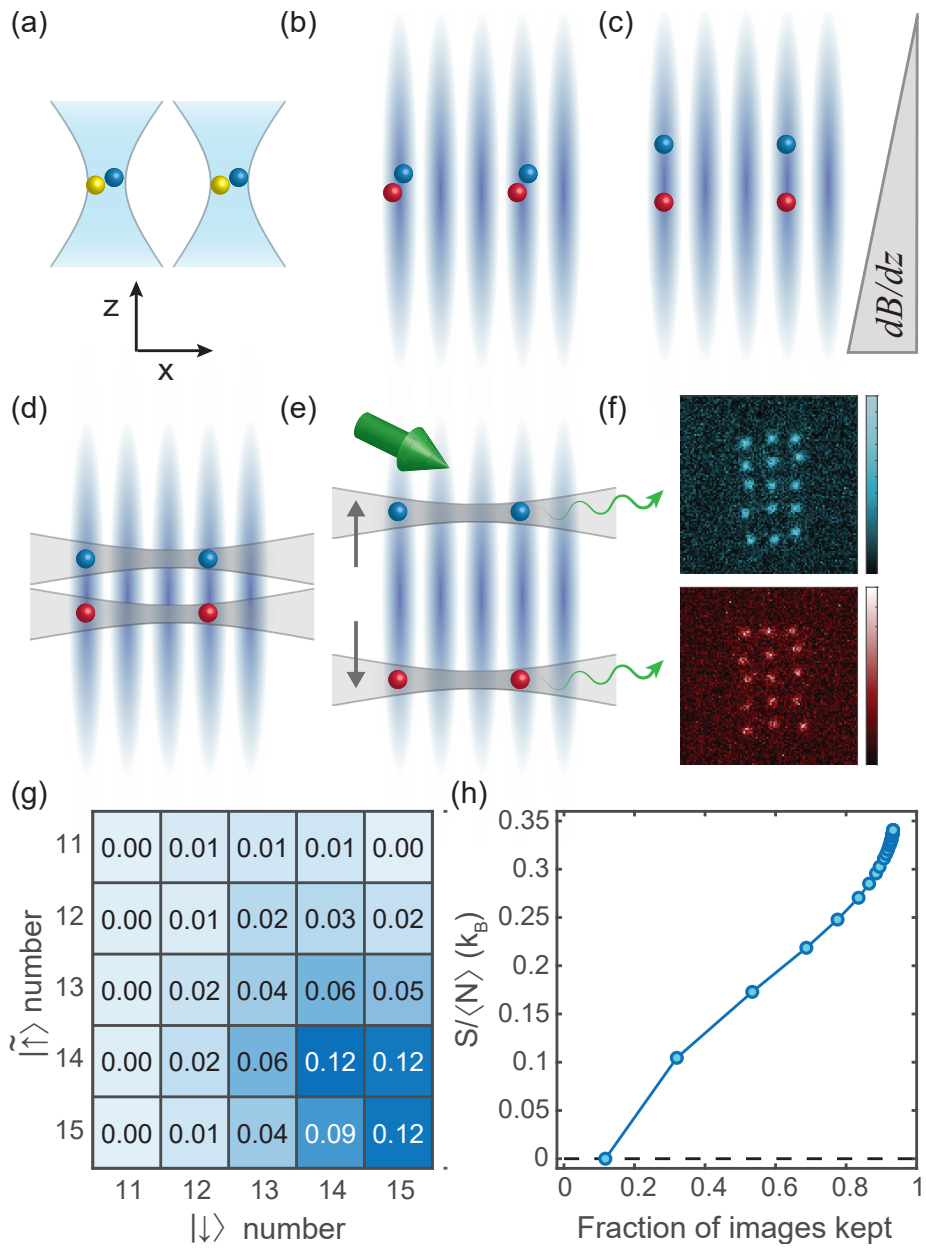

Figure 9.3 : **Bilayer imaging procedure and entropy reduction through post-selection**. (a) Atoms in $|\uparrow\rangle$ (yellow) and $|\downarrow\rangle$ (blue) are initially trapped in the tweezers, then adiabatically loaded into (b) a 2D lattice with vertical waist of 75 μm, where $|\uparrow\rangle$ is transferred to $|\tilde{\uparrow}\rangle$ (red). (c) A magnetic field gradient is applied to separate the spins in the vertical direction, after which (d) two lightsheet potentials turn on to fix the z-positions. (e) The lightsheets are further separated to 25 μm separation. Raman sideband imaging commences, producing simultaneous images of both spin states. (f) shows a single shot image of $|\downarrow\rangle$ and $|\tilde{\uparrow}\rangle$ originally from a 3×5 rectangular array. (g) Probability distribution versus number of atoms in each spin state over 972 shots. Here, all images with doublons (65 shots) were not used. (h) By post-selecting on the maximum number of holes, effective entropy can be reduced by varying amounts.

ramp is expected to have introduced an additional entropy of $0.04\,k_B$ per particle when starting with a defect-free state, but the presence of even a single localized hole would lead to a significant entropy increase of 0.2-0.3 k_B per particle depending on the position of the hole. The entropy reported in Fig. 9.3(h) should therefore be treated only as a lower bound for future experiments.

Post-selection on spin and density in this context should be distinguished from the context of optical lattice-based quantum gas microscopy measurements. For example, in a recent study with a fermionic microscopes [307], spin- and density- readout enabled post-selection of half-filled systems with zero total magnetization, keeping $\sim 9\%$ of data. However, post-selection there did not eliminate the finite spin temperature in the initial state. Furthermore, our post-selection approach is difficult to implement in optical lattice systems where it has proven challenging to engineer arrays with sharp boundaries and a well-defined number of sites [38].

Equipped with the ability to load near-zero-entropy band insulators after post-selection, we implement the simplest building block of a two-dimensional Fermi-Hubbard model: a tunnel-coupled 2×2 plaquette. The single-band Hamiltonian is

$$\hat{H} = -\sum_{\langle i,j\rangle_x,\sigma} t_x(\hat{c}^\dagger_{i\sigma}\hat{c}_{j\sigma}+\text{h.c.}) - \sum_{\langle i,j\rangle_y,\sigma} t_y(\hat{c}^\dagger_{i\sigma}\hat{c}_{j\sigma}+\text{h.c.}) + \sum_i U_i\hat{n}_{i\uparrow}\hat{n}_{i\downarrow} + \sum_{i,\sigma}\Delta_i\hat{n}_{i\sigma}, \quad (9.2)$$

where $\hat{c}^\dagger_{i\sigma}$ is the fermionic creation operator of spin σ at site i, $\hat{n}_{i\sigma}$ is the number operator, $t_{x(y)}$ is the tunneling matrix element in the $x(y)$ direction, Δ is the energy offset, and U is on-site interaction between opposite spin states. We start by loading two diagonal sites in a rectangular array with vertical (horizontal) spacing of 1520 (1690) nm [Fig. 9.4 (a,b)]. The correlated state at half-filling is prepared by adiabatically ramping on the two opposing diagonal sites in 50 ms [39], with tunnelings of $t_x\,[t_y] = h\times 140(5)[220(5)]$ Hz in the final configuration (see Section 9.4.4). We also

ramp $U/\bar{t}$ from 0 to 3.4(2) in the same time using the Feshbach resonance. Here, $\bar{t} = (t_x + t_y)/2$.

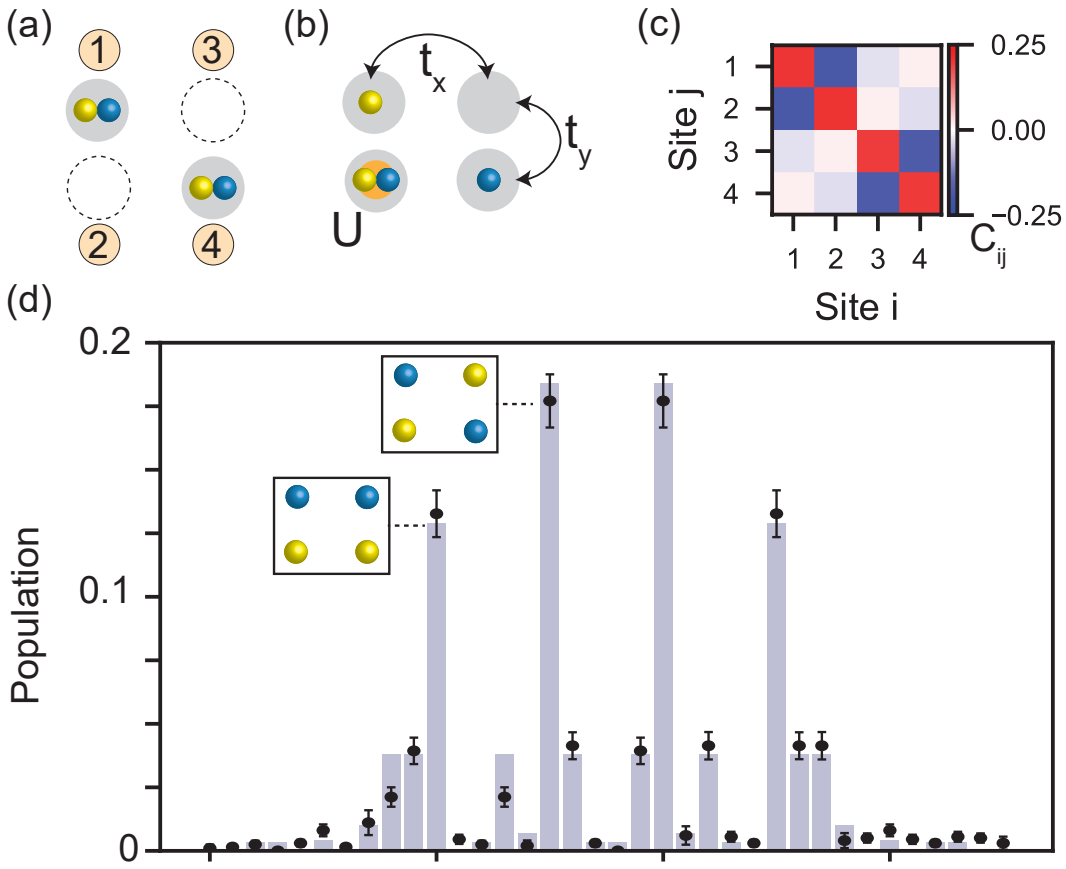

Figure 9.4 : **Low entropy preparation of a 2×2 array**. a) We load two atoms per site on one diagonal of the array. b) We create a correlated state by ramping on the additional lattice sites and increasing the scattering length to introduce on-site interactions. For the following data, we work with $t_x/h = 140(5)$ Hz, $t_y/h = 220(5)$ Hz and $U/\bar{t} = 3.4(2)$. c) Measured spin-spin correlations enabled by the bilayer imaging scheme. d) Best fit (purple bars) and measured (black dots) microstate populations for 671 post-selected experimental shots. The fit gives an entropy in the range [0,0.09] k_B per particle. Insets are shown for the two most common states.

The resulting spin-spin correlations are shown in Fig. 9.4(c), which depicts $C_{ij} = \langle S_{z,i} S_{z,j} \rangle - \langle S_{z,i} \rangle \langle S_{z,j} \rangle$, where $S_{z,i} \equiv \frac{1}{2}(n_{\uparrow,i} - n_{\downarrow,i})$. Here, data were post-selected to include only images that contained two $|\uparrow\rangle$ and two $|\downarrow\rangle$ atoms, for a total of 673 experimental cycles. With full spin- and density-readout, we are able reconstruct the diagonals of the density matrix $\rho = |\Psi\rangle\langle\Psi|$ in the basis of allowed number states

(with Hilbert space size $\binom{4}{2}^2 = 36$), and compare data with theory. In Fig. 9.4(d), we plot the experimental population in each microstate together with the populations expected theoretically for the plaquette ground state, which are consistent within error bars. Here, we reduce our statistical errors by taking advantage of the spin-symmetry of the Hubbard Hamiltonian to average the probabilities for spin-reversed microstates. Furthermore, we fit the temperature of the canonical ensemble to best reproduce the distribution of microstates. The fit gives an upper bound for the temperature of $k_B T \sim 0.3\bar{t}$ (with the fit losing sensitivity below that temperature). This corresponds to an entropy in the range [0,0.09] k_B per particle, which is consistent with the prediction from simulating the ramp dynamics (entropy gain of 0.02 k_B per particle).

9.4 Conclusions

In conclusion, we have realized a 2D tweezer array of fermions with software-programmable geometry using a novel stroboscopic technique that allows independent control over all tweezer depths and positions. We have realized the building blocks to implement programmable 2D Fermi-Hubbard models, and demonstrated these on a small scale. Future work will focus on increasing the system size of the tunnel-coupled arrays. A natural target for future work will be few-leg ladder systems. For example, two-leg triangular ladder systems can be used to explore the $J_1 - J_2$ model, including the special case of the Majumdar-Ghosh model and its valence-bond solid ground states [308]. Furthermore, upon introducing spin-imbalance and hole-doping, a triangular two-leg ladder is predicted to host magnon-hole binding at energy scales set by the tunneling, rather than the superexchange [309]. Multi-leg triangular ladders may potentially host other exotic states such as a chiral spin liquid at half filling and intermediate U/t that evolves to a 120°-antiferromagnetic order at strong U/t [310]. Ultimately, fully 2D tunnel-coupled arrays with arbitrary geometry will be a rich playground for

exploring novel phases of correlated fermions.

9.4.1 Measurement of Floquet heating

To measure the ground state lifetimes shown in Fig. 9.1, we perform the following experiment. We load two tweezers, spaced 8.1 μm apart to avoid any overlap, each with a spin up and a spin down atom. Atoms in higher vibrational states are removed by lowering the tweezer depth and applying a magnetic field gradient, as described in [39]. The tweezer depth is increased to 50 kHz, and a variable hold time is applied. The tweezer light is strobed such that only one tweezer is on at a time, resulting in Floquet heating for low strobe frequencies. Finally, atoms in newly populated higher vibrational states are again removed with an identical spilling process, and the remaining $|\uparrow\rangle$ atoms are imaged.

9.4.2 Theoretical calculations of Floquet heating

We determine the Floquet heating from the strobing of the trap by directly calculating the dynamics of a single atom in a tweezer potential using a method based on a discrete variable representation (DVR) of Hilbert space [303], which was applied to ground state properties of tunnel-coupled tweezers in [293, 304]. The tweezer potential is

$$V(\vec{r}) = -\frac{V_0}{1+\frac{z^2}{z_R^2}} \exp\left[-\frac{2r^2}{w_0^2(1+\frac{z^2}{z_R^2})}\right] \tag{9.3}$$

where V_0 is the trap depth when the tweezer is on, z_R is the Rayleigh range, and w_0 is the trap waist, and we use the measured parameters. We use a DVR basis of spatial-parity-adapted sinc functions on a three-dimensional cubic grid of (N_x, N_y, N_z) points spanning $(0, 0, 0)$ to (L_x, L_y, L_z) to represent our wavefunctions. Only even parity states occur for the dynamics considered.

The procedure is sketched in Fig. 9.5 and we proceed to describe it. The state at

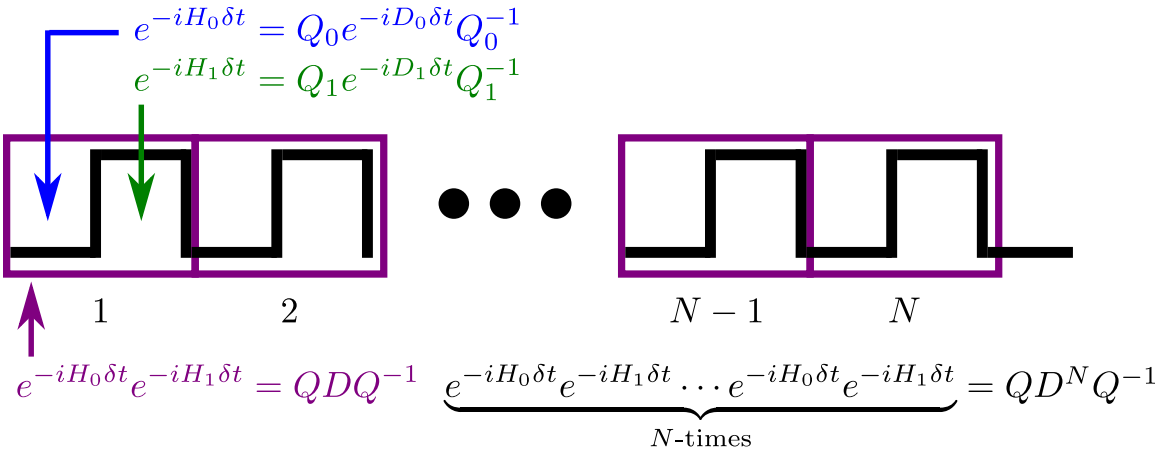

Figure 9.5 : **Theoretical calculations of Floquet heating**. Schematic of the procedure used to calculate Floquet heating.

time t after the strobed time evolution is

$$|\psi(t)\rangle = \underbrace{\left[e^{-i\hat{T}\delta t}e^{-i(\hat{T}+\hat{V})\delta t}\right]\cdots\left[e^{-i\hat{T}\delta t}e^{-i(\hat{T}+\hat{V})\delta t}\right]}_{t/2\delta t \text{ times}}|i\rangle \tag{9.4}$$

where $\hat{T} = -\hbar^2\nabla^2/2m + V_{\text{abs}}(\vec{r})$ is the kinetic energy operator ($\hbar$ is Planck's constant, and m is the mass of ^{6}Li) plus a potential $\hat{V}_{\text{abs}}$ to handle boundary conditions discussed below, $\hat{V}$ is the potential energy operator associated with Eq. (9.3), and $\delta t = 1/(2f_s)$, and assuming $t/2\delta t$ is an integer (the micromotion between such times is discussed later). The initial state $|i\rangle$ is assumed to be the ground state of the system in the time-averaged potential, i.e. of $H_{1/2} = T + V/2$. Directly solving Eq. (9.4) is challenging due to three factors: (1) the tweezer potential is 3D, (2) it involves a wide range of length scales (the wavefunction localization length, the Gaussian waist, and the Rayleigh range), and (3) the dynamics problem must account for a huge separation of timescales when f_s is large, the short time of the pulses and the long lifetime of the atoms, a ratio of timescales of more than 10^7.

We solve this by rewriting Eq. (9.4). First we can diagonalize to obtain $e^{-i\hat{T}\delta t} = U_0 D_0 U_0^{-1}$ where D_0 is diagonal and U_0 is the matrix whose columns are eigenvectors of

$\hat{T}$, obtained by first diagonalizing $\hat{T}$ and then exponentiating. (U_0 need not be unitary since $\hat{T}$ has non-Hermitian terms for the absorbing potential.) Similarly $e^{-i(\hat{T}+\hat{V})\delta t} = U_1 D_1 U_1^{-1}$. Therefore the terms in brackets – denote it $M \equiv e^{-i\hat{T}\delta t} e^{-i(\hat{T}+\hat{V})\delta t}$ – in Eq. (9.4) can be rewritten

$$M = U_0 D_0 U_0^{-1} U_1 D_1 U_1^{-1}. \tag{9.5}$$

One can multiply these matrices, and diagonalize the result to find $M = U_2 D_2 U_2^{-1}$, so

$$|\psi(t)\rangle = M^{t/2\delta t} |i\rangle = U_2 D_2^{t/2\delta t} U_2^{-1} |i\rangle . \tag{9.6}$$

The micromotion at times between integer multiples of $2\delta t$ can be treated by propagating to the largest multiple of $1/f_s$ as above, and then calculating the time evolution within a single period, which is straightforward and efficient in terms of the diagonalized evolution matrices (D_a, U_a) already obtained. The computational cost is dominated by diagonalizing to find D_0, D_1, and D_2, with several additional multiplications. Although this involves full diagonalization of three large matrices, it avoids the issues associated with separation of timescales.

To obtain accurate results, one must use a a fine enough DVR grid and a large enough system. Here, a challenge arises that is absent for ground state calculations: atoms can be excited from the ground state to scattering states and thus escape from the trap. They may move rapidly, and thus would require L_a that grow linearly with time to capture, in practice many orders of magnitude larger than we can calculate. However, in the experiment once particles move sufficiently far outside the trap, the probability they return is negligible. This can be accurately reproduced in the calculations by including an absorbing boundary region in our simulations, a standard

technique in calculations of, e.g., chemical dynamics [311]. We use a potential

$$V_{\text{abs}}(\vec{r}) = -i\Gamma \sum_{a\in x,y,z} \frac{|a| - L_a^{(0)}}{L_a - L_a^{(0)}}. \tag{9.7}$$

This is zero inside the cubic region from the origin to $(L_x^{(0)}, L_y^{(0)}, L_z^{(0)})$, and linearly increases as one moves outside this region. The whole calculation is performed inside a box of size (L_x, L_y, L_z) with (N_x, N_y, N_z) grid points. The calculations are performed with $(L_x^{(0)}, L_y^{(0)}, L_z^{(0)}) = (3, 3, 7.2)w_0$, $N = (27, 27, 23)$; $\Gamma = 57$ kHz; and $L_a = L_a(0) + S_a$ where $S_a \approx w_0$, and are well-converged in the number of grid points and system size (Fig. 9.6). (S_a varies slightly in the right panel: because we fix the grid spacing and ensure that the last grid point in the non-absorbing region doesn't change with L_a, we choose S_a closest to w_0 while constraining L_a to correspond to the location of the last grid points along the a'th direction.) The Γ and S are chosen to be sufficiently large so that particles leaving the trap are absorbed before reaching the boundary of the calculation, but Γ is maintained sufficiently small so that there is no Zeno effect that would reflect the particles. The choices we make are consistent with these conditions, as given in Ref. [311], and our results are insensitive to the specific choice of the parameters. For example, varying Γ over a range of a factor of hundred has a negligible effect on the atom lifetime. Calculated lifetimes are converged to have visually negligible errors from the number of grid points, system size, and absorbing boundary.

Using this method, we calculate the population of the ground state (of the time-averaged potential) as a function of time. We find it gives a nearly perfect exponential decay for the f_s shown, with small deviations from exponential at smaller f_s. The lifetimes shown in Fig. 9.1(d) are obtained by fitting an exponential $e^{-t/\tau}$ to the obtained dynamics. The numerical calculations do not include the effects that give the finite lifetime in the unstrobed tweezer (background gas collisions and off-resonant

light scattering), and which are expected to be the reason for the high-frequency lifetime saturation in Fig. 9.1(d). To incorporate those effects, the theory curve in Fig. 9.1(d) is a simple interpolation $1/\tau_{\text{eff}} = 1/\tau + 1/\tau_{\text{static}}$ where τ_{static} is the lifetime in the unstrobed tweezer. The plot is largely insensitive to the details of this interpolation.

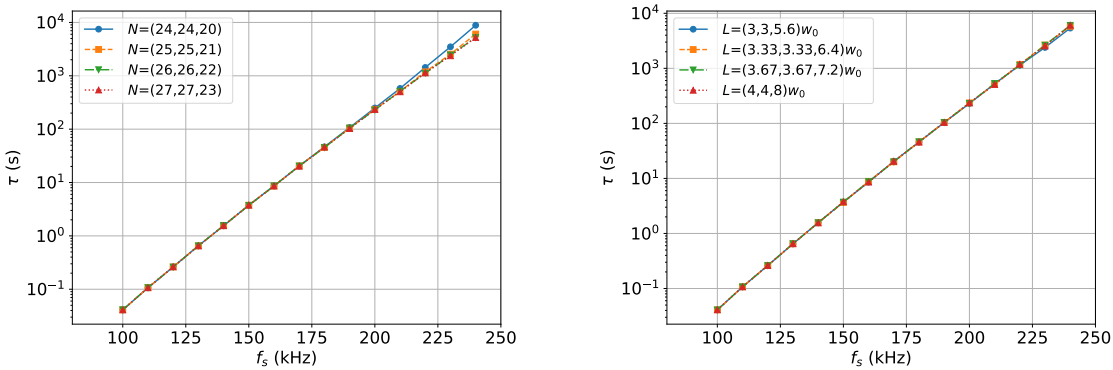

Figure 9.6 : **Convergence of the calculated atom lifetime with respect to number of DVR grid points and system size**. Left: Lifetimes for different numbers of DVR grid points are converged well in the number of grid-points for $(N_x, N_y, N_z) = (25, 25, 21)$ (or more) in systems of size $(L_x^{(0)}, L_y^{(0)}, L_z^{(0)}) = (3, 3, 7.2)w_0$. Right: lifetimes for different system sizes are converged well for $(L_x, L_y, L_z) = (3, 3, 5.6)w_0$ and larger. Right panel is at fixed grid point spacing $(0.16667, 0.166667, 0.4)w_0$, so the N_a vary with L_a. The spacing corresponds to $(N_x, N_y, N_z) = (24, 24, 20)$ for the largest system.

9.4.3 2D Array Generation

Our arrays are generated by two perpendicularly oriented AOMs from AA Optoelectronic (MT110-B50A1,5-IR) driven by a two-channel arbitrary waveform generator (Spectrum M4i.6621-x8 PCIe). In principle, digital micromirror devices or liquid crystal spatial light modulators can be used as alternatives for generating arbitrary arrays; however, these technologies suffer from low bandwidths (100 Hz-several kHz). Furthermore, the lowest spatial disorder demonstrated to date in state-of-the-art experiments with large arrays [312–314] (typically 1-2%) is large compared to the tun-

neling rate between tweezers in a strongly interacting Hubbard system. Therefore we choose to generate arrays with AOMs using a stroboscopic approach.

The typical strobing scheme, illustrated in Fig. 9.1, generates one column of the array at any given time. This gives the most flexibility for creating different geometries. The two AOMs operate with the longitudinal acoustic mode with a high speed of sound (4200 m/s) in the crystal. This speed, along with the aperture size of $1.5 \times 2\,\mathrm{mm}^2$, sets the minimum possible dwell time on a tweezer (the duration for which the tweezer is on). We find that dwell times below $0.5\,\mu s$ produce tweezers with profiles that are significantly distorted along the strobe axis. When generating a two-site array by strobing, we measure that the tweezer waist along the strobe axis increases at 1.4% per increase of 100 kHz strobing rate. Distortions in the tweezer profile can be partly mitigated by applying a cosine-sum window function on the waveform that is sent to the strobed AOM. Given the minimum dwell time per tweezer, the strobe period $1/f_s$ grows linearly with the number of strobed columns. This seemingly limits us to about 8 sites along the strobe axis due to Floquet heating based on the results shown in Fig. 9.1. However, we can surpass this limitation with the technique discussed in the following paragraph.

To reduce Floquet heating and distortion of the tweezer intensity profile, we combine 2D multitone arrays (produced by driving both AOMs with a set of radiofrequency tones) with strobing. For certain geometries, this allows us to reduce tweezer dwell times by using smaller modulation depths. We define modulation depth as the difference between the minimum and maximum relative intensity used over one strobe period. The principle is illustrated in Fig. 9.7 for 50% modulation depth, and was applied for the rectangular, Lieb, triangular, and ring lattices in Fig. 9.2. For the example of Fig. 9.7, a static 2D multitone configuration (modulation depth of 0%) can be used in principle to create the geometry shown, but would not give enough degrees of freedom to homogenize the depths of all sites.

The type of lattices that can be generated with this approach is restricted to combinations of patterns that can be generated by using 2D multitone arrays. Assume each of the two AOMs is driven by a set of tones such that it individually produces tweezers at positions P_x, P_y respectively, where $P_x = \{p_{x,1}, ...p_{x,n}\}$ and $P_y = \{p_{y,1}, ...p_{y,m}\}$. The result when driving both AOMs will be the Cartesian product of the two sets $P_x \times P_y = \{(p_{x,i}, p_{y,j}) \,|\, p_{x,i} \in P_x, p_{y,j} \in P_y\}$. For example, triangular and Lieb lattices can be generated by switching between two multitone rectangular arrays and overlaying a small amplitude strobed array to homogenize the tweezer depths. In general, most 2D patterns of interest that host some level of periodicity can be generated by switching between two or three multitone rectangular arrays at full modulation depth and overlaying a small amplitude strobed array for homogenization. When using 2D multitone arrays, we avoid square geometries, as equidistant tweezer spacing in x and y leads to diagonal sites having near degenerate tones, which results in low frequency beating between these tweezers and atom heating.

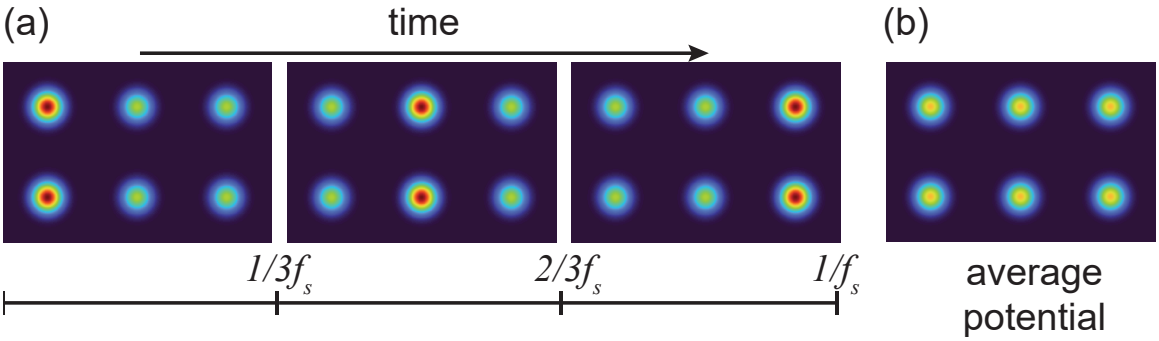

Figure 9.7 : **Illustration of using 50% modulation depth to generate a 2×3 array with strobe rate f_s.** (a) The individual strobe steps and (b) the time-averaged potential. This procedure can be thought of as superimposing a static 2×3 grid on top of a 3-step array with 100% modulation depth.

To scale our system sizes beyond currently demonstrated capabilities, up to the maximal size as limited by Floquet heating and AOM bandwidth, there are two considerations. First, the fidelity of image reconstruction (assigning the fluorescence from an imaging lattice site, spacing of 752 nm, to a unique tweezer site, spacing of

$\sim$1.5 μm) needs improvement for tweezer spacings that are small enough to support tunneling across the array at the $\sim$100 Hz level. We may implement a 532 nm-spaced imaging lattice for better discretization, or move the tweezers apart prior to imaging in the current 752 nm imaging lattice.

Secondly, post-selection will become costly at the current loading fidelity of $\sim$90-91% as the system size increases. In the near future, moderately sized ladder systems will be of interest. As our cycle time is 4 s, an order of magnitude lower than conventional quantum gas microscope experiments, post-selection at the level of even 5% is experimentally feasible. For large systems the loading fidelity must be improved. Indeed, our previous work [39] demonstrated a 96% loading fidelity. The bottleneck in loading fidelity stems from low axial trap frequencies (from large tweezer waists). This puts stringent requirements on intensity stability of the tweezers during the spilling procedure and also results in a poorer separation of tunneling timescales between when the ground vibrational state and the excited vibrational states leak out in this process. Low axial frequencies can be increased by introducing a lattice along the propagation direction of the tweezers, as has been demonstrated in Ref. [315], where ground state fidelities have been measured as high as 97% for two atoms, or 98.5% for a single atom.

9.4.4 2×2 plaquette

We calibrate the tunnelings in the horizontal and vertical directions in the 2×2 array as follows. We first load atoms on only one site, and reduce the tweezer intensities by 5 percent on all other sites except for the one in the direction we want to measure the tunneling. At a non-interacting magnetic field, we quickly initialize tunneling by zeroing the offsets among the target sites [39], and we measure Rabi oscillations between the two sites [293, 294].

To calibrate the on-site interaction energy U, we perform radiofrequency spec-

troscopy and measure the difference between single and double occupied sites. However, the most sensitive way to measure U/t is to fit the distribution of microstates. In particular, for temperatures far below the interaction energy, U/t sensitively determines the number of single occupied sites. The value of U/t reported comes from a best fit of the experimental data, which is in reasonable agreement with an independent spectroscopic calibration [$U/t = 4.4(5)$].

To prepare the 2×2 plaquette ground state, we initialize the ground state of sites 1 and 4 with doublons, as pictured in Fig. 9.4. To achieve a half-filled system, we turn on the opposing diagonal sites in a two-step sequence. First, the intensities of sites 2 and 3 are increased in 5 ms with an exponential time constant of 1 ms, until they are at $\sim$90% intensity of sites 1 and 4. Then, the intensities are further increased in a 50 ms exponential ramp with a time constant of 5 ms, until the offsets are zeroed. During this time, the magnetic field is ramped from a nearly non-interacting system at 573 G to its final value of 631 G using a two-point cubic spline function. A hold time of 4 ms is applied for further equilibration. Finally, tunneling is frozen by rapidly increasing the tweezer intensity to 2.5 times the science depth, and imaging commences.

In this Chapter, for the 2×2 tunneling data we average over states obtained by interchanging $|\uparrow\rangle$ and $|\downarrow\rangle$. This is because all potentials in the system are state independent. This reduces the statistical error due to the limited number of experimental shots (673 shots). Since we do not equalize the disorder entirely to zero, we do not assume any reflection symmetries that could be utilized in the ideal system to further reduce the statistical errors. We show the full microstate distribution without averaging in Fig. 9.8, and the full labelling of microstates in Table 9.1.

Index	$\|\uparrow\rangle$ population	$\|\downarrow\rangle$ population
0	1100	1100
1	1010	1100
2	1001	1100
3	0110	1100
4	0101	1100
5	0011	1100
6	1100	1010
7	1010	1010
8	1001	1010
9	0110	1010
10	0101	1010
11	0011	1010
12	1100	1001
13	1010	1001
14	1001	1001
15	0110	1001
16	0101	1001
17	0011	1001
18	1100	0110
19	1010	0110
20	1001	0110
21	0110	0110
22	0101	0110
23	0011	0110
24	1100	0101
25	1010	0101
26	1001	0101
27	0110	0101
28	0101	0101
29	0011	0101
30	1100	0011
31	1010	0011
32	1001	0011
33	0110	0011
34	0101	0011
35	0011	0011

Table 9.1 : The basis microstates for the data reported in Fig. 9.4. The order of the sites used corresponds to the numbering in Fig. 9.4(a).

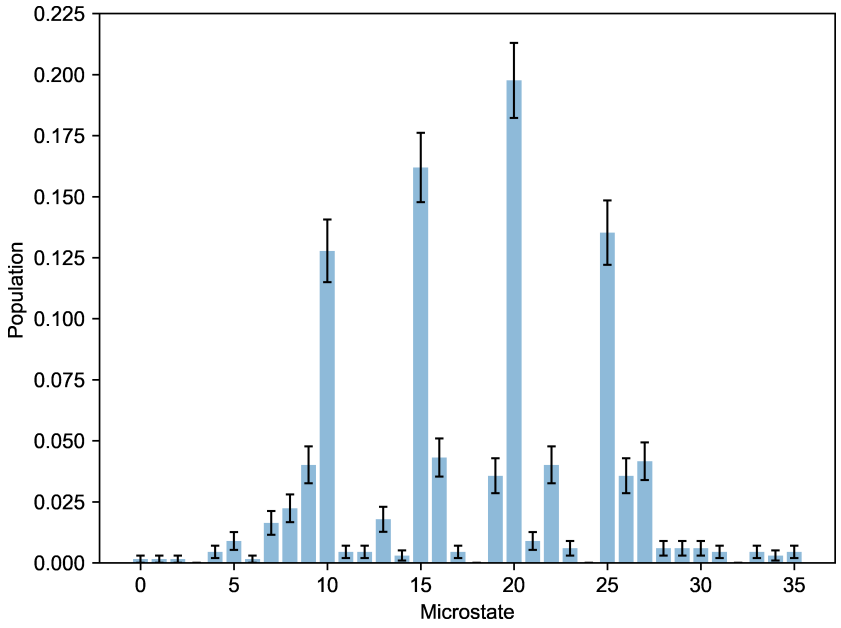

Figure 9.8 : **Full microstate data** for Fig.9.4 without averaging to take advantage of the spin symmetry of the Hamiltonian.

9.4.5 Entropy and Temperature

In order to fit the temperature of our system, we use the canonical ensemble as post-selection enables us to remove number fluctuations. Thus, with free parameters temperature T and U/t, the partition function is the sum over all energy eigenstates Ω, with

$$Z\left(U/t, T\right) = \sum_{\Omega} \exp\left(\frac{-E_{\Omega}(U/t)}{k_b T}\right). \tag{9.8}$$

For each temperature and interaction, we create an expected distribution of microstates, and we compare to the experimental data using a weighted least squares fit. We find that the weighted sum of the squared residuals reaches a local minimum (which depends very weakly on temperature) at $U/t = 3.4(2)$, where the errorbar is extracted from 500 bootstrapped samples of the data. We find that the temperature fit loses sensitivity below $k_B T \sim 0.3\bar{t}$ (Fig 9.9). This corresponds to an entropy range of [0,0.09] k_B per particle. Exact diagonalization performed by in the Python package Quspin [316] suggests that for our ramp parameters, the entropy gain would be

$0.02\,k_B$ per particle.

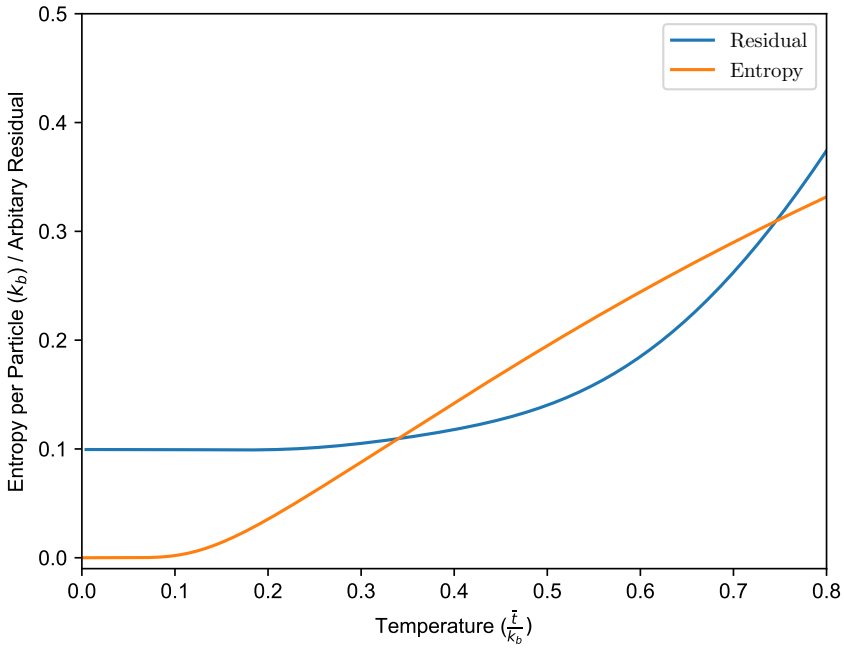

Figure 9.9 : **Entropy and least squares residual as a function of temperature**.Below around $k_BT = 0.3\bar{t}$, the least squares residual is minimized, corresponding to an entropy range of [0,0.09] k_B per particle.

In future studies, we wish to implement larger 2D ladder systems, preparing ground states of half-filled systems by the aforementioned technique of adiabatically ramping on additional tweezer sites. We use exact diagonalization on numerically tractable systems to estimate the many-body gaps sizes and therefore the feasibility of this approach. For instance, on a 2×5 triangular lattice at half filling, at $U/t = 6$, we can perform an adiabatic ramp in 100 ms that will only lead to an increase of 0.06 k_B per particle. For a 2×6 lattice with the same parameters, the increase is 0.07 k_B. These values were obtained by calculating dynamics with experimentally realistic ramp parameters. We are unable to perform exact diagonalization with our computing resources for larger 2D systems.

Chapter 10

Ongoing work on the SU(N) FHM and optical tweezer arrays

> The secret of genius is to carry the spirit of the child into old age, which means never losing your enthusiasm.
>
> Aldous Huxley

In this chapter we present short highlights and/or useful notes of the projects regarding the SU(N) Fermi-Hubbard model and quantum simulation with optical tweezers that we have conducted in the past months and correspond to ongoing work. These include: the precise measurement and characterization of the equation of state of the SU(N) FHM, the study of magnetic correlations for SU(3) fermions in square lattices, and the study of Hubbard parameters in optical tweezers.

10.1 Precise measurement and characterization of the equation of state of the SU(N) FHM

In this work we are collaborating with the group of Simon Fölling at LMU, Germany sparked by the desire to fully characterize the equation of state of the SU(N) FHM engineered with AEAs in optical lattices.

We have performed DQMC calculations in 6×6 lattices and NLCE calculations up to fourth-order for interaction strengths $U/t = 2.34, 7.43, 10.78, 33.34$ at temperatures $T/t \in [0.5, 20]$ and chemical potentials that span the densities $\rho \in [0, 1.5]$. Observables of interest are the density ρ, the number of on-site pairs $\mathcal{D}$, the density-density correlation function $C_d = \langle n_{\mathbf{0}} n_{\mathbf{r}} \rangle - \langle n_{\mathbf{0}} \rangle \langle n_{\mathbf{r}} \rangle$, the spin-spin correlation function $C_s = \sum_{\sigma \neq \tau} [\langle n_{\mathbf{0}\sigma} n_{\mathbf{r}\sigma} \rangle - \langle n_{\mathbf{0}\sigma} n_{\mathbf{r}\tau} \rangle]$, and the quantities $\langle p_\alpha \rangle$ which measure the number

of singly occupied sites "singlons" ($\alpha = 1$), doubly occupied sites "doublons" ($\alpha = 2$), triply occupied sites "triplons" ($\alpha = 3$), etc...

The results obtained numerically are calculated in a homogeneous system, where the chemical potential is constant across all lattice sites. In order to compare with experiments and perform thermometry, the local density approximation (LDA) is used (see Chapter 8 for a discussion on the subject). In Fig. 10.1 we present preliminary results of the equation of state for an SU(6) FHM in a two-dimensional square lattice, comparing our theory to the (unpublished) data from Fölling's group. Markers in blue correspond to the density and in green to the $\sum_{\alpha=\text{odd}} \langle p_\alpha \rangle$, which are obtained by measuring after a photoassociation process that removes pairs of atoms on a given site. In order to perform thermometry, both results are simultaneously fit against NLCE calculations, for which the only free parameter is the temperature.

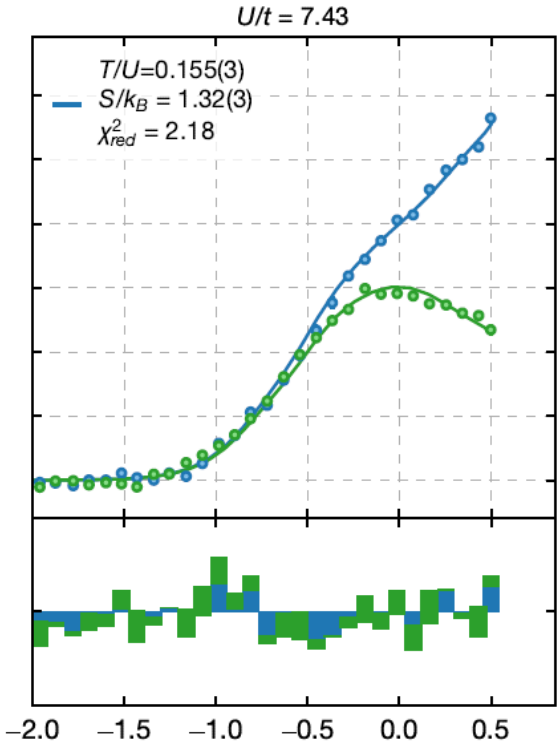

Figure 10.1 : **Equation of State of the SU(6) FHM (preliminary)**. Top: Experimental results for the density (blue markers) and photoassociation data (green markers) are presented for $U/t = 7.43$. Lines in blue and green correspond to fits to the third-order NLCE data. Bottom: Residuals of the fits.

10.1.1 High-Temperature Series Expansion

In addition to numerically exact results, we also derive a second-order HTSE for the quantity $\langle p_\alpha \rangle$. These results allow us to have simple expressions we can also use to compare against experiments and for understanding the relevant physics at different temperatures and fillings. Following a similar derivation as the one Section 5.1 we first obtain the results in the zeroth-order case and then the second-order.

10.1.1.1 Zeroth-order HTSE

In this case $t = 0$, and we define,

$$\epsilon_0(n) = \frac{U}{2} n(n-1) - \mu n + g\delta_{n,\alpha}, \tag{10.1}$$

where the last term is a fictitious term that will allow us to extract $\langle p_\alpha \rangle$ by differentiating with respect to g. The partition function for the single site is given by,

$$z_0 = \sum_{n=0}^{N} \binom{N}{n} e^{-\beta\epsilon_0(n)} \tag{10.2}$$

For simplicity, let us define $y = e^{-\beta U}$, $x = e^{\beta\mu}$, and $w = e^{-\beta g}$. Written like this, the partition function is:

$$z_0 = \sum_{n=0}^{N} \binom{N}{n} y^{\frac{1}{2}n(n-1)} x^n w^{\delta_{n,\alpha}}, \tag{10.3}$$

and the free energy in the grand canonical ensemble is $\Omega_0 = -T \ln z_0$.

In the zeroth-order HTSE,

$$\langle p_\alpha \rangle = \lim_{g\to 0} \frac{\partial \Omega_0}{\partial g} = \frac{1}{z_0} \lim_{g\to 0} -T \frac{1}{z_0} \left[\frac{-w}{T} \frac{\partial z_0}{\partial w} \right] = \lim_{g\to 0} w \sum_{n=0}^{N} \binom{N}{n} y^{\frac{1}{2}n(n-1)} x^n \delta_{n,\alpha} w^{\delta_{n,\alpha}-1}$$

$$\langle p_\alpha \rangle = \frac{1}{z_0} \lim_{g\to 0} \binom{N}{\alpha} y^{\frac{1}{2}\alpha(\alpha-1)} x^\alpha w = \frac{1}{z_0} \binom{N}{\alpha} y^{\frac{1}{2}\alpha(\alpha-1)} x^\alpha. \tag{10.4}$$

Therefore, in the zeroth-order HTSE, we get:

$$\langle p_\alpha \rangle_0 = \frac{\binom{N}{\alpha} y^{\frac{1}{2}\alpha(\alpha-1)} x^\alpha}{\sum_{n=0}^{N} \binom{N}{n} y^{\frac{1}{2}n(n-1)} x^n}. \tag{10.5}$$

The quantities $\langle p_\alpha \rangle$ are related for the zeroth-order HTSE to the density and the number of on-site pairs via the following equations:

$$\langle n \rangle_0 = \sum_{\alpha=1}^{N} \alpha \langle p_\alpha \rangle_0 = \frac{1}{z_0} \sum_{\alpha=0}^{N} \binom{N}{\alpha} \alpha y^{\frac{1}{2}\alpha(\alpha-1)} x^\alpha, \tag{10.6}$$

$$\frac{1}{2}\langle n(n-1) \rangle_0 = \langle \mathcal{D} \rangle_0 = \sum_{\alpha=0}^{N} \binom{\alpha}{2} \langle p_\alpha \rangle_0 = \frac{1}{z_0} \sum_{\alpha=0}^{N} \binom{\alpha}{2} \binom{N}{\alpha} y^{\frac{1}{2}(\alpha-1)} x^\alpha. \tag{10.7}$$

10.1.1.2 Second-order HTSE

Understanding the $g = 0$ limit

Let's consider for a second the case when $g = 0$ in eq. (10.1). This corresponds to the corrections to the free energy presented in Section 5.1:

$$-\beta\Delta\Omega = zN \left(\frac{\beta t}{z_0}\right)^2 \left[\frac{1}{2} \sum_{n=1}^{N} \binom{N-1}{n-1}^2 x^{2n-1} y^{(n-1)^2} - \frac{1}{\beta U} \sum_{n \neq m} \binom{N-1}{n-1} \binom{N-1}{m-1} \frac{x^{n+m-1} y^{\frac{1}{2}[n(n-1)+(m-1)(m-2)]}}{n-m} \right]. \tag{10.8}$$

Which we rewrote for simplicity in terms of $F[f(n,m)]$ and $G[f(n,m)]$ as

$$-\beta\Delta\Omega = zN \left(\frac{\beta t}{z_0}\right)^2 \Big[F[1] + G[1] \Big], \tag{10.9}$$

where

$$F[f(n,m)] = \frac{1}{2}\sum_{n=1}^{N}\binom{N-1}{n-1}^2 x^{2n-1}y^{(n-1)^2}f(n,m) \tag{10.10}$$

$$G[f(n,m)] = -\frac{1}{\beta U}\sum_{n\neq m}\binom{N-1}{n-1}\binom{N-1}{m-1}\frac{x^{n+m-1}y^{\frac{1}{2}[n(n-1)+(m-1)(m-2)]}}{n-m}f(n,m) \tag{10.11}$$

Studying the $g > 0$ case

We are interested deriving expressions for $\langle \Delta p_\alpha \rangle$, therefore the question is how eq. (10.8) gets modified when $g > 0$. The energies of two adjacent sites are:

$$E = \epsilon_0(n) + \epsilon_0(m-1), \tag{10.12}$$

and the energy differences are given by,

$$\Delta = \epsilon_0(n) + \epsilon_0(m-1) - \epsilon_0(n-1) - \epsilon_0(m). \tag{10.13}$$

When $g > 0$, these last 2 expressions get new terms, specifically,

$$E \to E + g\Big(\delta_{\alpha,n} + \delta_{\alpha,n-1}\Big) \tag{10.14}$$

$$\Delta \to \Delta + g\Big(\delta_{\alpha,n} + \delta_{\alpha,m-1} - \delta_{\alpha,m} - \delta_{\alpha,n-1}\Big) \to \Delta. \tag{10.15}$$

The split-up in $n = m$ and $n \neq m$ sums still works fine since $\Delta = 0$ when $n = m$

even when $g > 0$. With these results, the correction to the free energy is now,

$$\begin{aligned}-\beta\Delta\Omega =& zN\left(\frac{\beta t}{z_0}\right)^2\left[\frac{1}{2}\sum_{n=1}^{N}\binom{N-1}{n-1}^2 x^{2n-1}y^{(n-1)^2}w^{\delta_{\alpha,n}+\delta_{\alpha,n-1}}\right.\\ &\left.-\frac{1}{\beta U}\sum_{n\neq m}\binom{N-1}{n-1}\binom{N-1}{m-1}\frac{x^{n+m-1}y^{\frac{1}{2}[n(n-1)+(m-1)(m-2)]}w^{\delta_{\alpha,n}+\delta_{\alpha,m-1}}}{n-m}\right]\\ =& zN\left(\frac{\beta t}{z_0}\right)^2\left[\tilde{F}+\tilde{G}\right]\end{aligned} \tag{10.16}$$

And in order to obtain $\langle\Delta p_\alpha\rangle$ we need to follow the same recipe:

$$\langle\Delta p_\alpha\rangle = \lim_{g\to 0}\frac{\partial\Delta\Omega}{\partial g} = \lim_{g\to 0} -\beta z N t^2\left[\left(\tilde{F}+\tilde{G}\right)\left(\frac{\partial z_0^{-2}}{\partial g}\right)+\frac{1}{z_0^2}\left(\frac{\partial\tilde{F}}{\partial g}+\frac{\partial\tilde{G}}{\partial g}\right)\right]. \tag{10.17}$$

Taking the derivatives and taking the $g \to 0$ ($w \to 1$) limit we get the following expression,

$$\langle\Delta p_\alpha\rangle = zN\left(\frac{\beta t}{z_0}\right)^2\left[-2\langle p_\alpha\rangle_0\big(F[1]+G[1]\big)+F[\delta_{\alpha,n}+\delta_{\alpha,n-1}]+G\left[\delta_{\alpha,n}+\delta_{\alpha,m-1}\right]\right] \tag{10.18}$$

In Fig. 10.2 we present an example of $\langle p_\alpha\rangle$ computed to second-order in a HTSE.

10.1.1.3 Sanity checks: ρ and $\mathcal{D}$

For the zeroth-order HTSE we proved that $\langle n\rangle_0 = \sum_\alpha \alpha\langle p_\alpha\rangle_0$, and $\langle\mathcal{D}\rangle_0 = \sum_\alpha\binom{\alpha}{2}\langle p_\alpha\rangle_0$. We need to convince ourselves the corrections here computed are correctly connected to the corrections to the density $\langle\Delta n\rangle$ and the corrections to the number of on-site

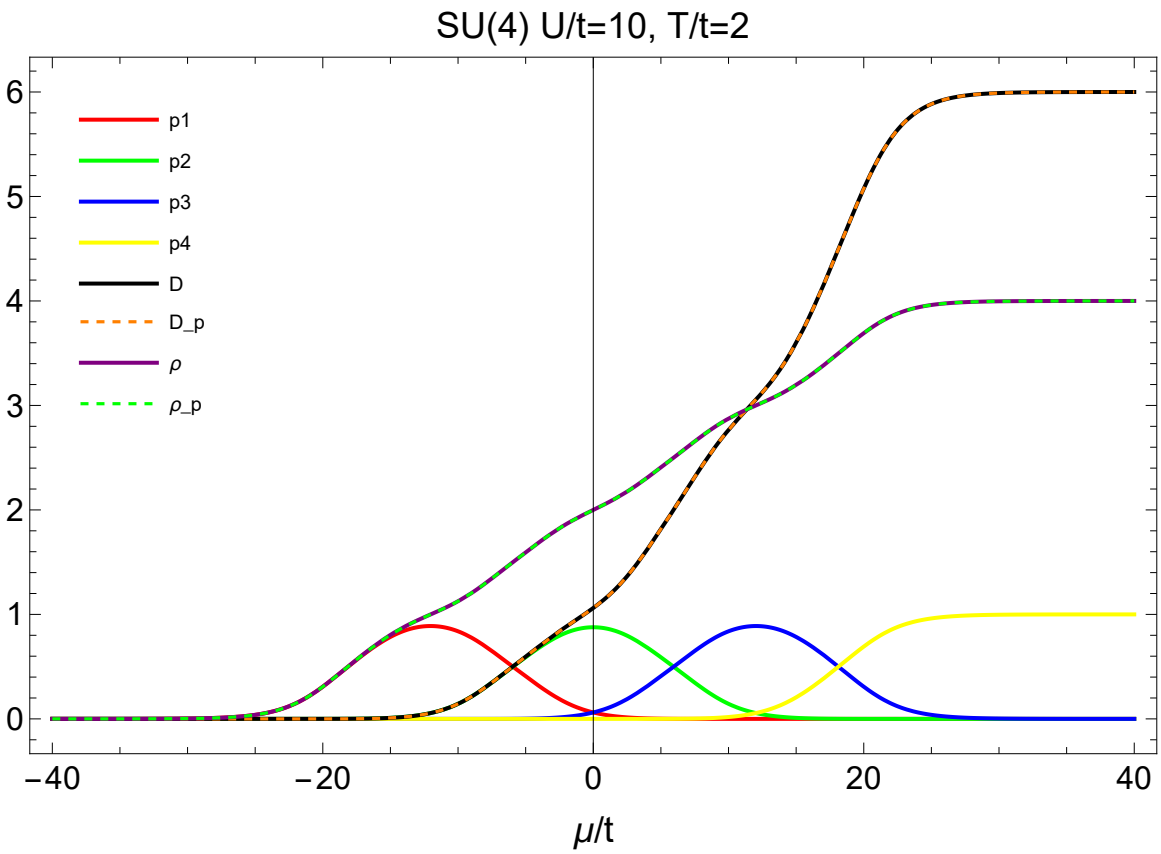

Figure 10.2 : **HTSE results for** $\langle p_\alpha \rangle$. Results for SU(4) at $U/t = 10$ and $T/t = 2$. In solid red, green, blue, and yellow $\langle p_1 \rangle_2$, $\langle p_2 \rangle_2$, $\langle p_3 \rangle_2$, $\langle p_4 \rangle_2$, respectively. Solid black and purple denote $\langle \mathcal{D} \rangle_2$ and $\langle n \rangle_2$ from eqs. (10.20) and (10.19), respectively. In dashed orange and green, the same quantities obtained as the weighted sums of the $\langle p_\alpha \rangle_2$. These expressions agree with each other, which corroborates the validity of our results.

pairs $\langle \Delta \mathcal{D} \rangle$. These 2 are given by,

$$\langle \Delta n \rangle = zN \left(\frac{\beta t}{z_0} \right)^2 \left[-2\langle n \rangle_0 \Big(F[1] + G[1] \Big) + F[2n-1] + G[n+m-1] \right], \quad (10.19)$$

$$\langle \Delta \mathcal{D} \rangle = zN \left(\frac{\beta t}{z_0} \right)^2 \left[-2\langle \mathcal{D} \rangle_0 \Big(F[1] + G[1] \Big) + F[(n-1)^2] + G\left[\frac{n(n-1) + (m-1)(m-2)}{2} \right] \right]. \quad (10.20)$$

In both cases, is clear that the first term in the sum in eq. (10.18) will give rise to the first terms in eqs. (10.19) and (10.20).

For the second term, we get:

$$\begin{aligned}
\sum_{\alpha} \alpha F[\delta_{\alpha,n} + \delta_{\alpha,n-1}] &= \frac{1}{2}\sum_{\alpha=0}^{N} \alpha \binom{N-1}{\alpha}^2 x^{2\alpha+1} y^{\alpha^2} + \frac{1}{2}\sum_{\alpha=0}^{N} \alpha \binom{N-1}{\alpha-1}^2 x^{2\alpha-1} y^{(\alpha-1)^2} \\
&= \frac{1}{2}\sum_{\alpha=1}^{N+1} (\alpha-1) \binom{N-1}{\alpha-1}^2 x^{2\alpha-1} y^{(\alpha-1)^2} \\
&\quad + \frac{1}{2}\sum_{\alpha=0}^{N} \alpha \binom{N-1}{\alpha-1}^2 x^{2\alpha-1} y^{(\alpha-1)^2} \\
&= \frac{1}{2}\sum_{\alpha=0}^{N} (2\alpha-1) \binom{N-1}{\alpha-1}^2 x^{2\alpha-1} y^{(\alpha-1)^2} \\
&= F[2\alpha-1] \qquad (10.21)
\end{aligned}$$

$$\begin{aligned}
\sum_{\alpha} \binom{\alpha}{2} F[\delta_{\alpha,n} + \delta_{\alpha,n-1}] &= \frac{1}{2}\sum_{\alpha=0}^{N} \binom{\alpha}{2} \binom{N-1}{\alpha}^2 x^{2\alpha+1} y^{\alpha^2} + \frac{1}{2}\sum_{\alpha=0}^{N} \binom{\alpha}{2} \binom{N-1}{\alpha-1}^2 x^{2\alpha-1} y^{(\alpha-1)^2} \\
&= \frac{1}{2}\sum_{\alpha=1}^{N+1} \binom{\alpha-1}{2} \binom{N-1}{\alpha-1}^2 x^{2\alpha-1} y^{(\alpha-1)^2} \\
&\quad + \frac{1}{2}\sum_{\alpha=0}^{N} \binom{\alpha}{2} \binom{N-1}{\alpha-1}^2 x^{2\alpha-1} y^{(\alpha-1)^2} \\
&= \frac{1}{2}\sum_{\alpha=0}^{N} \left[\binom{\alpha-1}{2} + \binom{\alpha}{2} \right] \binom{N-1}{\alpha-1}^2 x^{2\alpha-1} y^{(\alpha-1)^2} \\
&= \frac{1}{2}\sum_{\alpha=0}^{N} (\alpha-1)^2 \binom{N-1}{\alpha-1}^2 x^{2\alpha-1} y^{(\alpha-1)^2} \\
&= F[(\alpha-1)^2] \qquad (10.22)
\end{aligned}$$

Where in the 2nd, 3rd, 5th, and 6th lines we shifted the summation indexes, and used the fact that $\binom{x}{y} = 0$ if $y > x$ or $y < 0$.

The final step is to calculate the last term:

$$
\begin{aligned}
-\beta U \sum_{\alpha} \alpha G[\delta_{\alpha,n} + \delta_{\alpha,m-1}] = & \\
& \sum_{\alpha=0}^{N} \alpha \sum_{m \neq \alpha} \binom{N-1}{\alpha-1} \binom{N-1}{m-1} \frac{x^{\alpha+m-1} y^{\frac{1}{2}[\alpha(\alpha-1)+(m-1)(m-2)]}}{\alpha - m} \\
& + \sum_{\alpha=0}^{N} \alpha \sum_{n \neq \alpha+1} \binom{N-1}{n-1} \binom{N-1}{\alpha} \frac{x^{n+\alpha} y^{\frac{1}{2}[n(n-1)+\alpha(\alpha-1)]}}{n - (\alpha+1)} \\
& = \sum_{m \neq \alpha} \alpha \binom{N-1}{\alpha-1} \binom{N-1}{m-1} \frac{x^{\alpha+m-1} y^{\frac{1}{2}[\alpha(\alpha-1)+(m-1)(m-2)]}}{\alpha - m} \\
& + \sum_{\alpha=0}^{N} \alpha \sum_{m \neq \alpha+1} \binom{N-1}{m-1} \binom{N-1}{\alpha} \frac{x^{m+\alpha} y^{\frac{1}{2}[m(m-1)+\alpha(\alpha-1)]}}{m - (\alpha+1)} \\
& = \sum_{m \neq \alpha} \alpha \binom{N-1}{\alpha-1} \binom{N-1}{m-1} \frac{x^{\alpha+m-1} y^{\frac{1}{2}[\alpha(\alpha-1)+(m-1)(m-2)]}}{\alpha - m} \\
& + \sum_{\alpha=1}^{N+1} (\alpha-1) \sum_{m \neq \alpha} \binom{N-1}{m-1} \binom{N-1}{\alpha-1} \frac{x^{\alpha+m-1} y^{\frac{1}{2}[m(m-1)+(\alpha-1)(\alpha-2)]}}{m - \alpha} \\
& = \sum_{m \neq \alpha} \alpha \binom{N-1}{\alpha-1} \binom{N-1}{m-1} \frac{x^{\alpha+m-1} y^{\frac{1}{2}[\alpha(\alpha-1)+(m-1)(m-2)]}}{\alpha - m} \\
& + \sum_{m \neq \alpha} (m-1) \binom{N-1}{\alpha-1} \binom{N-1}{m-1} \frac{x^{\alpha+m-1} y^{\frac{1}{2}[\alpha(\alpha-1)+(m-1)(m-2)]}}{\alpha - m} \\
& = G[\alpha + m - 1] \qquad (10.23)
\end{aligned}
$$

$$
\begin{aligned}
-\beta U \sum_{\alpha} \binom{\alpha}{2} G[\delta_{\alpha,n} + \delta_{\alpha,m-1}] = \\
&\sum_{\alpha=0}^{N} \binom{\alpha}{2} \sum_{m\neq\alpha} \binom{N-1}{\alpha-1}\binom{N-1}{m-1} \frac{x^{\alpha+m-1} y^{\frac{1}{2}[\alpha(\alpha-1)+(m-1)(m-2)]}}{\alpha-m} \\
&+ \sum_{\alpha=0}^{N} \binom{\alpha}{2} \sum_{n\neq\alpha+1} \binom{N-1}{n-1}\binom{N-1}{\alpha} \frac{x^{n+\alpha} y^{\frac{1}{2}[n(n-1)+\alpha(\alpha-1)]}}{n-(\alpha+1)} \\
&= \sum_{m\neq\alpha} \binom{\alpha}{2} \binom{N-1}{\alpha-1}\binom{N-1}{m-1} \frac{x^{\alpha+m-1} y^{\frac{1}{2}[\alpha(\alpha-1)+(m-1)(m-2)]}}{\alpha-m} \\
&+ \sum_{\alpha=0}^{N} \binom{\alpha}{2} \sum_{m\neq\alpha+1} \binom{N-1}{m-1}\binom{N-1}{\alpha} \frac{x^{m+\alpha} y^{\frac{1}{2}[m(m-1)+\alpha(\alpha-1)]}}{m-(\alpha+1)} \\
&= \sum_{m\neq\alpha} \binom{\alpha}{2} \binom{N-1}{\alpha-1}\binom{N-1}{m-1} \frac{x^{\alpha+m-1} y^{\frac{1}{2}[\alpha(\alpha-1)+(m-1)(m-2)]}}{\alpha-m} \\
&+ \sum_{\alpha=1}^{N+1} \binom{\alpha-1}{2} \sum_{m\neq\alpha} \binom{N-1}{m-1}\binom{N-1}{\alpha-1} \frac{x^{\alpha+m-1} y^{\frac{1}{2}[m(m-1)+(\alpha-1)(\alpha-2)]}}{m-\alpha} \\
&= \sum_{m\neq\alpha} \binom{\alpha}{2} \binom{N-1}{\alpha-1}\binom{N-1}{m-1} \frac{x^{\alpha+m-1} y^{\frac{1}{2}[\alpha(\alpha-1)+(m-1)(m-2)]}}{\alpha-m} \\
&+ \sum_{m\neq\alpha} \binom{m-1}{2} \binom{N-1}{\alpha-1}\binom{N-1}{m-1} \frac{x^{\alpha+m-1} y^{\frac{1}{2}[\alpha(\alpha-1)+(m-1)(m-2)]}}{\alpha-m} \\
&= G\left[\frac{\alpha(\alpha-1)+(m-1)(m-2)}{2}\right]
\end{aligned}
\tag{10.24}
$$

Where in the second to last lines for each expression we shifted the summation indexes $\alpha \iff m$, and also used the fact of when do the binomial coefficients vanish. These results corroborate our findings and proof that eq. (10.18) is the correct expression for $\langle p_\alpha \rangle$, valid to second order in βt.

10.1.2 Measuring correlation functions from density fluctuations

In addition, we have derived expressions for a proposed protocol that explains how the measurements of density fluctuations can be utilized to also access spin correlations via shelving * some flavors prior to measurements.

Exploiting the SU(N) symmetry we simplify the expressions for eqs. (3.16) and (3.18). Given the flavor permutation symmetry, the different sums can be replaced by,

$$C_s = N(N-1)\overline{\langle n_{\mathbf{x}\sigma} n_{\mathbf{y}\sigma}\rangle} - N(N-1)\overline{\langle n_{\mathbf{x}\sigma} n_{\mathbf{y}\tau}\rangle}, \tag{10.25}$$

$$\tilde{C}_d = N\overline{\langle n_{\mathbf{x}\sigma} n_{\mathbf{y}\sigma}\rangle} + N(N-1)\overline{\langle n_{\mathbf{x}\sigma} n_{\mathbf{y}\tau}\rangle}, \tag{10.26}$$

where overlined quantities such as $\overline{\langle n_{\mathbf{x}\sigma} n_{\mathbf{y}\tau}\rangle}$ indicate that these are either obtained for a single (σ,τ) pair of flavors, or averaged over all the possible pairs†.

Experiments have access to $\tilde{C}_d = \langle n_{\mathbf{x}} n_{\mathbf{y}}\rangle$ averaged over a few lattice sites. Because of this, it is then useful to derive an expression for the spin-spin correlation function in terms of $\tilde{C}_d$ from eqs. (10.25) and (10.26):

$$C_s = N^2\overline{\langle n_{\mathbf{x}\sigma} n_{\mathbf{y}\sigma}\rangle} - \tilde{C}_d, \tag{10.27}$$

$$C_s = (N-1)\tilde{C}_d - N^2(N-1)\overline{\langle n_{\mathbf{x}\sigma} n_{\mathbf{y}\tau}\rangle}. \tag{10.28}$$

In order to extract $\overline{\langle n_{\mathbf{x}\sigma} n_{\mathbf{y}\sigma}\rangle}$ and $\overline{\langle n_{\mathbf{x}\sigma} n_{\mathbf{y}\tau}\rangle}$ to obtain the spin-spin correlation function one needs to obtain the expression for the density-density correlation function $\tilde{C}_d^{(M)} = \langle n_{\mathbf{x}}^{(M)} n_{\mathbf{y}}^{(M)}\rangle$, where the $^{(M)}$ superscript denotes that only M spin components

*Shelving refers to storing some spin components in the metastable state $^3P_0$, and therefore making it insensitive to the imaging laser.

†Ideally, the latter one would reduce the statistical errors and reduce systematics from possible imabalances in the populations. But the first procedure would allow for a fast readout in a single experimental sequence, and then averages of different realizations can be obtained.

are present in the measurement, i.e. $N - M$ components have been shelved:

$$\tilde{C}_d^{(M)} = M\overline{\langle n_{\mathbf{x}\sigma} n_{\mathbf{y}\sigma}\rangle} + M(M-1)\overline{\langle n_{\mathbf{x}\sigma} n_{\mathbf{y}\tau}\rangle}. \tag{10.29}$$

For any two numbers of shelved species, M and M', one can extract the two correlations,

$$\overline{\langle n_{\mathbf{x}\sigma} n_{\mathbf{y}\tau}\rangle} = \left(\frac{1}{M-M'}\right)\left(\frac{\tilde{C}_d^{(M)}}{M} - \frac{\tilde{C}_d^{(M')}}{M'}\right), \tag{10.30}$$

$$\overline{\langle n_{\mathbf{x}\sigma} n_{\mathbf{y}\sigma}\rangle} = \frac{1}{MM'(M-M')}\left[M(M-1)\tilde{C}_d^{(M')} - M'(M'-1)\tilde{C}_d^{(M)}\right]. \tag{10.31}$$

With these expressions, one can obtain via eqs. (10.30) and (10.31) the spin-spin correlation functions from any two number of shelved species by substituting in eqs. (10.27) and (10.28). For convenience, let's set $M' = N$:

$$C_s(M,N) = \frac{N}{M(M-N)}\left[M(M-1)\tilde{C}_d - N(N-1)\tilde{C}_d^{(M)}\right] - \tilde{C}_d, \tag{10.32}$$

$$C_s(M,N) = (N-1)\tilde{C}_d - N^2(N-1)\left(\frac{1}{M-N}\right)\left(\frac{\tilde{C}_d^{(M)}}{M} - \frac{\tilde{C}_d}{N}\right). \tag{10.33}$$

These 2 equations are equivalent and simplify to,

$$C_s(M,N) = \frac{N-1}{M(N-M)}\left[N^2\tilde{C}_d^{(M)} - M^2\tilde{C}_d\right] \tag{10.34}$$

where $\tilde{C}_d$ corresponds to the number fluctuations in a region for N un-shelved species, and $\tilde{C}_d^{(M)}$ to the number fluctuations in a region for M un-shelved species.

10.2 Mott transition and magnetism of SU(3) fermions in a square lattice

In this project we have focused on studying the $N = 3$ FHM in the square lattice. In particular, we explored two different fillings $\langle n \rangle = 1$ and $\langle n \rangle = 1.5$ since we are interested in understanding how the physics depends on the degree of Fermi Surface nesting.

A question of interest is to understand if results away from the Heisenberg limit [138] survive at lower interaction strengths and if predictions from mean-field and renormalization group [102] are also observed with exact numerical methods. For this reason, we have performed DQMC simulations in 6×6, 8×8 and 12×12 lattices and explored its thermodynamic and magnetic properties.

Preliminary results of DQMC simulations are presented in Fig. 10.3 where spin and density correlation functions are presented for a 6×6 lattice for a single DQMC trajectory at different temperatures at $\langle n \rangle = 1$. Results for the spin degree of freedom illustrate that as temperature is lowered the system starts developing a two-sublattice structure [going from Fig. 10.3(a) to Fig. 10.3(c)] and as one cools further down, a three-sublattice structure starts to emerge Fig. 10.3(e). Averaging over more realizations is needed to reach further conclusions.

10.3 Hubbard parameters in optical tweezers

Although optical lattices are one of the major tools in the quantum simulation community, they are not yet cold enough to access some of the most interesting regions of the FHM phase diagram. In Chapter 9 we discussed the development of quantum simulators using optical tweezer arrays, which might provide a platform to overcome this temperature issue.

Optical tweezers also have the potential to generate arbitrary lattice geometries (see Fig. 10.4) and can study very low entropy systems by a post-selection process.

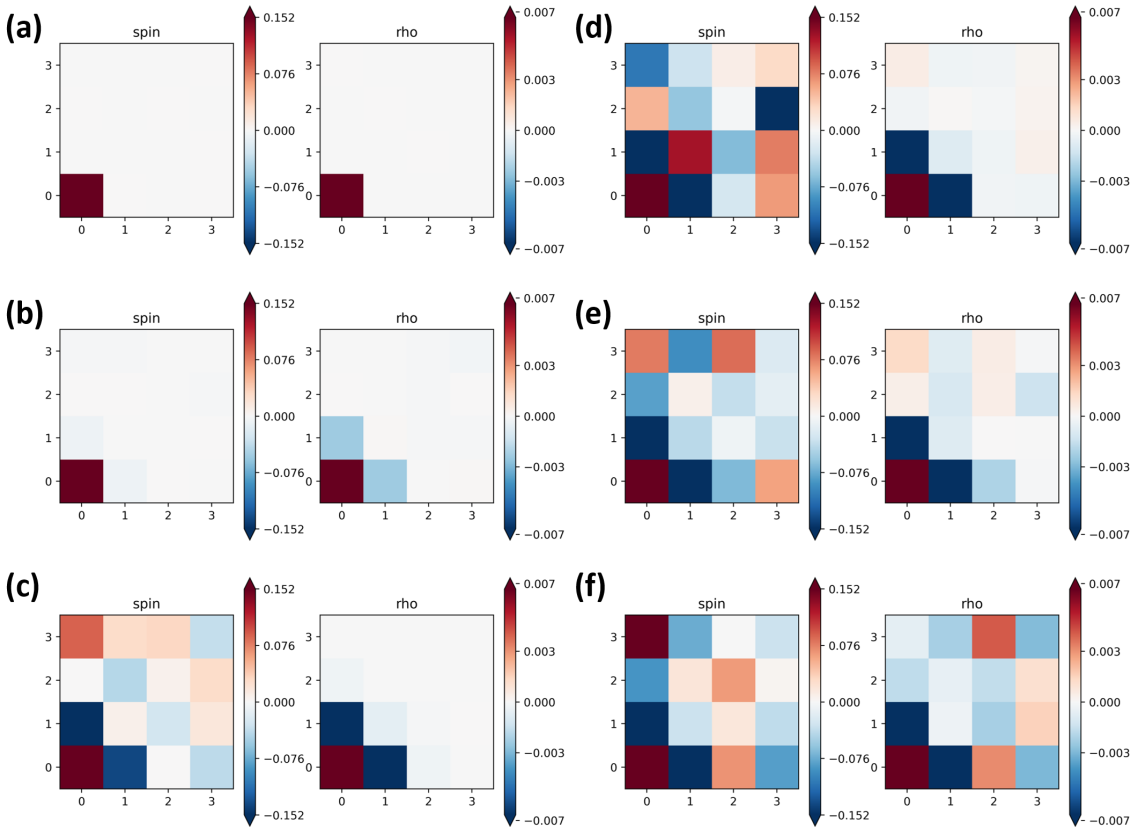

Figure 10.3 : **DQMC correlations in the SU(3) FHM (preliminary)**. $T/t =$ (a) 301.205 (b) 6.250 (c) 0.625 (d) 0.208 (e) 0.156 (f) 0.104.

However these experiments require: 1) a fine and long calibration procedure to ensure coherent tunneling rates, 2) comparison with numerical techniques (ED, NLCE, DQMC) to get access to the Hubbard parameters and the temperature.

One of the complications in optical tweezers that is not present in optical lattices arises from the lack of periodicity in the potential. In Chapter 4 we discussed why ultracold atoms in optical lattices are well described by the single band Fermi Hubbard Model. In particular we discussed how the solution of the eigenvalue problem in a periodic potential can be tackled with Bloch states and the construction of the Wannier functions. In addition to the periodicity, in simple 1D, 2D, and 3D cubic optical lattices the potential is also separable in the three spatial coordinates. These two properties (periodicity and separability) largely simplified the problem as discussed

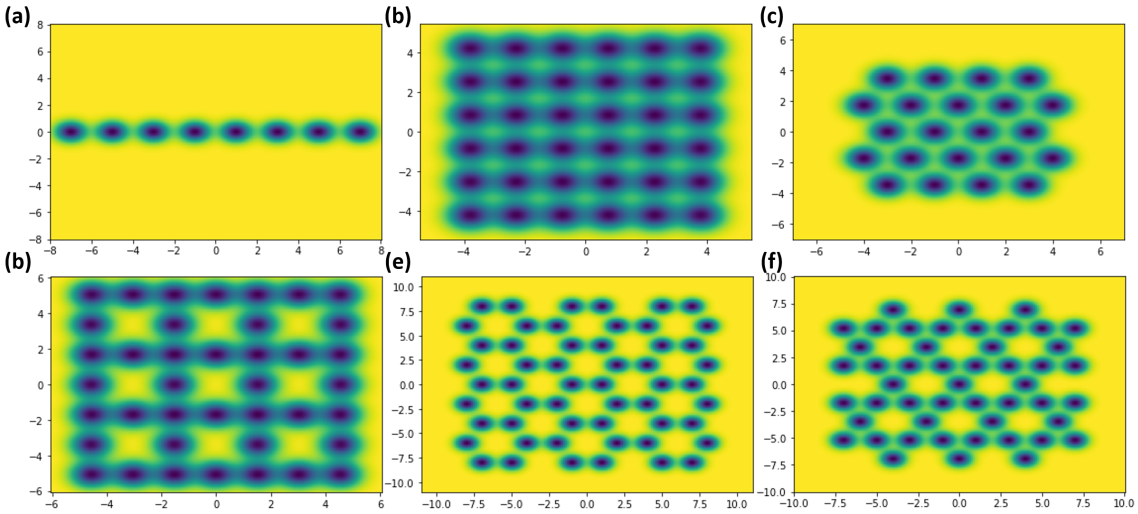

Figure 10.4 : **Examples of tweezer geometries**. (a) Chain (b) Square (c) Triangular (d) Lieb (e) Honeycomb (f) Kagome.

in Chapter 4. On the other hand, for optical tweezer arrays, none of these conditions are satisfied, which means one needs to diagonalize a large Hilbert space and the calculation of the maximally localized Wannier functions requires the construction of a unitary matrix that minimizes the spread of the Wannier functions (accomplished simply by performing a Fourier transform of the Bloch states for the periodic case). In this work, we are developing an algorithm to compute the Hubbard parameters for arbitrary geometries in 1D and 2D. The code receives as an input the experimental parameters and then equalizes the Hubbard parameters for an arbitrary geometry by tuning the separation between tweezers and the individual trap depths and waists (see preliminary Fig. 10.5).

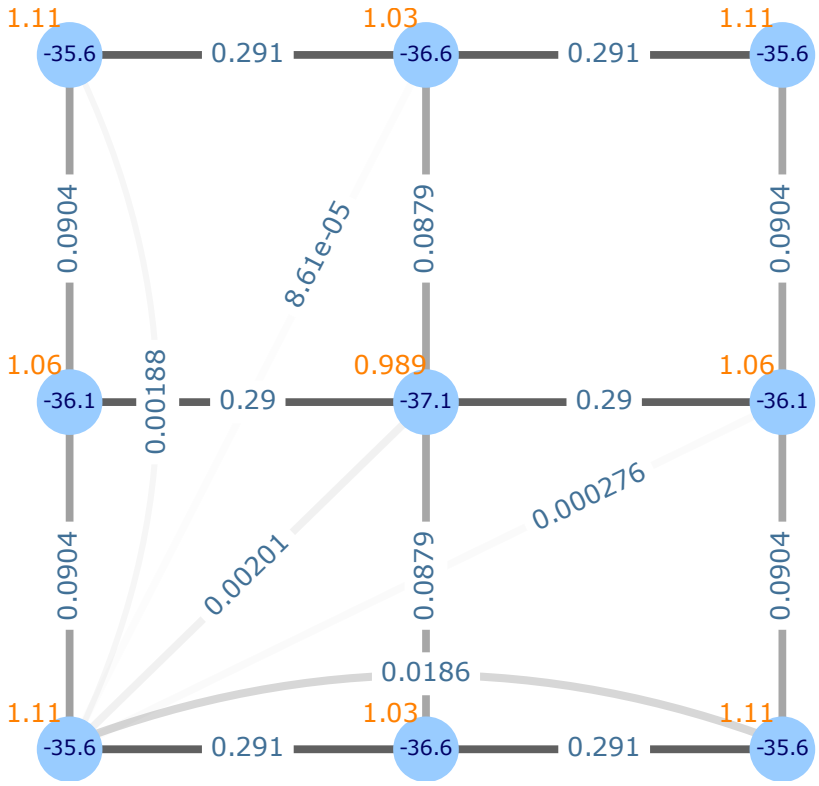

Figure 10.5 : **Example of Hubbard parameter calculation (preliminary)**. The algorithm receives the experimental parameters and then minimizes the cost function that creates the unitary matrix that allows to construct the maximally localized Wannier functions for the eigenstates of the Hamiltonian. Lattice spacings and individual trap depths are varied to equalize the Hubbard parameters t_{ij} (links between sites), Δ the energy offset (blue), and U the on-site interaction (orange).

Chapter 11

Conclusions and future perspective

> El viaje no termina jamás. Sólo los viajeros terminan. Y también ellos pueden subsistir en memoria, en recuerdo, en narración... El objetivo de un viaje es sólo el inicio de otro viaje.
>
> *Viaje a Portugal.* José Saramago

In this thesis we reported on the numerical results of the SU(N) Fermi-Hubbard Model for one-, two-, and three-dimensional cubic lattices for different values of N and interaction strengths U/t. Efforts mainly focused on exploring the $1/N$ filling regime, where most of experiments operate.

Throughout this thesis we discussed results for $N = 2$ in anisotropic lattices, where we realized a cooling protocol could be devised by exploiting how the entropy as a function of density depends on the degree of anisotropy.

Then, in order to study the physics for larger N we had to develop and adapt numerical techniques such as DQMC, ED and NLCE. Although I mainly focused on developing the DQMC algorithm, close collaboration with other graduate students in the group to develop, test, and implement all other numerical techniques has been an exciting journey. Applying these techniques we observed unexpected phenomena as a function of N such as the universal scaling of thermodynamic observables above the superexchange energy J. Furthermore, this has allowed us to build strong collaboration with experimental groups, which have nutured our desire to develop more techniques and come up with proposals to study. Of relevance are the groups of Yoshiro Takahashi with whom we detected the coldest Fermi gas in an optical lattice $T/t \sim 0.1$ and understood that antiferromagnetic nearest-neighbor correlations are

enhanced for larger N and in smaller dimensions. With Simon Fölling we have been performing a precise measurement of the equation of state of the SU(N) FHM.

There are still many areas to explore regarding the SU(N) FHM. In particular, the current development of Constrained Path Quantum Monte Carlo techniques with collaborators Richard Scalettar, Ettore Vitali, Chunhan Feng, Kaden Hazzard and Shiwei Zhang opens the possibility to explore ground state physics without a sign problem. Other Auxiliary DQMC Hubbard Stratonovich decompositions merit further exploration where the possibility of developing a hybrid method could allow for a deeper exploration of phase diagram for various values of N.

Results in spin imbalanced systems, or with different tunneling rates for each spin component open the avenue to study orbital physics and disentangle the effects of Fermi surface nesting. Additionally, the development of quantum gas microscopes opens now the possibility to understand long-range order in these systems.

On the other hand, new architectures, such as optical tweezers will allow for the exploration of low-temperature physics that is currently inaccessible to optical lattices. The degree of control these offers will certainly revolutionize the field of quantum simulation and pose new and exciting challenges for the theoretical groups working in many-body physics.

As I finish writing this thesis, it is a good moment to look at what are future questions of interest in the SU(N) FHM and with optical tweezer arrays. Some directions to explore using these new architectures correspond to:

- A deep understanding of the SU(N) quantum magnetism. In particular, what long-range order phases emerge, and if for large N there is a spin liquid.

- An exploration of the doped phase diagram of the SU(N) FHM, where there are no theoretical predictions yet. A possible starting point is to ask: What occurs when one introduces one hole into a system at $1/N$-filling? What occurs when one introduces two holes? Is behavior of one or two holes the SU(N) systems

similar to their $N = 2$ counterpart?

- A study of the symmetry of the superconducting gap for $N > 2$. What is the equivalent of Cooper pairing for $N > 2$? For $N = 2$ a Cooper pair requires two particles in a singlet state and in the case of the SU(2) FHM the symmetry of the gap is expected to be d-wave. For $N > 2$, N particles are required to form a singlet and an open question is what should be the symmetry of the superconducting gap?

- A thorough study of the doped SU(2) FHM using optical lattices. One of the subjects of debate is if the FHM supports a d-wave superconducting phase. Optical lattices are not yet cold enough to answer this question, but optical tweezers could (using post-selection methods) after they are scaled to larger system sizes.

Bibliography

[1] Anderson P W 1972 *Science* **177** 393–396 1

[2] Martin R M, Reining L and Ceperley D M 2016 *Interacting Electrons: Theory and Computational Approaches* (Cambridge University Press) 2

[3] Phillips P 2012 *Advanced Solid State Physics* 2nd ed (Cambridge University Press) 3

[4] Nolting W 2009 *Fundamentals of Many-body Physics* (Springer) 3

[5] Yamada K 2004 *Electron Correlation in Metals* (Cambridge University Press) 4

[6] Coleman P 2015 *Introduction to Many-Body Physics* (Cambridge University Press) 4

[7] Paschen S and Si Q 2021 *Nat. Rev. Phys* **3** 9–26 4, 5

[8] Auerbach A 1994 *Interacting Electrons and Quantum Magnetism* (Springer) 5, 14, 15, 16, 34, 36, 38, 110, 155

[9] Sachdev S 2011 *Quantum Phase Transitions* (Cambridge University Press) 5

[10] Morosan E, Natelson D, Nevidomskyy A H and Si Q 2012 *Advanced Materials* **24** 4896–4923 5

[11] Pethick C J and Smith H 2008 *Bose-Einstein Condensation in Dilute Gases* 2nd ed (Cambridge University Press) 6, 49, 121

[12] Altman E, Brown K R, Carleo G, Carr L D, Demler E, Chin C, DeMarco B, Economou S E, Eriksson M A, Fu K M C, Greiner M, Hazzard K R, Hulet R G, Kollár A J, Lev B L, Lukin M D, Ma R, Mi X, Misra S, Monroe C, Murch K, Nazario Z, Ni K K, Potter A C, Roushan P, Saffman M, Schleier-Smith M, Siddiqi I, Simmonds R, Singh M, Spielman I, Temme K, Weiss D S, Vučković J, Vuletić V, Ye J and Zwierlein M 2021 *PRX Quantum* **2** 017003 6, 81, 111

[13] 2013 *Nat Phys* **9** 523 6

[14] Esslinger T 2010 *Annual Review of Condensed Matter Physics* **1** 129–152 6, 81

[15] Tarruell L and Sanchez-Palencia L 2018 *Comptes Rendus Physique* **19** 365–393 6, 81

[16] Bloch I, Dalibard J and Nascimbène S 2012 *Nat. Phys.* **8** 267–276 6, 81, 111

[17] Gross C and Bloch I 2017 *Science* **357** 995–1001 6, 81, 111

[18] Jördens R, Strohmaier N, Günter K, Moritz H and Esslinger T 2008 *Nature* **455** 204–207 6, 81

[19] Duarte P M, Hart R A, Yang T L, Liu X, Paiva T, Khatami E, Scalettar R T, Trivedi N and Hulet R G 2015 *Phys. Rev. Lett.* **114** 070403 6, 81, 83

[20] Hart R A, Duarte P M, Yang T L, Liu X, Paiva T, Khatami E, Scalettar R T, Trivedi N, Huse D A and Hulet R G 2015 *Nature* **519** 211 6, 9, 22, 24, 69, 81, 83, 115, 156, 164

[21] Mazurenko A, Chiu C S, Ji G, Parsons M F, Kanász-Nagy M, Schmidt R, Grusdt F, Demler E, Greif D and Greiner M 2017 *Nature* **545** 462 6, 22, 24, 39, 82, 83, 105, 111, 140, 156, 164, 166, 191

[22] Brown P T, Mitra D, Guardado-Sanchez E, Nourafkan R, Reymbaut A, Hébert C D, Bergeron S, Tremblay A M S, Kokalj J, Huse D A, Schauß P and Bakr W S 2019 *Science* **363** 379–382 6, 22, 24, 69, 81, 83, 115, 185, 191

[23] Nichols M A, Cheuk L W, Okan M, Hartke T R, Mendez E, TSenthil, Khatami E, Zhang H and MartinWZwierlein 2019 *Science* **363** 383–387 6, 22, 24, 185

[24] Bohrdt A, Homeier L, Reinmoser C, Demler E and Grusdt F 2021 *Annals of Physics* **435** 168651 6, 24, 110, 185

[25] Gross C and Bakr W S 2021 *Nat Phys* **17** 1316–1323 6, 7, 189

[26] Khatami E, Guardado-Sanchez E, Spar B M, Carrasquilla J F, Bakr W S and Scalettar R T 2020 *Phys. Rev. A* **102** 033326 7

[27] Bohrdt A, Chiu C S, Ji G, Xu M, Greif D, Greiner M, Demler E, Grusdt F and Knap M 2019 *Nat Phys* **15** 921–924 7, 24

[28] Ch'ng K, Carrasquilla J, Melko R G and Khatami E 2017 *Phys. Rev. X* **7** 031038 7

[29] Ch'ng K, Vazquez N and Khatami E 2018 *Phys. Rev. E* **97**(1) 013306 7

[30] Abanin D A, Altman E, Bloch I and Serbyn M 2019 *Rev. Mod. Phys.* **91** 021001 7

[31] Guardado-Sanchez E, Brown P T, Mitra D, Devakul T, Huse D A, Schauß P and Bakr W S 2018 *Phys. Rev. X* **8**(2) 021069 7

[32] Monroe C, Campbell W C, Duan L M, Gong Z X, Gorshkov A V, Hess P W, Islam R, Kim K, Linke N M, Pagano G, Richerme P, Senko C and Yao N Y 2021 *Rev. Mod. Phys.* **93**(2) 025001 7

[33] Semeghini G, Levine H, Keesling A, Ebadi S, Wang T T, Bluvstein D, Verresen R, Pichler H, Kalinowski M, Samajdar R, Omran A, Sachdev S, Vishwanath A, Greiner M, Vuletić V and Lukin M D 2021 *Science* **374** 1242–1247 7

[34] Kittel C 2005 *Introduction to Solid Physics* 8th ed (John Wiley & Sons, Inc) 8

[35] Huang K 1987 *Statistical Mechanics* 2nd ed (John Wiley & Sons, Inc) 8

[36] Hazzard K R A 2011 *Quantum Phase Transitions in Cold Atoms and Low Temperature Solids* Ph.D. thesis Cornell University 8

[37] Ho T L and Zhou Q 2009 *Proceedings of the National Academy of Sciences* **106** 6916–6920 8, 82, 105

[38] Chiu C S, Ji G, Mazurenko A, Greif D and Greiner M 2018 *Phys. Rev. Lett.* **120** 243201 8, 82, 105, 185, 191, 193

[39] Spar B M, Guardado-Sanchez E, Chi S, Yan Z Z and Bakr W S 2022 *Phys. Rev. Lett.* **128** 223202 8, 24, 185, 186, 189, 191, 193, 196, 203

[40] Yan Z Z, Spar B M, Prichard M L, Chi S, Wei H T, Ibarra-García-Padilla E, Hazzard K R A and Bakr W S 2022 *arXiv:2203.15023* 8, 12, 24, 184

[41] Taie S, Ibarra-García-Padilla E, Nishizawa N, Takasu Y, Kuno Y, Wei H T, Scalettar R T, Hazzard K R A and Takahashi Y 2020 *arXiv:2010.07730* 8, 12, 111, 115, 126, 140, 141, 145, 154

[42] Langen T, Geiger R and Schmiedmayer J 2015 *Annual Review of Condensed Matter Physics* **6** 201–217 9

[43] Ibarra-García-Padilla E, Mukherjee R, Hulet R G, Hazzard K R A, Paiva T and Scalettar R T 2020 *Phys. Rev. A* **102** 033340 12, 80, 124, 126, 137, 138, 164

[44] Ibarra-García-Padilla E, Dasgupta S, Wei H T, Taie S, Takahashi Y, Scalettar R T and Hazzard K R A 2021 *Phys. Rev. A* **104** 043316 12, 109, 166

[45] Anderson P W 1987 *Science* **235** 1196–1198 14, 26

[46] Imada M, Fujimori A and Tokura Y 1998 *Rev Mod Phys* **70**(4) 1039–1263 14, 26, 110

[47] Montorsi A (ed) 1992 *The Hubbard Model: A reprint volume* (World Scientific) 14, 26, 110

[48] Tasaki H 1998 *J. Phys.: Condens. Matter* **10** 4353 14, 21, 110

[49] Arovas D P, Berg E, Kivelson S A and Raghu S 2022 *Annual Review of Condensed Matter Physics* **13** 239–274 14, 21, 22, 110

[50] Qin M, Schäfer T, Andergassen S, Corboz P and Gull E 2022 *Annual Review of Condensed Matter Physics* **13** 275–302 14, 110

[51] Duarte P M 2014 *Observation of antiferromagnetic correlations in the Fermi-Hubbard model* Ph.D. thesis Rice University 18, 47, 58

[52] Qin M, Chung C M, Shi H, Vitali E, Hubig C, Schollwöck U, White S R and Zhang S (Simons Collaboration on the Many-Electron Problem) 2020 *Phys. Rev. X* **10** 031016 18, 110

[53] Werner F, Parcollet O, Georges A and Hassan S R 2005 *Phys Rev Lett* **95** 056401 19

[54] dos Santos R R 2003 *Braz J Phys* **33** 36 21, 69, 70, 72, 75, 246

[55] Iglovikov V I, Khatami E and Scalettar R T 2015 *Phys Rev B* **92** 045110 21, 72, 79, 122

[56] Lee P A 2008 *Reports on Progress in Physics* **71** 012501 22

[57] Chen T, Yi M and Dai P 2020 *Frontiers in Physics* **8** 22

[58] Keimer B, Kivelson S A, Norman M R, Uchida S and Zaanen J 2015 *Nature* **518** 179–186 23

[59] Boll M, Hilker T A, Salomon G, Omran A, Nespolo J, Pollet L, Bloch I and Gross C 2016 *Science* **353** 1257–1260 22, 82, 156, 185, 186

[60] Imriška J, Iazzi M, Wang L, Gull E, Greif D, Uehlinger T, Jotzu G, Tarruell L, Esslinger T and Troyer M 2014 *Phys. Rev. Lett.* **112** 115301 22, 81, 83, 164

[61] Scherg S, Kohlert T, Herbrych J, Stolpp J, Bordia P, Schneider U, Heidrich-Meisner F, Bloch I and Aidelsburger M 2018 *Phys. Rev. Lett.* **121** 130402 22

[62] Parsons M F, Mazurenko A, Chiu C S, Ji G, Greif D and Greiner M 2016 *Science* **353** 1253–1256 22, 24, 82, 111, 164, 185

[63] Cheuk L W, Nichols M A, Lawrence K R, Okan M, Zhang H, Khatami E, Trivedi N, Paiva T, Rigol M and Zwierlein M W 2016 *Science* **353** 1260–1264 22, 24, 82, 83, 115, 164, 185

[64] Brown P T, Guardado-Sanchez E, Spar B M, Huang E W, Devereaux T P and Bakr W S 22

[65] Ji G, Xu M, Kendrick L H, Chiu C S, Brüggenjürgen J C, Greif D, Bohrdt A, Grusdt F, Demler E, Lebrat M and Greiner M 2021 *Phys. Rev. X* **11** 021022 22, 24, 111, 185

[66] Koepsell J, Bourgund D, Sompet P, Hirthe S, Bohrdt A, Wang Y, Grusdt F, Demler E, Salomon G, Gross C and Bloch I 2021 *Science* **374** 82–86 22, 24, 111

[67] Greif D, Uehlinger T, Jotzu G, Tarruell L and Esslinger T 2013 *Science* **340** 1307–1310 24, 81, 82, 115, 156, 158, 176

[68] Brown P T, Mitra D, Guardado-Sanchez E, Schauß P, Kondov S S, Khatami E, Paiva T, Trivedi N, Huse D A and Bakr W S 2017 *Science* **357** 1385–1388 24, 69, 83, 115, 185, 189, 190

[69] Chiu C S, Ji G, Bohrdt A, Xu M, Knap M, Demler E, Grusdt F, Greiner M and Greif D 2019 *Science* **365** 251–256 24, 81

[70] Salomon G, Koepsell J, Vijayan J, Hilker T A, Nespolo J, Pollet L, Bloch I and Gross C 2019 *Nature* **565** 56–60 24

[71] Taie S, Yamazaki R, Sugawa S and Takahashi Y 2012 *Nat Phys* **8** 825 24, 42, 64, 111, 121, 141, 161

[72] Li Y Q, Ma M, Shi D N and Zhang F C 1998 *Phys. Rev. Lett.* **81** 3527–3530 27, 37, 110, 155, 159

[73] Tokura Y 2000 *Science* **288** 462–468 27, 37, 110, 155

[74] Dagotto E, Hotta T and Moreo A 2001 *Physics reports* **344** 1–153 27, 37, 110

[75] Hermele M, Gurarie V and Rey A M 2009 *Phys Rev Lett* **103** 135301 27, 39, 110, 111, 156

[76] Hermele M and Gurarie V 2011 *Phys Rev B* **84** 174441 27, 39, 110, 111, 155, 167

[77] Wang D, Li Y, Cai Z, Zhou Z, Wang Y and Wu C 2014 *Phys Rev Lett* **112** 156403 27, 39, 77, 78, 110, 111, 115, 171

[78] Zhou Z, Cai Z, Wu C and Wang Y 2014 *Phys Rev B* **90** 235139 27, 39, 77, 78, 110, 111, 115, 171

[79] Yanatori H and Koga A 2016 *Phys. Rev. B* **94**(4) 041110 27

[80] Georgi H 1999 *Lie Algebras in Particle Physics* 2nd ed (Perseus Books) 29

[81] Zee A 2016 *Group Theory in a Nutshell for Physicists* (Princeton University Press) 29

[82] Cleveland C L and A R M 1976 *Am J Phys* **44** 34, 62

[83] Read N and Newns D M 1983 *J. Phys. C: Solid State Phys.* **16** 3273–3295 36, 38, 110, 155

[84] Affleck I 1985 *Phys. Rev. Lett.* **54** 966–969 36, 38, 110, 155

[85] Affleck I and Marston J B 1988 *Phys. Rev. B* **37** 3774–3777 36, 38, 110, 156

[86] Bickers N E 1987 *Rev. Mod. Phys.* **59** 845–939 36, 110, 155

[87] Beach K S D, Alet F, Mambrini M and Capponi S 2009 *Phys. Rev. B* **80** 184401 36

[88] Kuzmenko I, Kuzmenko T, Avishai Y and Jo G B 2016 *Phys. Rev. B* **93** 115143 38

[89] Hewson A C 1993 *The Kondo Problem to Heavy Fermions* (Cambridge University Press) 38

[90] Goerbig M O 2011 *Rev. Mod. Phys.* **83** 1193–1243 38, 110, 155

[91] Xu X Y, Law K T and Lee P A 2018 *Phys. Rev. B* **98** 121406 38, 110

[92] You Y and Vishwanath A 2019 *npj Quantum Mater.* **4** 16 38, 110

[93] Natori W M H, Nutakki R, Pereira R G and Andrade E C 2019 *Phys. Rev. B* **100** 205131 38, 110

[94] Liao Y D, Xu X Y, Meng Z Y and Kang J 2021 *Chin. Phys. B* **30** 017305 38, 110

[95] Da Liao Y, Kang J, Breiø C N, Xu X Y, Wu H Q, Andersen B M, Fernandes R M and Meng Z Y 2021 *Phys. Rev. X* **11** 011014 38, 110

[96] Chichinadze D V, Classen L, Wang Y and Chubukov A V 2022 *Phys. Rev. Lett.* **128** 227601 38, 110

[97] Gorshkov A V, Hermele M, Xu C, Julienne P S, Ye J, Zoller P, Demler E, Lukin M D and Rey A M 2010 *Nat Phys* **6** 289 38, 50, 52, 111, 155

[98] Cazalilla M A and Rey A M 2014 *Rep. Prog. Phys.* **77** 124401 38, 111, 155

[99] Takahashi Y 2022 *Proceedings of the Japan Academy, Series B* **98** 141–160 38

[100] Banerjee D, Bögli M, Dalmonte M, Rico E, Stebler P, Wiese U J and Zoller P 2013 *Phys Rev Lett* **110** 125303 38

[101] Sotnikov A, Darkwah Oppong N, Zambrano Y and Cichy A 2020 *Phys. Rev. Research* **2**(2) 023188 38

[102] Honerkamp C and Hofstetter W 2004 *Phys Rev Lett* **92** 170403 38, 39, 110, 156, 220

[103] Hofstetter W 2005 *Advances in Solid State Physics: Flavor Degeneracy and Effects of Disorder in Ultracold Atom Systems* (Springer, Berlin, Heidelberg) 38, 110

[104] Yamashita Y, Tomura M, Yanagi Y and Ueda K 2013 *Phys. Rev. B* **88** 195104 39, 110

[105] Titvinidze I, Privitera A, Chang S Y, Diehl S, Baranov M A, Daley A and Hofstetter W 2011 *New J. Phys.* **13** 035013 39, 110

[106] Sotnikov A and Hofstetter W 2014 *Phys. Rev. A* **89**(6) 063601 39, 110

[107] Sotnikov A 2015 *Phys. Rev. A* **92**(2) 023633 39, 40, 110

[108] Hafez-Torbati M and Hofstetter W 2018 *Phys. Rev. B* **98**(24) 245131 39, 110

[109] Hafez-Torbati M and Hofstetter W 2019 *Phys. Rev. B* **100**(3) 035133 39, 110

[110] Hafez-Torbati M, Zheng J H, Irsigler B and Hofstetter W 2020 *Phys. Rev. B* **101**(24) 245159 39, 110

[111] Nie W, Zhang D and Zhang W 2017 *Phys. Rev. A* **96** 053616 39, 110

[112] Gorelik E V and Blümer N 2009 *Phys Rev A* **80** 051602 39

[113] Unukovych V and Sotnikov A 2021 *Phys. Rev. B* **104** 245106 39, 110

[114] Chen G, Hazzard K R A, Rey A M and Hermele M 2016 *Phys. Rev. A* **93**(6) 061601 39, 110

[115] Wang D, Wang L and Wu C 2019 *Phys. Rev. B* **100**(11) 115155 39, 110

[116] Golubeva A, Sotnikov A, Cichy A, Kuneš J and Hofstetter W 2017 *Phys. Rev. B* **95**(12) 125108 39, 110

[117] Xu H, Wang Y, Zhou Z and Wu C 2019 *arXiv:1912.11791v1* 39, 110

[118] Zhou Z, Wu C and Wang Y 2018 *Phys. Rev. B* **97**(19) 195122 39, 110

[119] Zhou Z, Wang D, Wu C and Wang Y 2017 *Phys. Rev. B* **95**(8) 085128 39, 110

[120] Zhou Z, Wang D, Meng Z Y, Wang Y and Wu C 2016 *Phys. Rev. B* **93**(24) 245157 39, 110

[121] Ouyang Y and Xu X Y 2021 *Phys. Rev. B* **104**(24) L241104 39, 110

[122] Blümer N and Gorelik E V 2013 *Phys Rev B* **87** 085115 39

[123] Yamashita Y, Shibata N and Ueda K 1998 *Phys. Rev. B* **58** 9114 39, 110

[124] Assaraf R, Azaria P, Caffarel M and Lecheminant P 1999 *Phys. Rev. B* **60** 2299 39, 110

[125] Buchta K, Legeza Ö, Szirmai E and Sólyom J 2007 *Phys. Rev. B* **75** 155108 39, 110

[126] Manmana S R, Hazzard K R A, Chen G, Feiguin A E and Rey A M 2011 *Phys. Rev. A* **84**(4) 043601 39, 62, 83, 110, 159

[127] Bonnes L, Hazzard K R A, Manmana S R, Rey A M and Wessel S 2012 *Phys Rev Lett* **109** 205305 39, 41, 78, 110, 139, 141, 161

[128] Messio L and Mila F 2012 *Phys. Rev. Lett.* **109**(20) 205306 39, 110, 161

[129] Xu S, Barreiro J T, Wang Y and Wu C 2018 *Phys. Rev. Lett.* **121**(16) 167205 39, 110

[130] Tóth T A, Läuchli A M, Mila F and Penc K 2010 *Phys Rev Lett* **105** 265301 39, 41, 110, 111, 155, 167

[131] Nataf P and Mila F 2014 *Phys Rev Lett* **113** 127204 39, 41, 110, 111, 155, 167

[132] Corboz P, Läuchli A M, Penc K, Troyer M and Mila F 2011 *Phys Rev Lett* **107** 215301 39, 41, 110, 111, 155, 167

[133] Bauer B, Corboz P, Läuchli A M, Messio L, Penc K, Troyer M and Mila F 2012 *Phys Rev B* **85** 125116 39, 110, 111, 155, 167

[134] Yamamoto D, Suzuki C, Marmorini G, Okazaki S and Furukawa N 2020 *Phys. Rev. Lett.* **125**(5) 057204 39, 110, 155, 167

[135] Keselman A, Bauer B, Xu C and Jian C M 2020 *Phys. Rev. Lett.* **125**(11) 117202 39, 110

[136] Yao X P, Gao Y and Chen G 2021 *Phys. Rev. Research* **3**(2) 023138 39, 110

[137] Nataf P, Lajkó M, Corboz P, Läuchli A M, Penc K and Mila F 2016 *Phys Rev B* **93** 201113 39

[138] Romen C and Läuchli A M 2020 *Phys. Rev. Research* **2** 043009 39, 140, 155, 167, 220

[139] Song H and Hermele M 2013 *Phys Rev B* **87** 144423 39

[140] Savary L and Balents L 2016 *Rep Prog Phys* **80** 016502 39

[141] Hofrichter C, Riegger L, Scazza F, Höfer M, Fernandes D R, Bloch I and Fölling S 2016 *Phys Rev X* **6** 021030 42, 43, 64, 111, 121, 122, 164

[142] Ozawa H, Taie S, Takasu Y and Takahashi Y 2018 *Phys Rev Lett* **121** 225303 43, 44, 81, 111, 158, 168

[143] Tusi D, Franchi L, Livi L F, Baumann K, Orenes D B, Re L D, Barfknecht R E, Zhou T, Inguscio M, Cappellini G, Capone M, Catani J and Fallani L 2021 *arXiv:2104.13338v1* 44, 45, 111, 156

[144] Scazza F 2015 *Probing SU(N)-symmetric orbital interactions with ytterbium Fermi gases in optical lattices* Ph.D. thesis Ludwig-Maximilians-Universität München 47

[145] Hofrichter C 2016 *Probing the SU(N) Fermi-Hubbard model with ytterbium atoms in an optical lattice* Ph.D. thesis Ludwig-Maximilians-Universität München 47

[146] Duarte P M 2014 Band structure calculations for an optical lattice URL http://dx.doi.org/10.5281/zenodo.11612 47, 55, 56, 57, 58

[147] Yip S K and Ho T L 1999 *Phys. Rev. A* **59**(6) 4653–4656 50

[148] Grimm R, Weidemüller M and Ovchinnikov Y B 2000 Optical dipole traps for neutral atoms (*Advances In Atomic, Molecular, and Optical Physics* vol 42) ed Bederson B and Walther H (Academic Press) pp 95–170 52

[149] Ashcroft N W and Mermin N D 1976 *Solid State Physics* (Saunders College Publishing) 53

[150] Simon S H 2013 *The Oxford Solid State Basics* (Oxford University Press) 53

[151] Kohn W 1959 *Phys. Rev.* **115**(4) 809–821 57

[152] Lieb E H and Wu F Y 1968 *Phys Rev Lett* **20** 1445–1448 62

[153] ten Haaf D F B and van Leeuwen J M J 1992 *Phys Rev B* **46** 6313–6327 63

[154] Henderson J A, Oitmaa J and Ashley M C B 1992 *Phys Rev B* **46** 6328–6337 63

[155] Hazzard K R A, Gurarie V, Hermele M and Rey A M 2012 *Phys Rev A* **85** 041604 63, 120, 122, 138, 141

[156] Oitmaa J, Hamer C, and Zheng W 2006 *Series Expansion Methods for Strongly Interacting Lattice Models* (Cambridge University Press) 63

[157] Singh R R P and Oitmaa J 2022 *Phys. Rev. A* **105** 033317 65

[158] Hingorani R, Oitmaa J and Singh R R P 2022 *Phys. Rev. B* **105** L241410 65

[159] Singh R R P and Oitmaa J 2022 *arXiv:2202.01611* 65

[160] Pera J, Casulleras J and Boronat J 2022 *arXiv:2205.13837* 65

[161] Pera J, Casulleras J and Boronat J 2022 *arXiv:2206.06932* 65

[162] Lanczos C 1950 *J. Res. Natl. Bur. Stand.* **45** 255–282 67

[163] Dagotto E 1994 *Rev. Mod. Phys.* **66** 763–840 67

[164] Tang B, Khatami E and Rigol M 2013 *Computer Physics Communications* **184** 557–564 67, 68, 69, 115, 118, 143

[165] Blankenbecler R, Scalapino D J and Sugar R L 1981 *Phys Rev D* **24** 2278–2286 69, 83, 115

[166] Sorella S, Baroni S, Car R and Parrinello M 1989 *Europhys. Lett.* **8** 663–668 69, 83, 115

[167] Gubernatis J, Kawashim N and Werner P 2016 *Quantum Monte Carlo Methods: Algorithms for Lattice Models* (Cambridge University Press) 69, 70

[168] 2009 Multi-scale phenomena in complex fluids URL https://web.cs.ucdavis.edu/~bai/publications/bcsy09.pdf 69, 70

[169] Pavarini E, Koch E, van den Brink J and Sawatzky G (eds) 2016 *Quantum Materials: Experiments and Theory* (Forschungszentrum Jülich GmbH Institute for Advanced Simulation) chap 4 URL https://www.cond-mat.de/events/correl16/manuscripts/correl16.pdf 69, 70

[170] Scalettar R T 2010 How to write a determinant qmc code URL https://scalettar.physics.ucdavis.edu/michigan/howto1.pdf 69, 70

[171] White S R, Scalapino D J, Sugar R L, Loh E Y, Gubernatis J E and Scalettar R T 1989 *Phys Rev B* **40** 506–516 69, 85, 110

[172] Paiva T, Scalettar R, Randeria M and Trivedi N 2010 *Phys Rev Lett* **104** 066406 69, 81, 83

[173] Krauth W 2006 *Statistical Mechanics: Algorithms and Computations* (Oxford University Press) 69, 70

[174] Hastings W K 1970 *Biometrika* **57** 97–109 69, 70

[175] Sethna J P 2022 *Entropy, Order Parameters, and Complexity* (Oxford University Press) 70

[176] Binder K and Heermann D W 2022 *Monte Carlo Simulation in Statistical Physics: An Introduction* 5th ed (Springer) 70

[177] Scalettar R T, Noack R M and Singh R R P 1991 *Phys Rev B* **44** 10502–10507 76, 86, 116

[178] Assaad F F 2005 *Phys. Rev. B* **71**(7) 075103 77, 115, 156

[179] Assaad F F 1998 *arXiv:condmat/9806307 v1* 77, 115

[180] Van Houcke K, Kozik E, Prokovév N and Svistunov B 2008 *arXiv:0802.2923* 78

[181] Kozik E, Houcke K V, Gull E, Pollet L, Prokof'ev N, Svistunov B and Troyer M 2010 *Europhys Lett* **90** 10004 78

[182] Rossi R 2017 *Phys Rev Lett* **119** 045701 78

[183] Brown P T 2019 *Probing dynamical quantities in the 2D Fermi-Hubbard model with quantum gas microscopy* Ph.D. thesis Princeton University figure 5.5b 79

[184] Gorelik E V, Rost D, Paiva T, Scalettar R, Klümper A and Blümer N 2012 *Phys Rev A* **85** 061602 79, 103

[185] Schneider U, Hackermuller L, Will S, Best T, Bloch I, Costi T A, Helmes R W, Rasch D and Rosch A 2008 *Science* **322** 1520–1525 81

[186] Strohmaier N, Greif D, Jördens R, Tarruell L, Moritz H, Esslinger T, Sensarma R, Pekker D, Altman E and Demler E 2010 *Phys. Rev. Lett.* **104** 080401 81

[187] Cocchi E, Miller L A, Drewes J H, Koschorreck M, Pertot D, Brennecke F and Köhl M 2016 *Phys. Rev. Lett.* **116** 175301 81

[188] Cocchi E, Miller L A, Drewes J H, Chan C F, Pertot D, Brennecke F and Köhl M 2017 *Phys. Rev. X* **7** 031025 81

[189] Huang E W, Sheppard R, Moritz B and Devereaux T P 2019 *Science* **366** 987–990 81

[190] Simon J, Bakr W S, Ma R, Tai M E, Preiss P M and Greiner M 2011 *Nature* **472** 307–312 81

[191] Kim K, Chang M S, Korenblit S, Islam R, Edwards E E, Freericks J K, Lin G D, Duan L M and Monroe C 2010 *Nature* **465** 590–593 81

[192] Britton J W, Sawyer B C, Keith A C, Wang C C J, Freericks J K, Uys H, Biercuk M J and Bollinger J J 2012 *Nature* **484** 489–492 81

[193] Greif D, Jotzu G, Messer M, Desbuquois R and Esslinger T 2015 *Phys. Rev. Lett.* **115** 260401 81, 82, 164

[194] Schönmeier-Kromer J and Pollet L 2014 *Phys. Rev. A* **89** 023605 81

[195] Lenz B, Manmana S R, Pruschke T, Assaad F F and Raczkowski M 2016 *Phys. Rev. Lett.* **116** 086403 81

[196] Raczkowski M and Assaad F F 2012 *Phys. Rev. Lett.* **109** 126404 81

[197] Kung Y F, Bazin C, Wohlfeld K, Wang Y, Chen C C, Jia C J, Johnston S, Moritz B, Mila F and Devereaux T P 2017 *Phys. Rev. B* **96** 195106 81

[198] Ehlers G, Lenz B, Manmana S R and Noack R M 2018 *Phys. Rev. B* **97** 035118 81

[199] Bakr W S, Gillen J I, Peng A, Fölling S and Greiner M 2009 *Nature* **462** 74–77 81

[200] Sherson J F, Weitenberg C, Endres M, Cheneau M, Bloch I and Kuhr S 2010 *Nature* **467** 68–72 81

[201] Weitenberg C, Endres M, Sherson J F, Cheneau M, Schauß P, Fukuhara T, Bloch I and Kuhr S 2011 *Nature* **471** 319–324 81

[202] Endres M, Cheneau M, Fukuhara T, Weitenberg C, Schauss P, Gross C, Mazza L, Banuls M C, Pollet L, Bloch I and Kuhr S 2011 *Science* **334** 200–203 81

[203] Endres M, Cheneau M, Fukuhara T, Weitenberg C, Schauß P, Gross C, Mazza L, Bañuls M C, Pollet L, Bloch I and Kuhr S 2013 *Appl. Phys. B* **113** 27–39 81

[204] Greif D, Parsons M F, Mazurenko A, Chiu C S, Blatt S, Huber F, Ji G and Greiner M 2016 *Science* **351** 953–957 81

[205] Yamamoto R, Kobayashi J, Kuno T, Kato K and Takahashi Y 2016 *New J. Phys.* **18** 023016 81, 111

[206] Okuno D, Amano Y, Enomoto K, Takei N and Takahashi Y 2020 *New J. Phys.* **22** 013041 81, 111

[207] Haldar A and Shenoy V B 2014 *Sci. Rep.* **4** 06655 82, 105

[208] Brown P T, Guardado-Sanchez E, Spar B M, Huang E W, Devereaux T P and Bakr W S 2019 *Nat. Phys.* **16** 26–31 83

[209] Mitra D, Brown P T, Guardado-Sanchez E, Kondov S S, Devakul T, Huse D A, Schauß P and Bakr W S 2017 *Nat. Phys.* **14** 173–177 83

[210] Chan C F, Gall M, Wurz N and Köhl M 2020 *Phys. Rev. Research* **2** 023210 83

[211] Daré A M, Raymond L, Albinet G and Tremblay A M S 2007 *Phys. Rev. B* **76** 064402 83

[212] De Leo L, Bernier J S, Kollath C, Georges A and Scarola V W 2011 *Phys. Rev. A* **83** 023606 83

[213] Jördens R, Tarruell L, Greif D, Uehlinger T, Strohmaier N, Moritz H, Esslinger T, De Leo L, Kollath C, Georges A, Scarola V, Pollet L, Burovski E, Kozik E and Troyer M 2010 *Phys. Rev. Lett.* **104** 180401 83

[214] Burovski E, Prokof'ev N, Svistunov B and Troyer M 2006 *New J. Phys.* **8** 153–153 83

[215] Kozik E, Burovski E, Scarola V W and Troyer M 2013 *Phys. Rev. B* **87** 205102 83, 87, 101, 106

[216] Klebel-Knobloch B, Schäfer T, Toschi A and Tomczak J M 2021 *Phys. Rev. B* **103** 045121 83

[217] Chakravarty S, Halperin B I and Nelson D R 1988 *Phys. Rev. Lett.* **60** 1057–1060 83, 102

[218] Chubukov A V, Sachdev S and Ye J 1994 *Phys. Rev. B* **49** 11919–11961 83

[219] Xu J, Chiesa S, Walter E J and Zhang S 2013 *J. Phys.: Condens. Matter* **25** 415602 85

[220] Staudt R, Dzierzawa M and Muramatsu A 2000 *Eur. Phys. J. B* **17** 411–415 87, 106

[221] Khatami E 2016 *Phys. Rev. B* **94**(12) 125114 91

[222] Paiva T, Scalettar R T, Huscroft C and McMahan A K 2001 *Phys. Rev. B* **63**(12) 125116 96, 117, 137, 138, 139

[223] Shiba H and Pincus P A 1972 *Phys. Rev. B* **5**(5) 1966–1980 96

[224] Georges A and Krauth W 1993 *Phys. Rev. B* **48**(10) 7167–7182 96

[225] Sengupta P, Sandvik A W and Singh R R P 2003 *Phys. Rev. B* **68** 094423 99

[226] Sandvik A W 1998 *Phys. Rev. Lett.* **80** 5196–5199 102

[227] Scalettar R T, Cannon J W, Scalapino D J and Sugar R L 1994 *Phys. Rev. B* **50** 13419–13427 104

[228] Wang L, Beach K S D and Sandvik A W 2006 *Phys. Rev. B* **73** 014431 104

[229] Bang Y and Choi H Y 2008 *Phys. Rev. B* **78**(13) 134523 104

[230] Korshunov M M and Eremin I 2008 *Phys. Rev. B* **78** 140509(R) 104

[231] Wang F, Zhai H, Ran Y, Vishwanath A and Lee D H 2009 *Phys. Rev. Lett.* **102** 047005 104

[232] Falicov L M, Pierce D T, Bader S D, Gronsky R, Hathaway K B, Hopster H J, Lambeth D N, Parkin S S P, Prinz G, Salamon M, Schuller I K and Victora R H 1990 *J. Mater. Res.* **5** 1299–1340 104

[233] Fadley C S 1992 *Synchrotron Radiation Research* (Springer US) 104

[234] Scalapino D J and Trugman S A 1996 *Philos. Mag. B* **74** 607–610 104

[235] Arrigoni E, Fradkin E and Kivelson S A 2004 *Phys. Rev. B* **69** 214519 104

[236] Martin I, Podolsky D and Kivelson S A 2005 *Phys. Rev. B* **72** 060502(R) 104

[237] Kivelson S A and Fradkin E 2007 *Handbook of High-Temperature Superconductivity* (Springer New York) 104

[238] Tsai W F and Kivelson S A 2006 *Phys. Rev. B* **73** 214510 104

[239] Røising H S, Flicker F, Scaffidi T and Simon S H 2018 *Phys. Rev. B* **98** 224515 104

[240] Wachtel G, Baruch S and Orgad D 2017 *Phys. Rev. B* **96** 064527 104

[241] Baruch S and Orgad D 2010 *Phys. Rev. B* **82** 134537 104

[242] Yang S, Liu X, Li W, Yang J, Ying T, Li X and Sun X 2022 *Journal of Physics: Condensed Matter* **34** 375501 104

[243] Wachtel G, Bar-Yaacov A and Orgad D 2012 *Phys. Rev. B* **86** 134531 104

[244] Ho T L and Zhou Q 2009 *arXiv:0911.5506* 105

[245] Bernier J S, Kollath C, Georges A, De Leo L, Gerbier F, Salomon C and Köhl M 2009 *Phys. Rev. A* **79** 061601(R) 105, 185

[246] McKay D C and DeMarco B 2011 *Rep. Prog. Phys.* **74** 054401 105

[247] Schachenmayer J, Weld D M, Miyake H, Siviloglou G A, Ketterle W and Daley A J 2015 *Phys. Rev. A* **92** 041602(R) 105

[248] Goto S and Danshita I 2017 *Phys. Rev. A* **96** 063602 105

[249] Kantian A, Langer S and Daley A J 2018 *Phys. Rev. Lett.* **120** 060401 105

[250] Mirasola A E, Wall M L and Hazzard K R A 2018 *Phys. Rev. A* **98** 033607 105

[251] Venegas-Gomez A, Schachenmayer J, Buyskikh A S, Ketterle W, Chiofalo M L and Daley A J 2020 *Quantum Science and Technology* **5** 045013 105

[252] Werner P, Eckstein M, Müller M and Refael G 2019 *Nat. Commun.* **10** 105

[253] Yang B, Sun H, Huang C J, Wang H Y, Deng Y, Dai H N, Yuan Z S and Pan J W 2020 *Science* **369** 550–553 105

[254] Zaletel M P, Kaufman A, Stamper-Kurn D M and Yao N Y 2021 *Phys. Rev. Lett.* **126** 103401 105

[255] Daré A M, Vilk Y M and Tremblay A M S 1996 *Phys. Rev. B* **53** 14236–14251 106

[256] Schäfer T, Wentzell N, Šimkovic F, He Y Y, Hille C, Klett M, Eckhardt C J, Arzhang B, Harkov V, Le Régent F m c M, Kirsch A, Wang Y, Kim A J, Kozik E, Stepanov E A, Kauch A, Andergassen S, Hansmann P, Rohe D, Vilk Y M, LeBlanc J P F, Zhang S, Tremblay A M S, Ferrero M, Parcollet O and Georges A 2021 *Phys. Rev. X* **11** 011058 110

[257] Wu C 2006 *Mod. Phys. Lett. B* **20** 1707–1738 111, 155

[258] Cazalilla M A, Ho A F and Ueda M 2009 *New J. Phys.* **11** 103033 111, 155

[259] Stellmer S, Schreck F and Killian T C 2014 *Degenerate Quantum Gases of Strontium* (World Scientific) chap 1, pp 1–80 111

[260] Schäfer F, Fukuhara T, Sugawa S, Takasu Y and Takahashi Y 2020 *Nat. Rev. Phys.* **2** 411–425 111

[261] Nakamura Y, Takasu Y, Kobayashi J, Asaka H, Fukushima Y, Inaba K, Yamashita M and Takahashi Y 2019 *Phys. Rev. A* **99**(3) 033609 112

[262] Koepsell J, Hirthe S, Bourgund D, Sompet P, Vijayan J, Salomon G, Gross C and Bloch I 2020 *Phys. Rev. Lett.* **125** 010403 112, 186, 189

[263] Zhou Q and Ho T L 2011 *Phys. Rev. Lett.* **106** 225301 112

[264] Hartke T, Oreg B, Jia N and Zwierlein M 2020 *Phys. Rev. Lett.* **125** 113601 112, 189

[265] Rigol M, Bryant T and Singh R R 2006 *Phys. Rev. Lett.* **97** 187202 115

[266] McMahan A, Huscroft C, Scalettar R and Pollock E 1998 *J. Comput.-Aided Mater. Des.* **5** 131–162 117

[267] Batrouni G G and Scalettar R T 1990 *Phys. Rev. B* **42**(4) 2282–2289 122

[268] Batrouni G G and de Forcrand P 1993 *Phys. Rev. B* **48**(1) 589–592 122

[269] Lee S S B, von Delft J and Weichselbaum A 2018 *Phys. Rev. B* **97**(16) 165143 122

[270] Greger M, Kollar M and Vollhardt D 2013 *Phys. Rev. B* **87** 195140 131, 137

[271] Vollhardt D 1997 *Phys. Rev. Lett.* **78**(7) 1307–1310 137, 139

[272] Chandra N, Kollar M and Vollhardt D 1999 *Phys. Rev. B* **59**(16) 10541–10549 137, 139

[273] Duffy D and Moreo A 1997 *Phys. Rev. B* **55**(19) 12918–12924 137, 139

[274] Macedo C A and de Souza A M C 2002 *Phys. Rev. B* **65**(15) 153109 137, 139

[275] Paiva T, Scalettar R T, Zheng W, Singh R R P and Oitmaa J 2005 *Phys. Rev. B* **72**(8) 085123 137, 139

[276] Müller A M, Lajkó M, Schreck F, Mila F and Minář J c v 2021 *Phys. Rev. A* **104**(1) 013304 138, 141

[277] Khatami E and Rigol M 2011 *Phys. Rev. A* **84** 053611 143

[278] Del Re L and Capone M 2018 *Phys. Rev. A* **98** 063628 156

[279] Trotzky S, Chen Y A, Schnorrberger U, Cheinet P and Bloch I 2010 *Phys. Rev. Lett.* **105** 265303 158

[280] Kaufman A M and Ni K K 2021 *Nat. Phys.* **17** 1324–1333 184

[281] Madjarov I S, Cooper A, Shaw A L, Covey J P, Schkolnik V, Yoon T H, Williams J R and Endres M 2019 *Phys. Rev. X* **9** 041052 185

[282] Young A W, Eckner W J, Milner W R, Kedar D, Norcia M A, Oelker E, Schine N, Ye J and Kaufman A M 2020 *Nature (London)* **588** 408–413 185

[283] Graham T M, Kwon M, Grinkemeyer B, Marra Z, Jiang X, Lichtman M T, Sun Y, Ebert M and Saffman M 2019 *Phys. Rev. Lett.* **123** 230501 185

[284] Levine H, Keesling A, Semeghini G, Omran A, Wang T T, Ebadi S, Bernien H, Greiner M, Vuletić V, Pichler H and Lukin M D 2019 *Phys. Rev. Lett.* **123** 170503 185

[285] Omran A, Levine H, Keesling A, Semeghini G, Wang T T, Ebadi S, Bernien H, Zibrov A S, Pichler H, Choi S *et al.* 2019 *Science* **365** 570–574 185

[286] Madjarov I S, Covey J P, Shaw A L, Choi J, Kale A, Cooper A, Pichler H, Schkolnik V, Williams J R and Endres M 2020 *Nat. Phys.* **16** 857–861 185

[287] Endres M, Bernien H, Keesling A, Levine H, Anschuetz E R, Krajenbrink A, Senko C, Vuletic V, Greiner M and Lukin M D 2016 *Science* **354** 1024–1027 185

[288] Barredo D, De Léséleuc S, Lienhard V, Lahaye T and Browaeys A 2016 *Science* **354** 1021–1023 185

[289] Lienhard V, de Léséleuc S, Barredo D, Lahaye T, Browaeys A, Schuler M, Henry L P and Läuchli A M 2018 *Phys. Rev. X* **8** 021070 185

[290] Scholl P, Schuler M, Williams H J, Eberharter A A, Barredo D, Schymik K N, Lienhard V, Henry L P, Lang T C, Lahaye T *et al.* 2021 *Nature* **595** 233–238 185

[291] de Léséleuc S, Lienhard V, Scholl P, Barredo D, Weber S, Lang N, Büchler H P, Lahaye T and Browaeys A 2019 *Science* **365** 775–780 185

[292] Semeghini G, Levine H, Keesling A, Ebadi S, Wang T T, Bluvstein D, Verresen R, Pichler H, Kalinowski M, Samajdar R *et al.* 2021 *Science* **374** 1242–1247 185

[293] Kaufman A M, Lester B J, Reynolds C M, Wall M L, Foss-Feig M, Hazzard K R A, Rey A M and Regal C A 2014 *Science* **345** 306–309 185, 196, 203

[294] Murmann S, Bergschneider A, Klinkhamer V M, Zürn G, Lompe T and Jochim S 2015 *Phys. Rev. Lett.* **114** 080402 185, 203

[295] Bergschneider A, Klinkhamer V M, Becher J H, Klemt R, Palm L, Zürn G, Jochim S and Preiss P M 2019 *Nature Physics* **15** 640–644 185

[296] Becher J H, Sindici E, Klemt R, Jochim S, Daley A J and Preiss P M 2020 *Phys. Rev. Lett.* **125** 180402 185

[297] Young A W, Eckner W J, Schine N, Childs A M and Kaufman A M 2022 *arXiv:2202.01204* 185

[298] Vijayan J, Sompet P, Salomon G, Koepsell J, Hirthe S, Bohrdt A, Grusdt F, Bloch I and Gross C 2020 *Science* **367** 186–189 185

[299] Koepsell J, Vijayan J, Sompet P, Grusdt F, Hilker T A, Demler E, Salomon G, Bloch I and Gross C 2019 *Nature (London)* **572** 358–362 185

[300] Yang J, Liu L, Mongkolkiattichai J and Schauss P 2021 *PRX Quantum* **2**(2) 020344 185

[301] Lubasch M, Murg V, Schneider U, Cirac J I and Bañuls M C 2011 *Phys. Rev. Lett.* **107**(16) 165301 185

[302] Serwane F, Zürn G, Lompe T, Ottenstein T, Wenz A and Jochim S 2011 *Science* **332** 336–338 186, 189

[303] Light J C and Carrington Jr T 2000 *Advances in Chemical Physics* **114** 263–310 188, 196

[304] Wall M L, Hazzard K R A and Rey A M 2015 *Phys. Rev. A* **92** 013610 188, 196

[305] Preiss P M, Ma R, Tai M E, Simon J and Greiner M 2015 *Phys. Rev. A* **91** 041602 189

[306] Gall M, Wurz N, Samland J, Chan C F and Köhl M 2021 *Nature* **589** 40–43 189

[307] Sompet P, Hirthe S, Bourgund D, Chalopin T, Bibo J, Koepsell J, Bojović P, Verresen R, Pollmann F, Salomon G, Gross C, Hilker T and Bloch I 2021 *arXiv:2103.10421* 191, 193

[308] Girvin S M and Yang K 2019 *Modern Condensed Matter Physics* (Cambridge University Press) 195

[309] Morera I, Bohrdt A, Ho W W and Demler E 2021 *arXiv:2106.09600* 195

[310] Szasz A, Motruk J, Zaletel M P and Moore J E 2020 *Phys. Rev. X* **10** 021042 195

[311] Neuhasuer D and Baer M 1989 *The Journal of Chemical Physics* **90** 4351–4355 199

[312] Liang J, Kohn Jr R N, Becker M F and Heinzen D J 2009 *Applied optics* **48** 1955–1962 200

[313] Matsumoto N, Inoue T, Ando T, Takiguchi Y, Ohtake Y and Toyoda H 2012 *Opt. Lett.* **37** 3135–3137 200

[314] Kim D, Keesling A, Omran A, Levine H, Bernien H, Greiner M, Lukin M D and Englund D R 2019 *Optics letters* **44** 3178–3181 200

[315] Bayha L, Holten M, Klemt R, Subramanian K, Bjerlin J, Reimann S M, Bruun G M, Preiss P M and Jochim S 2020 *Nature* **587** 583–587 203

[316] Weinberg P and Bukov M 2019 *SciPost. Phys.* **7** 97 206

Appendix A

Probability distribution of the SU(N) FHM DQMC Algorithm

In the following notes we derive the *probability distribution* that is sampled in the DQMC algorithm of the SU(N) Fermi-Hubbard Model. First we rewrite the $N = 2$ case in a convenient way, and then do the same for $N > 2$. Subsequently, starting from the partition function we introduce the Hubbard-Stratonovich decomposition and derive the *probability distribution* that will be stochastically sampled. Later we discuss the $N = 2, 3$ cases and finally we conclude mentioning how the algorithm changes.

A.1 The SU(2) Fermi Hubbard Model

The SU(2) Hubbard Hamiltonian is,

$$H = -t \sum_{\langle i,j\rangle\sigma} \left(c^\dagger_{i\sigma} c_{j\sigma} + c^\dagger_{j\sigma} c_{i\sigma} \right) + U \sum_i n_{i\uparrow} n_{i\downarrow} - \mu \sum_{i,\sigma} n_{i\sigma} \tag{A.1}$$

where $\sigma = \uparrow, \downarrow$. We can notice that,

$$\begin{aligned} H &= \sum_{\sigma=\uparrow,\downarrow} K_\sigma + V_{\uparrow,\downarrow}(U) && \text{(A.2)} \\ K_\sigma &= -t \sum_{\langle i,j\rangle} \left(c^\dagger_{i\sigma} c_{j\sigma} + c^\dagger_{j\sigma} c_{i\sigma} \right) - \mu \sum_i n_{i\sigma} && \text{(A.3)} \\ V_{\uparrow,\downarrow}(U) &= U \sum_i n_{i\uparrow} n_{i\downarrow} && \text{(A.4)} \end{aligned}$$

and define

$$H^{(\sigma\sigma')}_{FH}(U) = K_\sigma + K_{\sigma'} + V_{\sigma,\sigma'}(U) \tag{A.5}$$

Note that $H_{FH}^{(\sigma\sigma')} = H_{FH}^{(\sigma'\sigma)}$. We know how to implement the DQMC algorithm for this Hamiltonian [54], so it is of our interest to express the SU(N) Hamiltonian in terms of the $N = 2$ one.

A.2 The SU(N) Fermi Hubbard Model

The SU(N) Hubbard Hamiltonian is,

$$H = -t \sum_{\langle i,j\rangle\sigma} \left(c_{i\sigma}^{\dagger} c_{j\sigma} + c_{j\sigma}^{\dagger} c_{i\sigma} \right) + \frac{U}{2} \sum_{i,\sigma\neq\sigma'} n_{i\sigma} n_{i\sigma'} - \mu_0 \sum_{i,\sigma} n_{i\sigma} - \sum_{i,\sigma} V_i^{ext} n_{i\sigma}, \quad \text{(A.6)}$$

that we can rewrite using local density approximation $\mu_i = \mu_0 - V_i^{ext}$ as,

$$H = \sum_{\sigma} \left[-t \sum_{\langle i,j\rangle} \left(c_{i\sigma}^{\dagger} c_{j\sigma} + c_{j\sigma}^{\dagger} c_{i\sigma} \right) - \sum_{i} \mu_i n_{i\sigma} \right] + \frac{U}{2} \sum_{i,\sigma\neq\sigma'} n_{i\sigma} n_{i\sigma'}, \quad \text{(A.7)}$$

and we can identify the K_σ terms easily and therefore rewrite it as,

$$H = \left(\frac{1}{2(N-1)} \right) \sum_{\sigma\neq\sigma'} (K_\sigma + K_{\sigma'}) + \frac{U}{2} \sum_{i,\sigma\neq\sigma'} n_{i\sigma} n_{i\sigma'}, \quad \text{(A.8)}$$

so rearranging terms we have,

$$H = \left(\frac{1}{2(N-1)} \right) \sum_{\sigma\neq\sigma'} \left[K_\sigma + K_{\sigma'} + U(N-1) \sum_{i} n_{i\sigma} n_{i\sigma'} \right] \quad \text{(A.9)}$$

Thus, writing it in terms of the $N = 2$ Hamiltonian, we have

$$H = \left(\frac{1}{2(N-1)} \right) \sum_{\sigma\neq\sigma'} H_{FH}^{(\sigma\sigma')}(U(N-1)). \quad \text{(A.10)}$$

Or it can be written as,

$$H = \left(\frac{1}{N-1} \right) \sum_{\sigma} \sum_{\sigma'>\sigma} H_{FH}^{(\sigma\sigma')}(U(N-1)). \quad \text{(A.11)}$$

A.3 DQMC

A.3.1 Computable approximation of the *probability distribution*

We know that for each individual $H_{FH}^{\sigma\sigma'}$, the kinetic and interaction terms do not commute, so let's start by applying the Trotter-Suzuki decomposition to approximate the partition function Z:

$$\begin{aligned} Z &= \mathrm{Tr}\left(e^{-\beta H}\right) = \mathrm{Tr}\left[\prod_{\ell=1}^{L} e^{-\Delta\tau H}\right] \\ &= \mathrm{Tr}\left[\prod_{\ell=1}^{L} \exp\left(-\left(\frac{\Delta\tau}{N-1}\right)\sum_{\sigma}\sum_{\sigma'>\sigma} H_{FH}^{(\sigma\sigma')}(U(N-1))\right)\right] \\ &= \mathrm{Tr}\left[\prod_{\ell=1}^{L}\prod_{\sigma}\prod_{\sigma'>\sigma} \exp\left(-\left(\frac{\Delta\tau}{N-1}\right) H_{FH}^{(\sigma\sigma')}(U(N-1))\right)\right] + O(\Delta\tau^2) \\ &\approx \mathrm{Tr}\left[\prod_{\ell=1}^{L}\prod_{\sigma}\prod_{\sigma'>\sigma} e^{-\left(\frac{\Delta\tau}{N-1}\right)(K_\sigma+K_{\sigma'})} e^{-\left(\frac{\Delta\tau}{N-1}\right)V_{\sigma,\sigma'}(U(N-1))}\right] \end{aligned} \tag{A.12}$$

Note that in the last line the Trotter-Suzuki approximation has appeared one more time, so that we can separate the kinetic part from the interaction part. The kinetic energy term is quadratic in the fermion operators and the σ and σ' operators are independent, therefore it can be written as

$$e^{-\left(\frac{\Delta\tau}{N-1}\right)(K_\sigma+K_{\sigma'})} = e^{-\left(\frac{\Delta\tau}{N-1}\right)K_\sigma} e^{-\left(\frac{\Delta\tau}{N-1}\right)K_{\sigma'}}, \tag{A.13}$$

where the operators K_σ are written in their quadratic form as,

$$K_\sigma = \vec{c}_\sigma^{\,\dagger}\mathcal{K}\vec{c}_\sigma \tag{A.14}$$

with the square matrix $\mathcal{K}$ (dimension $N_s \times N_s$ with N_s the total number of sites) is given by,

$$\mathcal{K} = \begin{pmatrix} -\mu_1 & -t & 0 & 0 & \dots \\ -t & -\mu_2 & -t & 0 & \dots \\ \vdots & & \ddots & & \end{pmatrix} \tag{A.15}$$

With this results, the partition function is now:

$$Z \approx \mathrm{Tr}\left[\prod_{\ell=1}^{L}\prod_{\sigma}\prod_{\sigma'>\sigma} e^{-\left(\frac{\Delta\tau}{N-1}\right)\vec{c}^{\dagger}_{\sigma}\mathcal{K}\vec{c}_{\sigma}} e^{-\left(\frac{\Delta\tau}{N-1}\right)\vec{c}^{\dagger}_{\sigma'}\mathcal{K}\vec{c}_{\sigma'}} e^{-\left(\frac{\Delta\tau}{N-1}\right)V_{\sigma,\sigma'}(U(N-1))}\right]. \tag{A.16}$$

Now, the potential energy term is quartic in the fermion operators so we need to perform a discrete Hubbard-Stratonovich transformation. First let's note the following:

$$e^{-\left(\frac{\Delta\tau}{N-1}\right)V_{\sigma,\sigma'}(U(N-1))} = e^{-\Delta\tau U\sum_i n_{i\sigma}n_{i\sigma'}} = \prod_i e^{-\Delta\tau U n_{i\sigma}n_{i\sigma'}} \tag{A.17}$$

Then,

$$\begin{aligned}\prod_i e^{-\Delta\tau U n_{i\sigma}n_{i\sigma'}} &= \prod_i\left[\frac{1}{2}\sum_{h_i=\pm1} e^{-\left(h_i\lambda+\frac{U\Delta\tau}{2}\right)n_{i\sigma}} e^{-\left(-h_i\lambda+\frac{U\Delta\tau}{2}\right)n_{i\sigma'}}\right] \\ &= \left(\frac{1}{2}\right)^{N_s}\sum_{\{\vec{h}:h_i=\pm1\}} e^{-\sum_i\left(h_i\lambda+\frac{U\Delta\tau}{2}\right)n_{i\sigma}} e^{-\sum_i\left(-h_i\lambda+\frac{U\Delta\tau}{2}\right)n_{i\sigma'}} \\ &= \left(\frac{1}{2}\right)^{N_s}\mathrm{Tr}_h\left[e^{\vec{c}^{\dagger}_{\sigma}\mathcal{V}(h)\vec{c}_{\sigma}} e^{\vec{c}^{\dagger}_{\sigma'}\mathcal{V}(-h)\vec{c}_{\sigma'}}\right]\end{aligned} \tag{A.18}$$

where $\cosh\lambda = \exp\left(U\Delta\tau/2\right)$ and,

$$\mathcal{V}(h) = \mathrm{diag}\left(-h_i\lambda - \frac{U\Delta\tau}{2}\right) \ ^{*}. \tag{A.19}$$

*We would like to notice here that if the Hamiltonian is written in the PHS form, the Hubbard-Stratonovich decomposition will gain an additional $e^{-U\Delta\tau/4}$ term that is irrelevant to the algorithm (since one will take ratios) and that the term $-U\Delta\tau/2$ can be disregarded since it will be captured by the chemical potential, rendering $\mathcal{V}(h) = \mathrm{diag}(-h_i\lambda)$.

We now need to take into account the fact that we have inserted $\binom{N}{2}$ Hubbard-Stratonovich transformations for each time slice l [one for each pair of (σ, σ')]. Therefore the following index relabeling needs to be done:

$$h_i \to h^{(\sigma,\sigma')}(i,l), \quad \mathrm{Tr}_h \to \mathrm{Tr}_{h_{\sigma\sigma'}}, \quad \mathcal{V}(h) \to \mathcal{V}^{(\ell)}(h)$$

Putting this back into the expression for the partition function, we now have:

$$\begin{aligned} Z &\approx \mathrm{Tr}\left[\prod_{\ell=1}^{L}\prod_{\sigma}\prod_{\sigma'>\sigma} e^{-\left(\frac{\Delta\tau}{N-1}\right)\vec{c}^{\dagger}_{\sigma}\mathcal{K}\vec{c}_{\sigma}} e^{-\left(\frac{\Delta\tau}{N-1}\right)\vec{c}^{\dagger}_{\sigma'}\mathcal{K}\vec{c}_{\sigma'}} \left(\frac{1}{2}\right)^{N_s} \mathrm{Tr}_{h_{\sigma\sigma'}}\left[e^{\vec{c}^{\dagger}_{\sigma}\mathcal{V}^{(\ell)}(h)\vec{c}_{\sigma}} e^{\vec{c}^{\dagger}_{\sigma'}\mathcal{V}^{(\ell)}(-h)\vec{c}_{\sigma'}}\right]\right], \\ &\approx \mathrm{Tr}\left[\prod_{\ell=1}^{L}\prod_{\sigma}\prod_{\sigma'>\sigma} \left(\frac{1}{2}\right)^{N_s} \mathrm{Tr}_{h_{\sigma\sigma'}}\left(e^{-\left(\frac{\Delta\tau}{N-1}\right)\vec{c}^{\dagger}_{\sigma}\mathcal{K}\vec{c}_{\sigma}} e^{-\left(\frac{\Delta\tau}{N-1}\right)\vec{c}^{\dagger}_{\sigma'}\mathcal{K}\vec{c}_{\sigma'}} e^{\vec{c}^{\dagger}_{\sigma}\mathcal{V}^{(\ell)}(h)\vec{c}_{\sigma}} e^{\vec{c}^{\dagger}_{\sigma'}\mathcal{V}^{(\ell)}(-h)\vec{c}_{\sigma'}}\right)\right]. \end{aligned} \tag{A.20}$$

We can move the time product $\prod_\ell$ inside the $\mathrm{Tr}_{h_{\sigma,\sigma'}}$.

$$\begin{aligned} Z \approx \mathrm{Tr}\Bigg[\prod_{\sigma}\prod_{\sigma'>\sigma}\left(\frac{1}{2}\right)^{LN_s} \mathrm{Tr}_{h_{\sigma\sigma'}}\Bigg\{ &\left(\prod_{\ell=1}^{L} e^{-\left(\frac{\Delta\tau}{N-1}\right)\vec{c}^{\dagger}_{\sigma}\mathcal{K}\vec{c}_{\sigma}} e^{\vec{c}^{\dagger}_{\sigma}\mathcal{V}^{(\ell)}(-h)\vec{c}_{\sigma}}\right) \\ &\left(\prod_{\ell=1}^{L} e^{-\left(\frac{\Delta\tau}{N-1}\right)\vec{c}^{\dagger}_{\sigma'}\mathcal{K}\vec{c}_{\sigma'}} e^{\vec{c}^{\dagger}_{\sigma'}\mathcal{V}^{(\ell)}(-h)\vec{c}_{\sigma'}}\right)\Bigg\}\Bigg], \end{aligned} \tag{A.21}$$

Then, we are able to trace over fermions explicitly, since there are only bilinear forms in fermion operators, and obtain:

$$\begin{aligned} Z \approx \left(\frac{1}{2}\right)^{LN_s\binom{N}{2}} \prod_{\sigma}\prod_{\sigma'>\sigma}\Bigg\{ \mathrm{Tr}_{h_{\sigma\sigma'}}\mathrm{Tr}\Bigg[&\left(\prod_{\ell=1}^{L} e^{-\left(\frac{\Delta\tau}{N-1}\right)\vec{c}^{\dagger}_{\sigma}\mathcal{K}\vec{c}_{\sigma}} e^{\vec{c}^{\dagger}_{\sigma}\mathcal{V}^{(\ell)}(h)\vec{c}_{\sigma}}\right) \\ &\left(\prod_{\ell=1}^{L} e^{-\left(\frac{\Delta\tau}{N-1}\right)\vec{c}^{\dagger}_{\sigma'}\mathcal{K}\vec{c}_{\sigma'}} e^{\vec{c}^{\dagger}_{\sigma'}\mathcal{V}^{(\ell)}(-h)\vec{c}_{\sigma'}}\right)\Bigg]\Bigg\}. \end{aligned} \tag{A.22}$$

And from our knowledge from the $N = 2$ case, we know to how to express those two

traces:

$$Z \approx C_1 \prod_{\sigma} \prod_{\sigma'>\sigma} \left(\mathrm{Tr}_{h_{\sigma\sigma'}} \det \left[M_\sigma(h^{(\sigma,\sigma')}) \right] \det \left[M_{\sigma'}(-h^{(\sigma,\sigma')}) \right] \right), \tag{A.23}$$

where we explicitly indicate that the interaction between σ and σ' is encoded in a single $N_s \times L$ matrix,

$$M_\sigma(h^{(\sigma,\sigma')}) = \mathrm{Id} + B_{L,\sigma}(h_L^{(\sigma,\sigma')}) B_{L-1,\sigma}(h_{L-1}^{(\sigma,\sigma')}) \dots B_{1,\sigma}(h_1^{(\sigma,\sigma')}), \tag{A.24}$$

and the $B_{\ell,\sigma}$ matrices are:

$$B_{\ell,\sigma}(h_\ell^{(\sigma,\sigma')}) = e^{-\left(\frac{\Delta\tau}{N-1}\right)\mathcal{K}} e^{\mathcal{V}^{(\ell)}(h_\ell^{(\sigma,\sigma')})}. \tag{A.25}$$

Finally the expression gets simplified after noticing that we can also interchange the trace over all $h's$ with the products that we will simply denote as $\mathrm{Tr}_{\{h\}}$ (to indicate that there's now a whole set of auxiliary fields for each imaginary time slice), and we are left with:

$$Z \approx C_1 \mathrm{Tr}_{\{h\}} \left(\prod_{\sigma} \prod_{\sigma'>\sigma} \det \left[M_\sigma(h) \right] \det \left[M_{\sigma'}(-h) \right] \right). \tag{A.26}$$

And from here we have obtained:

$$\rho(\{h\}) = \frac{C_1}{Z} \left(\prod_{\sigma} \prod_{\sigma'>\sigma} \det \left[M_\sigma(h^{(\sigma,\sigma')}) \right] \det \left[M_{\sigma'}(-h^{(\sigma,\sigma')}) \right] \right), \tag{A.27}$$

that encodes the *probability distribution* to be stochastically sampled. As we can see, it is now the product of $N(N-1)$ determinants, however, all of the terms come in pairs of products of determinants, which therefore allows us to perform the Metropolis algorithm to each pair (σ, σ') straightforwardly (i.e. using the subroutines written for the $N = 2$ case), except that now one has more auxiliary fields and therefore has to

loop over the set of spin pairs.

A.3.2 Sanity check N=2 and N=3

For $N = 2$, we have $\sigma = 1, 2 = \uparrow, \downarrow$, and $\{h\} = h^{(1,2)}$ therefore,

$$\mathcal{P}(\{h\}) = \frac{C_1}{Z}\left(\det\left[M_\uparrow(h)\right] \det\left[M_\downarrow(-h)\right] \right), \tag{A.28}$$

which is consistent with our previous results.

For $N = 3$, we have $\sigma = 1, 2, 3$, and $\{h\} = \{h^{(1,2)}, h^{(1,3)}, h^{(2,3)}\}$ so:

$$\begin{aligned}\mathcal{P}(\{h\}) = \frac{C_1}{Z}&\left(\det\left[M_1(h^{(1,2)})\right] \det\left[M_2(-h^{(1,2)})\right] \right)\left(\det\left[M_1(h^{(1,3)})\right] \det\left[M_3(-h^{(1,3)})\right] \right) \\ &\times \left(\det\left[M_2(h^{(2,3)})\right] \det\left[M_3(-h^{(2,3)})\right] \right),\end{aligned} \tag{A.29}$$

A.3.3 Algorithm

Given that the interaction terms are pairwise, the Metropolis ratios are calculated in the same way for each pair (σ, σ') and therefore the algorithm is identically to the one for $N = 2$ except that now one also has to loop over the spin degree of freedom.

1. Initialize all the Hubbard-Stratonovich fields $\{h\}$.

2. Set $(\ell, \sigma, \sigma', i)$

3. Perform the $(\ell, \sigma, \sigma', i)-$loop.

   (a) Propose new configuration $h^{(\sigma,\sigma')}_{new}$ by flipping the site, ie. $h^{(\sigma,\sigma')}(\ell, i) \rightarrow -h^{(\sigma,\sigma')}(\ell, i)$

   (b) Compute Metropolis ratio. Note that this looks exactly like the $N = 2$ case because only the determinants that involve the $h^{(\sigma,\sigma')}$ field are connected, and so the other determinants remain the same and cancel out.

(c) Calculate the acceptance-rejection.

(d) Go to the next $(\ell, \sigma, \sigma', i)$, where:

- If $i < N_s$, $i \to i + 1$
- If $i = N_s$, $i \to 1$ and $\sigma' \to \sigma' + 1$
- And so on. Then update the σ and finally the imaginary time. Do so until you have have "walked" all the auxiliary fields.

(e) After warm ups, starting performing physical measurements, which are related to the Green's functions that are computed in the exact way that is done in the $N = 2$ case: $G^{\sigma}_{ij}(\ell = L) = \langle c_{i\sigma} c^{\dagger}_{j\sigma} \rangle = [M_{\sigma}(h)]^{-1}_{ij}$.

Appendix B

Non-ergodicites in the SU(N) FHM DQMC Algorithm

In this appendix we discuss some aspects regarding non-ergodicities in DQMC (commonly refered as *sticking*). First we discuss the structure of the interaction matrices for $N > 2$ in terms of the auxiliary Ising fields $h_{\sigma\tau}$, and then we discuss how *global moves* might be constructed to mitigate *sticking* issues.

In our DQMC algorithm the Hubbard Stratonovich transformation decouples each interaction term in terms of the difference to the operators $n_\sigma - n_\tau$. For $N = 2$ this corresponds to the local magnetization $n_\uparrow - n_\downarrow$ and the interaction matrices have the following form:

$$v_{\uparrow,\downarrow}(i) = \exp[\pm\lambda h(i)], \tag{B.1}$$

where the $\pm$ sign corresponds to $\uparrow, \downarrow$ respectively. For larger N, we have $\binom{N}{2}$ (σ, τ) pairs, and each term is decoupled in the $n_\sigma - n_\tau$ channel. We decided to follow the convention of assigning the plus sign to the terms with the lowest σ. This convention simplifies the coding and is easy to remember. For example, following that convention, the interaction matrices for SU(6) have the following form:

$$\begin{aligned}
v_1(i) &= \exp\left[\lambda\left(+h_{12}(i) + h_{13}(i) + h_{14}(i) + h_{15}(i) + h_{16}(i)\right)\right], \\
v_2(i) &= \exp\left[\lambda\left(-h_{12}(i) + h_{23}(i) + h_{24}(i) + h_{25}(i) + h_{26}(i)\right)\right], \\
v_3(i) &= \exp\left[\lambda\left(-h_{13}(i) - h_{23}(i) + h_{34}(i) + h_{35}(i) + h_{36}(i)\right)\right], \\
\vdots &= \vdots
\end{aligned}$$

which means that the $N(N-1)/2$ auxiliary Ising fields couple asymmetrically to each spin flavor. This has consequences in the efficiency of the *global moves* to mitigate

non-ergodicites, i.e. *sticking*. The best way to understand this is to look into the single-site limit, where we can write the Boltzmann weights for an arbitrary Hubbard-Stratonovich configuration.

Let's start with $N = 2$ in the single-site case. In this case, we have a single Hubbard-Stratonovich field $S^{12}(\tau)$ * and the determinants of the matrices that define the *probability distribution* only depend on $\Sigma^{12} \equiv \sum_\tau S^{12}(\tau)$, where we have L imaginary time slices τ:

$$\det_i = 1 + e^{\pm\lambda\Sigma^{12}+\beta\mu}, \tag{B.2}$$

where the $+$ sign is for $i = 1$ and the $-$ sign for $i = 2$. The weight of such configuration is given by $\det = \prod_i \det_i$, and therefore the weight for a given configuration of Σ^{12} is $\binom{L}{(L-|\Sigma^{12}|)/2} \prod_i \det_i$, where the binomial coefficient counts how many ways the $S^{12}(\tau)$ fields can be chosen to get a given Σ^{12}.

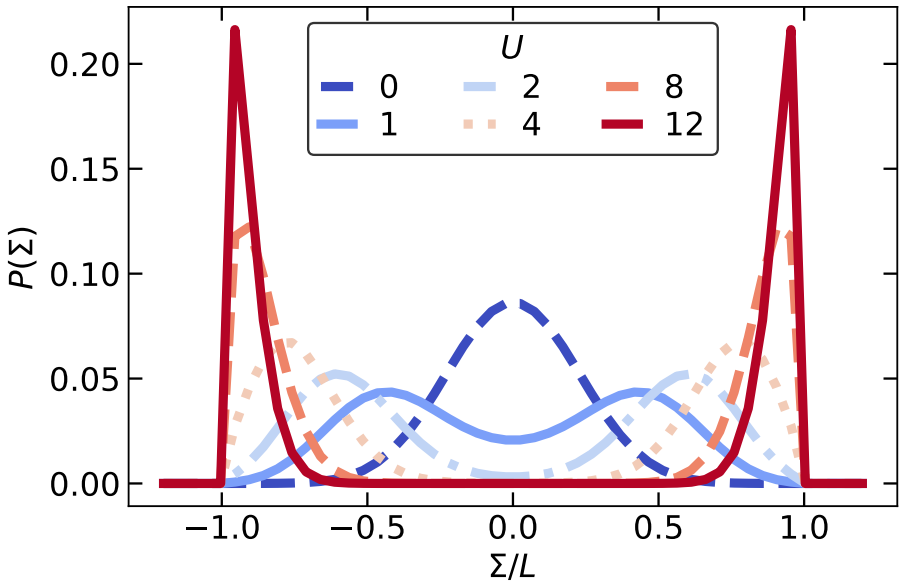

Figure B.1 : **Probability distributions for the Hubbard Stratonovich configurations for** $N = 2$. Results in the single-site limit for different values of U.

In Fig. B.1 we present the probability distributions for the different Hubbard-

*Here we use $S^{12}(\tau)$ to explicitly indicate we are working in the atomic limit, and corresponds to the value of the single-site auxiliary Ising field for the pair of spins 1 and 2 at the imaginary time slice τ.

Stratonovich configurations. As the interaction increases, the high probability configurations move towards $\Sigma^{12} = \pm L$, which correspond to configurations in which the site has $n_\downarrow \approx 1$ or $n_\uparrow \approx 1$, respectively. Furthermore, as the interaction strength increases, other values of Σ^{12} decrease their weight, and even vanish (for example at $U = 12$ near the $\Sigma^{12} = 0$ region). This is the origin of the *sticking*: single Ising spin flips in the Hubbard-Stratonovich fields cannot take us from one "bright spot" to the other, i.e they are unable to take us from the $\pm L$ configuration to the $\mp L$ configuration, since they would have to traverse a region of configurations with very low Boltzmann weights, which is render impossible since those moves would not be accepted by the Metropolis-Hastings algorithm. The ideal of *global move* is such that it allows us to visit the "bright spots", and in order to do, for $N = 2$ this is accomplished by performing the global update $\Sigma^{12} \iff -\Sigma^{12}$, which takes the system from the $\pm L$ configuration to the $\mp L$ configuration and therefore recovering the ergodicity of the algorithm. Moreover, since the probability of proposing the *global move* (identical for going $\pm$ to $\mp$ and viceversa), and its the probability of its acceptance depends on the Metropolis-ratio, this type of move preserves detailed balance. However, *global moves* come at a cost: when implementing this for the full Hamiltonian, one needs to compute $\det\left[M_\sigma(\{s\})\right]$ and $\det\left[M_\sigma(\{s'\})\right]$ for the configurations, which takes N_s^3 operations instead of N_s^2 for the single Ising spin flip.

Let us now analyze the case of $N = 3$ in the single site limit, which will illustrate how the pairwise Hubbard-Stratonovich decoupling affects the probability distributions of the Ising fields. For $N = 3$ we now have,

$$\det_1 = 1 + e^{\lambda(+\Sigma^{12}+\Sigma^{13})+\beta\mu}, \tag{B.3}$$

$$\det_2 = 1 + e^{\lambda(-\Sigma^{12}+\Sigma^{13})+\beta\mu}, \tag{B.4}$$

$$\det_3 = 1 + e^{\lambda(-\Sigma^{12}-\Sigma^{13})+\beta\mu}, \tag{B.5}$$

where $\Sigma^{ij} \equiv \sum_\tau S^{ij}(\tau)$, and $S^{ij}(\tau)$ is the Hubbard-Stratonovich field for the (σ_1, σ_2) interaction. We then compute the logarithm of the weight of such configuration, i.e. $\text{lndet} = \ln\left[\prod_i \det_i\right]$, as well as the logarithm of the products of the binomial coefficients: $\text{lnbinom} = \ln\left[\prod_{i<j} \binom{L}{(L-|\Sigma^{ij}|)/2}\right]$. In this way we can study the weight for a given configuration of Σ^{ij}'s by looking at lndet + lnbinom.

In Fig. B.2 we present lndet, lndet+lnbinom, the density $\rho = \langle n \rangle$, and the individual densities $\langle n_\sigma \rangle$ for different values of the auxiliary fields at an interaction strength of 15.3 and temperature of 1 in the atomic limit. For simplicity we present only 3 values of Σ^{23}/L while we present contour plots with axis Σ^{12}/L and Σ^{13}/L. In this figure we observe how the location of the "bright spot" depends on the configuration of the auxiliary fields (see Table B.1).

Σ^{12}	Σ^{13}	Σ^{23}	Dominant n_σ
0	$-L$	$-L$	n_3
L	L	0	n_1
$-L$	0	L	n_2

Table B.1 : "Bright spots" locations for $N = 3$ and the dominant flavor density for that configuration.

Currently, the DQMC algorithm incorporates the set of all possible $N = 2$-type *global moves* i.e. $\Sigma^{ij} \iff -\Sigma^{ij}$ for all ij pairs. The whole set of moves allows for the exploration of all "bright spots" in the auxiliary field configuration preserving ergodicity (although the connection between different "bright spots" only occurs after a few steps), and by construction respecting detailed balance. In practice we have found that using **numtry**=4 [†] in the algorithm we can mitigate *sticking* for values of $U/t \lesssim 15$ at temperatures and densities where the *sign problem* is still manageable. Additionally, we diagnose *sticking* by observing that the SU(N) symmetry is preserved in the individual spin populations $\langle n_\sigma \rangle = \rho/N$, the two-point correlators

[†]The argument **numtry** controls the number of times a single $N = 2$-type of *global move* is attempted for each auxiliary field Σ^{ij}.

$\langle n_\sigma n_\tau \rangle = \langle n_\alpha n_\gamma \rangle \, \forall (\sigma, \tau), (\alpha, \gamma)$, and the error bars of both quantities. We only analyze data when the SU(N) symmetry is conserved within the error bars of the observables and if the error bars are not anomalously small.

As a future direction, similarly to the $N = 2$ case, locating the "bright spots" allows one to propose efficient *global moves* that take you from one high probability configuration to another one in single step. For the $N = 3$ followed by the "bright spot" corresponds to a triangle in a three-dimensional space with the vertices given by the first three columns of Table B.1. Visualizing this for other higher values of N becomes more cumbersome, but will be needed if more efficient *global moves* want to be incorporated.

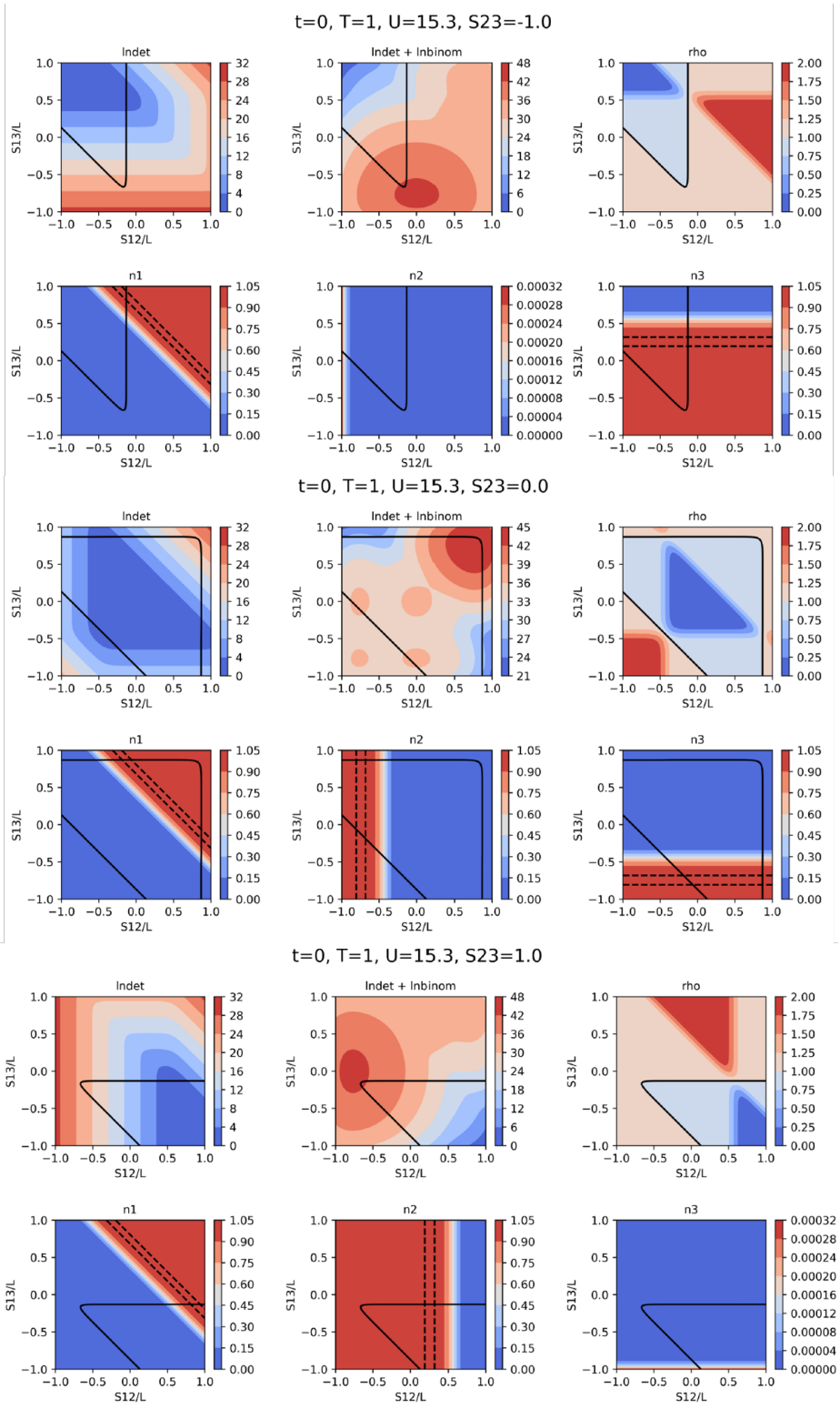

Figure B.2 : **Probability distributions for the Hubbard Stratonovich configurations for** $N = 3$. Results for different configurations of the Hubbard-Stratonovich fields for SU(3) in the atomic limit. Solid black line corresponds to $\langle n \rangle = 1$ and dashed lines to $\langle n_\sigma \rangle = 0.99$ and 0.999.

Appendix C

Convergence tests for the SU(N) FHM DQMC Algorithm

We developed the DQMC and ED simultaneously in the group and therefore we needed to run tests to check their convergence. We performed tests against:

- The atomic limit ($t = 0$), which allows us to check the interaction energy term of the Hamiltonian. In Fig. C.1 we compare some DQMC results against the atomic limit and we observe good convergence.

- The non-interacting limit ($U = 0$), which allows us to check the kinetic energy term of the Hamiltonian. In Fig. C.2 we compare some DQMC results against the non-interacting limit and we also observe good convergence.

- The $N = 2$ limit for $U \neq 0$ and $t \neq 0$, which allows to check that looping over the spin flavors is working correctly and we can reproduce the results of codes that only deal with $N = 2$ and are well established in the literature. In Fig. C.3 we compare some DQMC and ED results against the established $N = 2$ code and we observe convergence.

- Against each other for $N > 2$, $U \neq 0$, and $t \neq 0$. In Fig. C.4 we compare DQMC and ED results for $N = 3$ and $N = 6$ code. We observe how they both converge as we relax the Hilbert space truncation.

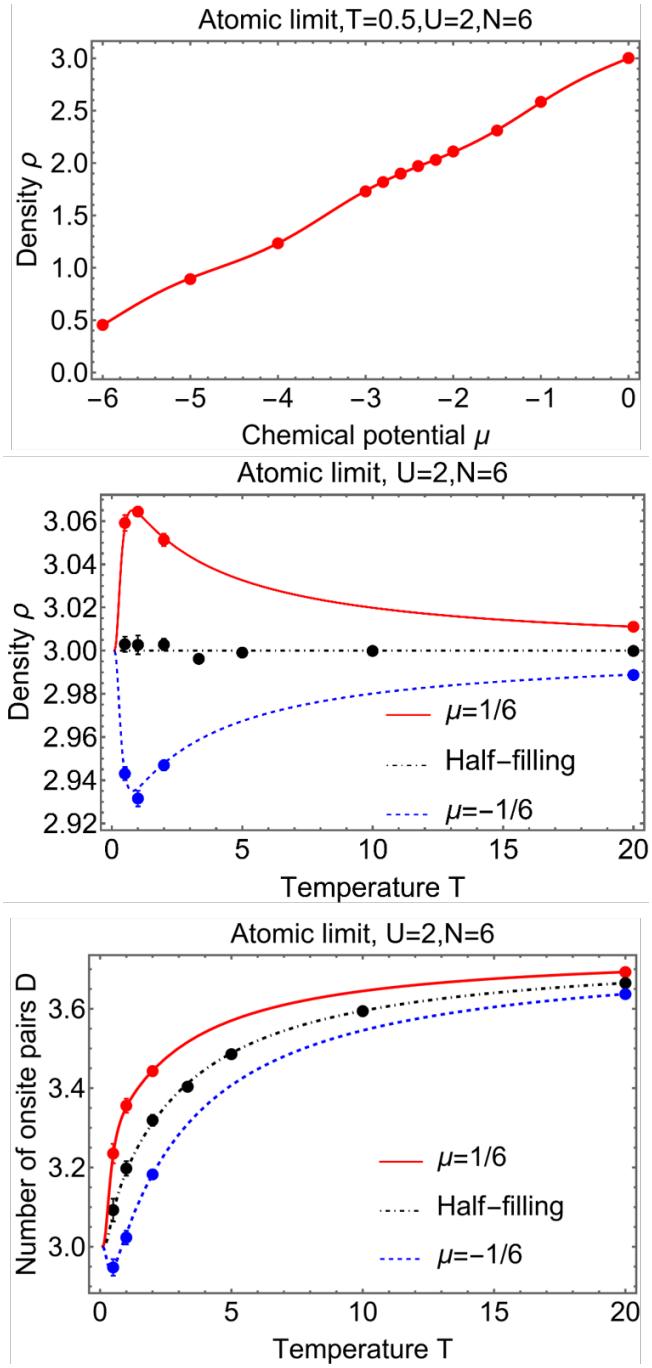

Figure C.1 : **DQMC tests vs the atomic limit**. Results for the density and the number of on-site pairs as a function of the chemical potential or the temperature. Markers correspond to DQMC and lines to the $t = 0$ limit.

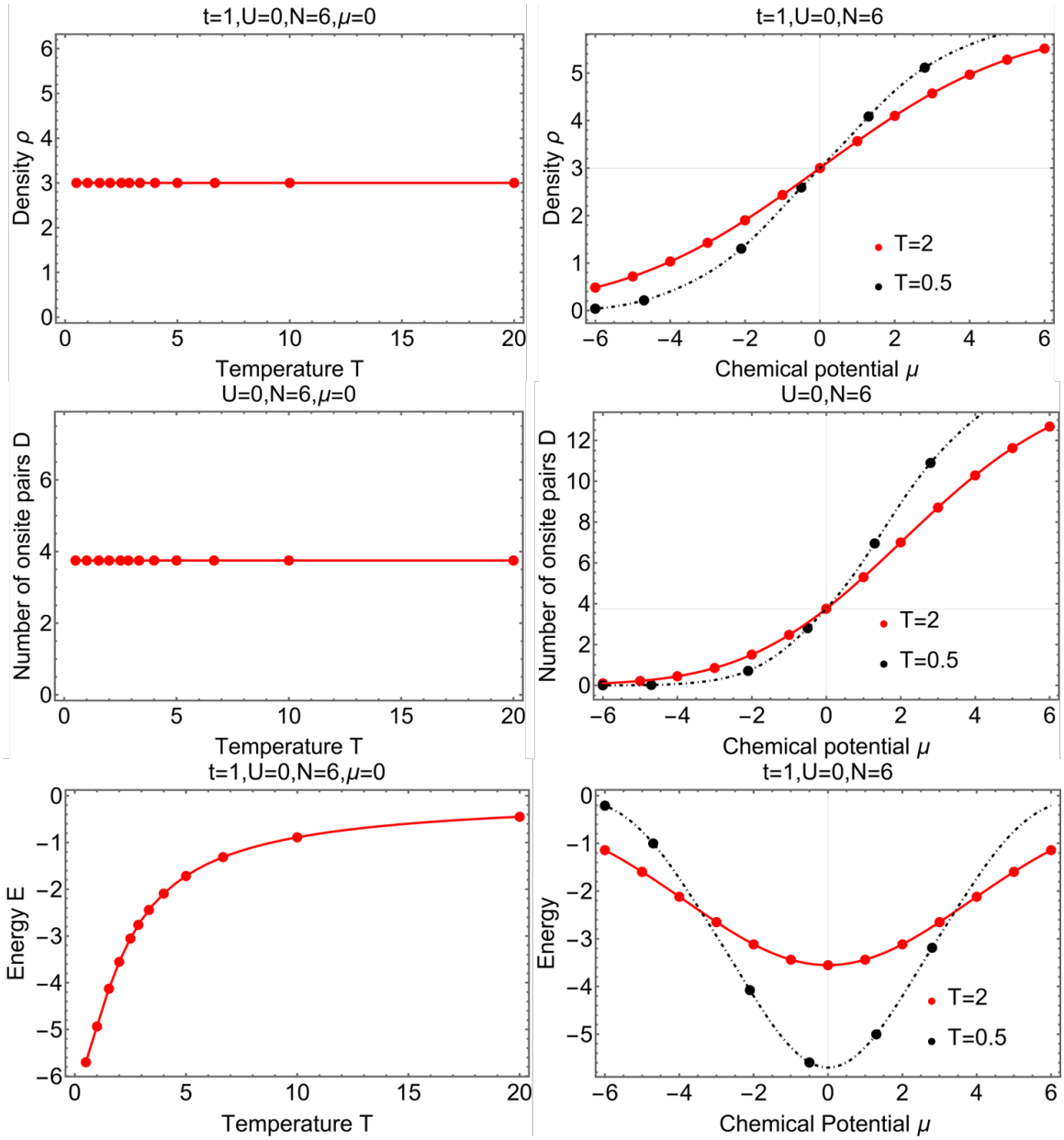

Figure C.2 : **DQMC tests vs the non-interacting limit**. Results for the density, number of on-site pairs, and the kinetic energy as a function of the chemical potential or the temperature. Markers correspond to DQMC and lines to the $U = 0$ limit.

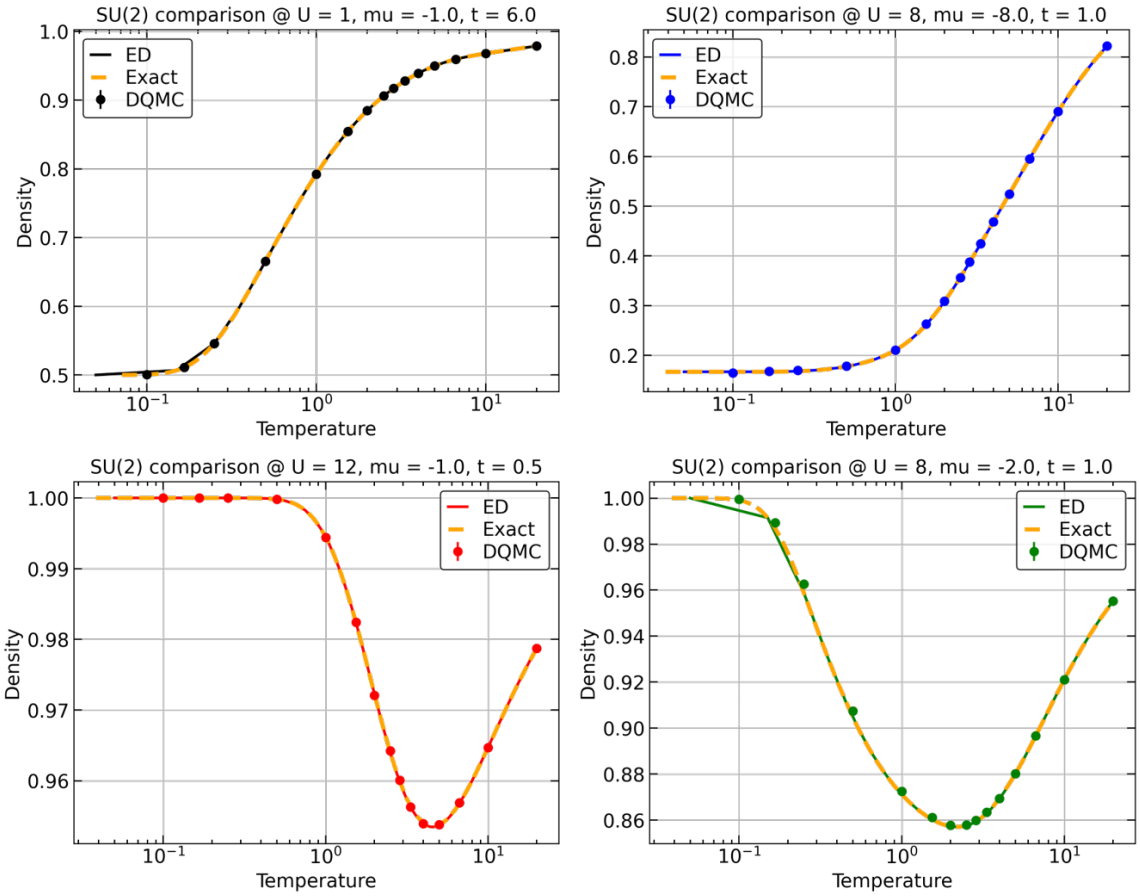

Figure C.3 : **DQMC tests and ED tests for** $N = 2$. Results for the density as a function of temperature at different values of U, t, μ. Markers correspond to DQMC, solid lines to the SU(N) ED code, and dashed orange lines to an ED code that only deals with $N = 2$.

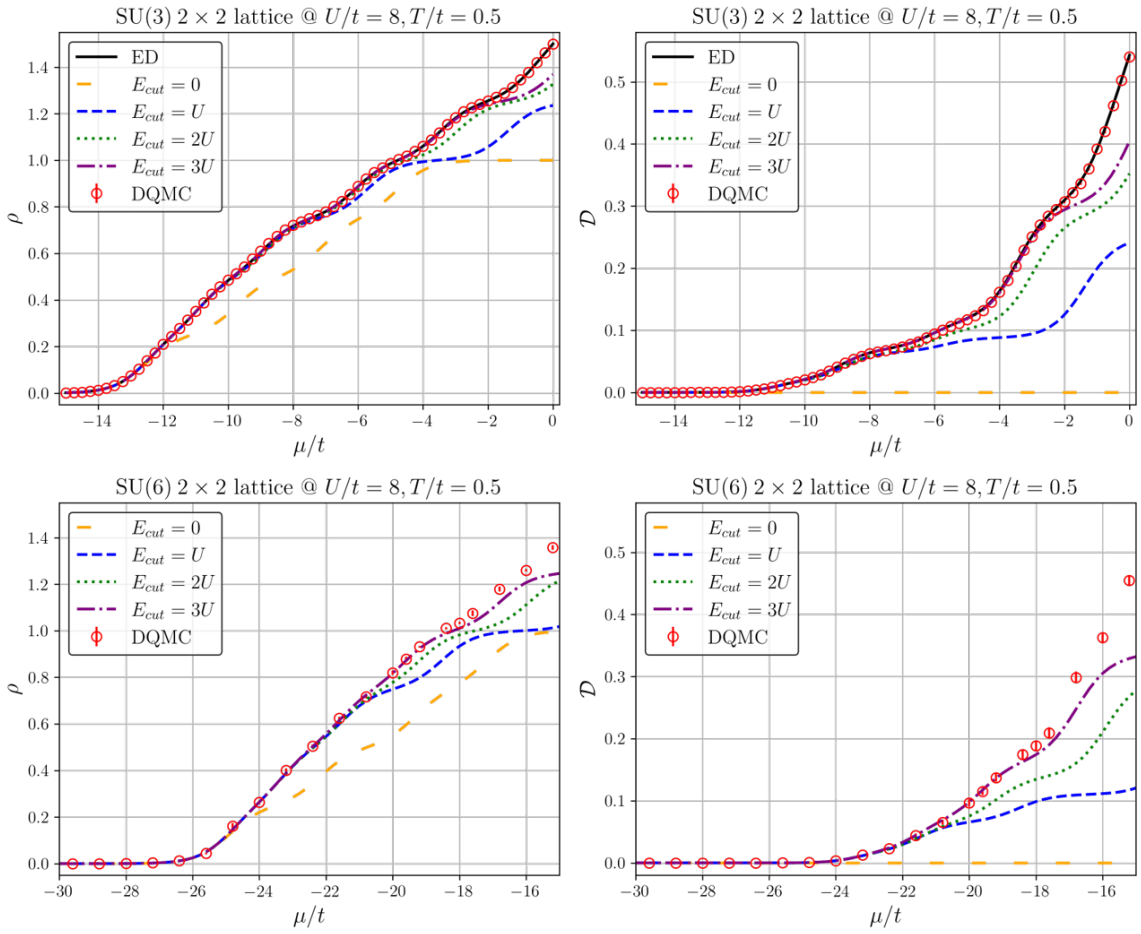

Figure C.4 : **DQMC tests and ED tests for $N = 3$ and $N = 6$.** Results for the density and the number of on-site pairs as a function of the chemical potential at fixed U/t and T/t. Markers correspond to DQMC, lines to the SU(N) ED code for different Hilbert space truncations (basis states with an on-site energy larger than the energy cutoff E_{cut} are disregarded). Solid black line correspond to a full ED calculation.